Title

Exciton-Polariton Complexes in Chip-Scale Cavity Quantum Electrodynamics: Localized Single-Site Arrays and Color Centers

Author

Huang, Jiahui

Publication Date

2024

Peer reviewed|Thesis/dissertation

UNIVERSITY OF CALIFORNIA

Los Angeles

Exciton-Polariton Complexes in Chip-Scale Cavity Quantum Electrodynamics: Localized Single-Site Arrays and Color Centers

A dissertation submitted in partial satisfaction of

the requirements for the degree

Doctor of Philosophy in Electrical and Computer Engineering

by

Jiahui Huang

2024

ABSTRACT OF THE DISSERTATION

Exciton-Polariton Complexes in Chip-Scale Cavity Quantum Electrodynamics: Localized Single-Site Arrays and Color Centers

by

Jiahui Huang

Doctor of Philosophy in Electrical and

Computer Engineering

University of California, Los Angeles, 2024

Professor Chee Wei Wong, Chair

Single photons are flying qubits which can carry quantum information over long distances with low decoherence. Integrated quantum photonics, which aims to generate, process, and detect single photons on tiny chips with minimum environment-induced decoherence essential for quantum information processing, has become the core of current quantum technology towards quantum computing, quantum communication, and quantum metrology.

Such applications require material platforms which can support single photon emitters with suitable properties, such as high single-photon purity, lifetime-limited spectral linewidth. high indistinguishability, near-unitary state preparation efficiency, and near unitary quantum efficiency, etc. Decoherence induced by environmental charge fluctuation and phonon scattering are also important factors to be considered in semiconductor-based platforms. In addition, site controllability of single photon emitters to be placed at the designed location is required for

reproducible fabrication of monolithic integrated quantum photonic devices in large scale with multiple single photon emitters. On the other hand, single photon emitters in the telecom band are beneficial for building metro scale quantum networks such that the computational power of induvial quantum processors can be scaled up using telecom fiber-based architecture.

Site-controlled pyramidal InGaAs quantum dots system as single photon emitters enable placing many quantum dots at designed positions in photonic structures with nanometer scale precisions which provides great potential for large scale integrated quantum photonic devices. However, previous studies on such quantum dots embedded in photonic crystal cavities suffer from low cavity quality factor which limits its operation at the weak coupling regime. In this thesis, we improve the cavity quality factor up to 12,000 by red shifting the emission energy of the quantum dot to ~ 1.24 eV and optimizing the photonic crystal cavity design. We demonstrate the coexisting strong-weak (intermediate) coupling and onset of strong coupling regime. We reveal the role of phonon scattering and exciton dephasing during QD-cavity interactions and further demonstrate a Rabi-like oscillation of luminescence intensity and energy splitting between excitonic and photonic components which occurs only at small QD-cavity detuning and can be well reproduced by our cavity quantum electrodynamics modeling. It represents milestone for device optimization of such quantum dot systems to realize strong coupling regime with applications in coherent control of site-controlled quantum states for quantum information processing. We further explore multi-site-controlled quantum dots systems in a spatially extended cavity mode pattern such that the quantum dot emission exhibits novel spatial features linked to quantum mode interference which enables applications in optical switching for quantum information routing in monolithic integrated quantum photonic circuits. This thesis also explores using silicon color centers as single photon emitters considering its telecom emission wavelength and mature silicon-based integrated photonic

and electronic platform. We explore T centers and transition-metal color centers for high-fidelity telecom spin-photon interfaces. We study the fabrication process of generating T centers and copper-related defects with reduced lattice distortion with their photophysics properties closer to ab initio calculations. The cryogenic photoluminescence and electron spin resonance studies on copper-related defects suggests its unpaired electrons as alternative candidates to T centers for high fidelity spin-photon interfaces.

The dissertation of Jiahui Huang is approved.

Elyahou Kapon

Hong-Wen Jiang

Kang Lung Wang

Wesley C Campbell

Chee Wei Wong, Committee Chair

University of California, Los Angeles

2024

This dissertation is dedicated to my family for their unwavering support.

TABLE OF CONTENTS

List of Figures x

List of Tables ..... **xv**

Abbreviations ..... **xvi**

Acknowledgements ..... **xviii**

Vita ..... **xx**

1. Introduction **1**

1.1 Integrated Quantum Photonics 1

1.2 Site-Controlled Pyramidal Quantum Dots as Single Photon Emitters 5

1.3 Silicon Color Centers as Single Photon Emitters 7

1.4 Photonic Crystal Cavities 11

1.5 Cavity Quantum Electrodynamics 12

1.6 Experimental Methods: Microphotoluminescence Spectroscopy 18

1.7 Numerical Methods: Finite-Difference Time Domain Simulations 26

1.8 Numerical Methods: Quantum Toolbox 28

1.9 Thesis organizations 32

2. Single Site-Controlled Quantum Dot-Nanocavity Operating in the Coexisting Strong-Weak (*Intermediate*) Coupling Regime **35**

2.1 Overview and Introduction 35

2.2 Site-Controlled InGaAs QD-L3 PhC cavity Devices 38

2.3 Exciton Complexes and Pure Dephasing in the Single Site-Controlled InGaAs QD- L3 PhC Cavity 40

2.4 Coexisting Strong-Weak (*Intermediate*) Coupling Regime in Single Site-Controlled InGaAs QD-L3 PhC cavity 46

2.5 Span of Degree of Linear Polarizations in the Coexisting Strong-Weak (*Intermediate*) Coupling Regime 53

2.6 Anti-Bunching and Collective State Photon Statistics in the Coexisting Strong-Weak (*Intermediate*) Coupling Regime. 56

2.7 Discussions. 61

3. Single Site-Controlled Quantum Dot-Nanocavity Operating in the Onset of Strong Coupling Regime 63

3.1 Introduction 63

3.2 Site-Controlled InGaAs QD-L7 PhC cavity Devices 66

3.3 Optical Properties and Recombination Dynamics 66

3.4 Phonon Dynamics and Dephasing Toward the Strong Coupling Regime 73

3.5 Rabi Oscillation and Quantum Beating of Coupled Spectral Components 84

3.6 Discussions 91

4. Spatially Resolved Landscapes of Exciton-Photon Polaritons with Multi-Site-Controlled Quantum Dots in Extended Cavity Modes 93

4.1 Introduction 93

4.2 Concept of the Multi-QD Devices and Observed Spatial Features 95

4.3 Optical Properties 97

4.4 Spatially Avoided Crossing of QD Excitons with CM1 104

4.5 Proposed Spatially Distributed Single-Photon Source 110

4.6 Discussions 113

5. Photophysics of O-band and Transition Metal Color Centers in Monolithic Silicon for Quantum Communications 114

5.1 Overview and Introduction 114

5.2 Sample Preparation and Process Variations 117

5.3 Statistical Variations of T center and *Cu PL emissions 125

5.4 Temperature-Dependent Microphotoluminescence Spectroscopy of T-center and ∗Cu center Emissions 128

5.5 Photoluminescence Dynamics of T-center and ∗Cu Center Emissions 135

5.6 Magnetic-Field Induced Broadening in the Ensemble $^{*}Cu^{m}_{n}$ Color Centers 141

5.7 Discussions 144

References 149

LIST OF FIGURES

1.1 Schematics of an integrated quantum photonic circuit using photonic crystal platforms 2

1.2 T center structure and energy levels 10

1.3 Energy level diagrams of the atom + cavity system 15

1.4 Energy level diagrams of the atom + cavity system as a function of detuning in the presence of the interaction Hamiltonian 15

1.5 A photo of μPL setup for characterizing site-controlled InGaAs QD systems built in Engineering VI building at UCLA 18

1.6 Schematic of the μPL setup 19

1.7 Schematic of the μPL setup combined with HBT measurement 23

1.8 Schematic of the time-resolved PL setup 25

1.9 Spatial distribution of the Electric field intensity of the first four cavity modes of a GaAs-based L7 PhC cavity using 3D FDTD methods 28

1.10 An example power spectrum of a QD-cavity system with varying pure dephasing rate from 0 – 80 μeV with 5 μeV step 31

2.1 3D FPTD simulation of the PhC membrane and L3 cavity 39

2.2 Exciton complexes and dark excitons in single site-controlled InGaAs QD-L3 PhC cavity .41

2.3 Dark exciton and its high-resolution fine structure, along with measurements in another QD-cavity sample 45

2.4 Power dependent μPL of X measured with 532 nm and 900 nm pump 46

2.5 Observations of the coexisting strong-weak coupling regimes probed by high-resolution cryogenic spectroscopy and stepped temperature dependent μPL 48

2.6 Example CM and X spectrum presented in Fig 2 fitted by double/single-Lorentzian function 49

2.7 QD-cavity detuning by varying temperature in the case of occasional blue-shift of CM due to the PhC membrane surface state change 52

2.8 Phonon-assisted coupling examined by the degree of linear polarization (DOLP).....53

2.9 Schematic of QD decay channel in a cavity 55

2.10 Polarization resolved μPL of X- at 25 K 56

2.11 Exciton dynamics and photon statistics of the site-controlled QD-cavity subsystem in the coexisting strong-weak (intermediate) coupling regime 58

2.12 μPL spectra of coupled X-CM with tunable long and short pass filtering 59

3.1 μPL spectra of site-controlled QD-L7 cavity 66

3.2 Second-order correlation function of the QD-L7 cavity system when QD and CM are coupled (T = 50 K) 67

3.3 Polarization-resolved μPL of the QD-L7 cavity system 68

3.4 Time-resolved PL measurement on QD-L7 cavity system 69

3.5 Power dependent time-resolved PL measurement on coupled QD-L7 cavity system 70

3.6 Power dependent PL measurement of QD and CM when they are decoupled 71

3.7 Power dependence of decay time 72

3.8 Temperature tuning of QD-cavity coupling 73

3.9 Double and single Lorentzian fits to the PL spectra at T = 47 K to 48.05 K 74

3.10 Temperature-dependent energy, intensity ratio, and linewidth extracted from Fig 3.9 75

3.11 cQED modeling of phonon-mediated QD-cavity coupling 78

3.12 Temperature tuning of QD-cavity coupling at 30 μW 80

3.13 cQED modeling of phonon-mediated QD-cavity coupling at 30 μW 81

3.14 cQED modeling of QD-cavity coupling without the phonon scattering 84

3.15 Power dependent PL spectra of two detuning cases 85

3.16 Power dependent Rabi-like oscillation of the coupled QD-cavity at small detuning ($\Delta 1 \approx$ 70 μeV) 86

3.17 PL spectrum at T = 46.6 K as a function of excitation power with 900 nm laser (20MHz) up to 480 μW 88

3.18 Integrated PL intensity of QD and CM as a function of excitation power for the small detuning case ($\Delta 1 \approx 70$μeV) using 532 nm cw laser 88

3.19 Blurring-out of Rabi-like oscillation of the coupled QD-cavity at larger detuning ($\Delta 2 \approx$ 137 μeV) 89

3.20 Power dependent PL and energy of QD and CM of two detuning cases 90

4.1 Schematic illustration of the experimental results 96

4.2 3D FDTD simulation of L7 PhC cavity mode pattern 97

4.3 PL spectra of all 4QD-L7 cavity devices using a large laser spot exciting all four QDs with high pump power (λexc = 785nm, Pexc = 5μW) 98

4.4 Spatial- and spectral-scanning map of four-QD exciton emissions for device 1 (a) and device 2 (b) at T = 10 K. 99

4.5 Second-order correlation measurements of (a) 1QD and (b) 4QD in a L7 PhC cavity 101

4.6 Temperature-dependent polarization-resolved μPL of device 1 102

4.7 Temperature-dependent polarization-resolved μPL of device 2 103

4.8 Imaging of the position-wavelength map of QD excitons and CM1 for device 1 at varying temperatures 105

4.9 Imaging of the position-wavelength map of QD excitons and CM1 for device 2 at varying temperatures 108

4.10 Spatial- and spectrally-measurements of device 3 for reference 109

4.11 Schematic of a proposed spatially distributed single-photon source 112

5.1 Family of color centers in silicon and the T center generation recipe. FIG. 1. Family of color centers in silicon and the T center generation recipe 118

5.2 SIMS profile of a silicon sample with PL emission corresponding to ∗Cu 122

5.3 Cryogenic μPL characterization of TX0, TX1 and $*Cu_m^n$ transitions in silicon 123

5.4 Statistical variations of T center PL emission over a FZ Silicon substrate 126

5.5 Statistical variations of ∗Cu01 and ∗Cu00 PL emission over a FZ Silicon substrate 127

5.6 Temperature-dependent PL spectra of *Cu emission 128

5.7 Polarization-dependent PL intensity of the T center and *Cu center emission 128

5.8 Temperature-dependent PL peak energy of the T center and *Cu center emission 129

5.9 Temperature-dependent peak energy difference of the T center and *Cu center emission ..131

5.10 Temperature-dependent PL intensity of the T center and *Cu center emission 133

5.11 Temperature-dependent linewidth of the T center and *Cu center emission 134

5.12 T center and *Cu bound exciton radiative dynamics 136

5.13 G center exciton radiative dynamics 137

5.14 Magnetic-field induced broadening in the ensemble of 0.56 meV-split doublet luminescence centers 143

5.15 Time evolution of occupation probability of TX0 exciton and photon in the strong coupling regime 145

LIST OF TABLES

1.1 Transition properties of ensemble T centers and single T centers in micropuck structures based on 28Si system 10

1.2 Milestones of site-controlled pyramidal InGaAs QD systems towards strong coupling regime 33

2.1 Value and standard error of energy, linewidth, and intensity as fitting parameters in the double/single Lorentzian fit 49

5.1 Comparison of quantum properties of InGaAs QDs and silicon T centers 147

ABBREVIATIONS

AR	Augmented Reality
CM	Cavity Mode
cQED	Cavity Quantum Electrodynamics
DBR	Distributed Bragg Reflector
DOLP	Degree of Linear Polarization
EBL	Electron Beam Lithography
ESR	Electron Spin Resonance
FM	Free Space Mode
FSS	Fine Structure Splitting
HBT	Hanbury-Brown and Twiss
FWHM	Full-Width-at-Half-Maximum
IRF	Instrument Response Function
JC	Jaynes-Cummings
LDOS	Local Density of States
MBE	Molecular Beam Epitaxy
MOVPE	Metalorganic Vapor-Phase Epitaxy
N. A.	Numerical Aperture
NIR	Near Infrared
NSOM	Near-Field Scanning Optical Microscope
NV	Nitrogen Vacancy
PhC	Photonic Crystal

PML	Perfectly Matched Layer
PMT	Photomultiplier Tube
PSB	Phonon Sideband
QD	Quantum Dot
QW	Quantum Well
QWR	Quantum Wire
RTA	Rapid Thermal Annealing
SIMS	Secondary Ion Mass Spectroscopy
SK	Stranski-Krastanov
SNR	Signal-to-Noise Ratio
SOI	Silicon-on-Insulator
SPE	Single Photon Emitter
SRH	Shockley-Read-Hall
SNSPD	Superconducting Nanowire Single Photon Detector
TCSPC	Time Correlated Single Photon Counting
TE	Transverse Electric
TO	Transverse Optical
TRPL	Time-Resolved Photoluminescence
VR	Virtual Reality
VRS	Vacuum Rabi Splitting
WG	Waveguide
ZPL	Zero Photon Line
μPL	Microphotoluminescence

ACKNOWLEDGEMENT

I would like to acknowledge that the site-controlled pyramidal InGaAs QD samples studied in this work were designed, fabricated, and provided by Prof. Eli Kapon's group including contributions from Dr. Benjamin Dwir, Dr. Alok Rudra, and Dr. Alessio Miranda at EPFL. The clean-room fabrication of silicon T centers and *Cu centers were performed by Murat Can Sarihan at UCLA and I participated in such fabrications.

I performed all optical measurements and data analysis presented in this work, except for the (1) SIMS profile of Cu and Ag concentration in silicon wafer (Fig 5.2), TRPL measurement of *Cu centers (Fig 5.12(c)), and modeling of T center integrated in an *L*5 PhC cavity (Fig 5.15) which are performed by Murat Can Sarihan and (2) ESR measurement of *Cu centers (Fig 5.14(b)) which is performed in Material Research Laboratory at UCSB. For cQED modeling in chapter 3, the code using Quantum Optics Toolbox was written by Dr. Xiang Cheng. Dr. Wei Liu and I jointly performed such cQED modeling. I performed all FDTD simulations in this work, except for the *L*3 PhC cavity simulation (Fig 2.1) which is performed by Murat Can Sarihan.

I would like to express my gratitude to my advisor Prof. Chee Wei Wong for his invaluable guidance and unwavering support throughout my academic journey. As my supervisor, he has not only provided me with financial support and academic guidance but has also provided me with many opportunities for training my technical skills at national laboratories. I am very grateful for Prof. Wong's insightful suggestions, engaging discussions, and the autonomy he granted me to explore innovative ideas.

Special thanks go to all members of the Fang Lu Mesoscopic Optics and Quantum Electronics Laboratory at UCLA. In particular, I am deeply grateful to Dr. Wei Liu for his exceptional guidance, supervision, and countless discussions on improving the experimental platform in the lab and also experimental details and physical insights, which contributed significantly to the work on site-controlled quantum dots presented in this thesis; Dr. Yujin Cho for her guidance for my training on laser alignment and building the prototype photoluminescence setup in the lab; Murat Can Sarihan for our cooperative studies and discussions on silicon color centers; Dr. Xiang Cheng for his discussion on cavity quantum electrodynamics simulations; Dr. Kai-Chi Chang for helping setting up the superconducting nanowire single-photon detectors (SNSPDs).

I would like to thank our collaborators: Prof. Eli Kapon for providing the site-controlled quantum dot samples fabricated at EPFL which constitute the studies presented in chapter 2-4 of this thesis and helping with manuscript revision, and many insightful discussions; Dr. Baolai Liang, who provided countless technical guidance when we were doing measurements in the INML, CNSI; Dr. Han Htoon who taught me the skills for microphotoluminescence spectroscopy during my visit at Los Alamos National Laboratory.

Finally, I extend my heartfelt appreciation to my parents for their unwavering support and love. Their encouragement, patience, and sacrifices have deeply shaped my journey and enabled me to reach my current position. Lastly, I deeply appreciate my girlfriend Shengjie Li. This thesis cannot be completed without her priceless encouragement and love.

VITA

2013-2016 B.S. (Physics), University of Illinois, Urbana-Champaign, USA

2016-2018 M.S. (Electrical and Computer Engineering), University of California, Los Angeles, USA

2018-2024 Ph.D. Candidate (Electrical and Computer Engineering), University of California, Los Angeles, USA

Chapter 1

Introduction

1.1 Integrated Quantum Photonics

Integrated electronic circuit (or integrated electronics) for processing currents (electrons) is the basic building block of modern computing and information technology. In analogy, integrated photonic circuits (or integrated photonics) have also been developed for decades in parallel with electronic aspect. Such developments lead to miniaturized photonic devices for on-chip information generation, processing, and detection, with applications including but not limited to building optical communication networks, optical sensing, light detection and ranging (Lidar), optical processors, and consumer optical devices such as augmented reality (AR) and virtual reality (VR).

The theory of quantum mechanical description of light has brought people's attention to the optical phenomena at the nanoscale where energy of the light is quantized with the smallest quanta called photons. Combined with the technology of integrated photonics, a new area, so-called integrated quantum photonics has become the core of current quantum technology towards the development of quantum computing, quantum communication, and quantum networks. Integrated quantum photonics are different from classical integrated photonics in the sense that light generation, processing, and detection in a level of single or few photons which are flying quantum bits (qubits). As demonstrated in Figure 1.1, the manipulation of single photons requires the exploration of suitable systems for (1) single photon generation consisting of single photon emitters (SPEs) which can generates bright indistinguishable high-purity single photons, including using semiconductor quantum dots (QDs) [1]–[9], color centers in crystals (Diamond [10]–[20],

Silicon [21]–[31], Silicon carbides [32]–[39], etc), defects in two-dimensional materials [40]–[48], and carbon nanotubes [49]–[53], etc. (2) single photon processing consisting of integrated photonic structures, such as high quality (Q) factor photonic crystal (PhC) cavities [54]–[59] which confines light in the subwavelength scale where the light-matter interaction can occur or evanescently coupled PhC waveguides (WGs) [60]. Such nanoscale quantum electrodynamic (QED) interactions between the dipoles from the embedded emitter and confined photons can induce the modification of exciton decay rates and spatial emission profile through Purcell effects [61] in the

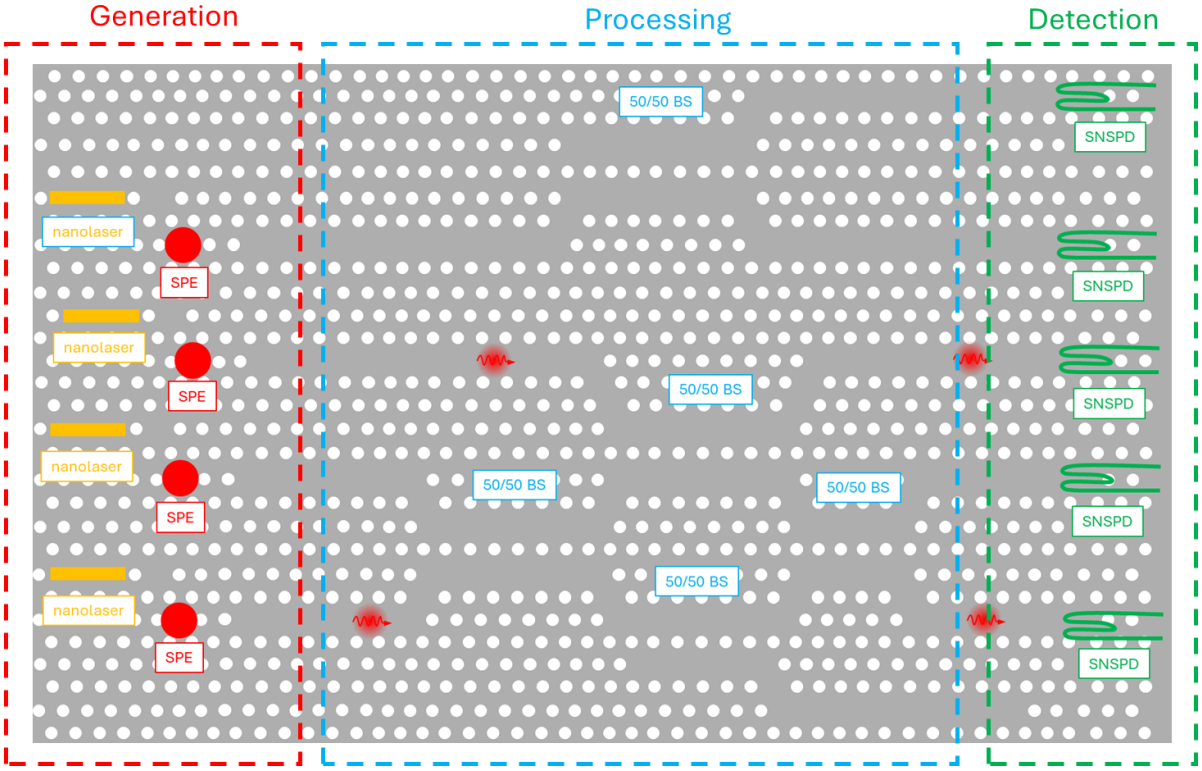

FIG 1.1 | Schematics of an integrated quantum photonic circuit using photonic crystal platforms. This device is suitable for gate operations with three regions of single photon generations using nanolasers and single photon emitters (red dash box), single photon processing using combinations of photonic crystal waveguides and 50/50 beam splitters (blue dash box), and single photon detections using on-chip superconducting nanowire single-photon detectors (green dash box).

weak coupling regime or exciton-polaritons through vacuum Rabi splitting in the strong coupling regime [62],[63]; (3) single photon detection ideally consisting of low jitter fully integrated on-chip superconducting nanowire single-photon detectors (SNSPDs) [64]–[69]. Importantly, benefiting from current nanofabrication technologies, having all these components on tiny integrated chips at the microscopic scale can prevent the system from environment-induced quantum decoherence which is essential for on-chip quantum information processing.

There are several considerations for characterizing SPEs suitable for integrated quantum photonic devices. Firstly, a general requirement for an ideal SPE is that they should exhibit high single-photon purity, lifetime-limited emission linewidth, high indistinguishability, near-unitary state preparation efficiency, and near-unitary quantum efficiency with minimal "blinking" effects. In a semiconducting environment, fluctuating charge-induced pure dephasing [70],[71], phonon scattering [72],[73], possible non-radiative decay channels, phonon sideband (PSB) or Auger channels can be detrimental [74]. But notably, in cavity QED, pure dephasing and phonon scattering are necessary for SPE non-resonantly coupling with cavities [75]–[77]. Additionally, for application requiring sending photons to remote locations via optical fibers, SPEs are required to emit in the telecommunication O-band (1310 nm) or C-band (1550 nm) for minimized dispersion and losses [78]. Secondly, for practical devices, precise controllability of the position of SPEs needs to be demonstrated for deterministic integration with complicated photonic crystal structures. Such controllability of positions also facilitates the capability to fabricate a large array of devices for statistical analysis of the functionality and enables scalability. Thirdly, certain applications require on-demand entangled photon generation at high photon flux, such as polarization-entangled [79]–[81], time-bin entangled [82], [83], hyper-entangled photons [84]. SPEs with long-lived coherent spin states, as matter qubits, can be entangled with emitted photons for the

realization of spin-photon interface [30], [85]–[90] and photonic cluster states [91]–[98] towards quantum memory.

Next, for photon processing using PhC structures, nanofabrication cannot prevent disorders in the PhC lattice which could induce photon losses [99]–[101] and Anderson localizations [102]–[107], which are photonic localized density of states (LDOS). However, study has shown that the disorder can also be used as resource rather than being considered as a nuisance [107]. Additioanlly, PhC structures are sensitive to surface states which are detrimental in certain scenerios but it can also be used as resources when used in a controlled way, such as tuning PhC cavity resonance [108]–[111].

In this thesis, we focus on two SPE systems and each exhibits part of the abovementioned properties making them suitable for certain applications. So far, the brightness SPE is InGaAs QD whose emits in the wavelength range of 850-1000 nm [9], [112], [113]. We firstly focus on the site-controlled pyramidal InGaAs QD system which exhibits precise controllability of position and emission energy, high symmetry, absence of wetting layer, and great scalability. All these features, in stark contrast with self-assembled QD system, make site-controlled QD systems an ideal platform for on-chip quantum information processing. However, QDs directly emitting in telecom band have not reached an overall high performance compared to InGaAs QD [112]. We will also explore the potential of using telecom silicon color centers for silicon quantum memories and quantum networks based on the consideration of dominant, scalable, and well-developed nanoelectronic and nanophotonic platform of silicon, telecommunicating emissions, and remarkably long coherence time. It is important to realize that no single SPE can possess all properties for every quantum applications and it is necessary to associate each SPE to specific applications.

1.2 Site-Controlled Pyramidal Quantum Dots as Single Photon Emitters

The self-assembled InGaAs QD system, fabricated using the Stranski-Krastanov (SK) method [114], is one of the most used QD systems. Using molecular beam epitaxy (MBE) or metalorganic vapor-phase epitaxy (MOVPE), a two-dimensional (2D) wetting layer of InAs is grown on a (100)-oriented GaAs wafer [115]. The lattice mismatch between InAs and GaAs induces random formation of small InAs islands on the 2D InAs wetting layer, which eventually form InGaAs/GaAs QD structures capped with GaAs upper layer [115]. There are several drawbacks of using self-assembled QD for practical cavity-QED devices: (1) Self-assembled QD forms in random locations [116]–[120]; (2) Large size distribution of self-assembled QD leads to poor QD emission energy control with large spectral inhomogeneity (30 – 50 meV) [116]–[120]; (3) Multiexcitonic emissions from 2D wetting layers can lead to spurious cavity feeding which are detrimental in cavity QED experiments [121]; (4) Its growth mechanism relying on strain leads to asymmetric QD shape and large fine-structure splitting (FSS) [122]–[126] which are detrimental in generation of polarization entangled and indistinguishable single photons. Although efforts have been made to overcome each drawback, an ultimate solution is needed to address all the limitations.

Alternatively, chapter 2-4 of this thesis explore the potential of using site-controlled pyramidal InGaAs QD system designed and fabricated by Prof. Eli Kapon's group at EPFL which overcomes most of the drawbacks mentioned above. Prof. Eli Kapon's group pioneered the development of the concept and technology of site-controlled pyramidal QD since the mid-1990s and accomplished most of its advances as briefly summarized below. With the first development of quantum wire (QWR) laser in 1989 [127], his group demonstrated first growth of QWR and QD heterostructures on nonplanar GaAs substrate, including V-grooved substrate and pyramidal recess patterned (111)B substrate, starting from 1990s [128]–[130]. The self-ordering growth mechanism

of QWR and QD on such nonplanar substrate, including growth-rate anisotropy, curvature-induced capillarity, and entropy mixing were reveled in the later years [131]–[135] with the structure and luminescence from single pyramidal AlGaAs/GaAs QDs being experimentally investigated [136]–[138]. Single photon emission from site-controlled pyramidal QD was revealed since 2004 [139]–[142] with its exciton dynamics investigated using photon correlations [143]. Statistical emission properties were studied using highly uniform dense arrays of site-controlled pyramidal QDs on prepatterned substrate [144], [145] with an achieved narrow (4 meV) spectral inhomogeneity [146]. Polarization anisotropy and fine structures of excitonic emission due to symmetries of pyramidal QDs were studied since 2006 [147]–[151]. Integration of site-controlled pyramidal QDs in PhC membrane cavities was demonstrated with precise alignment (50 nm) with cavity field pattern in 2008 [152]. Tunable emission energy by tuning pyramid size was demonstrated in 2009 [153] with several follow-up publications [154]–[156] which are essential for coupling QD emission with cavity mode. Then effect of pure dephasing and phonon scattering on the coupling of site-controlled pyramidal QD with PhC cavity was studied since 2011 [75], [157] as well as the revealed Purcell-enhanced exciton dynamics [158]. More complicated structures, such as incorporation of multiple site-controlled pyramidal QD systems in PhC cavity [159], [160], waveguides [161], tilted-potential cavity [162] or Fano cavities [163] and coupling with PhC molecule [164] were demonstrated recently. In 2022, site-controlled pyramidal QD was used to reveal the quantum interference effect of optical decay channels in PhC cavities thanks to its QD position controllability [165].

The fabrication process of site-controlled pyramidal InGaAs QD integrated in PhC cavities developed by Prof. Kapon's group can be briefly summarized as the following. Before QD growth, the (111)B-oriented GaAs wafer is patterned with pyramidal pits and the array of pyramidal

recesses are etched using electron beam lithography (EBL) and wet chemicals [153], [166]. The resulting high symmetric pyramids exhibit well-defined (111)A Ga-terminated facets. QDs are then grown by MOVPE of InGaAs/GaAs on such patterned GaAs substrate and eventually form at the apex of the pyramidal pits as a result of capillarity effects [153], [167] instead of strain, in stark contrast to self-assembled QDs. The resulting *pyramidal* QD exhibits high hexagonal symmetry (C_{3v}) [151] due to the self-limited growth mechanism [130], [168] and the symmetry of the pyramidal pits. Importantly, such growth mechanism does not involve the formation of 2D wetting layers, however, three InGaAs/GaAs quantum wires can present on the three wedges of the pyramid. Site-controlled pyramidal QD systems thus exhibit unique merits which cannot be reliably achieved with self-assembled QD systems in terms of: (1) Precise control of QD positions with nanometer accuracy (< 10 nm) [169]; (2) Precise control of QD emission energy by pyramid size with narrow spectral inhomogeneity (5-10 meV) [153], [167]; (3) Highly symmetric structure facilitate the elimination of FSS for polarization entangled single photon generation [170], [171]; (4) Absence of wetting layer facilitate the study of cavity QED of true two level system towards practical applications; (5) It enables the incorporation of many QDs in complicated nanophotonic structures [162], [163], [172]–[175] and the scalability of devices.

1.3 Silicon Color Centers as Single Photon Emitters

Silicon became the basis of modern electronics since the invention of the first integrated circuit [176]–[178]. Especially, Silicon-on-insulator (SOI) or SiO_2 with tailored doping and defect concentrations facilitates the dominance of silicon in the modern IC industry. However, Moore's law suggests an ultimate limit people can integrate tiny electronics together in an IC such that electrons can tunnel through potential barriers [179]. As a result, integrated quantum photonics based on silicon platform has become an emerging area which can benefit from already established

silicon integrated electronics and photonics technologies towards scalable quantum computing and information processing. By upscaling the silicon quantum computers, a practical quantum network can enhance computational power and facilitate secure quantum communications [180]. However, it requires sending photons as flying qubits over long distances between metropolitan areas which need to be in the telecommunication wavelengths at 1310 nm (O-band) and 1550 nm (C-band) for minimal dispersion and losses. Although efforts of developing telecommunicating emitting III-V QD system has been done [181]–[185], direct using silicon color centers in the telecommunication band become emergingly attractive. Besides the power of well-developed silicon integrated photonics, the reason that solid-state color center in silicon as a prominent candidate for building quantum networks can be due to (1) 99.9998% isotopically purified ^{28}Si substrate can effectively suppress the magnetic field fluctuation causing quantum decoherence [186]–[190] leading to silicon color centers with remarkable spin and optical properties; (2) Large family of silicon color centers can provide wide range applications, such as remarkably long spin lifetimes of phosphorus donors (3 hours) [191] and deep selenium donors (2.14 seconds) [29], [192] for quantum memories, bright and sharp luminescence from C, G, and W centers for telecom single photon sources [28], [193], [194], and unpaired electron spin from T, I, and M centers for telecom spin-photon interfaces [30], [90]. (3) Connectivity between silicon color centers in silicon nanophotonic circuits can be scale up using telecom fiber-based architecture which enables expansion of computational power and metro scale quantum networks [180].

Silicon color centers, or called silicon defect centers, are a family of radiation damage sites in the silicon lattice which emits bright luminescence with sharp linewidth within the telecommunication wavelengths. As the name suggests, silicon defects centers can be generated through radiation by high energy particles such as electrons (electron beam radiation) and atoms

(ion implantation). Such radiation damage to the silicon lattice induces dislocation of silicon atom out of their original sites and create vacancies. The resulting interstitial silicon atoms can be bonded with other substitutional atoms implanted externally, like carbon, hydrogen, copper, etc., and form new types of atomic configurations local defects in the silicon lattice [195]–[200]. A subsequent rapid thermal annealing (RTA) process at high temperature is conducted to enhancing the mobility of substitutional atoms and eventually facilitate the formation of specific color centers by precisely controlling the annealing temperatures, durations, and their combinations. At tailored annealing conditions, even single color center can be obtained from a broad beam implanted silicon substrate [201]. The vast majority of silicon defect centers have been studied in the 1980s before the emergence of quantum technologies. For example, C centers, emitting at 1571 nm, consist of an interstitial carbon atom and an interstitial oxygen atom [202], [203]. W centers, emitting at 1217 nm, consist of three interstitial silicon atoms [204]. G centers, emitting at 1280 nm, consist of an interstitial silicon atom and two substitutional carbon atoms [205], [206]. Recent study of color centers on highly enriched ^{28}Si also discovered remarkable emission linewidth of C, G, W centers and hidden fine structures of G centers [207] Although these color centers exhibit bright luminescence at telecommunication wavelength, G and W centers lack ground state unpaired electron or hole spins which limits their use for spin-photon interface [207]. However, other color centers, like T [30], [31], [90], [208], [209], M [210]–[214], and I [210], [215]–[217] centers, are found to have unpaired ground-state electron spins which are potentially useful for storing quantum information.

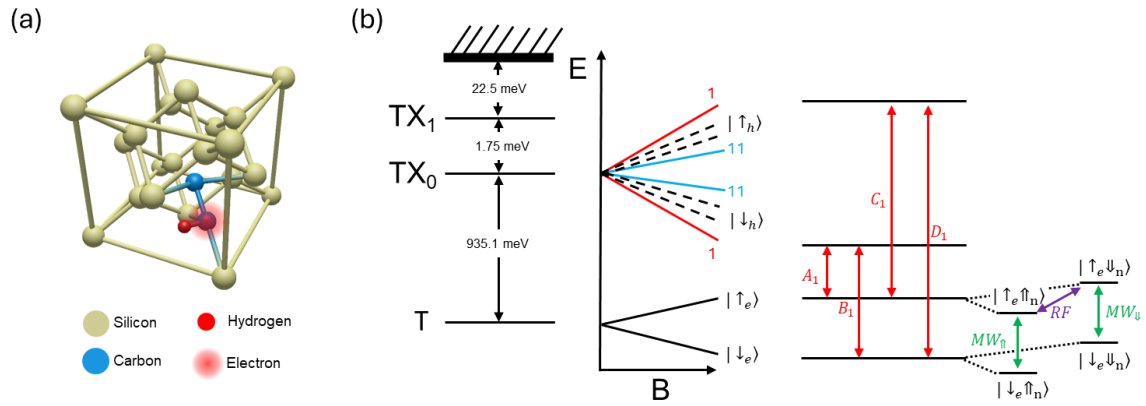

FIG 1.2 | T center structure and energy levels (a) Atomic structure of T centers. (b) Energy level diagram of T centers with magnetic field induced splitting of the excited state TX_0 and ground state T. TX_0 splits into 11 subsets due to anisotropic excited state g-factors. A_1, B_1, C_1, and D_1 are the optical transitions corresponding to subset 1. Ground state splitting due to electron and nuclear spin can be accessed by microwave and RF pulses. (b) is adapted from ref [30].

As shown in Fig 1.2(a), the structure of T center consists of two directly bounded carbon atoms together sharing a substitutional site of a silicon atom and one of the carbon atoms is terminated with a hydrogen atom, leaving an unpaired electron dangling bound on the other carbon atom, which is desirable for spin qubits [30], [209]. The ground state of T center has an unpaired electron (coherence time > 2.1 ms) and hydrogen/carbon nuclear spin (coherence time > 1.1s) [30]. Upon photoexcitation, the excited state (TX) includes a photogenerated bound exciton. Two bound

(a)	Transitional Properties (ensemble T centers)	
$\mu_{tot}(\mu_{ZPL})$	1.52 (0.73)	Debye
η	23	%
τ_{rad}	0.94	μs
T_1-e(n)	~	hrs
T_2-n	1.1	s
T_2 – e	2.1	ms
$\Delta\lambda_{rad}$	33	MHz
η_{rad}	?	%

(b)	Transitional Properties (single T center in micropuck)	
τ_{rad}	0.8	μs
$g^2(0)$	0.20	
T_1-e (B)	0.85	*ms*
T_1-e (C)	1.2	ms

$\mu_{tot}(\mu_{ZPL})$: total (ZPL) dipole moment
η: Debye-Waller factor
τ_{rad}: optical lifetime
T_1-e(n): electron(nuclear) spin T1 lifetime
T_2-n: nuclear spin T2 Hahn-echo coherence time
T_2-e: electron spin T2 Hahn-echo coherence time
$\Delta\lambda_{rad}$: ZPL linewidth by PLE
$g^2(0)$: second order correlation function at zero delay
T_1-e (B/C): electron spin T1 lifetime for B and C transitions

Table 1.1 | Transition properties of ensemble T centers [30] and single T centers in micropuck structures [31] based on ^{28}Si system.

electrons in TX form a spin-0 singlet state leaving an unpaired spin-3/2 hole weakly bound by the Coulomb potential from electron, forming a pseudo-acceptor [209]. The degeneracy of the unpaired hole is lifted by reduced symmetry (C_{1h}) of the defect and lead to splitting of TX states into TX_0 and TX_1, separated by 1.75 meV [209]. With the presence of an external magnetic field, it is reported that excited state TX_0 Zeeman splits into 11 subsets resulting from the strong anisotropic g-factor (g_h) of the weakly bound hole ranging from 1.069 to 3.457, while the ground state g-factor is isotropic with $g_e \approx 2$ [30]. The ground state (T) electron and nuclear spin can be accessed by microwave and RF, respectively [30]. The bound exciton exhibits a thermal dissociation energy of ~ 22.5 meV and it is much smaller than the total electron-hole binding energy of ~ 234.9 meV, which aligned with the fact that the excited state consists of a tightly bound electron and a weakly bound hole as a pseudo-acceptor. The transition properties of ensemble T centers [30] and single T centers isolated using micropucks [31] in ^{28}Si are summarized in Table 1.1.

In the chapter 5 of this thesis, we will explore novel silicon color centers based on transition metals, which are likely an alternative candidate for spin-photon interface of T centers [218].

1.4 Photonic Crystal Cavities

In analogy with semiconductors, where the periodic lattice structure offers a periodic potential leading to an electronic band gap between the valence and conduction energy bands, in *photonic* crystals, the "periodic potential" is a periodic refraction index which is created by lattice structure of media with periodic dielectric constants. PhC exhibits distinct refractive indices of the dielectric media and minimal absorption of light by the media, offering complete control over light propagation on a microscopic scale. By designing the periodic dielectric function, we can constructure a photonic band gap which prevents light propagation in specific directions with

certain range of wavelengths. By creating defects in the periodic structure, we can create an optical cavity with a cavity mode within the bandgap which exhibits a distinct photonic LDOS. As a result, the light can channel through the cavity mode with cavity decay rate and modified spatial profile. With tailored parameters [56], [59], such as tapering the holes, the cavity Q-factor can be enhanced and mode volume can be reduced for strong trapping of light and enables strong light-matter interaction with embedded SPEs for cavity quantum electrodynamics (cQED). Here the cavity Q-factor represents the number of photon round trips trapped in the cavity before the energy decays by $e^{-2\pi}$ and it can be expressed as $Q = \omega/\kappa$, where ω and κ are the mode energy and cavity decay rate, respectively.

In this thesis, we focus on PhC cavities based on PhC slab, a two-dimensional (2D) PhC with finite thickness. It consists of a triangular lattice of air holes in a dielectric material surrounded by air and the cavity is created through 3 ($L3$), 5 ($L5$), or 7 ($L7$) missing holes in a line. The propagation of light in the photonic bandgap is forbidden in the 2D plane (xy plane) and the thickness of the slab also stops the light in specific directions thanks to total internal reflections. The reader can refer to Fig 2.1 in chapter 2 as an example of the LDOS of the cavity mode of a $L3$ PhC slab cavity in the photonic bandgap designed for single site-controlled InGaAs QD. Note that the cavity mode is only in transverse electric (TE) due to the symmetry of the PhC cavity.

1.5 Cavity Quantum Electrodynamics

An atom can interact with a propagating radiation field with no boundaries. However, cQED study the case where the boundaries exist, and such boundaries are effectively reflecting. More specifically, the atom is embedded in a resonant cavity. In this case, the spontaneous emission rate or the energy level of the atom can be significantly modified by the cavity as we shall see.

We consider a case that an atom is embedded in a cavity with volume V. The cavity fields consist of a superposition of a set of discrete cavity modes, depending on the geometry of the cavity. For simplicity, we assume that the energy of only one cavity mode ($\hbar\omega_c$) is close to the transition energy ($\hbar\omega_0$) of the two-level atom with ground state $|a\rangle$ and excited state $|b\rangle$, and all other cavity modes are far detuned. The state space of the whole system ($|i,n\rangle$) can be expressed as a tensor product of atomic states $|a\rangle$ or $|b\rangle$ and the cavity photonic states $|n\rangle$ as $|a\rangle \otimes |n\rangle$ or $|b\rangle \otimes |n\rangle$, where $n = 0, 1, 2, 3$ ... is the photon numbers. The total Hamiltonian of the whole system (atom + cavity) can then be expressed as Jaynes-Cummings (JC) model [219]

$$\hat{H}_{tot} = \hat{H}_{at} + \hat{H}_c + \hat{H}_{int}, \tag{1.1}$$

with

$$\hat{H}_{at} = \hbar\omega_0 |b\rangle\langle b| \tag{1.2}$$

$$\hat{H}_c = \hbar\omega_c \hat{a}^\dagger \hat{a} \tag{1.3}$$

Here we assume the ground state of the system $|a, 0\rangle$ has zero energy. Assuming low field intensities, the interaction Hamiltonian can be expressed as

$$\hat{H}_{int} = \frac{\hbar\Omega_1^{(1)}}{2}(|a\rangle\langle b| + |b\rangle\langle a|)(\hat{a}^\dagger + \hat{a}). \tag{1.4}$$

$\Omega_1^{(1)}$ is called the single photon Rabi frequency and is expressed as [219]

$$\Omega_1^{(1)} = -\frac{2q}{m}\frac{1}{\sqrt{2\hbar\varepsilon_0\omega_c V}}\langle a|\hat{\boldsymbol{p}}\cdot\boldsymbol{\varepsilon}|b\rangle, \tag{1.5}$$

where $\hat{\boldsymbol{p}}$ is the momentum operator. We can consider firstly the decoupled atom + cavity system with total Hamiltonian $\hat{H}_{at} + \hat{H}_c$. Such Hamiltonian can be easily diagonalized as the following [219]

$$\left(\widehat{H}_{at} + \widehat{H}_c\right)|a,n\rangle = \hbar n\omega_c|a,n\rangle, \tag{1.6}$$

$$\left(\widehat{H}_{at} + \widehat{H}_c\right)|b,n\rangle = (\hbar\omega_0 + \hbar n\omega_c)|b,n\rangle. \tag{1.7}$$

Now we include the effect of atom-cavity interactions. The matrix elements of the interaction Hamiltonian can be calculated as [219]

$$\langle i,n|\,\widehat{H}_{int}|i',n'\rangle = \frac{\hbar\Omega_1^{(1)}}{2}[\langle i|a\rangle\langle b|i'\rangle + \langle i|b\rangle\langle a|i'\rangle]\langle n|(\hat{a}^\dagger + \hat{a})|n'\rangle. \tag{1.8}$$

It can be seen that all diagonal elements are zero and it only couples states like $|a,n\rangle$ and $|b,n-1\rangle$ or $|a,n\rangle$ and $|b,n+1\rangle$. For a given coupled states, the interaction Hamiltonian can be written as [219]

$$\widehat{H}_{int} = \frac{\hbar\Omega_1^{(1)}}{2}[|a\rangle\langle b|\hat{a}^\dagger + |b\rangle\langle a|\hat{a}]. \tag{1.9}$$

And the total Hamiltonian for a given coupled states can be expressed as [219]

$$\widehat{H}_{tot} = \hbar\begin{bmatrix} n\omega_c & \frac{\Omega_1^{(1)}\sqrt{n}}{2} \\ \frac{\Omega_1^{(1)}\sqrt{n}}{2} & n\omega_0 \end{bmatrix}. \tag{1.10}$$

The corresponding eigenenergies are [219]

$$E_{\pm,n} = \hbar\left(n\omega - \frac{\delta}{2} \pm \frac{1}{2}\sqrt{n\left[\Omega_1^{(1)}\right]^2 + \delta^2}\right) \tag{1.11}$$

where $\delta = \omega_c - \omega_0$ is the detuning between atom and cavity mode. As a result, the effect of interaction Hamiltonian is to repel the energy levels of the doublet states of the decoupled system as shown in Fig 1.3. Eigenenergies of the coupled system (black solid curves) as a function of detuning exhibits avoided crossing around zero-detuning as shown in Fig 1.4. Such behavior is significantly deviated from the crossing of the decoupled system (dotted curves). These coupled

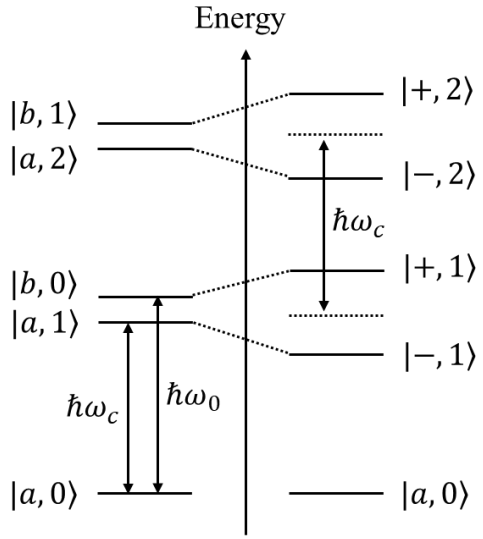

FIG 1.3 | **Energy level diagrams of the atom + cavity system** (a) without and (b) with the interaction Hamiltonian. Fig 1.3 is adapted from [219].

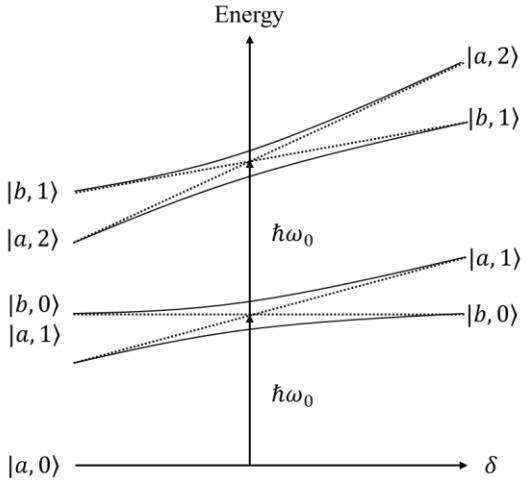

FIG 1.4 | Energy level diagrams of the atom + cavity system as a function of detuning in the presence of the interaction Hamiltonian. Fig 1.4 is adapted from [219].

states are also called atomic *dressed* states (dressed by photons) or *polariton* states which are a quasiparticle states or *entangled* states with hybrid light-matter features which cannot be factorized into purely atomic part and purely photonic part. On resonance, the two upper and lower states are separated by the vacuum Rabi splitting (VRS) of $\sqrt{n}\hbar\Omega_1^{(1)}$[219].

For simplicity, the JC Hamiltonian can also be expressed as [220]

$$\hat{H}_{tot} = \frac{1}{2}\hbar\omega_0\hat{\sigma}_z + \hbar\omega_c\hat{a}^\dagger\hat{a} + \hbar g(\hat{a}^\dagger\hat{\sigma}_- + \hat{\sigma}_+\hat{a}), \tag{1.12}$$

using pseudospin operator $\hat{\sigma}_z$ and atom-photon coupling strength g, which is given by [220]

$$g = \sqrt{\frac{1}{4\pi\varepsilon}\frac{\pi e^2 f}{m_0 V}} \propto \frac{f}{V}. \tag{1.13}$$

Here m_0 is the free electron mass, e is the electron charge, and f is the oscillator strength. For real cavities, there is cavity decay rate κ or limited cavity Q-factor. Assume the atomic spontaneous decay rate is γ_0, then the eigenenergies of the system can be rewritten as [220]

$$E_{1,2} = \frac{\hbar\omega_c + \hbar\omega_0}{2} - i\frac{\kappa + \gamma_0}{4} \pm \sqrt{g^2 - \frac{(\kappa - \gamma_0 - 2i\delta)^2}{16}} \tag{1.14}$$

The VRS is then [220]

$$\Delta E = 2\sqrt{g^2 - \frac{(\kappa - \gamma_0)^2}{16}} \tag{1.15}$$

Two cQED regime can then be distinguished. In the strong coupling regime where VRS is presented and the polaritons states are formed, $g > \frac{\kappa - \gamma_0}{4}$. It leads to coherent energy exchange between the atom and the cavity fields, known as Rabi oscillations. In the weak coupling regime,

$g < \frac{\kappa - \gamma_0}{4}$. The VRS disappears and the cavity decays with a fast rate leading to a modified spontaneous decay rate of the coupled atom with a Purcell factor [61] of $F_P = \frac{3\lambda^3}{4\pi^2}\frac{Q}{V}$, where Q is the cavity Q-factor. The transition between the two regimes, namely *intermediate* coupling regime, can be realized by controlling the cavity decay rate κ or the cavity Q-factor. Since the coupling strength g is proportional to $\frac{f}{V}$ as shown by Eq. (1.13), a figure of merit to achieve strong coupling regime is to maximize $Q \cdot \sqrt{\frac{f}{V}}$ [220].

1.6 Experimental Methods: Microphotoluminescence Spectroscopy

Photoluminescence (PL) spectroscopy is an optical spectroscopy method to study the spectral and dynamical properties of the photogenerated excitons in semiconductor materials by using the resonant or off-resonant laser excitation and collection of the induced luminescence from the sample. To study nanostructures at microscopic scale, such as single SPEs or PhC cavities, microphotoluminescence (μPL) spectroscopy is needed for focusing the laser onto the studied structure with ~ μm spot size using a microscope objective with high numerical aperture (NA). To ensure the laser spot is focused on the specific structure interested, a simultaneous microscope image of the structure and the laser spot is required. The luminescence emitted by the specific structure that is photoexcited is then collected through the same microscope objective and guided to the spectrometer for measurement.

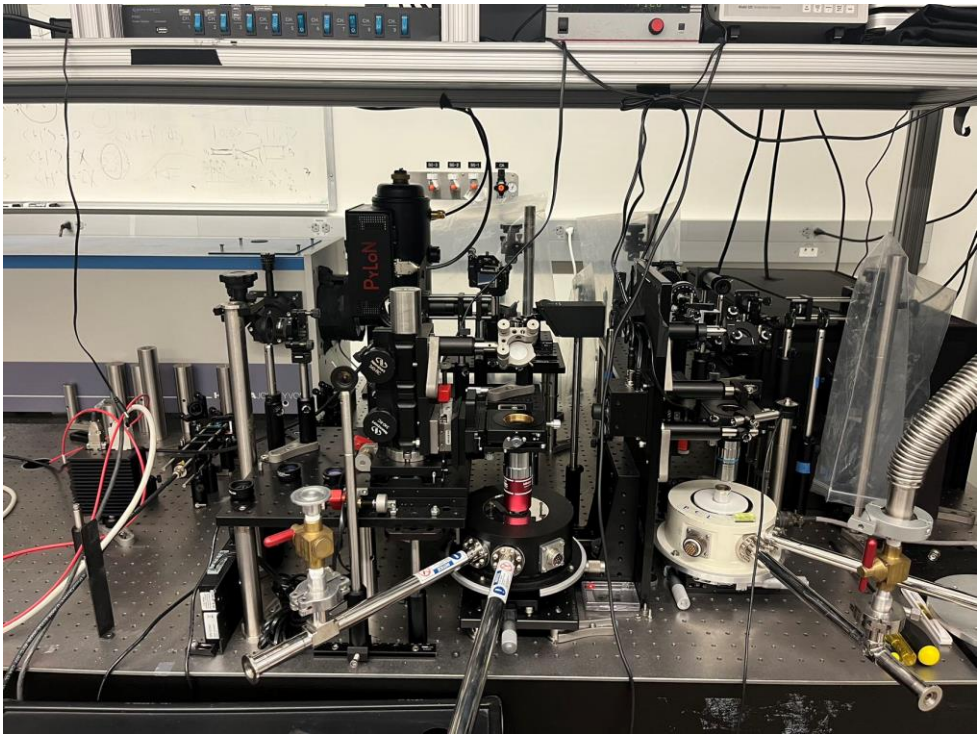

FIG 1.5 | A photo of μPL setup for characterizing site-controlled InGaAs QD systems built in Engineering VI building at UCLA.

- **Microphotoluminescence setup**

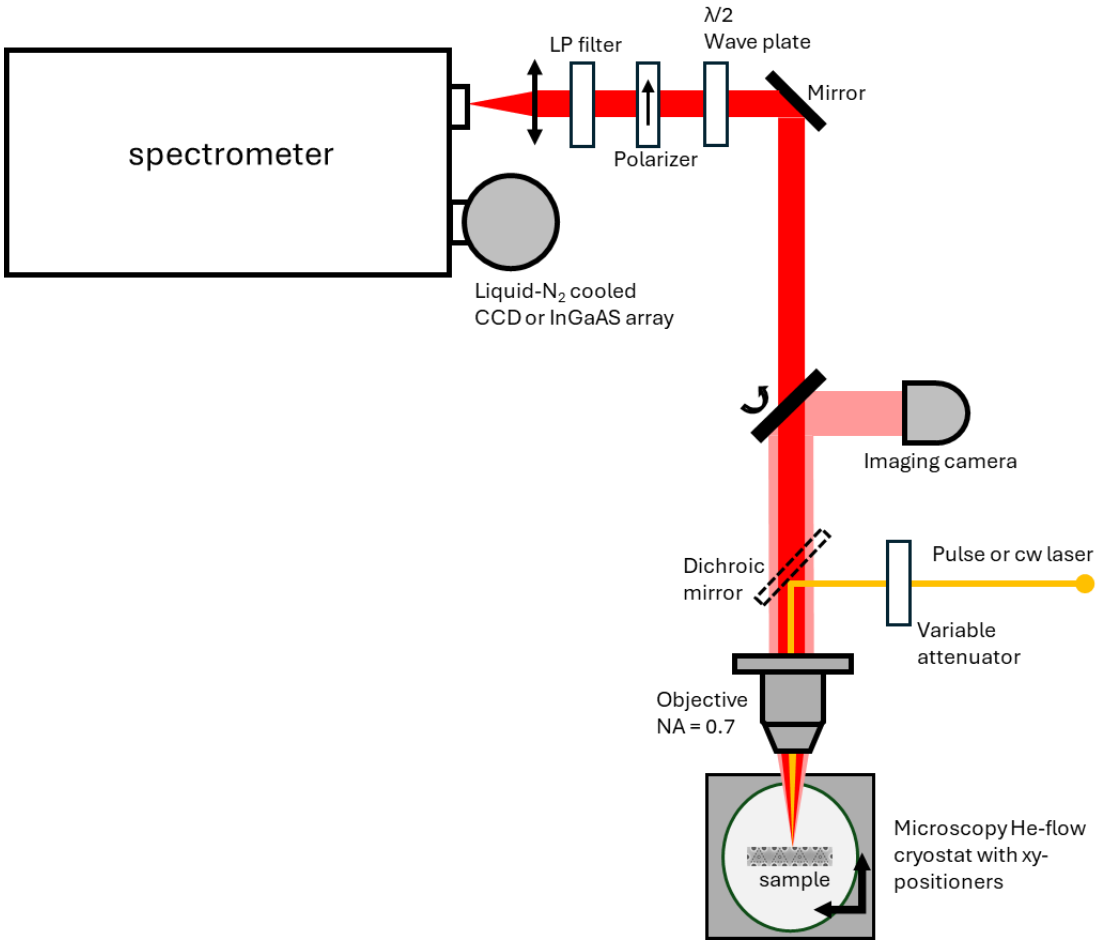

FIG 1.6 | Schematic of the µPL setup. The laser path for optical excitation is indicated in orange. The PL path for optical detection is indicated in red. And the white light path for microscopic imaging is indicated in light red.

In Fig 1.6, a schematic of the µPL setup used for measurements in this thesis is shown. A cw laser (532 nm or 785 nm) or pulse laser (900 nm), passing through a set of variable attenuation, is reflected on a dichroic mirror with cut-off wavelength at 925 nm (Semrock FF925-Di01). This dichroic mirror allows reflection of light with wavelength shorter than 925 nm and transmission of light with wavelength longer than 925 nm (edge steepness ~ 30 nm). The laser is then focused on the sample through a Mitutoyo microscope objective. A series of objectives can be selected:

100X with 0.7NA, 50X with 0.42NA, and 20X with 0.42NA. To achieve the tightest laser spot on the sample (~ 1 μm), the objective of 100X with 0.7NA is normally selected for QD study. The sample is glued to the cold stage of a helium flow cryostat (Janis ST-500) using copper tapes or thermal grease. Before cooling down the sample, a turbo station (Pfeiffer HiCube ECO 80) is used where a backing pump is used for vacuuming the pressure inside the cryostat down to 10^0 Torr and then a turbomolecular pump is used for bringing the pressure down to 10^{-6} Torr. Then the cryostat is isolated from the pump to avoid cryopumping which could contaminate the sample, and the liquid helium flow is used for cooling the cold stage and thus the sample. The sample temperature is controlled via a temperature controller (Lakeshore 325). The cryostat is mount on an XY stage with piezoelectric linear actuators (Newport Picomotor) which allows moving the sample in the XY direction with a spatial resolution of ~ 30 nm. A CMOS camera is placed after the dichroic mirror to obtain a microscopic image of the studied structure and focused laser spot, helping the alignment of the laser spot with the interested structure. The emission is collected by the same microscope objective and focused through a convex lens onto the slit of a spectrometer (Horiba 1000M – 1 m focal length, 1200 grooves/mm grating) equipped with a 2D liquid Nitrogen-cooled silicon CCD (Princeton Instruments PyLon 400BR_eXcelon with 1340 x 400 array), enabling a spectral resolution of ~ 40 μeV. For near IR wavelength (e.g. silicon color centers), a spectrometer (Princeton Instruments Acton SP2500 – 0.55 m focal length, triple grating of 1200, 600, 60 grooves/mm) equipped with a 2D InGaAs array (Princeton Instruments Acton 2D-OMA V:320 with 320 x 256 array) is used. A 2D PL imaging is obtained using these detectors, and the optical spectra are then obtained by integrating the vertical axis of the PL image. The residual laser is filtered with a long pass optical filter. A linear polarizer and λ/2 waveplate are place in front of the

spectrometer for polarization-resolved μPL measurement to obtain the vertically and horizontally polarized PL components.

- **Hanbury-Brown and Twiss (HBT) setup**

Single photon emission can be characterized using Hanbury-Brown and Twiss (HBT) setup which measure the second order correlation function [221] of the photons, which can be classically expressed as:

$$g^{(2)}(\boldsymbol{r}_1, t_1; \boldsymbol{r}_2, t_2) = \frac{\langle E^*(\boldsymbol{r}_1,t_1)E^*(\boldsymbol{r}_2,t_2)E(\boldsymbol{r}_1,t_1)E(\boldsymbol{r}_2,t_2)\rangle}{\langle|E(\boldsymbol{r}_1,t_1)|^2\rangle\langle|E(\boldsymbol{r}_2,t_2)|^2\rangle}. \tag{1.16}$$

Here, $E(\boldsymbol{r}, t)$ are the electric field of the light at position **r** and time t. It represents the probability of simultaneous detection of light at ($\mathbf{r_1}$,t_1) and light at ($\mathbf{r_2}$,t_2). Assume the light propagates in plane parallel wave, then:

$$g^{(2)}(\tau) = \frac{\langle I(t)I(t+\tau)\rangle}{\langle I(t)\rangle^2}. \tag{1.17}$$

Here $\tau = t_2 - t_1$ is the time difference from one light and $I \propto |E(t)|^2$ is the average intensities of the light at a given time t. To explain the quantum nature of light emission from SPEs, the classical electric fields $E(\boldsymbol{k}, t)$ need to be rewritten into quantum operators using the second quantization as

$$\hat{E}_k(t) = \hat{E}_k^+(t) + \hat{E}_k^-(t). \tag{1.18}$$

And

$$\begin{aligned} \hat{E}_k^+(t) &\propto \hat{a}_k \times \exp\left(-i(\omega_k t - \boldsymbol{k}\cdot\boldsymbol{r})\right) \\ \hat{E}_k^+(t) &\propto \hat{a}_k^\dagger \times \exp\left(+i(\omega_k t - \boldsymbol{k}\cdot\boldsymbol{r})\right) \end{aligned} \tag{1.19}$$

Eq (1.19) represents the positive and negative frequency components of the light. For single mode light, using the Eq (1.19), the second order correlation function in the quantum mechanical description can be expressed as:

$$g^{(2)}(\tau) = \frac{\langle \hat{E}_k^-(t)\hat{E}_k^-(t+\tau)\hat{E}_k^+(t+\tau)\hat{E}_k^+(t)\rangle}{\langle \hat{E}_k^-(t)\hat{E}_k^+(t)\rangle^2}. \tag{1.20}$$

When $\tau = 0$, then:

$$g^{(2)}(\tau = 0) = \frac{\langle \hat{a}_k^\dagger \hat{a}_k^\dagger \hat{a}_k \hat{a}_k\rangle}{\langle \hat{a}_k^\dagger \hat{a}_k\rangle^2} = \frac{\langle n(n-1)\rangle}{\langle n\rangle^2}. \tag{1.21}$$

$g^{(2)}(\tau = 0)$ is particularly interesting for characterizing single photon emissions from SPEs because it represents the probability of simultaneous detection of another photon at the same time when one photon was already detected. Using 2nd factorial moment and the variance (Δn), Eq (1.21) can be simplified as

$$g^{(2)}(\tau = 0) = 1 + \frac{(\Delta n)^2 - \langle n\rangle}{\langle n\rangle^2}. \tag{1.22}$$

For superpoisson (thermal state), Poisson (coherent state), and Subpoisson (Fock state) distribution,

$$\begin{aligned} (\Delta n)^2_{thermal} &= \langle n\rangle^2 + \langle n\rangle \\ (\Delta n)^2_{coherent} &= \langle n\rangle \\ (\Delta n)^2_{Fock} &= 0 \end{aligned} \tag{1.23}$$

Then,

$$\begin{aligned} g(\tau = 0)^2_{thermal} &= 2 \text{ (bunched light)} \\ g(\tau = 0)^2_{coherent} &= 1 \text{ (coherent light)} \end{aligned} \tag{1.24}$$

$$g(\tau = 0)^2_{Fock} = 1 - \frac{1}{n} < 1 \text{ (antibunched light)}$$

As shown by Eq (1.24), thermal state has a higher probability of detecting more than one photon at the same time. But it occurs in a period shorter than coherence time which is called photon bunching. For Fock state, it has reduced probability of detecting more than one photon at the same time and it is called photon *antibunching*. Ideal SPEs should emit light in the Fock state with photon number $n = 1$ and characterized by $g(\tau = 0) = 0$.

Fig 1.7 shows the Hanbury Brown and Twiss (HBT) setup to measure the second order correlation function. Instead of sending luminescence to the spectrometer in the μPL setup shown

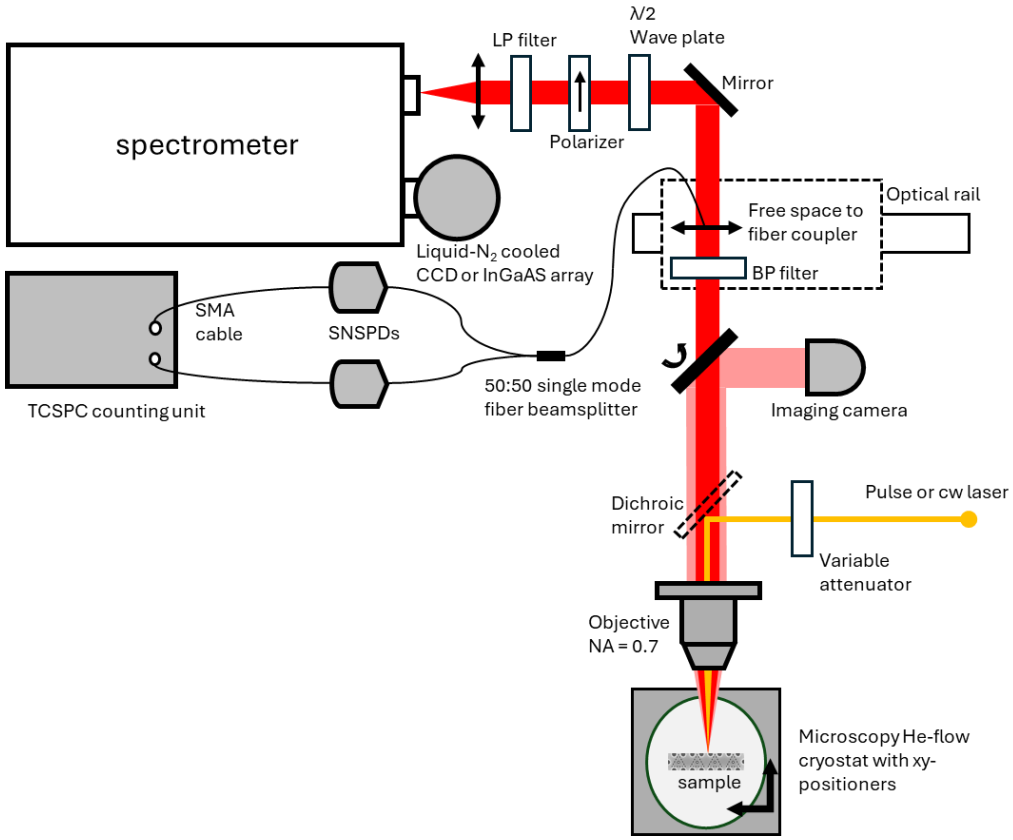

FIG 1.7 | Schematic of the μPL setup combined with HBT measurement. Instead of sending luminescence into the spectrometer, it is now coupled into a 50:50 single mode fiber beamsplitter. The laser path for optical excitation is indicated in orange. The PL path for optical detection is indicated in red. And the white light path for microscopic imaging is indicated in light red.

in Fig 1.7, after filtering by combined tunable short and long pass filter (Semrock VersaChrome) as a narrow bandpass filter, it is now coupled into a 50:50 single mode fiber-based beamsplitter and each outputs (50% of the total intensity) are fed to a single photon detector (Excelitas SPCM-AQRH single photon counting module with a dark count rate of ~ 25 Hz and timing resolution of ~ 300 picosecond or PhotonSpot superconducting nanowire single-photon detector (SNSPDs) with a dark count rate of ~ 100 Hz and timing resolution of ~ 70 picosecond). Detector outputs are connected to the time correlated single photon counting (TCSPC) unit (PicoHarp 300 with a minimal 4 picosecond binwidth) which repeatedly measures the time difference τ between the photon detection event of the two detectors. And eventually builds a histogram of the events when detector 1 detect a photon at time t and detector 2 detect a photon at time $t + \tau$. The second order correlation function can be constructed using such histogram for each time difference τ [222].

- **Time-resolved photoluminescence setup**

For time-resolved photoluminescence (TRPL) measurement, a pulse laser with repetition rate f_{rep} and pulse duration T is used as the excitation laser. The internal clock frequency f_{rep} of the pulse laser can be obtained by using a photodiode measuring the pulse laser after a beamsplitter. For the detection path, the luminescence is then coupled into a single mode fiber after filtering by the combined tunable short and long pass filter (Semrock VersaChrome) as a narrow bandpass filter and fed into a single photon detector (Excelitas SPCM-AQRH single photon counting module with a dark count rate of ~ 25 Hz and timing resolution of ~ 300 picosecond or PhotonSpot superconducting nanowire single-photon detector (SNSPDs) with a dark count rate of ~ 100 Hz and timing resolution of ~ 70 picosecond) for single photon counting. The photodiode output is connected to the reference channel of the TCSPC unit (PicoHarp 300 with a minimal 4 picosecond binwidth) and the output of the single photon detector is connected to the signal channel as shown

in Fig 1.8. Alternatively, the clock output of the pulse laser can directly connect to the reference channel of the TCSPC unit.

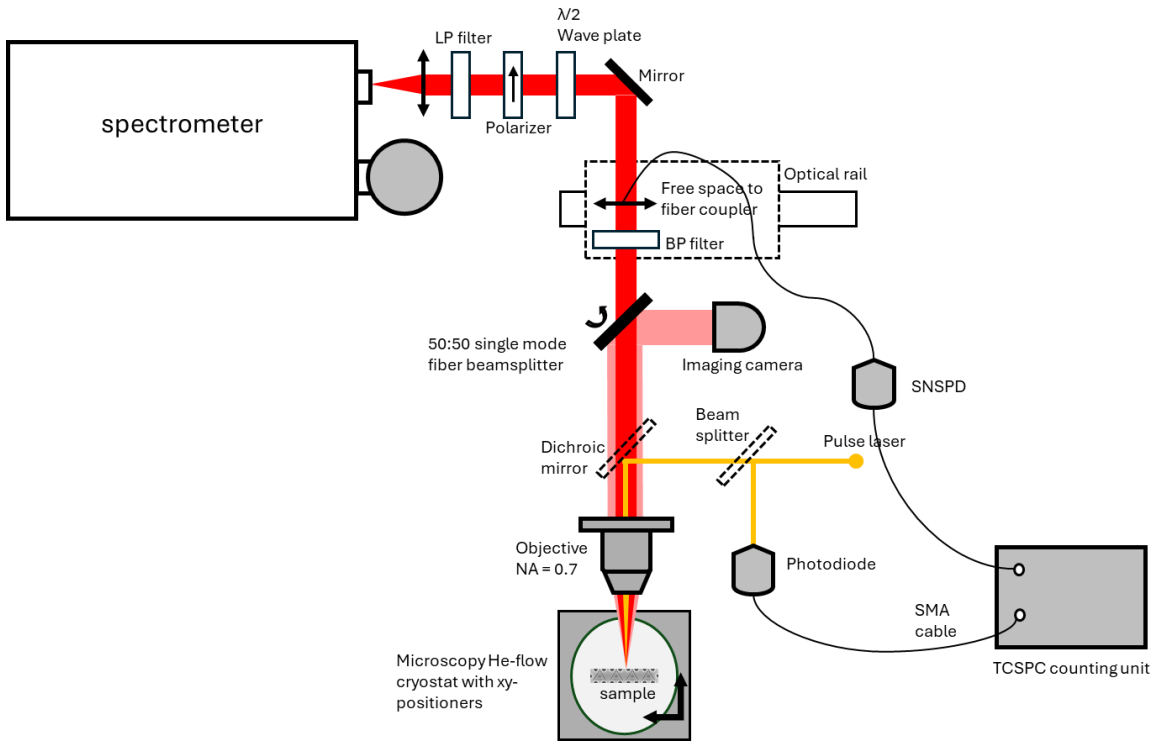

FIG 1.8 | Schematic of the time-resolved PL setup. Instead of sending luminescence into the spectrometer, it is now coupled to a single mode fiber fed into a single photon detector. The laser path for optical excitation is indicated in orange. The PL path for optical detection is indicated in red. And the white light path for microscopic imaging is indicated in light red.

After the SPE is excited by laser pulses, the single photon detector records the arrival time of the photon emission. Meanwhile, the photodiode that measures the laser excitation event. Through the TCSPC unit, the photon emission event (signal channel) is synchronized with laser excitation event (reference channel). The time difference between the two events is recorded that acts like a stopwatch and is measured over multiple cycles of the laser repetition. As a result, a histogram of the stopwatch reading per time bin can be constructed which represents the emission intensity decay of the SPE [222]. Because of the finite time response of the system (largely depending on

the time response of the single photon detectors), to extract the real decay time of the SPE, deconvolution from the instrument response function (IRF) is sometimes necessary. The IRF can be measured by directly feeding the single photon detector with laser pulses at attenuated power.

1.7 Numerical Methods: Finite-Difference Time-Domain Simulations

The electric field distribution of a PhC cavity can be simulated using finite-difference time-domain (FDTD) methods. As the name suggests, this method calculates the electromagnetic field in the time domain. During the simulation, the photonic structure to be simulated (area of interest) are surrounded by boundaries normally using perfectly matched layer (PML) which is an artificial layer for absorbing the propagating electromagnetic waves. The area of interest is discretized into unit cells forming a grid. Considering a space without any electric or magnetic sources, then

$$\boldsymbol{B} = \mu \boldsymbol{H}, \boldsymbol{D} = \varepsilon \boldsymbol{E}, \boldsymbol{J_m} = \rho \boldsymbol{H}, \boldsymbol{J_e} = \sigma \boldsymbol{E} \tag{1.25}$$

The time dependent Maxwell's curl equations governing the electromagnetic wave propagation are given as below:

$$\begin{aligned} \frac{\partial \boldsymbol{H}}{\partial t} &= -\frac{1}{\mu}\boldsymbol{\nabla} \times \boldsymbol{E} - \frac{\rho}{\mu}\boldsymbol{H} \\ \frac{\partial \boldsymbol{E}}{\partial t} &= \frac{1}{\varepsilon}\boldsymbol{\nabla} \times \boldsymbol{H} - \frac{\sigma}{\varepsilon}\boldsymbol{E} \end{aligned} \tag{1.26}$$

The FDTD algorithm is proposed by Yee based on Eq (1.26) [58], using staggered Cartesian grids to discretize the electric and magnetic field components within each unit cell. Specifically, each electric field component is surrounded by four magnetic field components, and conversely, each magnetic field component is surrounded by four electric field components. Consequently, each node within the grid represents three electric and magnetic field components situated around a volume element. Time discretization is also performed in a *leapfrog* manner by using a

temporally shifted updating for the electric field at time t from its value at $t + \Delta t$ and the magnetic field value at time $t - \Delta t/2$ (shifted by half time step) and vice versa for updating the magnetic field, with a globally defined time step Δt.

To calculate the electric field distribution of the modes of a PhC cavity, the 3D FDTD method is used that the PhC slab within a certain area of interest is discretized into a 3D grid. The PML boundary is set to be large enough to avoid the reflection of electromagnetic waves back into the structure which is undesired. Proper periodic boundary conditions can be used according to the symmetry of the structure to shorten the simulation time. A cloud of point source consists of short pulse are placed inside the cavity, and the Maxwell equations iterates for sufficient number of time steps until the fields completely decay. The time monitors are placed at desired locations as detectors. The Fourier transform of a field component then gives the frequency response of the systems where the localized cavity modes can be identified as strong resonance in the frequency spectrum. The cavity resonance frequency ω be obtained and the cavity Q-factor can then be calculated $Q = \omega/\Delta\omega$, where $\Delta\omega$ is the full-width-at-half-maximum (FWHM). Note for the cavity with high Q-factor where the fields cannot completely decay in a reasonable simulation time, Q-factor cannot be determined using FWHM because it is affected by simulation time. Alternatively, it should be calculated from the slope of the envelope of the field decaying using [223]:

$$Q = \frac{-2\pi\omega \log_{10}(e)}{2k} \tag{1.27}$$

Here k is the slope of the decay.

Fig 1.9 shows the field intensity distribution of the first four cavity modes of a GaAs-based $L7$ PhC cavity.

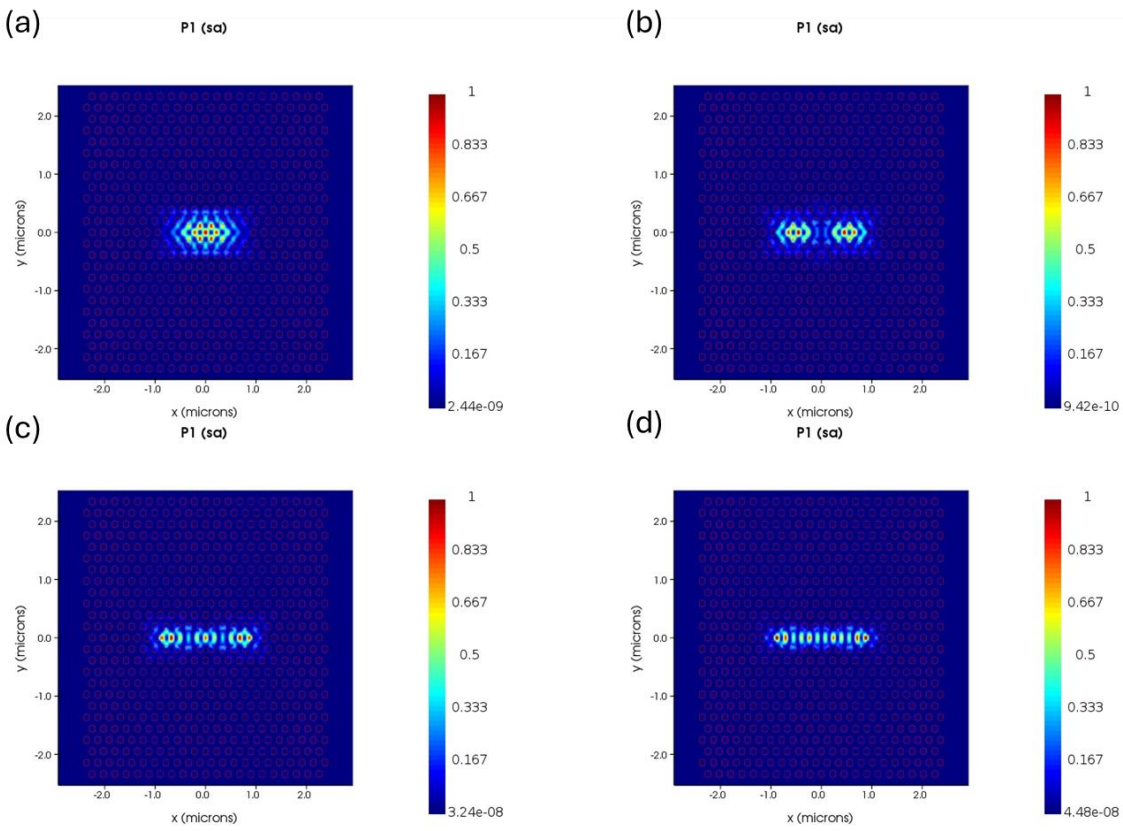

FIG 1.9 | Spatial distribution of the Electric field intensity of the first four cavity modes of a GaAs-based *L*7 PhC cavity using 3D FDTD methods.

1.8 Numerical Methods: Quantum Toolbox

In cQED simulations, it is necessary to consider the system subject to environmental dephasing processes. The theory can start with the Hamiltonian of the system and the dephasing processes can be captured by Lindblad master equations. The equation of motion of coupled emitter-cavity system can then be generated directly from the Hamiltonian and coupling to environment. In this section, we introduce using Quantum Toolbox [224] which is a MATLAB package to set up the equation of motion and solve for solution. Our system is about a two-level system coupled to a monochromatic cavity mode and subject to exciton pure dephasing and phonon scattering that the eigenvectors and eigenvalues of time invariant Liouvillians can be calculated explicitly.

We are particularly interested in calculating the power spectrum which can be evaluated from the two-time covariance functions. The system and the environment evolution are governed by the total Hamiltonian $\widehat{H}_{tot}$. The time evolution of the total density matrix is [224]:

$$\rho_{tot}(\tau) = exp\left(-i\widehat{H}_{tot}\tau\right)\rho_{tot}(0)exp\left(i\widehat{H}_{tot}\tau\right) \tag{1.28}$$

Then the time evolution of the expectation value of the creation operator $\hat{a}^{\dagger}$ is [224]

$$\langle\hat{a}^{\dagger}(\tau)\rangle = Tr\{\hat{a}^{\dagger}\rho_{tot}(\tau)\} = Tr\left\{\hat{a}^{\dagger}\, exp\left(-i\widehat{H}_{tot}\tau\right)\rho_{tot}(0)exp\left(i\widehat{H}_{tot}\tau\right)\right\} \tag{1.29}$$

Then the two-time correlation function can be written as [224]

$$\begin{aligned}\langle\hat{a}^{\dagger}(t+\tau)a(t)\rangle &= Tr\{\hat{a}^{\dagger}(t+\tau)a(t)\rho_{tot}(0)\}\\ &= Tr\left\{exp\left(-i\widehat{H}_{tot}(t+\tau)\right)\hat{a}^{\dagger}\, exp\left(-i\widehat{H}_{tot}\tau\right)a\, exp\left(-i\widehat{H}_{tot}\tau\right)\rho_{tot}(0)\right\}\\ &= Tr\left\{\hat{a}^{\dagger}\, exp\left(-i\widehat{H}_{tot}\tau\right)a\rho_{tot}(t)\exp\left(i\widehat{H}_{tot}\tau\right\}\right.\end{aligned} \tag{1.30}$$

The below example code shows how to calculate the stationary two-time covariance function $\langle\hat{a}^{\dagger}(t+\tau), a(t)\rangle$.

```
function [corrES,covES] = probcorr(E,kappa,gamma,g,wc,w0,wl,N)
%
% [corrES,covES] = probcorr(E,kappa,gamma,g,wc,w0,wl,N)
%  returns the two-time correlation and covariance of the intracavity
%  field as exponential series for the problem of a coherently driven
%  cavity with a two-level atom
%
%  E = amplitude of driving field, kappa = mirror coupling,
%  gamma = spontaneous emission rate, g = atom-field coupling,
%  wc = cavity frequency, w0 = atomic frequency, wl = driving field frequency,
%  N = size of Hilbert space for intracavity field (zero to N-1 photons)
%
ida = identity(N); idatom = identity(2);
ida2 = identity(N);
```

```
% Define cavity field and atomic operators
a  = tensor(destroy(N),idatom);
sm = tensor(ida,sigmam);
%sm2 = tensor(ida2,signma2);

% Hamiltonian
H = (w0-wl)*sm'*sm + (wc-wl)*a'*a + i*g*(a'*sm - sm'*a) + E*(a'+a);

% Collapse operators
C1  = sqrt(2*kappa)*a;
C2  = sqrt(gamma)*sm;
C1dC1 = C1'*C1;
C2dC2 = C2'*C2;

% Calculate the Liouvillian
LH = -i * (spre(H) - spost(H));
L1 = spre(C1)*spost(C1')-0.5*spre(C1dC1)-0.5*spost(C1dC1);
L2 = spre(C2)*spost(C2')-0.5*spre(C2dC2)-0.5*spost(C2dC2);
L = LH+L1+L2;

% Find steady state density matrix and field
rhoss = steady(L);
ass = expect(a,rhoss);

% Initial condition for regression theorem
arho = a*rhoss;

% Solve differential equation with this initial condition
solES = ode2es(L,arho);

% Find trace(a' * solution)
corrES = expect(a',solES);

% Calculate the covariance by subtracting product of means
covES = corrES - ass'*ass;
```

To calculate the power spectrum, the code first expands the two-time covariance function into an exponential series [224]

$$\phi(\tau) = \langle \hat{a}^{\dagger}(t+\tau), a(t) \rangle = \begin{cases} \sum_j c_j \exp(s_j \tau) & \text{for } \tau \geq 0 \\ \phi^*(-\tau) & \text{for } \tau < 0 \end{cases} \tag{1.31}$$

The power spectrum is then calculated by [224]

$$S(\omega) = 2Re \sum_j \frac{c_j}{i\omega - s_j} \tag{1.32}$$

The below code shows this process:

```
% esspec calculates the power spectrum from an exponential series in the frequency span in wlist
Ps = esspec(covES,wlist);
f1 = figure(1); plot(wlist,Ps);
xlabel('Frequency'); ylabel('Spectral amplitude');
```

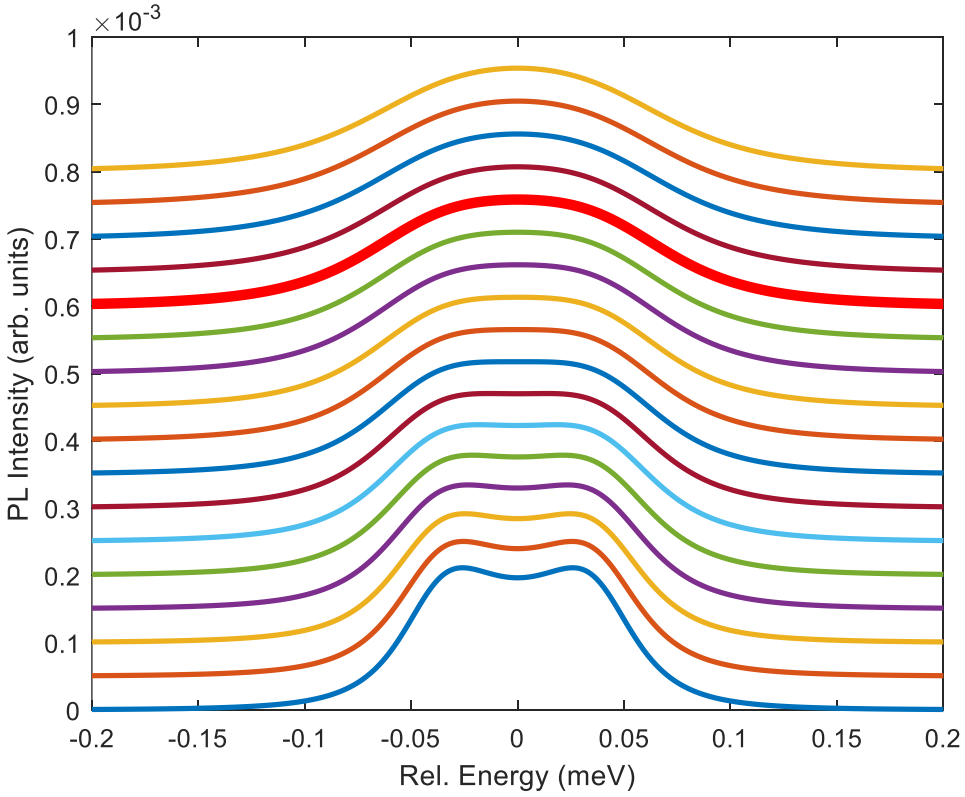

FIG 1.10 | An example power spectrum of a QD-cavity system with varying pure dephasing rate from 0 – 80 μeV with 5 μeV step. The bold red spectrum is for pure dephasing rate at 60 μeV.

Fig 1.10 shows an example power spectrum of a QD-cavity system with varying pure dephasing rate using the following parameters: cavity loss = 150 μeV, QD spontaneous emission rate = 0.2 μeV, Incoherent pumping rate = 1 μeV, QD-cavity coupling strength = 150 μeV, pure dephasing rate = 0 – 80 μeV with 5 μeV steps.

1.9 Thesis organizations

The objective of this thesis is to experimentally explore the light-matter interaction of solid-state single photon emitters based on two systems: site-controlled pyramidal InGaAs QDs and silicon color centers. The first system has been developed by Prof. Eli Kapon's group at EPFL for decades and it is relatively mature in the context of position control and PhC cavity integration towards functional integrated quantum photonic devices. However, such systems, based on (111)B-oriented GaAs substrate, were suffered from relatively low cavity Q factor (< 3,500) and thus limited by weak coupling regime [75], [157], [158].

In chapter 2, we describe our efforts to improve the Q factor of a $L3$ PhC cavity up to ~ 4,500 by red shifting the QD emission energy towards ~ 1.25 eV. We present an optical study of such red-shifted site-controlled pyramidal InGaAs QD can be operated in the intermediate coupling regime where the strong and weak coupling coexists with detailed spectral analysis of the coupled QD-cavity emission. We also present the time-resolved and photon correlation measurements of the coupled QD-cavity emission in such intermediate coupling regime. This chapter serves as a guideline for further device optimization towards strong coupling regime.

In chapter 3, we obtain a cavity Q factor up to ~ 12,000 using a $L7$ PhC cavity at the red shifted QD emission energy of ~ 1.24 eV. With combined optical study and cQED modeling, we demonstrate such red-shifted site-controlled pyramidal InGaAs QD placing in a $L7$ PhC cavity can be operated at the onset of strong coupling regime. We also reveal the role of phonon scattering

and exciton dephasing during QD-cavity interactions. We further demonstrate a Rabi-like oscillation of luminescence intensity and energy splitting between excitonic and photonic components which occurs only at small QD-cavity detuning and can be well reproduced by our cQED modeling.

	Pyramid size (S)	QD emission energy (E)	PhC cavity type	Cavity decay rate (Γ)	Cavity *Q*-factor	Cavity QED regime
Huang et al, *J. Appl. Phys.* 134, 223103 (2023)	**200 nm**	**~ 1.24 eV**	***L*7-cavity**	**~ 100 μeV**	**~ 12,000**	**Onset of strong coupling**
Huang et al, *New J. Phys.* 25 03301 5 (2023)	**200 nm**	**~ 1.25 eV**	***L*3-cavity**	**~ 270 μeV**	**~ 4,500**	**Intermediate coupling**
Jarlov et al, *Phys. Rev. Lett.* 117, 076801 (2016)	300 nm	~ 1.41 eV	*L*3-cavity	~ 400 μeV	~ 3,200	Weak coupling
Jarlov et al, *Appl. Phys. Lett.* 107, 191101 (2015)	300 nm	~ 1.42 eV	*L*3-cavity	~ 400 μeV	~ 3,500	Weak coupling
Calic et al, *Phys. Rev. Lett.* 106, 227402 (2011)	300 nm	~ 1.44 eV	*L*3-cavity	~ 570 μeV	~ 2,500	Weak coupling

TABLE 1.2 | Milestones of site-controlled pyramidal InGaAs QD systems towards strong coupling regime.

Chapter 4 explore a more complex structure of four site-controlled pyramidal QDs embedded in the same *L*7 PhC cavity, which leads to onset of strong coupling as suggested in chapter 3. We focus on the spatial features of QD excitons interacting with a high-order cavity mode of the *L*7 PhC cavity which exhibits spatially extended photonic states. We observe a detuning dependent spatial avoided crossing of QD excitonic states by measuring the polarized imaging of the luminescence. A theory of quantum interference of QD decay channel is used to explain the observed novel phenomena. The result suggests the potential of incorporating multi-site-controlled QD at prescribed locations in a photonic structure in applications such as optical switching for quantum information routing.

Here we acknowledge that site-controlled pyramidal InGaAs QD samples studied in chapter 2-4 are designed, fabricated, and provided by Prof. Eli Kapon's group at EPFL.

In chapter 5, we turn our focus to the second system: silicon color center. Compared to QD systems, silicon color centers are less mature in terms of site controllability and cavity integration, but they are particularly useful for spin-photon interface and telecom quantum communication towards large scale quantum networks. A brief overview and introduction of silicon color center is given. We then present an optical study of transformation of various color centers during our fabrication process to generate silicon T center and Cu-related defects. A study the photophysics of the Cu-related defects with comparison of T centers, including power dependent, temperature dependent, and time-resolve PL measurements, is given and suggests the potential of using Cu-related defects as a potential spin-photon interface. Further electron spin resonance and magneto-PL is presented to strengthen such claim.

Chapter 2

Single Site-Controlled Quantum Dot-Nanocavity Operating in the Coexisting Strong-Weak (*Intermediate*) Coupling Regime.

2.1 Overview and Introduction

In the microscale, interactions between light and matter in the solid state serve as a crucial foundation for practical quantum communications, both in unbreakable quantum communication [225]–[229] and long-distance quantum communication through a trusted repeater node architecture [230]–[233]. The advancement in this domain, particularly with InGaAs quantum dots (QDs), has been driven by demonstrations of on-demand bright single-photon sources [8], [234], [235], achieving a strong coupling regime in high-quality factor (Q) microcavities [220], [236]–[246], deterministic coupling of single quantum dots (QDs) in single cavity modes [247], entanglement generation [231], [248]–[251], and coherent control [238], [240], [252], [253]. Recent studies on the quantum network protocol, based on deterministic cluster state generation [96], [97], [251], [254], and solid-state quantum memory enabling single-photon switching [233], [240], have attracted significant attention. Notably, the cavity-enhanced biexciton-dark-exciton cascaded system in GaAs-based QDs [93], [255] is emerging as a promising platform for implementing such a protocol. Importantly, the pure dephasing of two-level systems, defined as any disruption of the quantum state without causing population relaxation but introducing random phase evolution, plays a fundamental role in error-tolerant networks [256] and frequency-stabilized on-chip scalable indistinguishable single-photon emitters [257], [258] for on-chip

quantum information processing (QIP). In GaAs-based QDs, the primary pure dephasing mechanisms leading to spectral broadening are associated with rapidly fluctuating electrical charges [259] and carrier-phonon interactions [260]–[265]. In the weak coupling regime, the pure dephasing mediated Purcell effect facilitates a large fraction of the QD emission to be channeled into the cavity mode, resulting in efficient off-resonance cavity feeding up to a few meV detuning [75], [259], [266]. Simultaneously, finite coupling between QD exciton and cavity can lead to the emission of cavity photons at the QD exciton energy, resembling a dissipative cavity where the cavity loses photons at a rate much faster than the QD [75], [267]. Conversely, in the strong coupling regime, the vacuum Rabi splitting and polariton state are modified by the damped coherent Rabi oscillations induced by pure dephasing [268]. Beyond the clear distinction between strong and weak coupling, recent studies suggest the existence of an *intermediate* coupling regime, combining features of both strong and weak coupling, as observed in self-assembled GaAs-based QDs in micropillar [40], [41] and PhC cavities [271]. Notably, recent theoretical studies underscore the importance of phonon-assisted QD-cavity interaction in this intermediate coupling regime [43], [44] This underscores the significance of investigating pure dephasing in cavity quantum electrodynamical (cQED) systems to achieve practical quantum information processing with suppressed environmental fluctuations.

The intrinsic pure dephasing of the two-level system in QDs and its interaction with the cavity remains to be difficult to access, particularly due to the use of self-assembled QDs in most studies. These self-assembled QDs introduce spurious cavity feedings [121] related to multiexcitonic background due to their wetting layer, creating a complication. The hybridization of localized self-assembled QD states with delocalized wetting layer states results in broadband quasi-continuum states, contributing to background emission [274], [275]. Moreover, the random nucleation of self-

assembled QDs makes precise positioning challenging, impacting the physical properties of incorporated QDs and, consequently, their interaction with cavities. In contrast, the precise positioning of single site-controlled highly symmetric pyramidal InGaAs QDs in photonic crystal (PhC) cavities with nanometer-scale accuracy presents distinct advantages over self-assembled QDs. The deterministic nucleation in this approach allows for the creation of large-scale arrays of similar QD-cavity configurations [169], [276]. The growth mechanism also eliminates spurious cavity feeding, thanks to the absence of wetting layers [169], [276], facilitating the study of the intrinsic interaction between emitters and cavities. Furthermore, deterministic incorporation of several QDs into cavities, WGs, or more intricate photonic structures, essential for single photon generation and processing in integrated quantum photonic circuits, cannot be accomplished reliably with self-assembled QDs.

To the best of author's knowledge, prior experimental studies on site-controlled InGaAs QD-cavity systems have predominantly concentrated on the weak coupling regime, as reported in references [75], [157]. This limitation may stem from the use of (111)B-oriented GaAs substrates for etching high-symmetric inverted pyramids, which are employed in the site-controlled InGaAs QD epitaxy within PhC cavities. These (111)B-oriented PhC cavities tend to exhibit larger losses compared to the conventional (100)-oriented PhC system. Previous studies have reported a relatively low cavity Q-factor of approximately ~2500 at the QDs s-shell emission wavelength of ~860 nm [75], [157]. In this chapter, we addressed this limitation by optimizing the Indium content and pyramid size of our single site-controlled InGaAs QD – *L*3 PhC cavities. This optimization allowed us to tailor the QDs s-shell emission wavelength to a longer wavelength, approximately 1 µm, where reduced cavity losses could be achieved while maintaining a sub-100 µeV narrow excitonic linewidth. Consequently, we observed a notable improvement in the *Q*-factor of the

(111)B-oriented PhC cavity, surpassing ~ 4200. This improvement can be attributed to the reduced impact of absorption losses from the Urbach tails of GaAs [277], [278] and smaller structural disorders resulting from larger structural parameters [175]. Using our tailored device, we successfully attained the *intermediate* coupling regime and systematically investigated the associated phonon-mediated coupling and carrier recombination dynamics. This exploration was conducted through high-resolution polarization-resolved micro-photoluminescence (μPL), time-resolved PL, and second-order photon correlation measurements which are introduced in chapter 1. Our findings elucidate the pump power-dependent anti-bunching photon statistical dynamics within the coexisting strong-weak coupled system and unveil the optical features of strongly confined exciton-polaritons and dark-exciton-like states.

2.2 Single Site-Controlled InGaAs QD-*L*3 PhC cavity Devices

For the devices studied in this chapter, the single site-controlled pyramidal QDs are fabricated on the (111)B-orientated GaAs substrate using electron-beam lithography (EBL) with precision within ± 5 nm to pattern inverted pyramidal pits in a triangular lattice with a pitch of 450 nm. Metalorganic vapor-phase epitaxy (MOVPE) is then employed to grow $In_{0.25}Ga_{0.75}As$/GaAs, resulting in lens-shaped, highly hexagonal symmetric QDs at the apex of a highly symmetric inverted pyramids. These pyramids exhibit well-defined (111)A gallium terminated facets, and no 2D wetting layer is formed during the growth. The pyramid side is around 180 nm and the QD size is around 20 nm in plane and around 5 nm in the growth direction. Prior characterization from ref [175] indicates a center energy of 1.2711 eV (~ 975 nm) and FWHM of 15.1 meV (~ 11.56 nm) of s-shell at 10 K of such QDs ensemble. Under certain circumstances, InGaAs/GaAs QWR may form on the three wedges of the inverted pyramid during the growth. A PhC membrane with membrane thickness of approximately 250 nm, lattice constant of about 225 nm, and air hole radius

∈ [30, 50] nm is lithographically written on top of the QD pattern. For *L*3 PhC cavities, the first three side holes on the left and right of the cavity are shifted outwards by 0.23a, 0.15a, and 0.048a to enhance the cavity *Q*-factor. Subsequently, all QDs are etched away except the one at the center of the cavities. The overall patterning size is approximately 725 x 740 µm comprising of 820 QD-cavity devices. For further details of site-controlled QD growth and PhC cavity integration, refer to chapter 1.

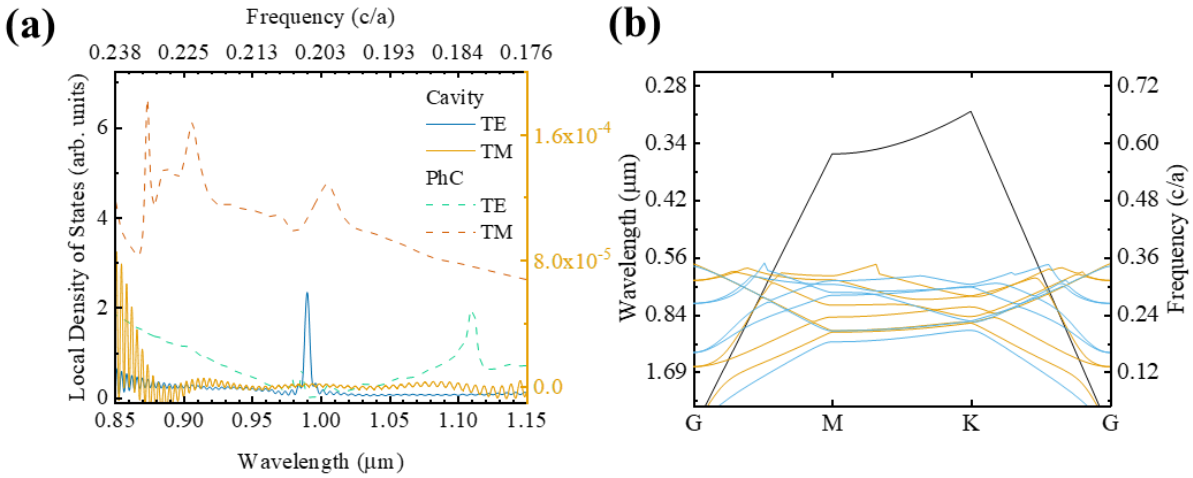

FIG 2.1 | 3D FDTD simulation of the PhC membrane and *L*3 cavity. (a) 3D FDTD Simulated local density of states. **(b)** Energy dispersion of the L3 photonic crystal cavity. The right axis only corresponds to the cavity TM mode (yellow solid line) in (a). For lattice constant *a*, air hole radius *r*, and PhC thickness *t*, the following values are used: $a = 202.6$ nm, $r/a = 0.15$, $t/a = 1.25$. The refractive index of GaAs is taken to be 3.52. *c* is the speed of light in vacuum. Fig 2.1 is published in [77].

Three-dimensional finite difference time domain (3D FDTD) simulation is conducted on the PhC cavities investigated in this chapter. The simulation considers a PhC membrane with lattice constant (a), air hole radius (r), and thickness (t). The specific values used in the simulation, based on our sample fabrication, are as follows: a = 202.6 nm, r/a = 0.15, and t/a = 1.25. As shown in Fig 2.1(a), The FDTD simulation of our PhC membrane reveals a band gap of approxmiately 40 nm

in the LDOS for the TE mode (green dashed line). The TM mode (brown dashed line) is continuous covering all the wavelengths. Notably, the *L*3 PhC cavity exhibits a distinct isolated TE mode (blue solid line) at 990 nm within the photonic band gap. The simulation does not identify any isolated TM mode within the bandgap (yellow solid line) which is expected

from the symmetry of the cavity. Fig 2.1(b) presents the photon energy dispersion from Γ to M and K point.

2.3 Exciton Complexes and Pure Dephasing in the Single Site-Controlled InGaAs QD- *L*3 PhC Cavity

Fig 2.2(a) demonstrates the PL spectrum of the resulting excitonic emissions from a single pyramidal InGaAs QD and the *L*3-PhC cavity mode (CM) at 25 K with X-CM detuning of approximately 2 meV, using a 532 nm non-resonant excitation. As illustrated in Fig 2.2(a), the s-state excitonic emission [169], [276] involves the negatively charged exciton (X^-), neutral exciton (X), biexciton (BX), and likely an excited light hole (LH) state. Notably, the QD s-state emission is around 1.252 eV (990 nm) indicating reduced influences from the Urbach tails of GaAs bandgap [277], [278] in this device thanks to the optimized device fabrication described in section 2.2. The relative binding energies [279] of the BX and X^- with respect to X are -1.06 meV and 3.41 meV respectively. The pronounced X^- population, even at low excitation of 10 nW, is primarily attributed to background-doping donors incorporated during QD growth. Additionally, the significant asymmetric mobility between electrons and holes further promotes the formation of X^- over the positively charged exciton (X^+) [280]. In the low excitation regime, (<150 nW), the FWHM linewidths of the X^-, X, BX, and LH transitions remain nearly constant, with γ_{X-} = 173 ± 9 μeV, γ_X = 143 ± 10 μeV, γ_{XX} = 117 ± 42 μeV, and γ_{LH} = 202 ± 5 μeV respectively, extracted using Lorentzian fitting. The observed linewidth broadening larger than the Fourier transform

limits of the typical QD nanosecond lifetime (≈ 7 μeV), suggests the contribution of pure dephasing via fluctuating environmental charges. Although phonon scattering can contribute to the linewidth broadening, it is not expected to be dominant below 50 K [281]. The larger linewidth

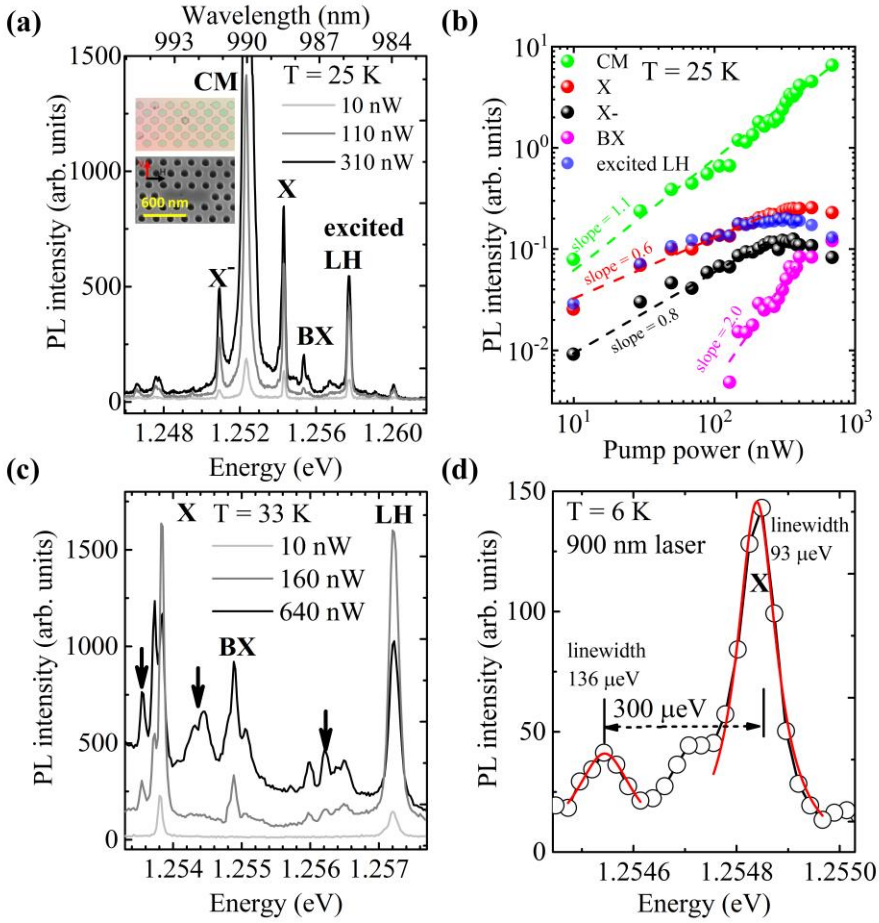

FIG 2.2 | Exciton complexes and dark excitons in single site-controlled InGaAs QD-*L*3 PhC cavity. (a) μPL spectrum of a single pyramidal InGaAs QD-*L*3 PhC cavity system at 25 K with 532 nm non-resonant pumping at 10 nW, 110 nW, and 310 nW. Inset: an image of the PhC cavity. Scale bar: 600 nm. **(b)** Integrated μPL intensity of different QD exciton species and cavity mode as a function of pump power at 25 K. **(c)** A zoom-in of the exciton complex species marked by arrows at 33 K (near the X and BX emission) with 532 nm non-resonant pumping at 10 nW, 160 nW, and 640 nW. **(d)** Sample zoom-in of the peak 300 μeV below X emission, at 6 K with 900 nm pumping. Fig 2.2 is published in [77].

observed at low excitation for X^- compared to X can be contributed by additional charge carriers with increased Coulomb interactions with fluctuating environmental electric fields. It is noteworthy that γ_{X-} monotonically decreases by approximately 30 μeV as excitation power increases from 200 to 700 nW, which is due to the saturation of the local charge states. Meanwhile, the significantly larger γ_{LH} is attributed to a more delocalized LH state, experiencing stronger fluctuations of the surrounding charges. Apart from the excitonic emission, the CM line has a FWHM of κ_{CM} of 296 ± 12 μeV, which corresponds to a Q factor of approximately 4,230, placing it in the dissipative cavity regime of $\kappa_{\mathrm{CM}} \gg \gamma_{exciton}$, where κ_{CM} and $\gamma_{exciton}$ are the cavity loss and QD radiative decay rates, respectively.

It is crucial to highlight that the absence of a 2D wetting layer in our single pyramidal QD growth eliminates the possibility of far-off-resonance cavity feeding by a spurious multiexcitonic emission background. Additionally, despite the pyramidal QD nucleating in the promimity of three 1-dimensional ridge quantum wires at the wedges of the pyramid, the quantum wire influence is demonstrated to be negligible for low QD excitation powers. This is attributed to the large energy difference and absence of hybridization between the localized QD states and 1D delocalized state. The lower mobility of charges in the disordered 1D barrier further contributes to the negligible impact. To further validate the above assignment of each sharp transition line, Fig 2.2(b) presents the excitation power-dependent μPL at 25 K. The excitation power-dependent integrated μPL intensity of X, X^- and LH in logarithmic scale [169] reveals a sublinear slope of 0.6 ± 0.1, 0.8 ± 0.1, and 0.6 ± 0.1 respectively, correlated with the increase in the CM intensity. In contrast, the far-off resonance BX exhibits a distinctive slope of 2.0 ± 0.2 and features a saturation excitation power larger than other excitonic emissions. Furthermore, the off-resonance CM as a function of excitation power exhibits a slope of 1.1 ± 0.1.

With a further increase in the excitation power, additional lines appear next to the BX and X transitions as indicated by arrows in the magnified Fig 2.2(c). These additional lines are likely attributed to charged exciton complexes and potential recombination involving ground state QD electrons with higher-order QD hole states, which exhibits small energy spacing (< meV). Notably, the sharp emission line slightly below the BX line exhibits a super-linear power-dependent behavior, suggesting the decay of a negatively charged biexciton (BX^-) [282] or excited biexcitonic states [151]. The dense lines approximately 1 meV above the BX line represent apparently positively charged complexes [283]. This behavior can be attributed to the fact that the QD hole capture rate is proportional to the excitation power [143]: the enhanced direct hole capture by the QD at stronger excitation changes the population from negatively charged to neutral X and, with further hole capture, eventually to an X^+. Furthermore, an intriguing observation is the presence of an additional sharp shoulder below X line at sub-barrier pumping at 900 nm, as noted in Fig 2.2(c). This feature is further elucidated in the high-resolution μPL spectrum in Fig 2.2(d), measured at 6 K. Specifically, it reveals an excitonic species at a transition energy of approximately 300 μeV below the X line (Fig 2.2(d)), which matches the reported exchange interaction-induced splitting between the bright and dark excitons (DX) [255]. However, the appearance of charged complexes (1.2547 eV) may overlap and change their power-dependent behavior. To further investigate the power-dependent characterization of the DX-like state, we examine another QD-*L*3 cavity device in the absence of charge complexes as shown in Fig 2.3. The residual optical activity observed in the DX is attributed to the mixing of the heavy hole (HH) ground state with the LH component due to slightly reduced QD symmetry [150], [255], [284]. This mixing results in a small in-plane polarized dipole moment and partially relieves the spin conservation. DX, featuring a parallel electron and hole pair, typically exhibits a relatively long

lifetime and optical inactivity compared to bright exciton with an antiparallel electron and hole pair due to spin and momentum conservation [285]. Prior studies reported the observation of DX optical activity in self-assembled InGaAs QD and explained the residual optical activity from the reduced symmetry in a real QD and resulting bright and dark exciton mixing from electron and hole spin flipping process [255], [286]. Fig 2.3(a) illustrates the high-resolution μPL spectra at 30 K, measured on another QD-L3 cavity system on our sample with 532 nm excitation. A distinct sharp emission is observed at around 300 μeV below X at low excitation power (10 nW), indicative of the typical feature of DX. Additionally, the energy difference of approximately 300 μeV is preserved up to 30 K and 100 nW. Fig 2.3(b) provides a zoom-in view of the DX-like emission. The excitation power dependence of μPL intensities for X and DX at 30 K is shown in Fig 2.3(d). DX-like luminescence presents a maximum intensity three orders of magnitude weaker than X. Moreover, while X saturates at around 100 nW, the DX-like μPL intensity saturates at a power one or two orders of magnitude lower than X. At a higher excitation power, the carrier accumulation rate could exceed the slow radiative decay rate of DX-like emission, leading to its early saturation [255]. This suggests a radiative lifetime of DX-like emission one or two orders of magnitude longer (approximately 100 - 1000 ns) than X. But the direct measurement on the lifetime of DX-like emission is not feasible due to its weak intensity and low count rates. An in-plane magnetic field can be used to facilitate the symmetry breaking and enhance the DX optical activity [287]. And the intrinsic lifetime can then be extrapolated from the magnetic field dependent lifetime [287] but it is beyond the scope of this study. The observation of such a signature on another QD-cavity system underscores the generality and repeatability of the measurement. It also suggests the possibility of implementing DX spin qubit in our system for

coherent manipulation of semiconductor stationary and flying qubit, such as cluster state generation [93], [97].

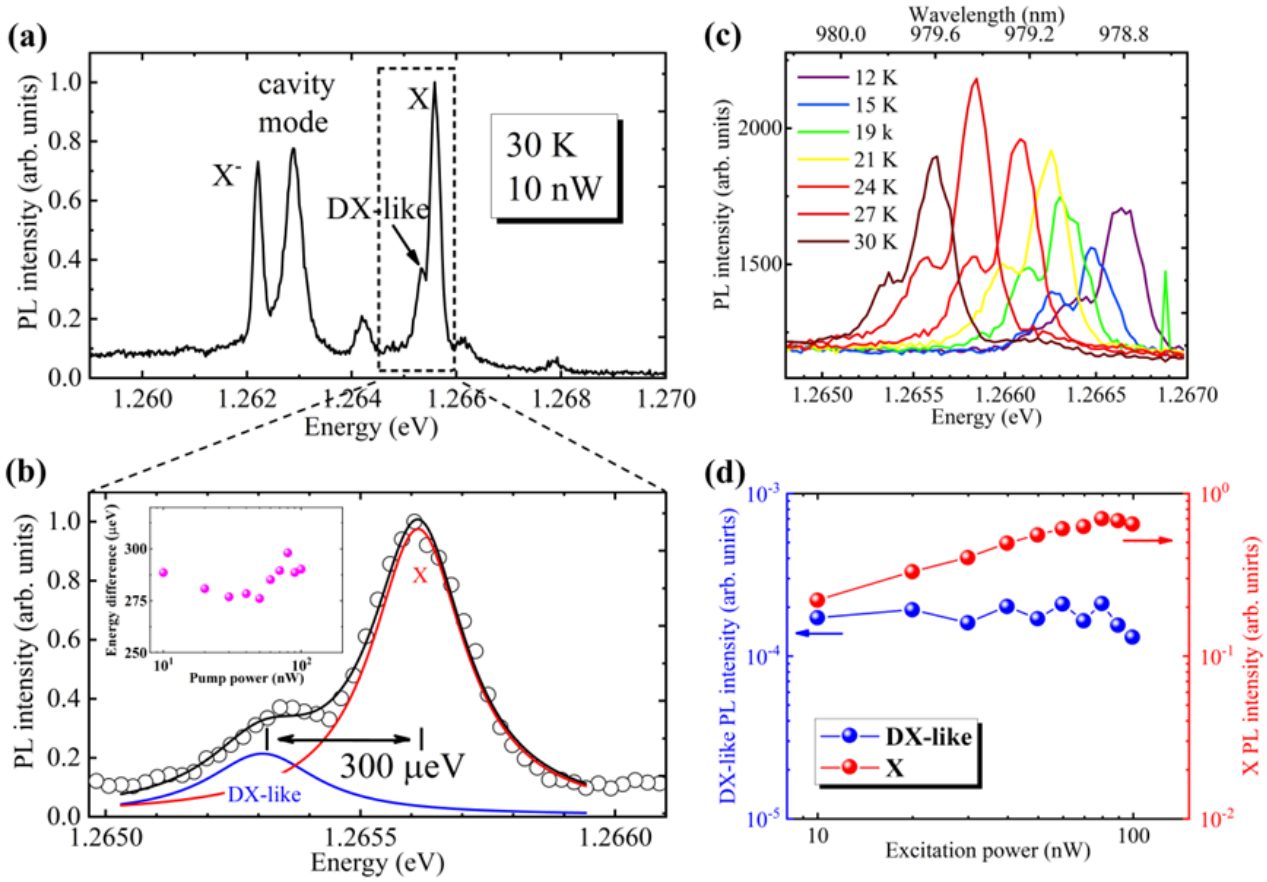

FIG 2.3 | Dark exciton and its high-resolution fine structure, along with measurements in another QD-cavity sample. (a) μPL spectrum of singular pyramidal InGaAs QD-L3 PhC cavity system at 30 K with 532 nm non-resonant pumping at 10 nW. **(b)** Zoom-in of the sharp peak (DX-like) approximately 300 μeV below X. Inset: energy separation between DX-like and X emission as a function of pump power. **(c)** DX-like and X spectra at different temperatures. **(d)** Integrated μPL intensities of DX-like and X emission as a function of pump power. All measurements are performed by using the 532 nm CW laser. Fig 2.3 is published in [77].

2.4 Coexisting Strong-Weak (*Intermediate*) Coupling Regime in Single Site-Controlled InGaAs QD-*L*3 PhC Cavity

To gain deeper insights into the interaction between the cavity and QD, we carefully tune the X-CM coupling of the same QD-cavity device studied in Fig 2.2. This fine-tuning is performed with steps as small as approximately 300 mK temperature increments in our cryostat. For this measurement, we use the sub-barrier excitation at 900 nm to suppress charge fluctuation induced linewidth broadening of X due to the above GaAs bandgap excitation.

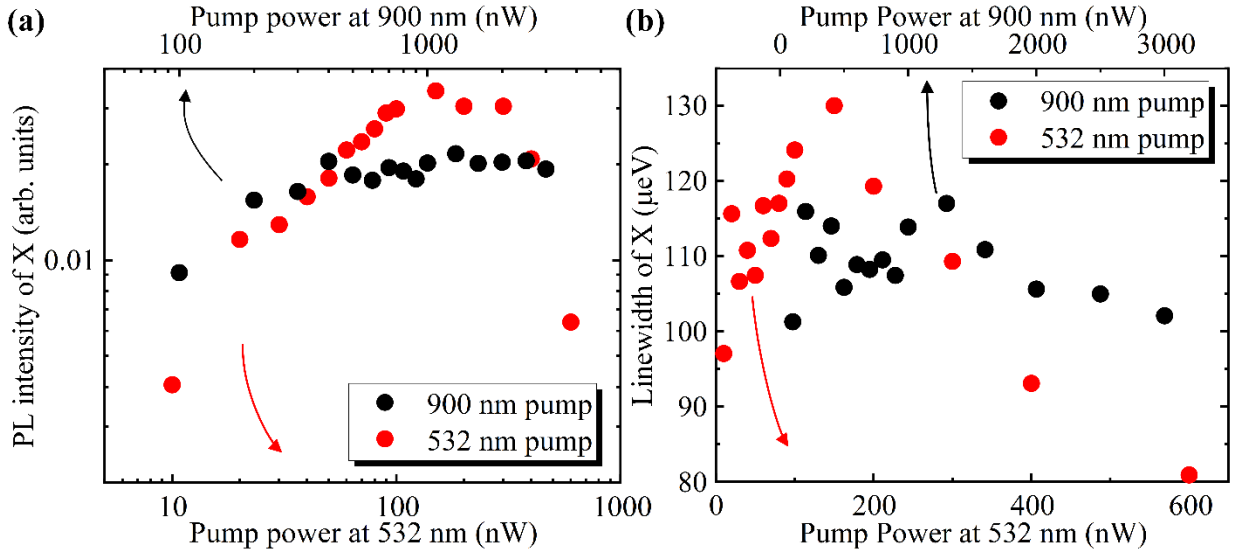

FIG 2.4 | Power dependent μPL of X measured with 532 nm and 900 nm pump (a), Emission intensity of X as a function of pump power at 532 nm (red) and 900 nm (black). **(b),** Linewidth of X as a function of pump power at 532 nm (red) and 900 nm (black). Fig 2.4 is published in [77].

To demonstrate the effect of suppression of charge fluctuations due to sub-barrier excitation, we compare the excitation power-dependent μPL measurement of X with 532 nm and 900 nm excitation. As shown in Fig 2.4, both power-dependent emission intensities of X exhibit saturation, as expected for the single QD. However, the lower intensity with the 900 nm excitation indicates a reduced number of photon-generated carriers with sub-bandgap pump are captured by the QD

aligning with expectations. In Fig 2.4(b), the linewidth at the onset of saturation with the 532 nm excitation is generally larger than that with the 900 nm excitation. Thus suggests a larger charge fluctuation-induced linewidth broadening with the above-bandgap excitation. The narrowing of linewidth after the saturation at increased excitation power indicated the laser-induced stabilization of the charge environment. This stabilization can be attributed to the saturation of local charges, and it leads to suppression of charge fluctuations.

Fig 2.5(a) demonstrates the temperature dependent PL spectra of X and CM from T = 41.8 K to 51.2 K. In Fig 2.5(b), we present the X and CM peak energy as a function of temperature extracted from the spectral Lorentzian fits, with the X-CM coupling observed around 47 K. Single Lorentzian fittings are used for T = 46.55 K and 47.1 K due to the indistinguishable overlap between the X and CM spectra. The slope of the temperature-dependent CM energy undergoes dramatic changes from T = 44.8 K to 46.3 K, corresponding to a detuning range of $75\ \mu eV < \delta < 120\ \mu eV$, where $\delta = \omega_0 - \omega_c$ with ω_0 and ω_c as the X transition and CM energies. The manner in which its slope changes suggest a trend of an avoided crossing of CM from X. Near zero-detuning, the CM energy remains unchanged within the spectral fitting error as the temperature increases from T = 46.3 K to 47.5 K (data marked by the blue arrow in Fig 2.5(b)). The temperature-dependent CM energy regains its slope at far detuning. As shown in Fig 2.5(c), the CM and X linewidths exhibit a tendency to become equal when approaching the zero-detuning temperature, although the CM linewidth minimum does not align with the X linewidth maxima. It is noteworthy that the detuning range where the CM linewidth is minimized corresponds to its dramatic slope change at positive detuning. Simultaneously, the X linewidth maximum occurs at the position where the CM energy crosses the X line. Fig 2.5(d) further illustrates the ratio of

integrated PL intensity of CM (and X) to the total intensity, indicating their inversion with each

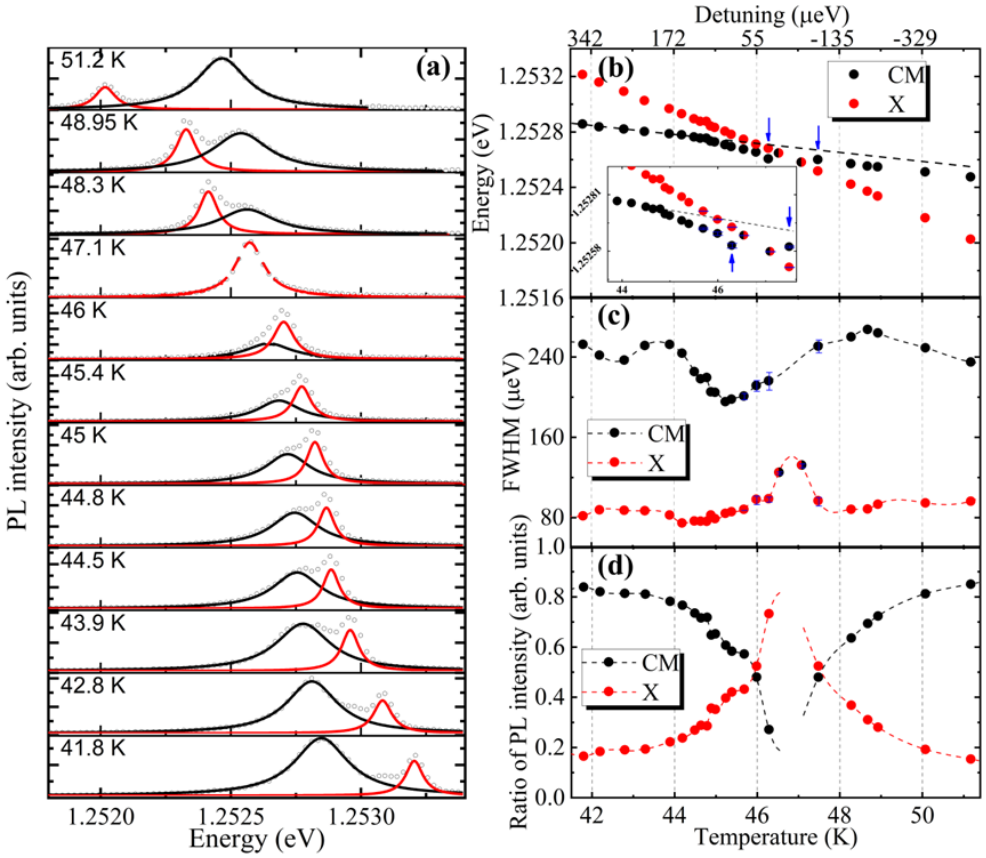

FIG 2.5 | Observations of the coexisting strong-weak coupling regimes probed by high-resolution cryogenic spectroscopy and stepped temperature dependent μPL. (a) Temperature-dependent μPL traces of CM and X emission. **(b)** Peak energy of CM and X emission as a function of temperature extracted by spectral Lorentzian fitting of a. The black dashed line indicates the slopes of CM at large X-CM detuning. Inset: zoom-in of the mode crossing. (**c)** Linewidth of CM and X as a function of temperature. The partial out-of-the synchronization linewidth averaging supports an intermediate coupling region mediated by phonon scattering, with a collective state emission. **(d)** Ratio of the integrated CM and X emission intensity as a function of temperature. Half black and red circles near zero detuning are from single Lorentzian fits. Black and red dash lines are guides to the eyes. Measurements are with 900 nm pulsed excitation. Fig 2.4 is published in [77].

other as QD-CM coupling is controlled from far-detuning to resonance.

The double and single Lorentzian fitting of the μPL measured from T = 45.7 K to 47.5 K (around the blue arrows in Fig 2.5(b)) is detailed in Fig 2.6, with fitting parameters (energy, linewidth, and intensity) and errors shown in Table 2.1.

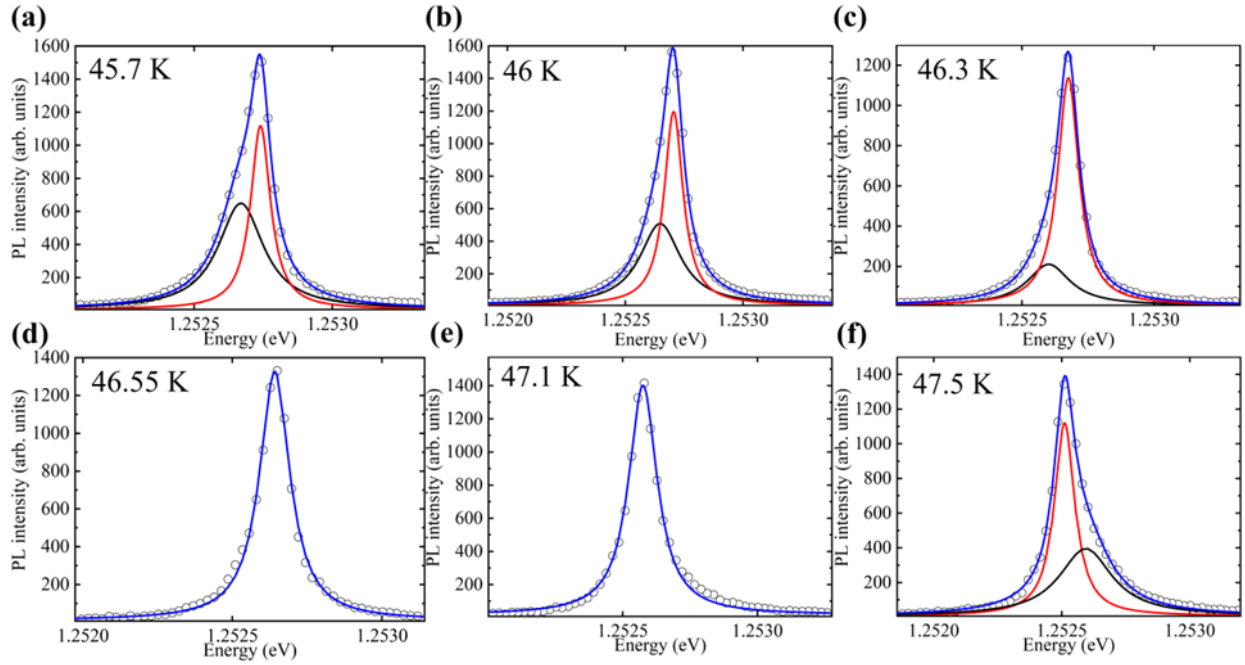

FIG 2.6 | Example CM and X spectrum presented in Fig 2 fitted by double/single-Lorentzian function. Double or single Lorentzian fitted CM (black) and X (red) spectrum at **(a)** 45.7 K, **(b)** 46 K, **(c)** 46.3 K, **(d)** 46.55 K, **(e)** 47.1 K, and **(f)** 47.5 K presented in Fig 2. Empty circles are the raw data and the blue curves are the cumulative fit. The identification of CM and X is based on their relative linewidth. Fig 2.6 is published in [77].

	CM			X		
	Energy (eV)	Linewidth (eV)	Intensity (a.u.)	Energy (eV)	Linewidth (eV)	Intensity (a.u.)
45.7 K	1.25267±3.53992e-6	2.0064e-4±3.17944e-6	0.2028±0.00993	1.25274±5.76187e-7	8.72466e-5±2.74222e-8	0.15285±0.00874
46 K	1.25265±6.84805e-6	2.1157e-4±5.40998e-6	0.16686±0.01803	1.25271±8.63351e-7	9.72482e-5±4.22407e-6	0.18227±0.0169
46.3 K	1.25260±1.02389e-5	1.97861e-4±8.8519e-6	0.0637±0.00984	1.25268±5.99468e-7	9.73744e-5±2.53406e-6	0.17376±0.0083
46.55 K	-	-	-	1.25264±4.6430e-7	1.24223e-4±1.30423e-6	0.25791±0.00192
47.1 K	-	-	-	1.25258±6.739e-7	1.31552e-4±1.91122e-6	0.28714±0.00295
47.5 K	1.25260±3.68148e-6	2.5056e-4±6.40776e-6	0.15387±0.00442	1.25251±5.1424e-7	9.6882e-5±4.21759e-6	0.16815±0.00295

Table 2.1 | Value and standard error of energy, linewidth, and intensity as fitting parameters in the double/single Lorentzian fit.

It is noteworthy that the observed distortion in the slope of the temperature-dependent CM energy occurs within a small detuning range (< 120 μeV) from T = 44 K to 46 K. Importantly, the observed behavior of the avoided-like crossing of CM *deviates from the mode pulling effect*, which is a tendency of CM energy shifting towards X near resonance. The mode pulling effect results from the spectral overlaps of a low-*Q* CM and the X phonon sideband in the weak coupling regime [269]. Moreover, the avoided crossing trend of the CM cannot be explained by simple spectral overlaps between CM and X with bulk phonon dispersion, as observed in the weak coupling regime. Instead, the simultaneous occurrence of QD-CM avoided crossing, the unchanged CM energy crossing X, and their partial out-of-synchronization linewidth averaging points to the effect of *intermediate coupling* mediated by phonon scattering. In this intermediate coupling regime [272], both strong and weak coupling features coexist, as studied theoretically recently. This indicates that the avoided crossing can be attributed to the Rabi doublet in the canonical strong coupling regime, with the unchanged CM energy near zero-detuning serving as a signature of the phonon-mediated collective states emission in the intermediate coupling regime [272], [273].

In the coexisting strong and weak coupling regime, with increased phonon scattering as the bath temperature increases, each eigenstate derived from the JC model undergoes a distinct increase in the dephasing rate. The optical transition of lower and upper polaritons within the first rung of the JC ladder exhibits a reduced dephasing rate, which resembles the strong coupling feature and induces the observed avoided crossing of CM with X in our system. Concurrently, higher-order eigenstates experience larger dephasing and form a collective state [43], [44], located in the vicinity of the zero-detuning center, with the resultant constant CM energy around zero-detuning. The phenomenon of linewidth averaging, a characteristic manifestation of the strong coupling regime, where the CM and X linewidths collapse to the averaged value due to their hybrid

light-matter nature (or polaritons as quasiparticles). The observed partially out-of-synchronization QD-CM linewidth averaging, however, indicates the mixture of the collective state and fundamental Rabi doublet [61], [272], [273]. Such mixture perturbs the linewidth averaging of X and CM in the strong coupling regime.

From the perspective of the effective decay rate and cavity Q-factor [288], the effective linewidth of CM can be obtained from renormalization by an effective cavity pumping P_{CM}. This cavity pumping primarily originates from the phonon-mediated energy transfer from X to CM, leading to the expression $\Gamma_{CM}^{eff} = \gamma_{CM} - P_{CM}$, where Γ_{CM}^{eff} is the effective linewidth of CM. This behavior is analogous to the narrowing of the CM linewidth as the system approaches resonance. Coversely, a reverse process is observed, resulting in the effective linewidth broadening of X as the system approaches resonance. It is noteworthy that our site-controlled single QD-cavity system safely excludes the spurious pumping contributions from any parasitic QD and wetting layer in the P_{CM}, which commonly occurs in self-assembled QDs.

During our measurement, occasional shifts of CM around 1 to 3 nm are observed. Increasing the sample temperature to T = 305 K while maintaining low pressure (10^{-6} Torr) for several hours effectively restores the original CM wavelength, implying that the shift can be attributed to the unintentional deposition of impurities from the cryostat to the surface of the PhC membrane during the cooling process. Prior studies also reported CM energy shifts attributed to gas condensation at the edge of the air hole surrounding the cavity on the PhC membrane, leading to modified membrane thickness and hole dimeter [109], [289]. In our measurement, using the same QD-cavity device depicted in Fig 2.5, with occasional CM energy shift as a result of the PhC membrane surface state changes, the avoided crossing is observed at lower temperatures such as T = 41 K. A slight blue shift in CM energy is observed as it crosses X when the temperature increases from T

= 39.9 K to 41.6 K, indicating the reproducibility of the collective states of the intermediate coupling regime in this QD-cavity device. Fig 2.7(a-c) illustrates the emission energy, linewidths, and ratio of PL intensity as a function of temperature. Fig 2.7(d-g) presents the double-Lorentzian fitting of the spectrum at the data points marked by arrows in (a). The previously observed avoided crossing remains evident, along with the CM energy blue shift when crossing X, suggesting the repeatability of the phenomena.

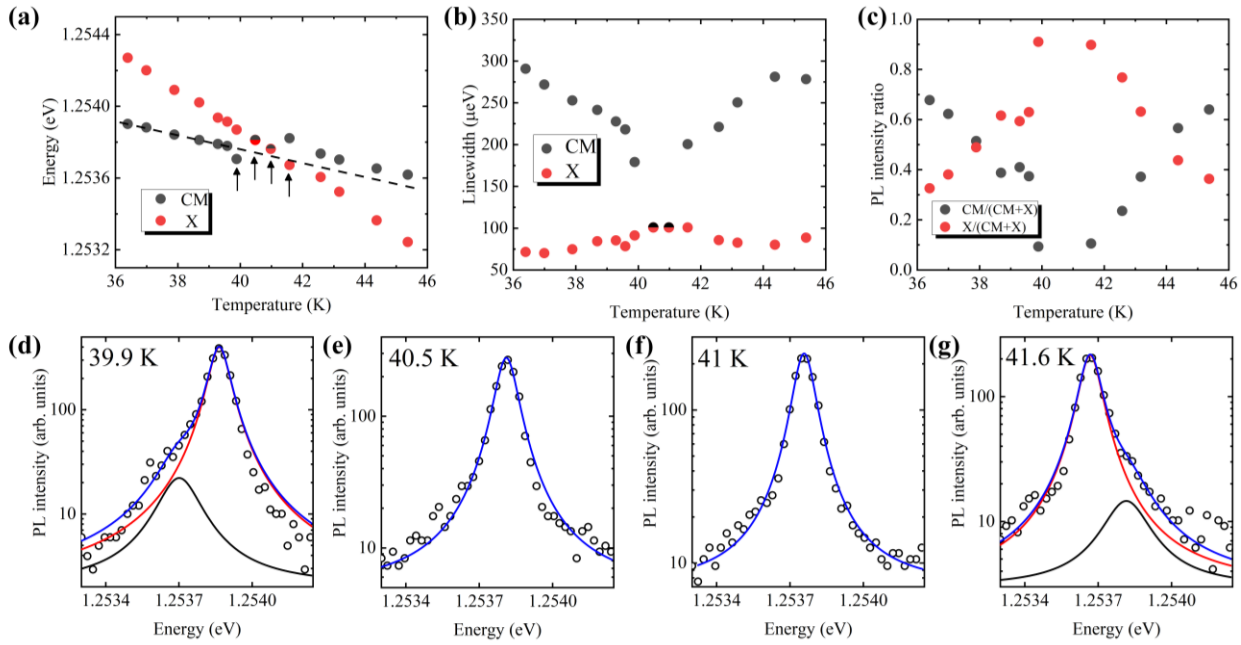

FIG 2.7 | QD-cavity detuning by varying temperature in the case of occasional blue-shift of CM due to the PhC membrane surface state change. Now the X-CM occurs around 41 K. **(a)** Emission energies**. (b)** Linewidths. **(c)** The ratio of PL intensity of X and CM emission as a function of temperature. **(d-g)** Single- and double-Lorentzian fits of the PL spectrum for data points marked by arrows in **(a)**. Fig 2.7 is published in [77].

2.5 Span of Degree of Linear Polarizations in the Coexisting Strong-Weak (*Intermediate*) Coupling Regime

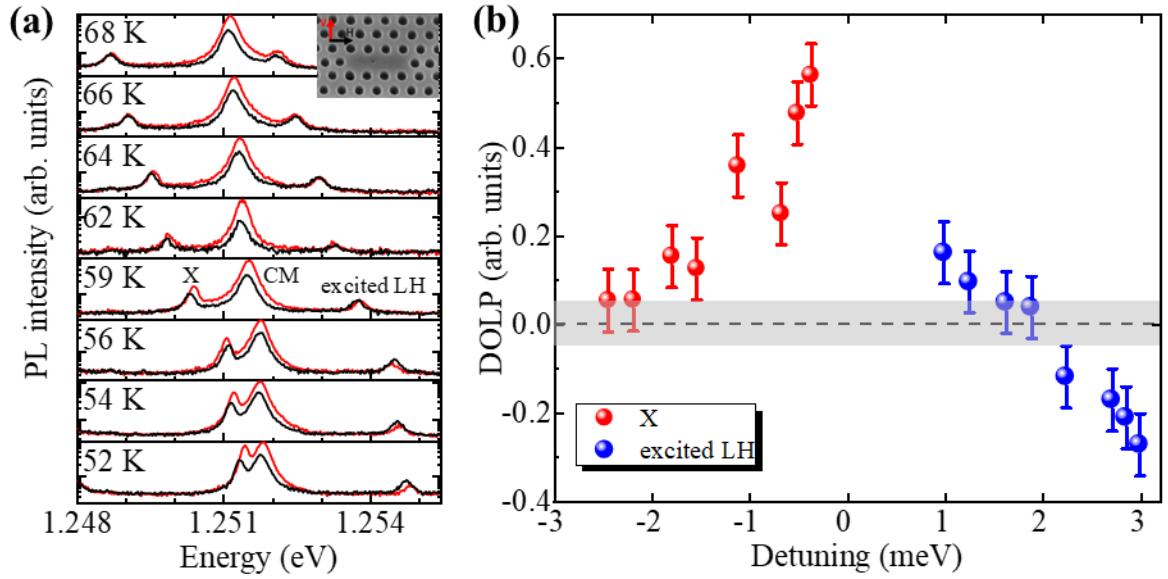

FIG 2.8 | Phonon-assisted coupling examined by the degree of linear polarization (DOLP). **(a)** μPL spectrum resolved in x (black) and y (red) polarizations in the QD-CM detuning range from -3 meV to 3 meV. Inset: H (x) and V (y) polarization with respect to the cavity orientation. **(b)** DOLP of X and LH as a function of their detuning with respect to CM extracted from **a**. The black dash line marks the zero-DOLP line, and the grey shaded region is the typical DOLP value for bare QDs without the presence of a cavity. Negative DOLP is observed over a much larger ≈ 2 meV detuning range, likely due to intrinsic LDOS of the *L*3 cavity. Detuning is defined as the energy difference with respect to CM. Measurements are with 532 nm CW excitation. Inset: X emission energy as a function of the half-wave plate fast-axis angle, indicative of the fine-structure splitting. The data deviates from a linear energy shift due to temperature drift during the measurement. Fig 2.8 is published in [77].

To further investigate phonon-assisted coupling in the intermediate coupling regime, as shown in Fig 2.8(a), we performed the polarization-resolved detuning-dependent μPL on the same QD-

cavity measured in Fig 2.5. The method of polarization-resolved PL measurement can be referred to chapter 1. The degree-of-linear polarization (DOLP) [157], defined as DOLP $= \frac{I_y - I_x}{I_y + I_x}$, where I_y and I_x represent the y (vertical) and x (horizontal)-polarized components of the QD emission aligned with TE and TM modes respectively, is examined. Note that CM is dominated in TE mode as calculated using 3D FDTD in Fig 2.1(a). Fig 2.5(b) provides a comprehensive overview of the DOLP for the X and excited LH across the detuning range of ± 3 meV (which is also the detuning range studied in Fig 2.5(b-d)). The DOLP of QD excitons as a function of detuning serves as a probe to elucidate the pure dephasing mediated QD-CM coupling. The results indicate co-polarization (positive DOLP) between the X and LH exciton species when in close proximity to CM resonance. This co-polarization gradually diminishes with DOLP reducing from + 0.6 to 0, as the system is detuned from resonance to approximately ± 1.2 meV.

Importantly, the detuning range exhibiting pronounced co-polarization (DOLP > 0.5) aligns with the detuning range (approximately -110 μeV to +170 μeV) corresponding to the appearance of dramatic slope distortion in Fig 2.5(b). Within this detuning range, the x polarized components of QD excitation undergo transfer into the cavity decay channel through the phonon-assisted coupling between the CM and QD [36], [38]. This process leads to a relative depletion of the y polarized QD energies. Subsequently, this depletion enhances the y polarized decay channel of QD itself due to Purcell-enhanced cavity photon channeling to the QD energy. This results in the significant co-polarized QD emission of DOLP > 0.5, aligned with the CM. Given that the cavity loss rate is generally much larger than the QD radiative decay rate, the observed overall co-polarization effect occurs at detunings where QD and CM sufficiently interact. And the significant co-polarization roughly coincides with the detuning range exhibiting dramatic slope changes in Fig 2.5(b), suggesting the vital contribution of the phonon-mediated Purcell enhancement in our

observed coexisting strong-weak (intermediate) coupling regimes. The fact that the CM modifies the QD polarization only within a relatively small detuning range strongly suggests the absence of far-off-resonant coupling induced by wetting layers or multiexcitonic background emissions. Additionally, a negative DOLP is observed at a larger detuning range (approximately 2 meV), forming an overall S-shape DOLP curve [75], [169].

As shown in Fig 2.9, a recent study also explains the negative DOLP of QD excitons as the destructive quantum interference of direct QD emission to the free space mode in the y polarization ($|\eta_y|e^{i\phi_{\eta_y}}$) with the QD emission through the cavity decay channel ($|\xi|e^{i\phi_\xi}$), which leads to dominant decay channel of direct QD emission to free space mode in the x polarization (η_x) [165]. Conversely, the positive DOLP is due to the constructive mode interference of such two emission channels leading to dominant QD decay in the y polarization [165].

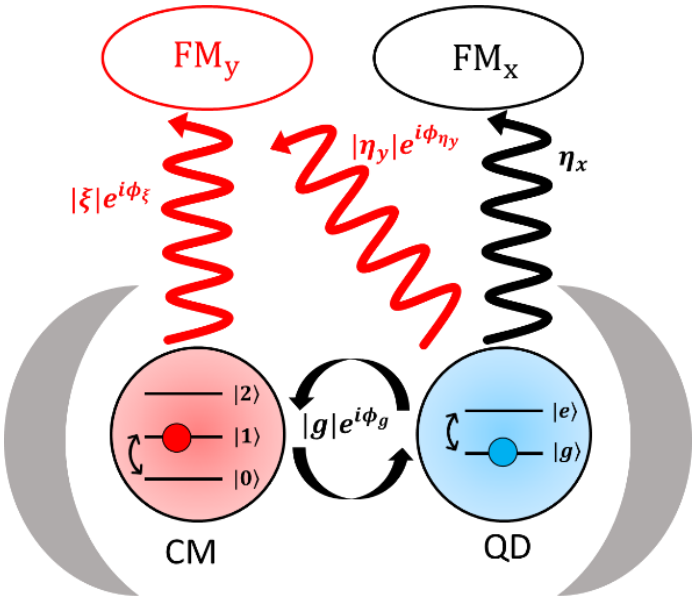

FIG 2.9 | Schematic of QD decay channel in a cavity. Free space mode consists of components in the y-polarization (FM$_y$) and x-polarization (FM$_x$). QD can decay into FM$_y$ through the cavity decay channel ($|\xi|e^{i\phi_\xi}$) mediated by the QD-CM coupling $|g|e^{i\phi_g}$. It can also decay into FM$_y$ and FM$_x$ directly through a y-polarized ($|\eta_y|e^{i\phi_{\eta_y}}$) and x-polarized ($\eta_x$) emission, respectively.

2.6 Anti-Bunching and Collective State Photon Statistics in the Coexisting Strong-Weak (*Intermediate*) Coupling Regime.

To investigate the radiative recombination dynamics of our coupled QD-cavity system, we conduct the TRPL on the X^- emission with different detuning as depicted in Fig 2.10(a). The choice of X^- over the X line is made because at relatively low temperatures (approximately 38 K), the suppression of non-radiative recombination is more effective. To illustrate X^- emission is also co-polarized with CM, like X emission, polarization resolved PL of X^- emission is measured at T = 25 K (the detuning is approximately -1.43 meV) as shown in Fig 2.10(a). In Fig 2.10(b), the extracted DOLP of X- emission is around +0.2 which well fits into the positive DOLP trend of X demonstrated in Fig 2.8(b).

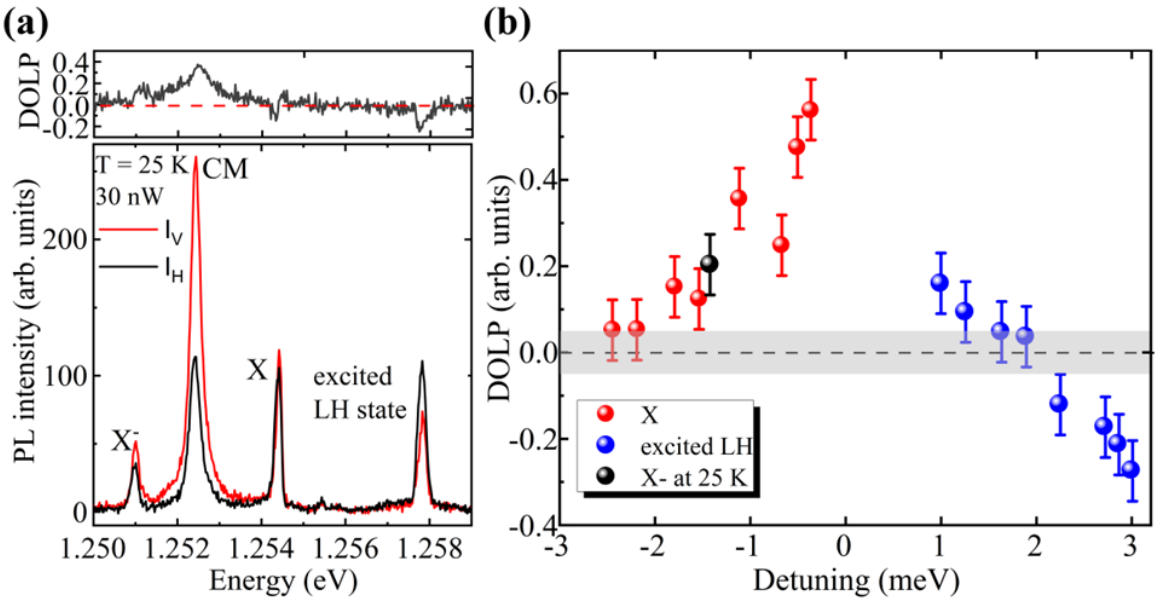

FIG 2.10 | Polarization resolved µPL of X- at 25 K. (a), Lower: polarization resolved µPL spectra of CM and QD excitons including X^- at 25 K. Upper: the corresponding DOLP at 25 K. **(b),** The extracted DOLP of X- plotted in Fig 2.8(b) indicates it is copolarized with the cavity mode. Fig 2.10 is published in [77].

As shown in Fig 2.11, when X^- is near resonance with the CM under 160 μW excitation, Purcell enhancement results in a decay time of 1.2 ns, extracted using a single-exponential decay convolved with an instrument response function of approximately 500 ps. To examine the decay time of the X^- emission far-detuned from resonance (approximately 6 K), the excitation power is doubled to achieve an adequate signal-to-noise ratio (SNR). The PL rise time exhibits a clear time delay [158], attributed to the finite p-state occupation under higher-power excitation. The extracted off-resonance decay time for X^- emission increases to 3.0 ns. Subsequently, the Purcell factor [64] is determined through the equation:

$$\frac{\tau_0}{\tau_{X^-}(\delta)} = \frac{F_P(\kappa_{CM}+\gamma_{X^-}+\gamma_{leak})^2}{4\delta^2+(\kappa_{CM}+\gamma_{X^-}+\gamma_{leak})^2} f^2 + \frac{\tau_0}{\tau_{leak}}, \tag{2.1}$$

Here, $\tau_{X^-}(\delta)$ = 1.2 ns is the measured lifetime of X^- emission near-resonance with the CM, τ_{leak} = 3.0 ns is the lifetime of X^- off-resonance, τ_0 = 1 ns is the typical lifetime of bulk exciton, δ = 130 μeV is the detuning, Q = 5,500 is the near-resonance cavity Q factor, κ_{CM} = 227 μeV is the near-resonance cavity linewidth, and γ_{X^-} = 311 μeV is the pure dephasing rate of X^- estimated from the FWHM of its off-resonance line. The dimensionless constant f depends on the spatial alignment between the site-controlled QD and the antinode of cavity electric fields, as well as the orientation matching between the QD dipole and cavity field. The corresponding Purcell factor F_P for the case of ideal dipole alignment with respect to cavity electric fields is ≈ 2.46. The coupling strength can then be estimated from equation:

$$F_P = \frac{4|g|^2}{(\kappa_{CM}+\gamma_{X^-}+\gamma_{leak})\gamma_0} \tag{2.2}$$

to be around 37 μeV [290].

To gain deeper insights into the coexisting strong-weak (intermediate) coupling regime, we explore the excitation power-dependent photon statistics of the neutral exciton X coupled to the

CM by measuring the second-order correlation function, $g^2(\tau)$, of the coupled X-CM emission. As shown in Fig 2.11(b), an antibunching feature ($g^2(0) < 1$) is evident as the excitation power varies from 300 to 800 nW, with the residual background photon subtracted. The raw histogram

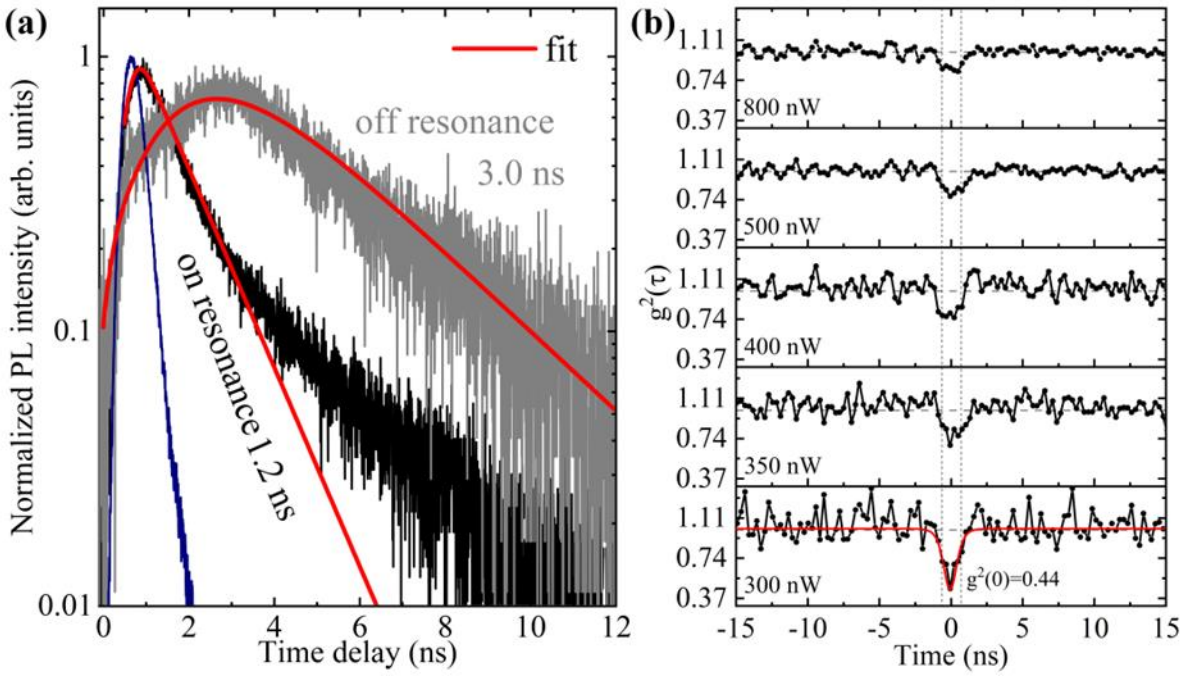

FIG 2.11 | Exciton dynamics and photon statistics of the site-controlled QD-cavity subsystem in the coexisting strong-weak (intermediate) coupling regime. (a), Time-resolved μPL when X- is off- and on-resonance with the CM. The system instrument response is represented by the dark blue curve. The red curves are the single exponential fits. A 900 nm pulse laser is used for the excitation. **(b)**, Second-order correlation function measured when X is in resonance with the CM under 532 nm excitation from 300 nW to 800 nW. The red curve is fit by a Gaussian convolved second-order autocorrelation function of a two-level system $g^2(\tau) = \int_{-\infty}^{\infty}(1 - e^{-|t|/\tau_d})\frac{e^{-\frac{(\tau-t)^2}{2\sigma^2}}}{\sigma\sqrt{2\pi}}dt$ where the FWHM of the Gaussian is equal to the timing jitter of the system 300 ps. The horizontal dash line indicates $g^2(\tau) = 1$. The vertical dash lines indicate the region of the flattened antibunching bottom. Fis 2.11 is published in [77].

(in the unit of counts) is firstly normalized by the factor $\frac{T^2}{\Delta t(T-\tau)N^2}$, where T represents the measurement time, Δt is the time bin, and N represents the number of photon events [291]. Following the approach in Ref. [292], to suppress the impact of detector dark counts and leaked photons from ambient and laser, the residual background photon is subtracted using the noise-influenced correlation function:

$$g^2_{sub} = [g^2 - (1-\rho^2)]/\rho^2 \tag{2.3}$$

Here ρ is the signal-to-background ratio. Eventually, at a low excitation power of 300 nW (onset of the saturation of X emission) we obtain $g^2(0) = 0.44$. By simply considering a two-level system at low carrier injection, the antibunching feature is fit with a Gaussian-convoluted expression:

$$g^2(\tau) = \int_{-\infty}^{\infty}(1 - e^{-|t|/\tau_d})\frac{e^{-\frac{(\tau-t)^2}{2\sigma^2}}}{\sigma\sqrt{2\pi}}dt \tag{2.4}$$

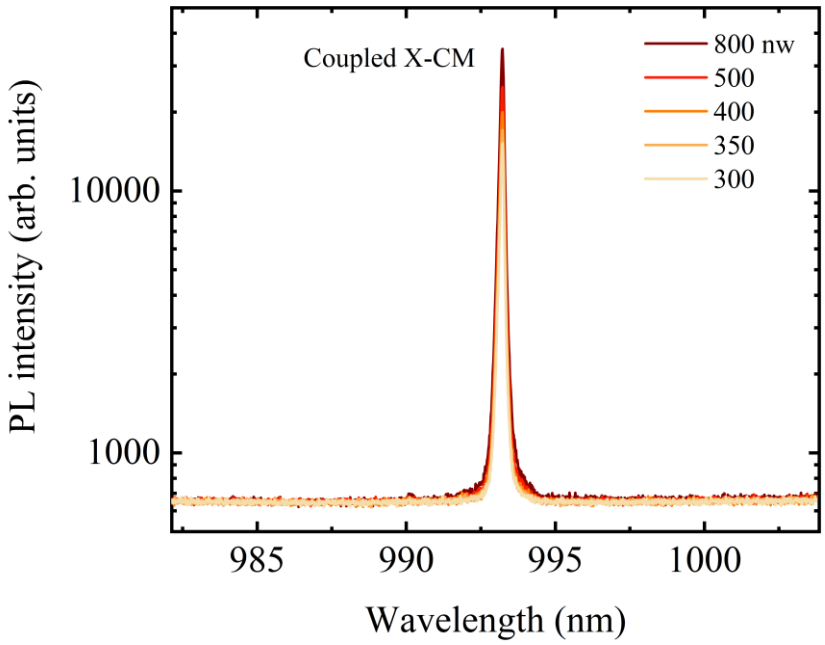

FIG 2.12 | µPL spectra of coupled X-CM with tunable long and short pass filtering. It is measured at 300 to 800 nW, for photon correlation measurement in Fig 4(b). Fig 2.12 is published in [77].

The FWHM of the Gaussian equals to the timing jitter of the system (300 ps) and τ_d is taken to be 400 ps. With these fitting parameters, the fit accurately reproduces the observed antibunching signature of the coupled X-CM emission at 300 nW. As the excitation power increases up to 800 nW, an elevated $g^2(0)$ value up to 0.82 is observed. Note that the clean spectra of coupled X-CM after applying band pass filtering shown in Fig 2.12 is feeding the HBT setup. It indicates no direct emission from other excitonic species is involved in this measurement.

It is noteworthy that the non-zero $g^2(0)$ observed at 300 nW, even after the background subtraction, might be attributed to limited phonon-assisted cavity feeding by X^- or LH-related transition, resulting in occasional uncorrelated photon feeding the HBT setup. However, this contribution is likely weak because the primary emission feeding the cavity is from X which is resonantly coupled to CM. Importantly, the *absence* of the multiexcitonic background emission from wetting layer and parasite QDs in our single site-controlled QD systems excludes any cavity feeding from the excitonic continuum. On the other hand, the non-zero $g^2(0)$ can be arise from the short decay time (400 ps) which is comparable to the timing jitter of the HBT setup (300 ps). Further reducing the excitation power could potentially bring $g^2(0)$ closer to zero, although this becomes challenging due to the decrease in photon counts.

Additionally, as the excitation power increases, the antibunching dip gradually evolves into a plateau in contrast to the sharp dip at 300 nW. Note that there is no observed bunching signature up to 800 nW at a larger time scale outside the antibunching notch which is reported in previous QD studies as a result of the detection of biexciton transition [293] or spectral diffusion [294]. It suggests that the cavity feeding by biexciton is limited in our systems. Therefore, the increase in $g^2(0)$ due to increased cavity feeding from biexciton can be ruled out. Instead, our tentative interpretation of the non-zero $g^2(0)$ and flattened antibunching bottom is that increased excitation

power induces elevated photon number accumulation in the cavity Fock states. The resulting increased collective state [295], attributed to multiphoton emission, dominates the photon statistics in the intermediate coupling regime, flattening the antibunching dip. The flattened antibunching bottom within a time window ±τ suggests that the probability of the resonantly coupled QD-cavity occupied with electron-hole pair is non-zero and remains unchanged up to a time delay τ after the first photon emission, indicating the formation of collective states. The width of the antibunching notch, representing the population regeneration time of the collective states, does not change significantly with excitation power. This suggests that the collective states and their population in higher rungs of the JC ladder are not saturated up to 800 nW. The observed flattening of antibunched photon statistics aligns with the formation of collective states resulting from phonon-mediated coupling in the intermediate coupling regime.

2.7 Discussions

The precise positioning of single site-controlled pyramidal InGaAs QDs at specified locations in PhC cavities holds significant promise for the development of functional monolithic quantum photonic circuits. However, such a system is based on (111)B-oriented GaAs membrane and the increased loss and low *Q*-factor in PhC cavities often results in operation within the weak coupling regime.

In this chapter, we successfully attain the intermediate coupling regime in our single site-controlled pyramidal InGaAs QD – *L*3 PhC cavities. This is facilitated by tailoring the Indium content and pyramid size, lead to a red-shifted QD emission wavelength of up to approximately 1 μm and an increased cavity *Q*-factor compared to previous studies on similar systems. The detuning-dependent μPL spectrum reveals the co-occurrence of QD-CM avoided crossing, indicative of the Rabi doublet in a strongly coupled system. Simultaneously, it shows the trend of

maintaining constant or slight blue shift of CM energy near zero-detuning due to the formation of collective states mediated by phonon-assisted coupling. The partial out-of-synchronization linewidth-narrowing is linked to their mixed behavior. Further polarization-resolved high-resolution μPL uncovers the contribution of phonon-mediated coupling in the intermediate coupling regimes, complementing the dynamical and anti-bunching photon statistical signatures.

This chapter presents a guideline for improving the cavity *Q*-factor and achieving the stronger coupling regime for quantum states preparation, control, and nonlinear quantum optics, which will be presented in the next chapter.

Chapter 3

Single Site-Controlled Quantum Dot-Nanocavity Operating in the Onset of Strong Coupling Regime.

3.1 Introduction

The strongly coupled QD-cavity system serves as a crucial component in integrated quantum photonic circuits, playing an important role in non-classical light generation and quantum information processing. This system enables on-demand generation of non-classical light through phenomena such as photon-induced tunneling and photon blockade via strong exciton-photon coupling [296]–[298]. Additionally, it facilitates spin-controlled quantum switch through strong QD spin-photon coupling [85], [87], [89], [253], [299], [300]. In the coupled exciton-photon hybrid architecture, the decoherence, has dual implications. On one hand, it fundamentally affects the information losses through the environment during the quantum information processing, influencing coherent control for secure quantum communications [86], [88], [238], [301], [302], quantum memory enabled single-photon switch [233], [303], [304], coherent emitter-emitter coupling [305]–[307], and quantum network protocol based on deterministic cluster state generation [91]–[93], [97], [98], [308]. On the other hand, exciton pure dephasing [259], [309]–[311] and phonon-induced dephasing [157], [264], [265], [272], [273], [312] play important roles in the dynamics of QD-cavity interactions, JC nonlinearities, and intermediate coupling regimes [77].

As mentioned, to date, most quantum applications based on semiconductor QDs mostly rely on self-assembled QDs, suffering from the challenge of random QD locations. This limitation hampers further optical lithography steps, scalable integration, and practical implementation in

integrated quantum photonics [313]. We have seen that a promising alternative is presented by single site-controlled InGaAs QDs grown at patterned pyramidal pits on the (111)B-oriented GaAs substrate. These pyramidal QDs offer unique advantages compared to self-assembled QDs [314], holding remarkable promise for monolithic functional integrated quantum photonic circuits. As a concise summary, also discussed in chapter 1, the pyramidal QD systems have the following advantages: (1) The deterministic QD nucleation and position control of pyramidal QD allow efficient light-matter interaction by placing multiple-QD systems at the desired antinodes of PhC cavities and WGs with nanometer accuracy [169]. (The multi-QD system will be discussed in chapter 4.) (2) Their high structural symmetry contributes to reduced fine structure splitting for polarization-entangled photon generation [170], [171]. (3) The absence of spurious cavity feeding from wetting layers [121] and parasite QDs in the vicinity of the QD is a result of the peculiar MOVPE growth of QD at the sharp tip of the pyramid [136], [315]. (4) The inhomogeneous broadening of pyramidal QD is as low as 1.4 meV thanks to precise control of the nominal pyramid size [153], [167]. These features enable the fabrication of large-scale arrays of similar QD-cavity systems [171]. Furthermore, more complicated functional quantum photonic circuits, which are challenging to achieve reliably with self-assembled QDs, have been realized using site-controlled pyramidal QDs in PhC WGs [172], tilted cavities [162], and Fano cavities [163].

As discussed in chapter 2, research on achieving the strong coupling regime and understanding the impact of dephasing in strong exciton-photon interaction has predominantly based on self-assembled QDs [62], [220], [236], [237], [241], [243]–[246]. However, there is limited literature on achieving strong coupling regime using site-controlled pyramidal InGaAs QDs, which hinders their potential in applications demanding strong light-matter interactions which are mentioned in prior paragraph. This limitation arises from two main factors: (1) Previously studied pyramid

InGaAs QDs exhibit s-state emission around 1.4 eV, where the cavity *Q*-factor is relatively low [75], [157], [158]; (2) (111)B-oriented GaAs substrates and membranes, crucial for etching highly symmetric pyramidal recesses for site-controlled QD epitaxy [169], [276], demonstrate increased optical cavity losses compared to the conventional (100)-oriented substrates and membranes.

To address the limitation, as we have seen in chapter 2, red shifting the QD s-state energy to approximately 1.24 eV without compromising its sub-100 μeV excitonic linewidth [153], [155] can effectively improve the cavity *Q*-factor. This is due to the reduced absorption losses from the Urbach tails of GaAs [277], [278] and smaller structural disorder thanks to larger PhC parameters. In this chapter, we change to an single site-controlled QD-*L*7 PhC cavity system and observe a significantly improved cavity *Q*-factors of the fundamental CM up to ~ 12000 surpass previous studies with lower *Q*-factor (< 4500) that conducted in the weak coupling [75], [157], [158] or the system operating in the intermediate coupling regime [77] as shown in chapter 2. We observed that such improved *L*7 PhC cavity bring the cavity quantum electrodynamics **(**cQED) operating at the onset of the strong coupling regime, mediated by phonon induced dephasing. This exploration is conducted through cryogenic μPL supported by cQED modeling. By adjusting the QD-CM detuning through temperature variation, we observe linewidth narrowing and energy splitting at resonance. A corresponding cQED model sheds light on the role of pure and phonon-induced dephasing in our system, confirming its operation at the onset of strong coupling. This assertion is further reinforced by our experimental observation of Rabi-like oscillation and quantum beating between the upper and lower energy components by varying the pump power. Importantly, these phenomena only occur at small QD-CM detuning and can be well reproduced by our modeling of the system's initial states. Such observation of the onset of strong coupling regime mediated by phonons in our QD-*L*7 cavity device extends the potential applications of site-controlled pyramidal

InGaAs QD systems. These systems, previously mainly operating in weak or intermediate coupling regimes, now prove valuable for applications requiring strong exciton-photon coupling, such as nonlinear optics and coherent control for quantum information processing in a monolithic functional integrated quantum photonic circuit.

3.2 Site-Controlled InGaAs QD-*L*7 PhC Cavity Devices

For the devices studied in this chapter, the site-controlled QD is the same as the one used in chapter 2. The PhC structures with slab thickness t ≈ 265 nm, lattice constant a ≈ 225 nm, and air hole radius r ranging from 30 nm to 50 nm are lithographically written on top of the QD pattern and all the surrounding QDs are etched away except the one at the center of the *L*7 cavity. The following modification is made to further improve the cavity *Q*-factor: first three side holes on the left and right of the cavity are shifted outwards by 0.23a, 0.15a, and 0.048a.

3.3 Optical Properties and Recombination Dynamics

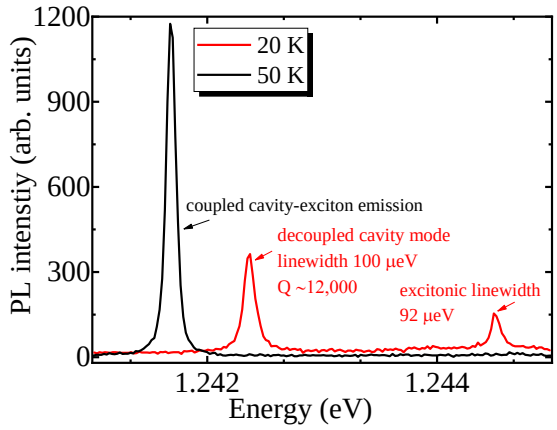

FIG 3.1 | μPL spectra of site-controlled QD-*L*7 cavity. The black and red spectra are the μPL of the system when QD exciton and CM are coupled (T = 50 K) and decoupled (T = 20 K), respectively. The decoupled CM at T = 50 K exhibits a linewidth of approximately 100 μeV with cavity *Q*-factor of approximately 12000. The linewidth of the decoupled QD exciton at T = 20 K is approximately 92 μeV. Fig 2.1 is published in [76].

We first characterize the μPL spectra of our site-controlled QD - L7 photonic crystal cavity (PhC) cavity system (a SEM image of the device is shown in the inset in Fig 2.3). Fig 3.1 illustrates the μPL spectra of decoupled (red) and coupled QD-cavity (black) systems measured at two sample temperatures, excited by a 900 nm pulsed diode laser with an average excitation power of 40 μW. At 20K, the QD s-state exciton line is observed around 1.2445 eV with a linewidth as narrow as 92 ± 4 μeV. Correspondingly, the linewidth of the fundamental mode of the *L*7 cavity is approximately 100 ± 2 μeV, resulting in a cavity Q-factor of approximately 12,000, significantly larger than values reported in similar (111)B-based membrane cavities and chapter 2 [75], [157], [158]. We note that a low rate of excitonic dephasing and cavity dissipation, along with large coupling strength by accurately positioning the QD at the maximum of the cavity field is a prerequisite for strong exciton-photon coupling [62], [316]. As the temperature increases to around T = 50 K, the exciton emission becomes resonantly coupled with CM. The Purcell-enhanced coupled QD-CM PL intensity is approximately eight times larger than the PL intensity of the

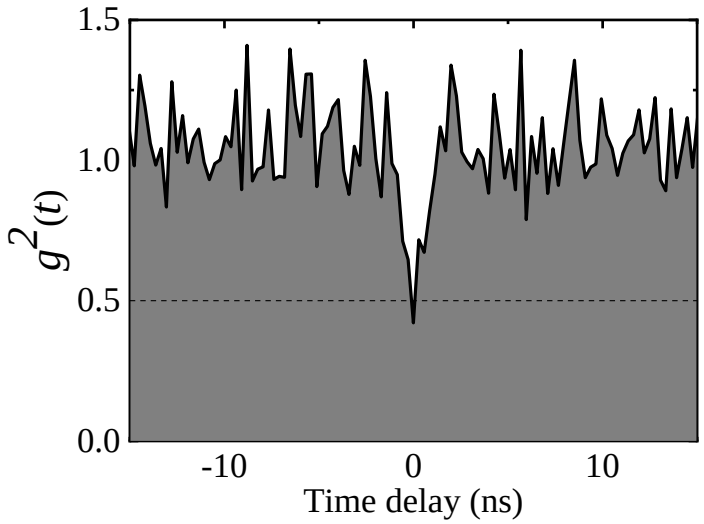

FIG 3.2 | Second-order correlation function of the QD-L7 cavity system when QD and CM are coupled (T = 50 K). Fig 3.2 is published in [76].

decoupled exciton emission. In Fig 3.2, HBT measurements, using a 532 nm continuous-wave laser excitation and narrow band pass filtering, confirm the single photon emission characteristics, evidenced by the degree of second-order coherence $g^{(2)}(\tau=0) \approx 0.42 < 0.5$ at QD-CM resonance. This result supports that the coupled QD-CM is at the single-exciton and single-photon levels. Note that the limited single photon timing resolution of the avalanche photodiode used (350 ps) can contribute to the observed non-zero g(2)(τ=0). Such distortion of g(2)(τ=0) can be improved using superconducting nanowire single photon detectors (SNSPDs) or resonant/quasi-resonant pumping.

Fig 3.3 examines the polarization features of the CM and QD excitonic emission with a detuning of approximately 3.8 meV at T = 35 K. The inset presents the scanning electron

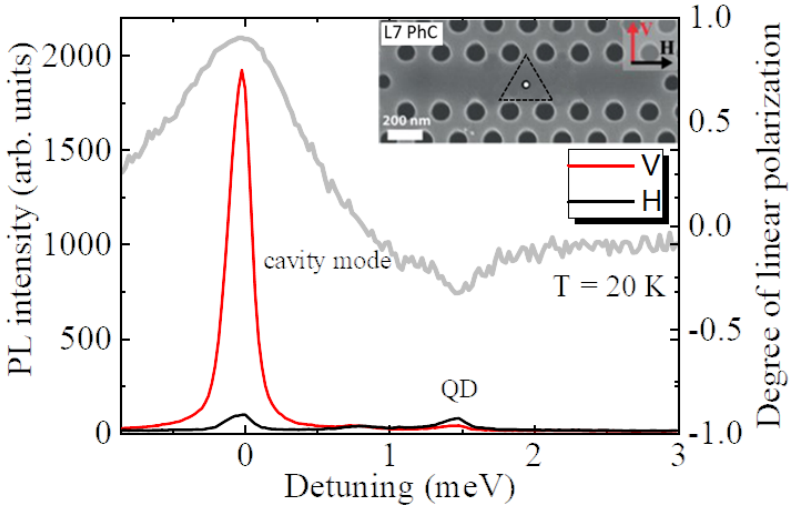

FIG 3.3 | Polarization-resolved μPL of the QD-*L*7 cavity system. μPL of TE and TM cavity mode and QD single excitonic line measured at T = 20 K, with y (V, red) and x (H, black) polarization. The grey line indicates the degree of linear polarization $P = (I_y - I_x)/(I_y + I_x)$. Inset: SEM image of single site-controlled QD - *L*7 PhC cavity, where the position of pyramidal QD, as dot-triangle labeling, matches the antinode of the cavity electric field distribution. Fig 3.3 is published in [76].

microscope (SEM) image of the QD-cavity structure, where the dot-triangle sign indicates the position of the inverted pyramidal QD. The luminescence emission through the CM predominantly exhibits y-polarization (or vertical polarization), resulting from the coupling of the QD emission to the TE-polarized field of the CM. In contrast, the QD excitonic emission not resonant with the CM exhibits anti-polarization with respect to that of the CM shown as a negative DOLP. As explained in Fig 2.9 in chapter 2, such anti-polarization at large detuning and overall S-shape DOLP is a result of the destructive mode interference of the y-polarized component of direct QD decaying into free-space mode and QD decaying through the y-polarized cavity mode [165]. Such destructive interference leads to x-polarized component of direct QD decaying into free-space mode to be dominant in the DOLP [165].

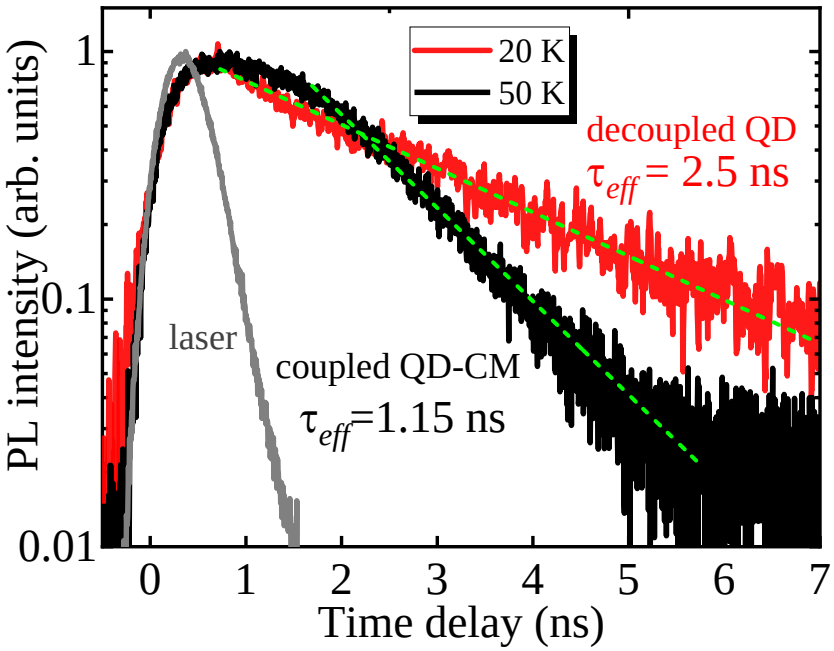

FIG 3.4 | Time-resolved PL measurement on QD-*L*7 cavity system. PL decay of decoupled excitonic emission (red) at T = 20 K and coupled QD-CM (black) at T = 50 K, corresponding to 2.46 ns and 1.15 ns decay time, extracted by single exponential decay, respectively. The grey

decay curve records the laser decay, which suggests an about 500 ps instrument response. Measurement is performed with an average power of 40 μW at 80MHz repetition rate with a 900 nm pulse laser. Fig 3.4 is published in [76].

We further perform the TRPL measurement with sub-bandgap 900 nm pulsed excitation at a 20 MHz repetition rate with a lower average power at 10 μW. This allows us to characterize the QD-cavity interaction dynamics at low excitation levels with lower excitonic dephasing (a comparison between above-bandgap and sub-bandgap excitation can be referred to Fig 2.4 in chapter 2.) Fig 3.4 illustrates a shortening of the decay time from 2.5 ns for the decoupled QD excitonic emission to 1.2 ns for the resonantly coupled QD-CM emission, indicating the Purcell enhancement. The instrument response is approximately 0.5 ns, as confirmed by probing the laser pulse. Notably, the PL decay of the resonantly coupled QD-CM system reveals a slower decay at an early time delay, likely associated with the coupled QD-CM dynamics [317]. In comparison, the decay of decoupled excitonic emission is mono-exponential and starts at an early time delay, confirming the absence of saturation of the QD in the low injection region.

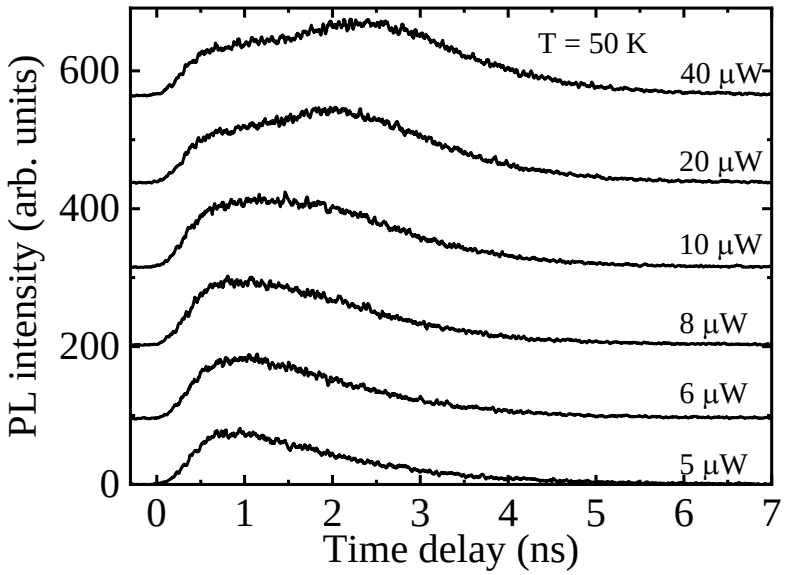

FIG 3.5 | Power dependent time-resolved PL measurement on coupled QD-*L*7 cavity system. Time-resolved PL traces of the resonantly coupled QD-CM as a function of pump power at T = 50 K. Measurement is performed at 20MHz repetition rate with a 900 nm pulse laser. Fig 3.5 is published in [76].

Fig 3.5 further presents the decay of the coupled QD-CM emission (linear scale of the Y axis) as a function of excitation power from 5 μW to 40 μW. Up to 20 μW, the QD-CM coupling-induced plateau at early time delay extends up to 2 ns with increasing power. This plateau is unlikely attributed to multiexcitonic transitions originating from the wetting layer or quantum wire (QWR) along the edges of the pyramids. The multiexcitonic background induced by wetting layers typically observed in self-assembled QD systems is not present in the pyramidal QD systems [157], [158] and the latter reported to appear as an additional peak at early delay with fast dynamics [158] is not observed in our results. Note that the intensity of CM and QD exciton saturated around the

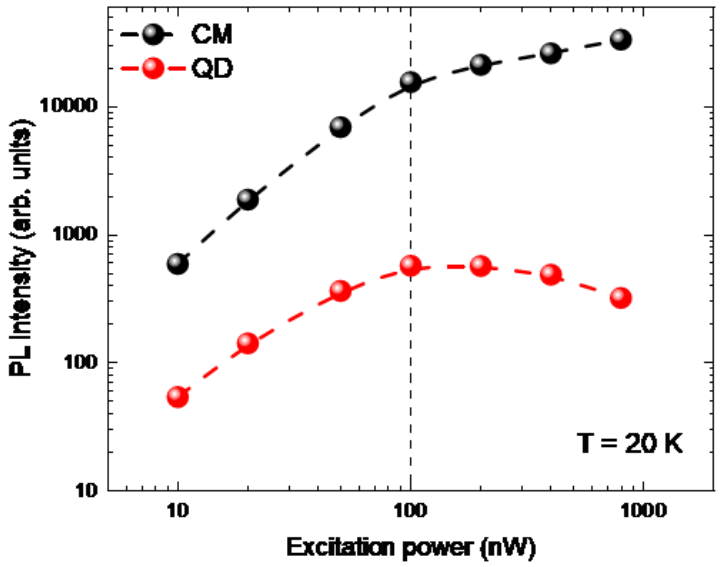

FIG 3.6 | Power dependent PL measurement of QD and CM when they are decoupled. Power dependent PL intensity of decoupled QD exciton and CM at T=20K using a 532 nm cw laser. Fig 3.6 is published in [76].

same power suggests the absent contribution from multiexcitonic background continuum as demonstrated in Fig 3.6.

Instead, this PL plateau may be related to the QD-CM interactions. However, further measurements with finer time sampling should be performed with a longer laser pulse with energy resonance with coupled QD-CM for more in-depth investigation. This resonant excitation scheme is however beyond our current capability and will be implemented in the future. As the power increases to > 20 μW, a secondary raising of PL intensity appears around 2 ns, resulting from the finite p-state occupation of QD due to carrier feeding [158]. This finite p-state feeding leads to a reduction of lifetime in the lifetime of coupled QD-CM decay as shown in Fig 3.7(b).

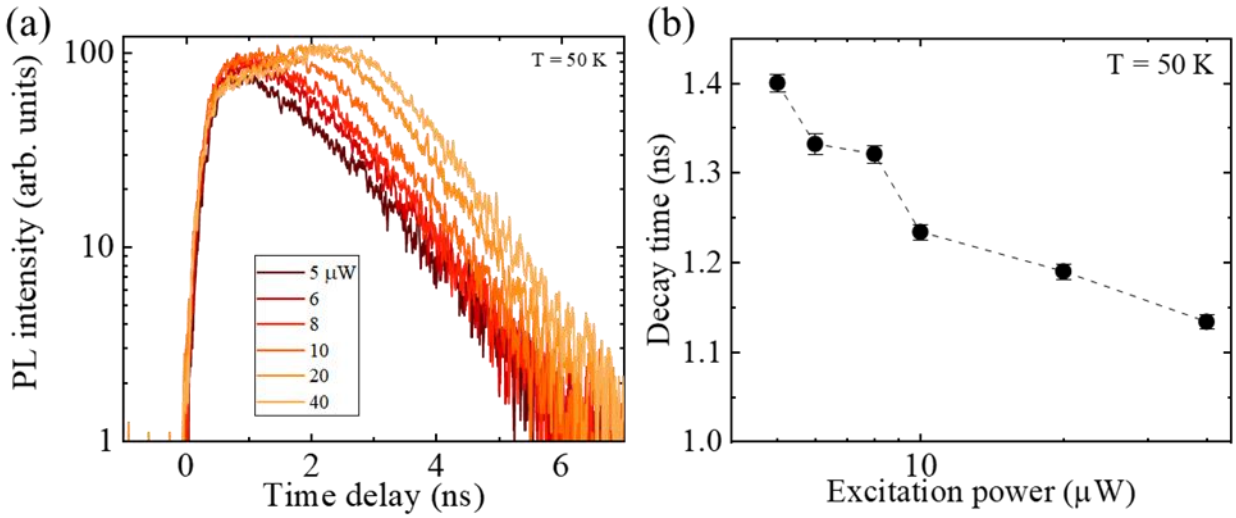

FIG 3.7 | Power dependence of decay time (a) PL decay of coupled QD-CM (black) at T = 50 K with pump power from 5 μW to 40 μW with PL intensity axis in log scale. Measurement is performed at 20MHz laser repetition rate. **(b)** Extracted lifetime as a function of excitation power. Fig 3.7 is published in [76].

3.4 Phonon Dynamics and Dephasing Toward the Strong Coupling Regime

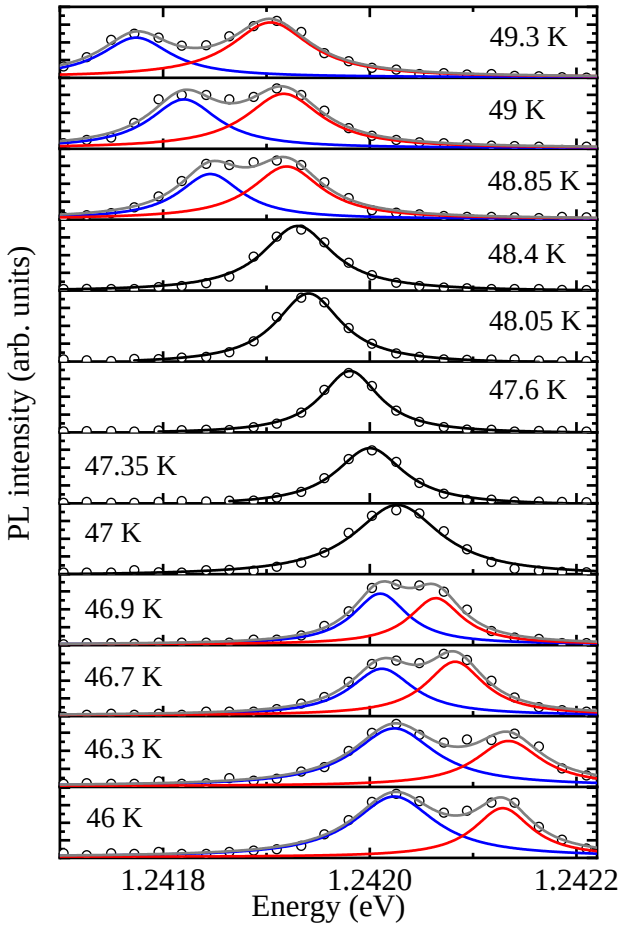

FIG 3.8 | Temperature tuning of QD-cavity coupling Experimental PL spectra (circle) of the coupled QD and CM around resonance fine-tuned by varying temperature. The red and blue curves represent the double Lorentzian fitting to the upper and lower energy components, respectively. The grey curve is their cumulative fit. The black curves at 47 K to 48.4 K are the single Lorentzian fitting. Fig 3.8 is published in [76].

We subsequently characterize the μPL spectra during fine-tuning of the QD-cavity coupling near resonance by varying the sample temperature, using a much lower pumping of 3 μW to suppress free-carrier-induced charge fluctuation. The QD energy changes rapidly with temperature, following the temperature dependence of GaAs bandgap, while the CM changes at a slower rate,

dependent on the thermal induced refractive index change of the PhC. The coupling temperature is determined to be approximately 47.6 K. The cavity pulling effect, previously reported as a result of the interaction of phonon sideband of the self-assembled QD with the CM [269] is not visible in our results. Fig 3.8 shows the phenomenological double Lorentzian fitting performed to the PL spectrum at temperatures where the CM and QD exciton peak can be visually distinguished. However, from T = 47 K to 48.4 K, the merging of high and low energy components leads to very closed R-square values (~ 0.99) for both double and single Lorentzian fits to the spectrum. As shown in Fig 3.9, the R-square values for single and double Lorentzian fits are: R_S^2(48.05K) = 0.9809, R_S^2(47.60K) = 0.9890, R_S^2(47.35K) = 0.9931, R_S^2(47.00K) = 0.9919 and R_D^2(48.05K) = 0.9934, R_D^2(47.60K) = 0.9965, R_D^2(47.35K) = 0.9983, R_D^2(47.00K) = 0.9978. It suggests that the

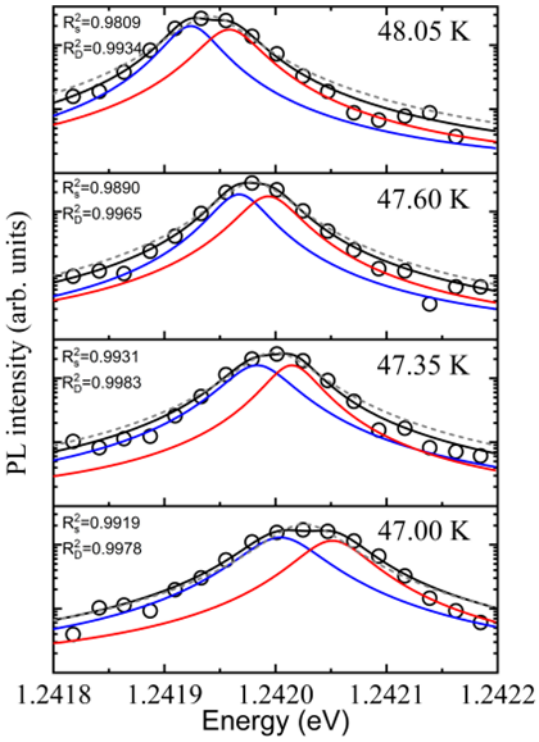

FIG 3.9 | Double and single Lorentzian fits to the PL spectra at T = 47 K to 48.05 K. Single (grey dash) and double (solid) Lorentzian fitting of PL spectra measured at T = 47 K to 48.05 K. R-square values for single and double Lorentzian fitting are denoted by R_S^2 and R_D^2, respectively. Fig 3.9 is published in [76].

double Lorentzian analysis at T = 47 to 48.4 K is not reliable although their R-square values are close to 1. As a result, the anti-crossing of QD-CM is not resolved at near-zero detuning range, indicating a small coupling strength in this system which will be discussed later. However, it is noted that the typical doublet splitting in the strong coupling regime can be concealed by various factors such as pure dephasing, phonon scattering, and incoherent pumping, resulting in a plateau or even a single peak in our QD-cavity system [309]. Indeed, as shown in Fig 3.10(c), the intensity

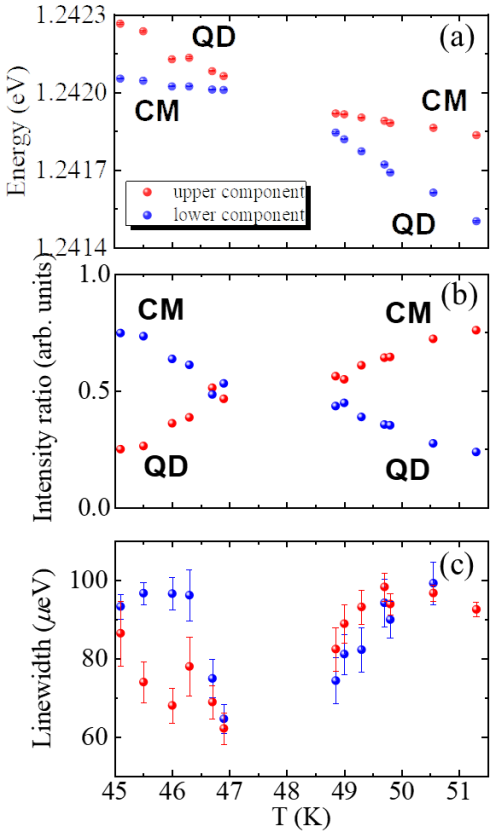

FIG 3.10 | Temperature-dependent energy, intensity ratio, and linewidth extracted from Fig 3.9. (a) Dependences of PL peak energies of coupled QD-cavity system over a wide temperature range. **(b)** Corresponding detuning dependent PL intensity ratio between the upper and lower energy components to their summation, which reveals averaging near resonance. **(c)** Corresponding detuning-dependent linewidth of the upper and lower energy components. Fig 3.10 is published in [76].

ratio of the CM and QD to their summation exhibits averaging behavior near resonance as a feature of polariton that inherit the properties from both photon and exciton [62]. Importantly, the linewidth at T = 46.7 K obtained from the single Lorentzian fitting is 68.9 ± 2.5 μeV. It reveals a clear narrowing behavior, compared to the decoupled cavity linewidth of 100 ± 2 μeV, suggesting that the QD-cavity is operating at the onset of strong coupling regime. The cavity and exciton linewidths, as shown in Fig 3.10(d), are close at far-off resonance. They exhibit a mutual narrowing when tuned near resonance, indicating the suppression of dissipation of both upper and lower energy components. This contrasts with the typical linewidth averaging in the strongly coupled system, where the cavity loss is larger than the excitonic pure dephasing rate [62], [318].

In order to study the impact of the dephasing mechanism, including fluctuating environmental charges and phonon scattering, in the QD-cavity system, a cQED modeling is employed. The simulation is performed using the Quantum Optics Toolbox [224] and the coupled QD-cavity PL spectrum as a function of detuning is calculated. In brief, the density matrix $\hat{\rho}$ of QD-cavity system embedded in an environment with dephasing is described by the Lindblad master equation:

$$\frac{d\hat{\rho}}{dt} = -\frac{i}{\hbar}\left[\hat{H}, \hat{\rho}\right] + \mathcal{L}(\hat{\rho}), \tag{3.1}$$

where $\hat{H}$ is the JC Hamiltonian given by

$$\hat{H} = \hbar\omega_C \hat{a}^\dagger \hat{a} + \frac{\hbar\omega_X}{2}\hat{\sigma}_z + \hbar g(\hat{a}^\dagger \hat{\sigma}_- + \hat{\sigma}_+ \hat{a}) \tag{3.2}$$

and ω_C, ω_X, $\hat{a}$, and g represent the energy of the cavity mode, transition energy of the QD exciton, annihilation operator of the cavity photon, and QD-cavity coupling strength, respectively. Additionally, $\hat{\sigma}_{+/-/z}$ are the pseudospin operators of the two-level QD excitons. The environmental dephasing is incorporated through the Liouvillian superoperator $\mathcal{L}(\hat{\rho})$ given by

$$\mathcal{L}(\hat{\rho}) = \frac{\kappa_C}{2}\mathcal{L}_{\hat{a}}(\hat{\rho}) + \frac{\gamma_X}{2}\mathcal{L}_{\hat{\sigma}_-}(\hat{\rho}) + \frac{P_X}{2}\mathcal{L}_{\hat{\sigma}_+}(\hat{\rho}) + \frac{\gamma_{deph}}{2}(\hat{\sigma}_z\hat{\rho}\hat{\sigma}_z - \hat{\rho}) + \frac{P_{ph}}{2}\mathcal{L}_{\hat{\sigma}_-\hat{a}^\dagger}(\hat{\rho}), \quad (3.3)$$

where κ_C, γ_X, P_X, γ_{deph}, and P_{ph} are the cavity loss rate, exciton decay rate, QD incoherent pumping rate, exciton pure dephasing rate causing the Lorentzian broadening of the exciton line, and phonon-mediated coupling rate from the QD excitations to the cavity, respectively [75], [263]. Note that γ_X is set to be 0.7 μeV which corresponds to practical spontaneous decay rate of bulk QD excitons. It's worthnoting that the phononic backscattering term describing the phonon mediated transferring of CM excitations to the QD is neglect because $\kappa_C \gg \gamma_X$ in our system [75], [312]. The superoperator $\mathcal{L}_{\hat{X}}$ with an arbitrary operator $\hat{X}$ in the subscript has the below form:

$$\mathcal{L}_{\hat{X}}(\hat{\rho}) = 2\hat{X}\hat{\rho}\hat{X}^\dagger - \hat{X}^\dagger\hat{X}\hat{\rho} - \hat{\rho}\hat{X}^\dagger\hat{X}. \quad (3.4)$$

The experimental PL spectrum is modeled through the steady-state power spectrum of the QD-CM system $S(\omega)$. It can be obtained from the Fourier transform of the two-time covariance function of the excitonic operator $(\hat{\sigma}_+, \hat{\sigma}_-)$ and photon operator $(\hat{a}^\dagger, \hat{a})$ and can be expressed by:

$$S(\omega) = \int_{-\infty}^{\infty} \lim_{t\to\infty}\langle A(t+\tau)B(t)\rangle e^{-i\omega\tau}d\tau. \quad (3.5)$$

Here, $A, B = \hat{\sigma}_+, \hat{\sigma}_-, \hat{a}^\dagger, \hat{a}$. Importantly, in this system, only a single QD is incorporated in the cavity with all surrounding QDs etched away. It eliminates the parasitic cavity pumping that is typical in self-assembled QDs. Thus, using site-controlled QD systems simplifies the system and allows for a clearer understanding of the QD-CM interaction without unwanted contributions from nearby QDs.

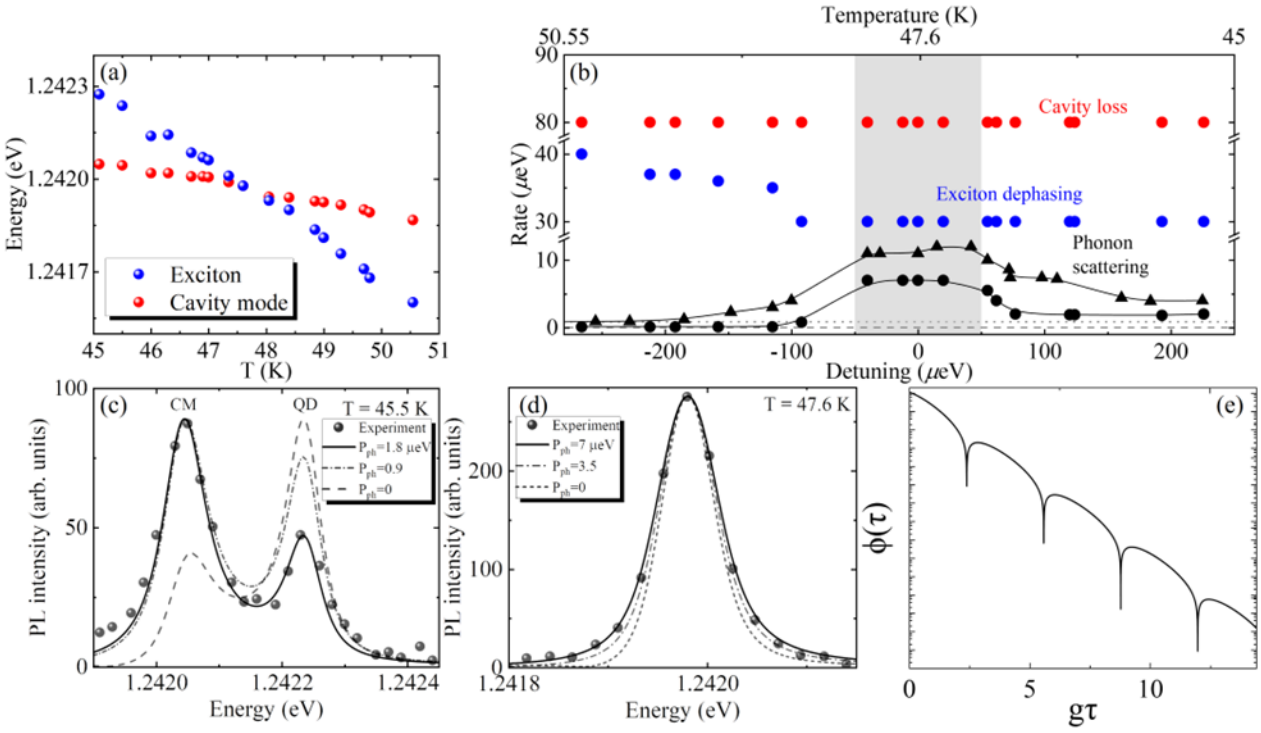

FIG 3.11 | cQED modeling of phonon-mediated QD-cavity coupling (a) Fitting of energy of exciton (blue) and cavity mode (red) as a function of temperature in Fig 3.8 (a) by modeling. **(b)** Cavity loss (red), exciton dephasing (blue), and phonon scattering (black) rate as a function of temperature in the QD-cavity system extracted from the modeling in **(a)**. Black triangles denote the phonon scattering rate at a higher pump power at 30 μW. The grey dashed and dotted lines mark the phonon scattering rate at the large negative detuning, indicating an overall asymmetric shape across ± 200 μeV detuning range. **(c)** PL spectra (dot) of the decoupled QD-cavity system at 45.5 K. The dash, dot-dash, and solid lines are the fitting corresponding to the phonon mediated QD-cavity coupling rate P_{ph}=0, 0.9, and 1.8 μeV, respectively. **(d)** PL spectra (dot) of the resonantly coupled QD-cavity system at 47.6 K. The dash, dot-dash, and solid lines are the fitting corresponding to the phonon mediated QD-cavity coupling rate P_{ph}=0, 3.5, and 7 μeV, respectively. **(e)** Time evolution of the two-time correlation for spectra in (d). Fig 3.11 is published in [76].

Fig 3.11(a) shows the energies associated ω_C and ω_X extracted from the modeling of the experimental spectrum in Fig 3.8. In Fig 3.11(b), we extract the dephasing terms as a function of temperatures (detuning). we initially adjusted κ_C to be 80 μeV deconvolved system response to reproduce the spectral linewidth of CM at the large detuning. κ_C is then kept constants for all temperatures (detuning). Similarly, γ_{deph} is set to be 30 μeV to align with the linewidth of the QD exciton at the lower temperatures. A slight increase in exciton pure dephasing γ_{deph} at 49 K is observed, which can be attributed to the small increase in fluctuations of the environmental charges at higher temperatures, consequently contribute to a broadening of exciton linewidth. The phonon scattering rate P_{ph} is also treated as a fitting parameter to reproduce the experimental spectrum shown in Fig 3.8. The coupling strength is adjusted to be $g = 18$ μeV and kept constants for all fittings. Note that such coupling strength places our system at the onset of the strong coupling regime ($g \approx \kappa_C/4$), consistent with our observation of single peak rather than an explicit mode splitting. The obtained g is relatively smaller than 20-50 μeV reported in similar systems [75]. This discrepancy can be attributed to a larger mode volume of the $L7$ cavity used. The phonon scattering rate P_{ph} exhibits a raising from 2 μeV as the system approaches the QD-CM resonance and reach a plateau at 7 μeV within ± 50 μeV detuning range (grey shaded region). Subsequently, it falls when gradually decoupling between QD and cavity occurs. The overall trend indicates the enhanced phonon scattering rate for transferring QD excitations to the cavity in the vicinity of the near-zero detuning region. Here, cavity mode can also be regarded as a sensitive probe of virtual states of QD induced by the emission or absorption of a phonon [263], which continuously extends over approximately 200 μeV around the QD exciton line [276]. Therefore, the elevated P_{ph} within ± 50 μeV detuning range is a result of the convolution of the energy range of QD virtual states with the CM linewidth. Notably, the small temperature changes of approximately 2.5 K during the

coupling (corresponding to ± 100 μeV detuning range) do not affect the phonon bath significantly which agrees with the plateau of P_{ph} in such detuning range. It suggests that the pronounced P_{ph} primarily arises from the QD-cavity coupling. P_{ph} also exhibits an asymmetric shape between the positive and negative detuning, which indicates it is more efficient for QD excitons to emit a phonon than absorb a phonon for bridging the QD-cavity energy gap. Such asymmetry suggests that the phonon bath is not fully populated around 50 K, which is different from previous theoretical predictions of site-controlled QDs operating at the weak coupling regime [75], [276].

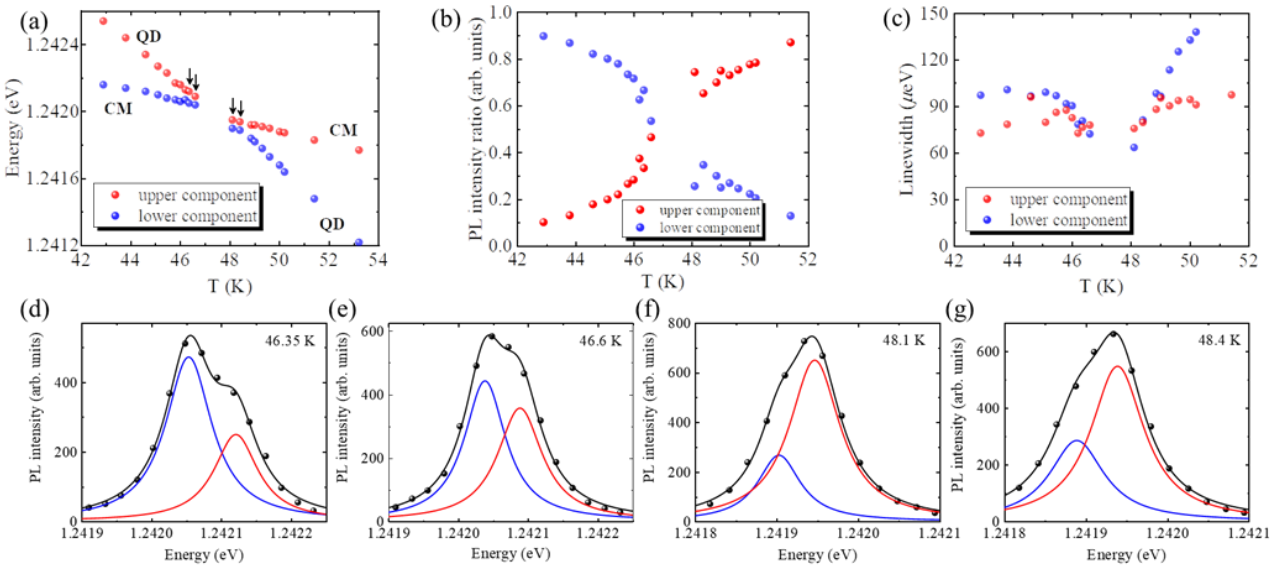

FIG 3.12 | Temperature tuning of QD-cavity coupling at 30 μW. **(a)** Dependences of PL peak energies of coupled QD-cavity system over a wide temperature range. **(b)** Detuning dependent ratio of PL intensity between upper and lower energy components to their summation, which reveals averaging at near resonance. **(c)** Detuning dependent linewidth of the upper and lower energy components, which presents mutual narrowing. **(d-f)** Double Lorentzian fitting of PL spectrum at four representative temperatures marked by the arrows in **(a)**. Fig 3.11 is published in [76].

We also study the QD-CM coupling at a higher excitation power of 30 μW with the results of double Lorentzian fitting shown in Fig 3.12. As shown in Fig 3.12(a-c) the double Lorentzian fitting to the spectrum shows a PL intensity ratio averaging and mutual linewidth narrowing of the upper and lower components which is similar to the lower pump power case in Fig 3.10. The double Lorentzian fitting near zero detuning is shown in Fig 3.12(d-f). To demonstrate the robustness of our modeling and further investigate the phonon scattering rate, we fit the PL spectrum at 30 μW with same cQED modeling. P_{ph} is then extracted in Fig 3.13 (b) and also denoted as black triangles in Fig 3.11(b) for comparison. It reveals a plateau similar to the trend observed at 3 μW. But interestingly, P_{ph} now reaches a larger maximum value of 12 μeV and exhibits increased asymmetry. Higher excitation power leads to increased carrier populations and, assuming a constant amount of phonon populations in our system since the coupling temperature stays the same, a higher P_{ph} is necessary to facilitate the transfer of QD excitations to the cavity

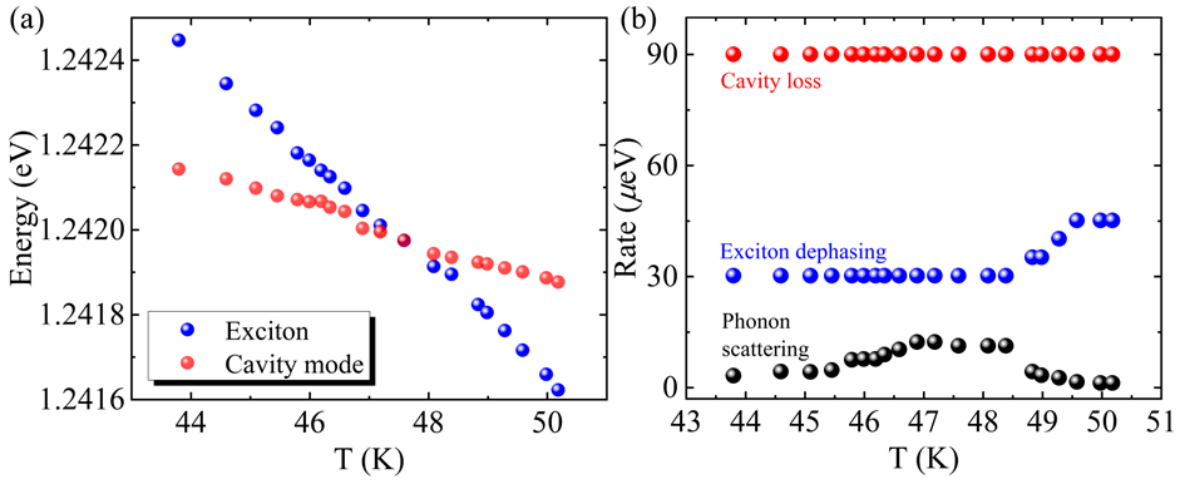

FIG 3.13 | cQED modeling of phonon-mediated QD-cavity coupling at 30 μW (a) PL peak energies of coupled QD-cavity system as a function of temperatures extracted from the cQED modeling. **(b)** cavity loss, exciton pure dephasing, and phonon scattering rate as a function of temperatures extracted from the cQED modeling. Fig 3.13 is published in [76].

decay channel. Deterministically engineering QD-cavity at desired coupling temperature can open opportunities for studying temperature effects on the shape of P_{ph}. A large amount of devices need to be fabricated and a statistical study is required, which fall beyond the scope of this thesis.

To better illustrate the significant impact of P_{ph} on phonon-assisted cavity feeding under different detuning conditions, we present the modeled spectrum with various P_{ph} at larger detuning (T = 45.5 K) and near-zero detuning (T = 47.6 K) in Fig 3.11(c) and (d), respectively. At T = 45.5 K, if not considering the phonon-mediated coupling ($P_{ph} = 0$, dashed line in Fig 3.11(c)), the intensity of QD emission is stronger than the cavity mode, which deviates from the experiment (dot in Fig 3.11(c)). With a slightly increasing P_{ph} from 0 to 0.9 μeV, the PL intensity of QD decreases significantly, accompanied by an increasing CM intensity. This effect results from the enhanced process of phonon-mediated transferring of QD excitations to the cavity decay channel. Ultimately, when P_{ph} reaches 1.8 μeV, the modeled spectrum converges well to the experimental spectra. Similarly, at T = 47.6 K, where QD and CM are coupled, the fitting is converged with $P_{ph} = 7$ μeV to well match both sides of spectral tails. Increasing P_{ph} broaden the spectrum which is consistent with the fact that P_{ph} is a decoherence process in our modeling. The high sensitivity of our modeling accurately captures the subtle impact of phonon scattering on the QD-CM coupling and solidifies the observed asymmetric shape. It is noteworthy that the phonon effect itself does not induce a shift in the emission energy as we don't observe an energy shift in Fig 3.11(c) and (d). We further evaluate the steady state two-time covariance function of cavity photons given by

$$\phi(\tau) = \langle \hat{a}^{\dagger}(t+\tau), \hat{a}(t) \rangle, \tag{3.6}$$

near zero detuning as shown in Fig 3.11(e). The plot clearly reveals oscillations in τ with an exponentially damped envelope. The field correlation exhibits multiple local minimums in τ equivalent to the Rabi frequency [288], [319], indicating the coherent exchange between photon and exciton fields in our system, even operating at the onset of the strong coupling regime. The exponential damping arises from the dissipation and pumping due to environmental interactions, leading to the de-correlation of exciton and photon fields.

It's worth mentioning that if P_{ph} is neglected and the exciton pure dephasing rate γ_{deph} is treated as a fitting parameter to converge the fit to the experimental spectrum, the γ_{deph} needs to be forced to increase as QD and CM decouples, resulting in an unphysical scenario. Fig 3.14 shows the cQED modeling of the same QD-cavity system modeled in Fig 3.11 without phonon-mediated coupling P_{ph}. The cavity loss κ_C is taken to be 80 μeV which is the same as in Fig 3.11 but now the phonon scattering rate P_{ph} is set to 0 μeV for all temperatures. For the PL spectrum near zero detuning, the exciton pure dephasing rate γ_{deph} must be reduced to converge the fitting. An example of the modeling at T = 45.1 K, where QD and CM are out of resonance, is shown in Fig 3.14(b). At T = 45.1 K, the modeled spectra with a larger $\gamma_{deph} = 70\ \mu eV$ (solid) reproduces the experimental spectra better than $\gamma_{deph} = 45\ \mu eV$ (dash) but still cannot completely reproduce the experimental spectra of QD. It's worth noting that increased γ_{deph} reduces QD exciton excitations but keeps the CM excitations constant and does not correspond to a physical scenario. These results highlight the important role of phonon-mediated coupling in our system operating at the onset of strong coupling subject to environmental interactions.

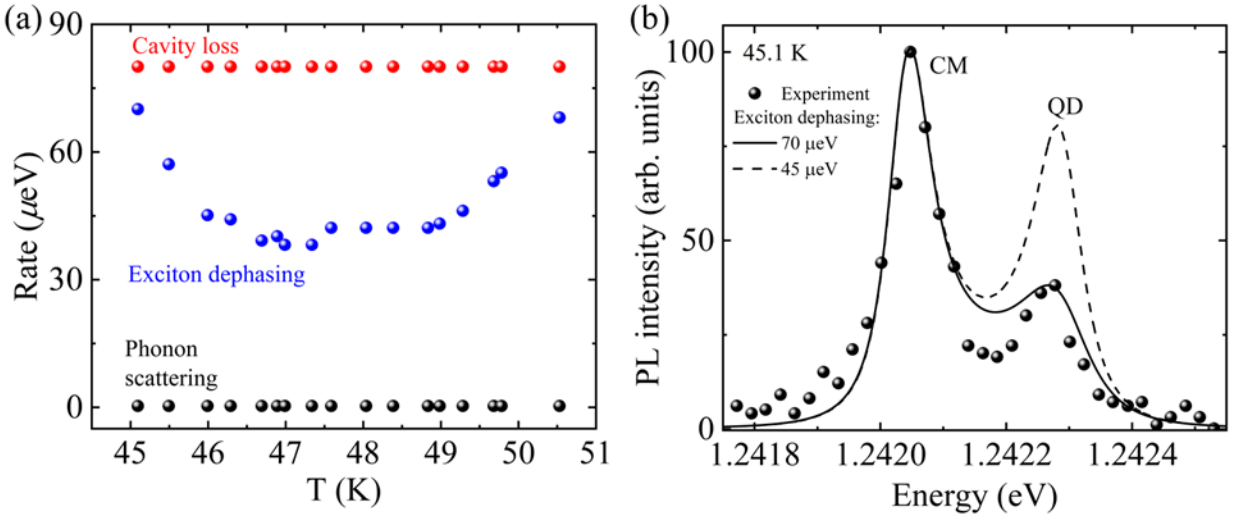

FIG 3.14 | cQED modeling of QD-cavity coupling without the phonon scattering (a) Cavity loss and exciton pure dephasing rate as a function of temperature with a vanishing phonon scattering rate. **(b)** Fitting of the measured PL spectra at T = 45.1 K (dot) by the cQED model with exciton pure dephasing at 70 μeV (solid line) and 45 μeV (dash line) in the case that phonon scattering rate is set to be 0. Fig 3.14 is published in [76].

3.5 Rabi Oscillation and Quantum Beating of Coupled Spectral Components

To gain further insight into the interaction in the coupled QD-CM system operating at the onset of strong coupling regime, we perform the excitation power-dependent PL measurements using a sub-bandgap 900 nm pulse laser. The pulses have a fixed duration of 100 ps, and we carry out these measurements at two different QD-CM detuning.

In Fig 3.15(a) and (b), the PL spectrum is presented at excitation power of 5, 7, and 9 μW at a small ($\Delta_1 \approx 70$ μeV) and large ($\Delta_2 \approx 137$ μeV) detuning, respectively. As shown in Fig 3.16(a), by varying excitation power, the PL intensity of upper and lower energy components undergoes an out-of-phase oscillation observed up to 20 μW. The behavior resembles a Rabi-like oscillation and indicates quantum beating between the two components. The three points marked by the arrow

correspond to excitation power in Fig 3.15(a). The oscillation diminishes beyond 20 μW likely attributed to the decoherence arising from finite QD p-state feeding. This aligns with the power-dependent TRPL results in Fig 3.5, where significant carrier feeding above 20 μW induces the decoherence of QD-cavity interaction. Furthermore, the energy separation between the lower and upper energy components also exhibits an oscillatory signature correlated with their intensity oscillation.

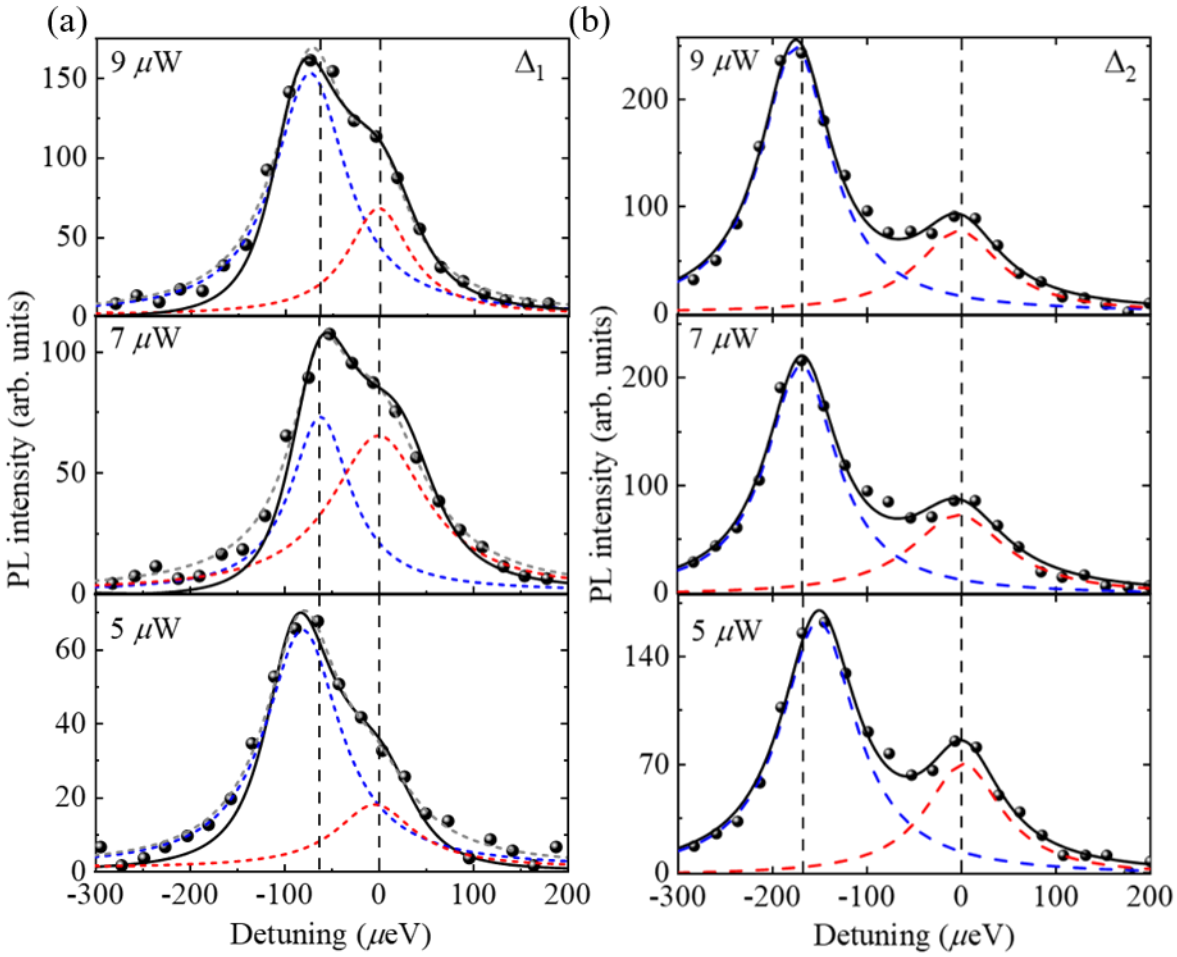

FIG 3.15 | Power dependent PL spectra of two detuning cases. PL spectra (black sphere) of the nearly resonantly coupled QD and CM excited by the 900nm pulsed laser at average power 5 μW, 7 μW, and 9 μW for **(a)** smaller ($\Delta_1 \approx 70$ μeV) and **(b)** larger ($\Delta_2 \approx 137$ μeV) QD-CM detuning cases at T = 50 K and 52.3 K, respectively. The blue and red dash lines are the double

Lorentzian fitting with the accumulative fitting as the grey dashed line. The black solid line in **(a)** is from the cQED modeling. The vertical dashed line marks the peak center energies of lower and higher energy components at 7 μW. Fig 3.15 is published in [76].

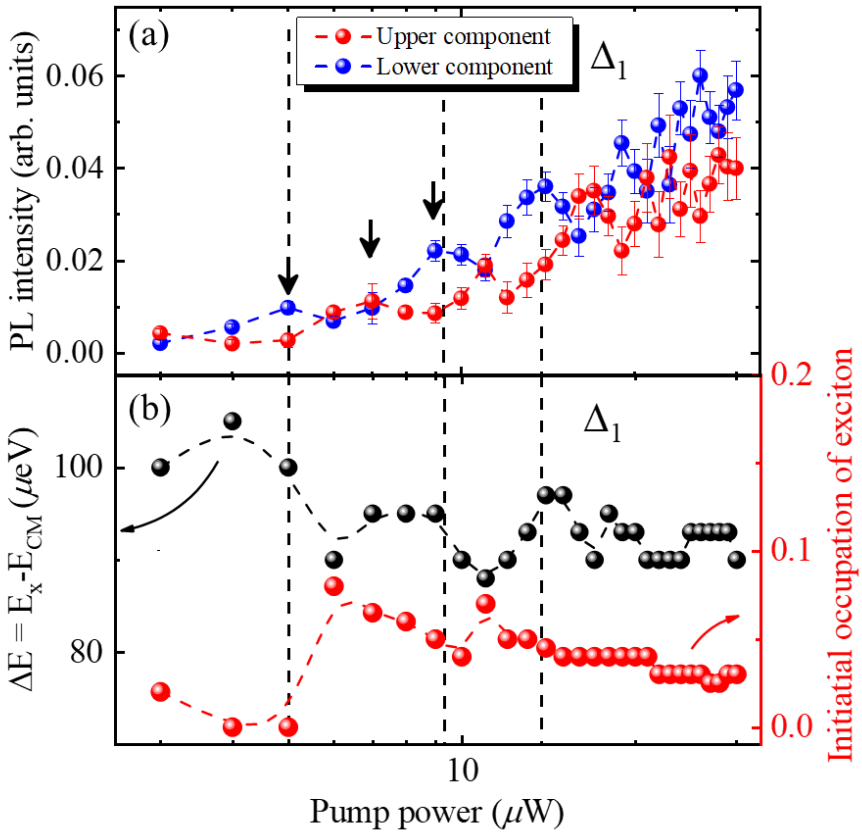

FIG 3.16 | Power dependent Rabi-like oscillation of the coupled QD-cavity at small detuning ($\Delta_1 \approx 70$ μeV) (a) PL intensity of upper and lower energy components as a function of average excitation power extracted for the small detuning ($\Delta_1 \approx 70$ μeV) at T = 50 K, which reveals clear oscillation under low excitation power. The three arrows mark the excitation power at 5 μW, 7 μW, and 9 μW. **(b)** Energy separation between upper and lower energy components (black) and initial occupation of exciton in the coupled QD-cavity system (red) for the small detuning case ($\Delta_1 \approx 70$ μeV) as a function of pump power extracted from the fitting by cQED modeling. The black and red dash curves are the guide to the eye. The vertical dashed lines are guides to the eye marking the oscillation period. Fig 3.16 is published in [76].

Note that the 900 nm pulse laser (20MHz) used in this measurement excites carriers in the QWR which are subsequently captured by the single QD. As previously explained, in such excitation scheme of our site-controlled QD-cavity system, the cavity is exclusively fed by the single QD s-state at low power (< 20 μW) and is not contaminated by multiexcitonic background or QWR tails. To interpret the oscillatory behavior, we consider the measured spectrum of our coupled QD-CM as an outcome of the spontaneous decay from an initial state, prepared by the pulse area. In brief, the initial state of the system can be defined by the weighting factor x in the superposition of QD exciton and cavity photon operator $x\hat{\sigma}_{-} + (1-x)\hat{a}$, with x denoting the initial occupation percentage of QD excitons, which is complementary to the cavity photons. By varying x and calculating the cavity output spectra, our model well captures the variation of the measured PL spectrum at different pump power. The three representative modeled spectra that fit the experiments at 5, 7, and 9 μW are shown as black solid curves in Fig 3.15(a). In Fig 3.16(b), the initial occupation of QD excitons is plotted as red dots with the corresponding extracted QD-cavity energy splitting ΔE shown as black dots from the modeling. Importantly, we note that a lower occupation of QD excitons as an initial state of the system corresponds to a large splitting between the upper and lower components, and vice versa. This leads to an out-of-phase excitation power dependent oscillation of the initial occupation of exciton and ΔE. Such behavior of PL intensity beating and splitting oscillation is consistent with the prior theoretical prediction of the spontaneous emission spectra [288], reflecting the spectral shape evolution with the initial state as either one exciton or one photon in a strongly coupled system. Note that the complete photon domination (x=0) of the system appears as excitation power increases to around 4.5 μW in the first oscillation period but smears out in the subsequent oscillation periods. The drops in the visibility at higher excitation power (>20 μW) align with the blurred PL intensity oscillation and thus the

decoherence of QD-cavity interaction due to increased carrier feeding, as evidenced by the TRPL measurement in Fig 3.5. With the continuing increase in power up to 480 μW, the two peaks merge and shows a single peak which suggests the system either remain in the strong coupling in disguise as a single peak [309] or enters the weak coupling regime [288], [320], [321] as illustrated in Fig 3.17. Not that such oscillation cannot be observed using a 532 nm continuous-wave laser which is shown in Fig 3.18 where the above GaAs bandgap pump introduces significant broadening and decoherence and importantly continuous-wave excitation sets the system in the *steady state*.

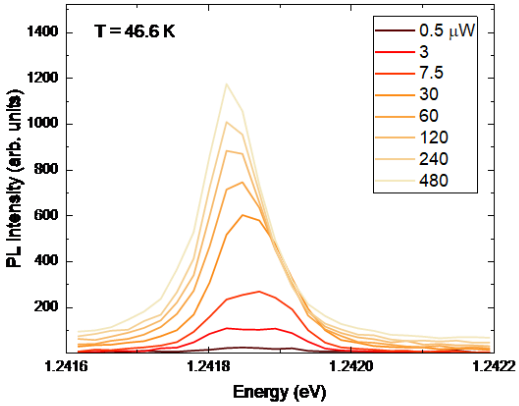

FIG 3.17 | PL spectrum at T = 46.6 K as a function of excitation power with 900 nm laser (20MHz) up to 480 μW. Fig 3.17 is published in [76].

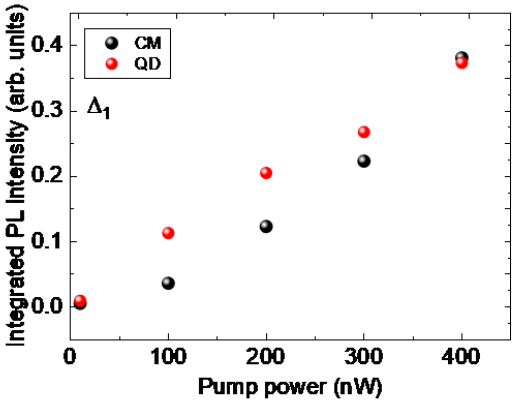

FIG 3.18 | Integrated PL intensity of QD and CM as a function of excitation power for the small detuning case ($\Delta_1 \approx 70\mu eV$) using 532 nm cw laser. Fig 3.18 is published in [76].

The analysis of excitation power-dependent PL performed at the large detuning Δ_2 is presented in Figure 3.19(a) and (b). Notably, the Rabi-like oscillation of the intensity and the energy separation of the upper and lower energy components, which is pronounced at smaller detuning, now blurs out. Although a weak oscillatory signature is barely observed at low excitation power, the PL intensity of upper and lower components saturates at higher excitation power, suggesting

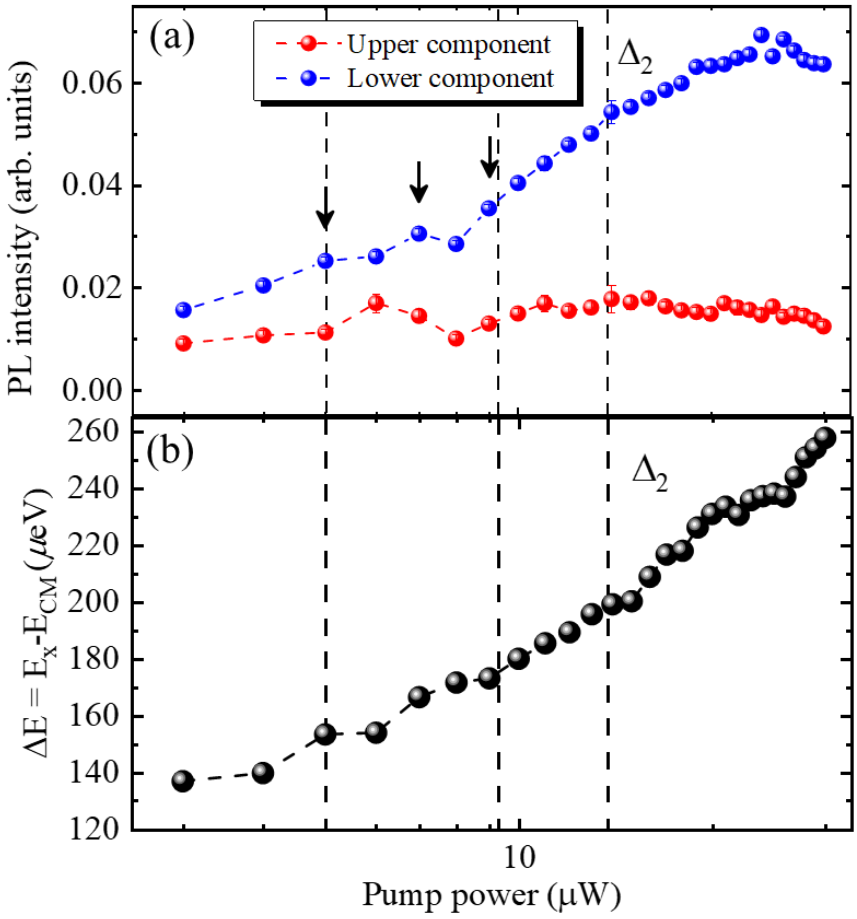

FIG 3.19 | Blurring-out of Rabi-like oscillation of the coupled QD-cavity at larger detuning ($\Delta_2 \approx 137$ μeV) (a) PL intensity of upper and lower energy components as a function of average excitation power extracted for the larger detuning ($\Delta_2 \approx 137$ μeV) at T = 52.3 K. The three arrows mark the pump power at 5 μW, 7 μW, and 9 μW. **(b)** energy separation as a function of average pump power for a larger detuning ($\Delta_2 \approx 137$ μeV) at T = 52.3 K. The vertical dashed lines are copied from Fig 3.16(a) and (b). Fig 3.19 is published in [76].

that the two components become photon or exciton-dominated so that the QD and CM are decoupled at such detuning. This result indicates that the oscillatory behavior, observable only at small detuning, is closely related to the phonon-mediated coherent exchange between exciton and photon states through the vacuum Rabi splitting (VRS), which is only significant when the QD and CM sufficiently interact. Regarding Fig 3.19(d), it is noteworthy that in the large detuning case (Δ_2), the energy splitting between QD and CM states gradually increases with increasing excitation power. As shown in Fig 3.20(d), such decoupling is a result of the CM red shifting. The power dependent red shift of CM energy in Fig 3.20(c)(d) is unlikely due to the thermally induced

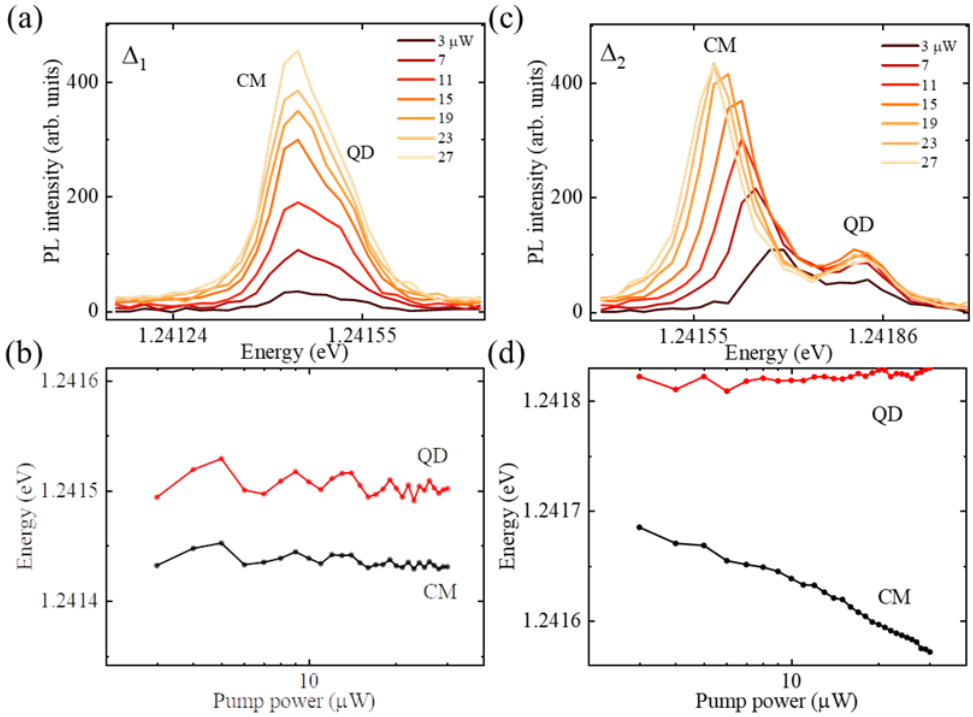

FIG 3.20 | Power dependent PL and energy of QD and CM of two detuning cases. (a) Power dependent PL spectra of QD-CM for $\Delta_1 \approx 70\mu W$. **(b)** Emission energy of QD and CM as a function of excitation power extracted from (a). **(c)** Power dependent PL spectra of QD-CM for $\Delta_2 \approx 137\mu W$. **(d)** Emission energy of QD and CM as a function of excitation power extracted from (c). Fig 3.20 is published in [76].

refractive index change of the PhC membrane due to local laser heating because (1) the 900 nm pumping at low power only excites finite carriers in the 3 QWRs along the wedges of the pyramid (2) QD energy which shifts with temperature at a faster rate than CM remain constant. (3) no red shift in CM energy is observed at 70 μeV detuning at the same power range. PhC surface condensation of impurities due to Xenon [109] or nanofluid can lead to CM shift [110], [111]. However, none of them applied to our case because the measurement is performed when the cryostat is at thermal equilibrium so that any unintentional impurities already condense on the sample surface. Importantly, the measurements at two detuning were conducted under the same conditions. The cause of the observed red shift is currently unclear and needs further investigation. However, such pulsed excitation induced cavity resonance shifts may be useful for extract the single photon after the strong coupling is *turned off*. Starting with a strong coupled QD-cavity system with a negative detuning (such as -137 μeV), with pulsed excitation and the induced red shifting of the cavity resonance, the system can traverse an avoided crossing and then cools down. If such process is adiabatic, the single photon may be extracted with system state evolution from $|e,0\rangle$ on one side to $|g,1\rangle$ on the other side of the avoided crossing with potentially high probability, which is the Landau-Zener at the bottom of the JC ladder. A time-resolved emission spectrum during such evolution can be measured using streak camera.

3.6 Discussions

Highly symmetric, site-controlled InGaAs QDs formed in patterned inverted pyramid on GaAs (111)B-oriented substrates combined with deterministic PhC cavity integration offers great promise for integrated quantum photonics. However, this geometry is subject to increased cavity loss in contrast to equivalent systems involving (100)-oriented GaAs membranes and self-assembled QDs. Based on the tailored Indium content and pyramid nominal size in the prior

chapter, in this chapter, using a *L*7 PhC cavity with *Q*-factor exceeding 12000, we demonstrate and investigate the cQED of the site-controlled InGaAs QD systems operating at the onset of the strong coupling regime. Further cQED modeling of the power spectra accounting for environmental dephasing reveals the pronounced phonon-mediated-coupling rate and an oscillatory two-time covariance function near zero QD-CM detuning. This indicates that our phonon-mediated QD-cavity system, even at the onset of strong coupling, supports the coherent exchange of exciton and photons. It is further substantiated in the pump pulse area-dependent PL measurement that Rabi-like out-of-phase oscillation and quantum beating between emission intensity of the upper and lower energy components occurs, which is also correlated with an oscillatory feature of their energy splitting, taking place only at small QD-CM detuning and lower excitation power. The oscillation of energy splitting of upper and lower components can be well reproduced by modeling the initial occupation of excitons in the system. This chapter demonstrates the feasibility of using single site-controlled InGaAs QD system near the strong coupling regime and provides guidelines for further optimizing the fabrication process to further reduce the cavity loss in this geometry. This advancement and milestone open avenues for the applications of such systems in coherent control of site-controlled exciton and photon states for quantum information processing in monolithic functional integrated quantum photonic circuitry for practical applications.

Chapter 4

Spatially Resolved Landscapes of Exciton-Photon Polaritons with Multi-Site-Controlled Quantum Dots in Extended Cavity Modes.

4.1 Introduction

In prior chapters, we have seen that the emission characteristics of QD excitons may undergo modification via the Purcell effect using microcavities. In this context, the light emission rate and spatial profile can be effected in accordance with the LDOS of photons within the optical cavity. Extensive investigation on the subwavelength spatial characteristics of photon LDOS have been done by employing site-controlled pointlike dipole sources within the cavity, such as deterministically positioned Ge QDs [322] or DNA origami structures [323]. Furthermore, scanning electron beams serve as another effective point dipole source for achieving deep subwavelength imaging of photonic modes [324]. Near-field scanning optical microscopy (NSOM) is widely employed to probe the evanescent contributions of the electrical field within PhC cavities [325], [326]. Beyond surface imaging via NSOM, high-energy resolution electron energy-loss spectroscopy offers a way to extract photonic modes within the dense core of cavities, enabling high-resolution tomography of nanocavities [327].

The spatial distribution of polariton condensates [328]–[332] within semiconductor microcavities is extensively examined using various potential traps, and the resulting confined polariton wavefunction is characterized in both momentum and real space [332]–[341]. The repulsive nature of polariton-exciton interactions also permits the trapping of polariton

wavefunctions using optically generated exciton reservoirs, providing flexibility in visualizing the spatial modulation of trapped polariton wavefunctions in real space [336]. In summary, investigations have thoroughly explored both spatial features of cavity mode patterns and polaritons trapping. However, the spatial features of excitonic wavefunctions modified through the Purcell effect and strong light-matter interactions are less studied. This deficiency stems from the difficulty in distinguishing such features from the photonic component, particularly since many studies on polariton spatial features are based on two-dimensional materials or quantum wells (QWs) within distributed Bragg reflector (DBR) cavities, where excitonic states are spatially extended. Additionally, these features can subtly vary based on the precise position of the dipole source within a specific photonic mode pattern, requiring the spatial controllability of the dipole. Conversely, excitonic wavefunctions from QDs confined within sub-wavelength regions can, in principle, be distinguished from the photonic component.

In this chapter, we experimentally explore a more complicated system which contains four evenly spaced site-controlled pyramidal InGaAs QDs embedded along the longitudinal axis (x-axis) of a *L*7 PhC cavity. Interactions between QDs and fundamental as well as higher-order cavity modes are spatially resolved along the x-axis of the *L*7 cavity by analyzing the far-field PL emission. We observed a spatial avoided crossing in the optical emission of QD excitons with 1st order cavity mode (CM1) within small detuning ranges. Notably, these spatial characteristics are solely evident in the *y*-polarized components of the QD excitons, which align with the cavity mode emission. The phenomena are also absent during interaction with the more spatially confined fundamental cavity mode (CM0). Furthermore, the spatial avoided crossing is observed only in the two QDs positioned close to the cavity center, underscoring the dependence of QD positioning within the cavity. Using the theory of quantum interference of QD decay channels within a cavity

[165], we estimate the coupling strength of the QD-cavity interaction from the observed phenomena.

While there exists experimental evidence of quantum light extraction using WG modes with site-controlled QDs [161] and investigations into spatially extended Airy-Bloch modes of tilted-potential PhC cavities [162], direct measurements on the spatial characteristics of excitonic states interacting with photonic states are lacking. The spatial superposition of excitonic and photonic states in QD-cavity interaction described in this chapter holds significance for understanding the localized spatial extent of a single QD exciton interacting with a cavity photonic mode pattern, with implications in quantum engineering and metrology. Leveraging this observed phenomenon, the integration of site-controlled QDs at designated positions within a photonic structure, featuring tailored extended spatial patterns of photonic states, can facilitate the development of novel integrated quantum photonic devices for on-chip quantum information processing.

4.2 Concept of the Multi-QD Devices and Observed Spatial Features

As depicted in the inset of Fig 4.1(a), four site-controlled pyramidal InGaAs QDs, evenly spaced by 450 nm, are positioned along the x-axis within a modified *L*7 PhC cavity (with a hole pitch of a = 225 nm), symmetrically arranged relative to the cavity center. Fig 4.1(a) and (b) provide an artistic illustrative representation of our experimental findings concerning the spatial features of the QD excitons within an extended cavity photonic state corresponding to the CM1. The overall intensity distribution patterns of the CM1, obtained through 3D FDTD simulations, are superimposed onto the *L*7 cavity region in Fig 4.1. CM1 manifests as a spatially extended

pattern featuring two lobes along the x-axis of the *L*7 cavity, artistically depicted as two yellow

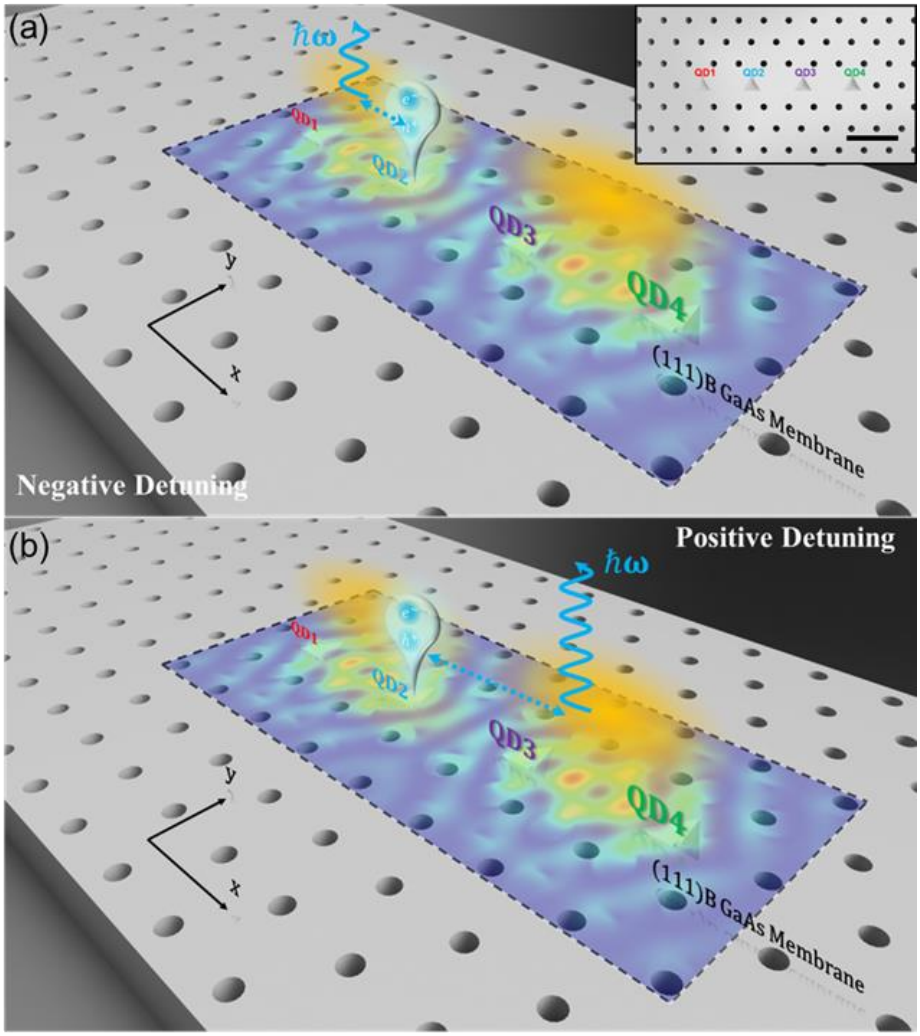

FIG 4.1 | Schematic illustration of the experimental results. Schematic illustration of the spatial feature of excitonic states of QD2 at **(a)** negative and **(b)** positive detuning. Inset: Schematic illustration of the four site-controlled InGaAs QDs embedded in a *L*7 PhC cavity (PhC hole not to scale). Four QDs are arranged symmetric with respect to the cavity center. Scale bar: 450 nm. The yellow clouds represent the two lobes of the spatially extended electromagnetic field of the 1st order cavity mode of the *L*7 PhC cavity. The blue balloon represents the QD2 exciton. The blue dot double arrows represent the QD-cavity coupling. The wavy arrows represent the cavity-mediated QD2 exciton decay to the free space.

clouds. It is observed that the photogenerated exciton from QD2 (depicted as a blue balloon) can couple with either the left or right lobes by adjusting the detuning between the exciton and CM1 energies. Such spatially distributed coupling of QD2 excitons with the two lobes of CM1 can result in photon emission (indicated by blue wavy arrows) at different locations within the $L7$ cavity. Fig 4.2 illustrates the electric field distribution patterns for the x- and y-polarized components of the

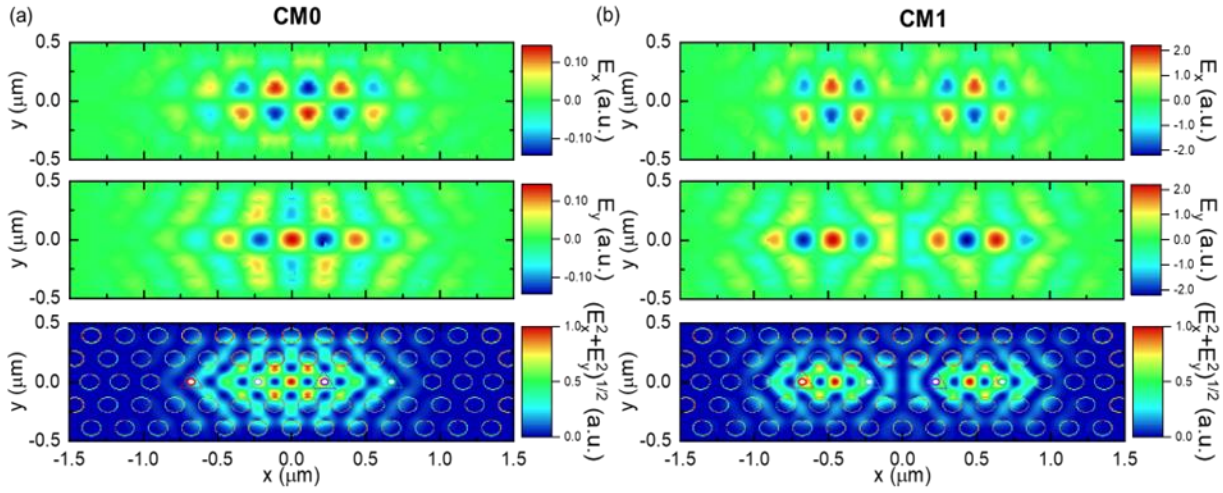

FIG 4.2 | 3D FDTD simulation of $L7$ PhC cavity mode pattern. 3D FDTD simulation of the spatial pattern of electric field E_x, E_y, and the total intensity $(E_x^2 + E_y^2)^{1/2}$ of the fundamental cavity mode (CM0) and 1st order cavity mode (CM1) of the $L7$ PhC cavity. Parameters: hole pitch a = 225 nm, membrane thickness t = 250 nm, air hole radius r = 31 nm.

CM0 and CM1.

4.3 Optical Properties

Four QDs are simultaneously excited using a large laser spot (~ 3 μm) with high power (5 μW) for each device across various air hole radii. Under these conditions, the saturated QD transitions exhibit broadband emission, and all CMs are adequately pumped and can be easily identified as shown in Fig 4.3. Shift of CM0 and CM1 emissions are marked by red and blue dash lines. QWR emissions can also be observed at shorter wavelengths. For some devices, we observe mode

splitting of CM0 (r = 41 and 42 nm) and CM1 (r = 38 and 39 nm) are observed likely due to fabrication disorders.

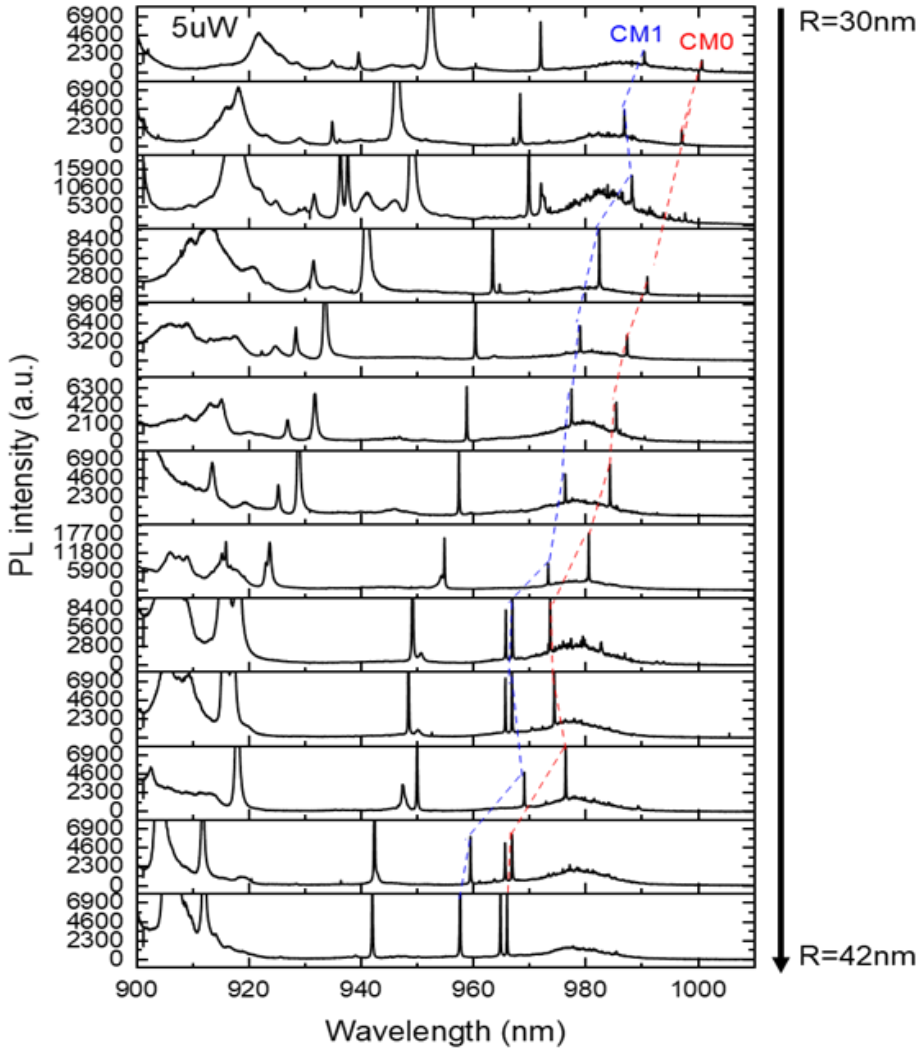

FIG 4.3 | PL spectra of all 4QD-L7 cavity devices using a large laser spot exciting all four QDs with high pump power (λ_{exc} = 785nm, P_{exc} = 5μW). The air hole radius of the PhC changes from r = 30 nm to 42 nm from top to bottom. Shift of CM0 and CM1 emission are marked by red and blue dash lines. T = 10 K.

Specifically, we focus on two 4QD-*L*7 devices, designated as device 1 and device 2, characterized by PhC hole radii r_1= 32 nm and r_2 = 31 nm, respectively. These devices demonstrate a favorable spectral overlap between the QD emissions and CM1. Subsequently, at a temperature

of 10 K, the μPL spectra of devices 1 and 2 are measured with a small laser spot (~ 1 μm) at the

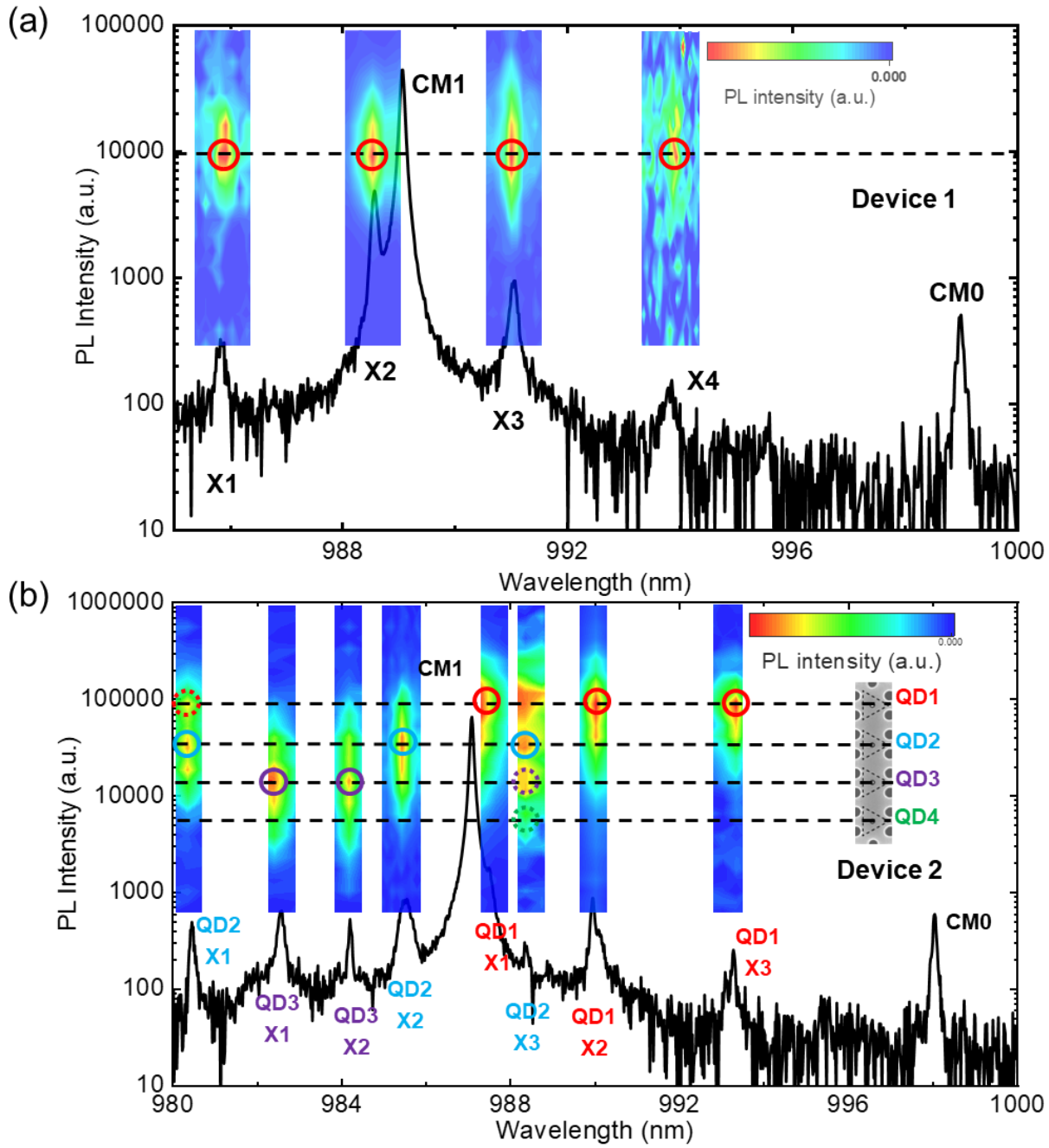

FIG 4.4 | Spatial- and spectral-scanning map of four-QD exciton emissions for device 1 (a) and device 2 (b) at T = 10 K. The spectrum at the bottom of are obtained around the center of the cavity. The brightness of different QD exciton lines is shown as bars where the vertical axis corresponds to the scanning steps.

cavity center, as depicted in the bottom spectrum of Fig 4.4(a) and (b), respectively. We then systematically scan the focused laser spot across QD1 to QD4 along the x-axis of the *L*7 cavity. Variations in the exciton emission intensity enable the identification of specific QDs contributing to each emission peak in the μPL spectra. The results of this scanning are summarized as intensity bars on top of each exciton peak.

For device 1, four distinct exciton lines (X1-X4) are identified proximal to CM1, all attributed by the same QD. Conversely, for device 2, eight exciton lines are observed, associated with QD1, QD2, and QD3, while QD4's emission is too weak to be measured. Notably, some exciton emissions stem from multiple QDs concurrently. For instance, as illustrated in Fig 4.4(b), the exciton line at ≈ 980.46 nm originates from both QD1 and QD2, while the exciton line at ≈ 988.34 nm arises from QD2, QD3, and weakly from QD4. Notably, the high-intensity region near the position of QD1 for the exciton line at ≈ 988.34 nm results from the saturation of CM1 intensity. To simplify analysis, we attribute these two exciton peaks to QD2, given its predominant emission compared to other QDs. Additionally, CM0 is observed at the longer wavelength side of the μPL spectra (≈ 12 meV below CM1) for both devices. The *Q*-factor of device 1 is approximately ≈ 12,000 for CM1 and ~ 9,000 for CM0, while for device 2, the *Q*-factor is approximately ≈ 11,000 for CM1 and ≈ 7,000 for CM0. These observed *Q*-factors are comparable to the *L*7 cavity studied in chapter 3 operating at the onset of the strong coupling regime [76].

Second order correlation measurement is performed for device 2. CM1 is tuned between QD2-X2 and QD1-X1 with detuning $E_{QD2-X2} - E_{CM1} \approx 1.39\, meV$ and $E_{QD1-X1} - E_{CM1} \approx -1.15\, meV$. A narrow bandpass filter is used to select only CM1 for feeding the HBT setup. A

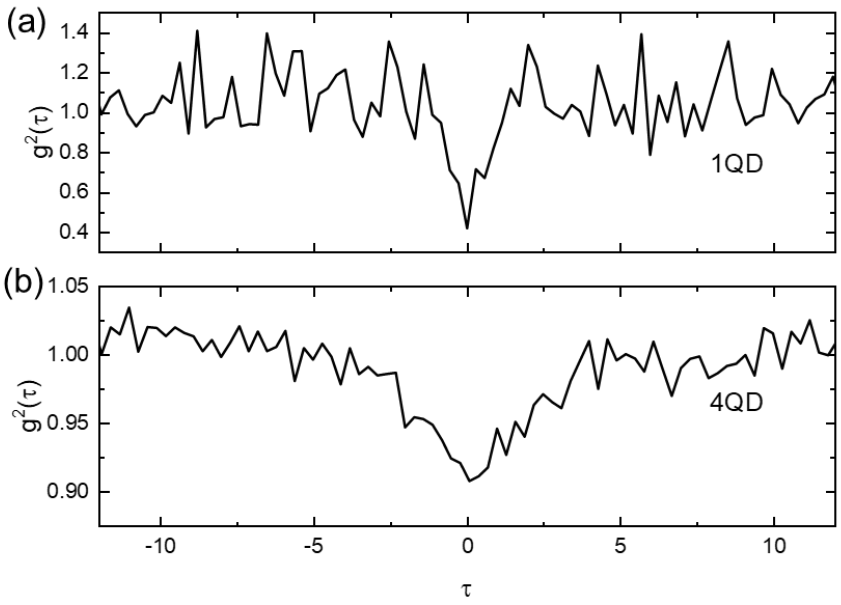

FIG 4.5 | Second-order correlation measurements of **(a)** 1QD and **(b)** 4QD in a $L7$ PhC cavity.

weak antibunching with $g^2(0) \approx 0.9$ is observed, as illustrated in Fig 4.5 (b). It can be the result of uncorrelated single-photons emitted through the CM1 decay channel by each QD and no photon bunching is observed suggests that no cooperative emission occurs in our system likely due to large dephasing process because of non-resonant pumping. Different coupling efficiency of QDs with CM1 can lead to cavity decay channel dominated by a specific QD so a measurement of $g^2(0)$ as a function of detuning with fine steps would be needed to observe the possible photon bunching. As a comparison, the second order correlation function is also measured on single QD embedded at the center of a $L7$ PhC cavity as shown in Fig 4.5(a). The measurement is taken when a QD exciton line is tuned in resonance with the CM0. A narrow bandpass filter is used to select only CM0 for feeding the HBT setup. The observed antibunching with $g^2(0) \approx 0.4 < 0.5$, supports that single QD coupled with CM0 is at the single-photon level. The non-zero value of $g^2(0)$ is likely due to finite time response of the system and non-resonance pumping induced dephasing. Note the weaker fluctuation of 4QD case than 1QD case which is due to much higher photon counts in 4QD case during the measurement.

The DOLP of QD emission, given by $(I_y - I_x)/(I_y + I_x)$, is also measured through polarization-resolved PL, where I_x and I_y represent the intensity of QD emissions in the x- and y-polarized directions, respectively. Notably, CM0 and CM1 predominantly exhibit y-polarization, resulting in large positive DOLP values due to the geometry of the $L7$ cavity. Tuning of QD exciton lines across CM1 is accomplished by adjusting sample temperatures. The temperature-dependent polarization-resolved μPL spectra and corresponding DOLP values for devices 1 and 2 are depicted in Fig 4.6 and Fig 4.7, respectively. In Fig 4.6, for device 1, the excitonic transition X2

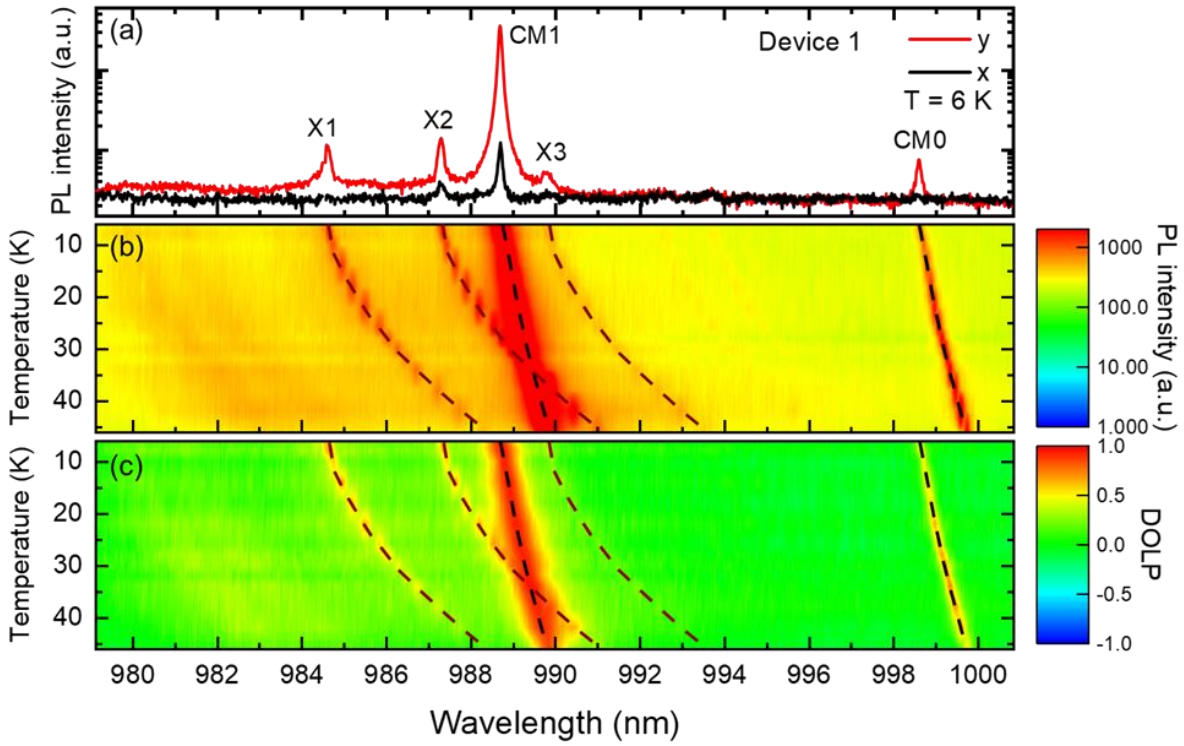

FIG 4.6 | Temperature-dependent polarization-resolved μPL of device 1. (a) PL spectrum measured at 6 K. The cavity Qs for CM1 and CM0 are respectively ≈ 12,000 and 9,000. **(b)** PL spectra of the y-polarized component measured at various sample temperatures. The PL intensity is in saturated logarithmic scale for better visibility of QD excitons. **(c)** DOLP measured at various sample temperatures. The dashed lines are guides to the eyes of the wavelength shifts of QD exciton lines and CMs.

shifts through CM1 from T = 6 K to 46 K, attaining a maximum DOLP of approximately 0.96 around T = 34 K when X2 resonates with CM1. Other exciton lines exhibit lower but positive DOLP values across all temperatures. Similarly, in Fig 4.7(b) for device 2, excitonic transitions QD1-X1, QD2-X2, and QD3-X2 sequentially shifts through CM1 as temperatures vary from T = 6 K to 48 K. Large positive DOLP values are observed when they resonate with CM1, with other exciton lines displaying lower but positive DOLP values across all temperatures.

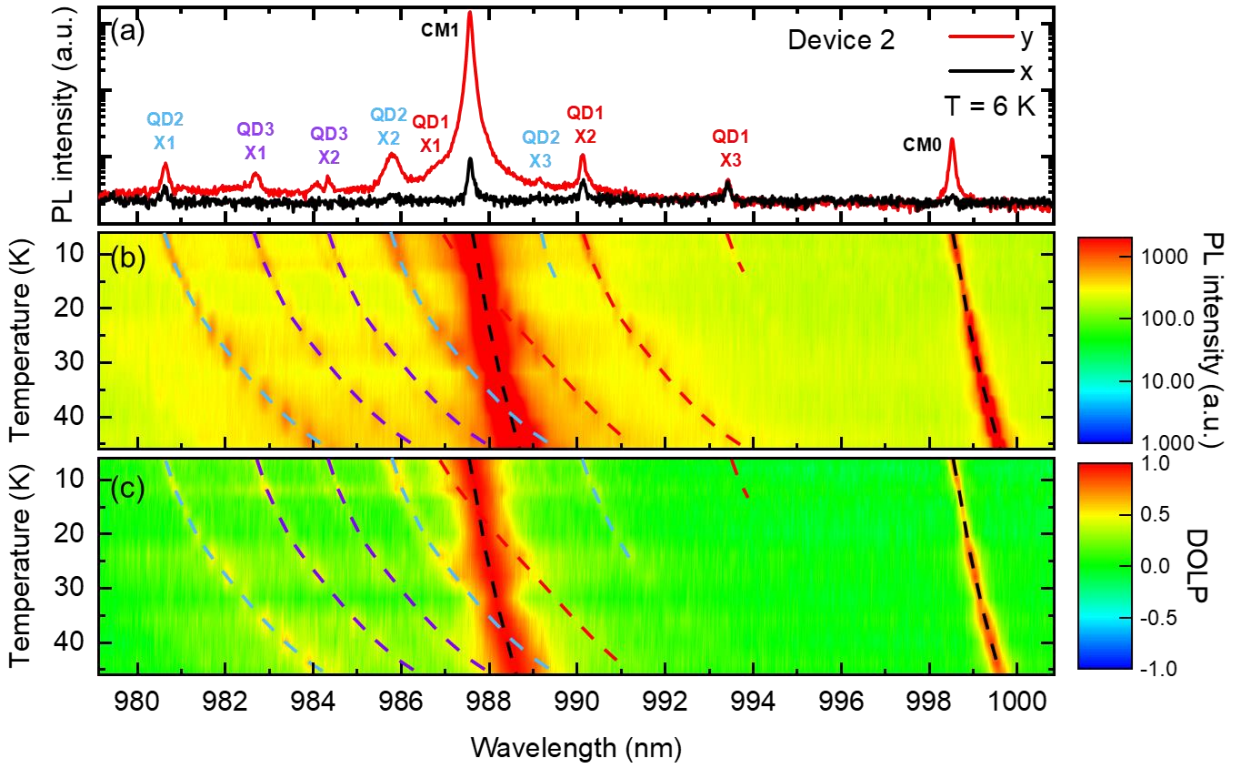

FIG 4.7 | Temperature-dependent polarization-resolved μPL of device 2. (a) PL spectrum measured at 6 K. The cavity *Q*s for CM1 and CM0 are respectively ≈ 11,000 and 7,000. **(b)** PL spectra of the *y*-polarized component measured at various sample temperatures. The PL intensity is in saturated logarithmic scale for better visibility of QD excitons. **(c)** DOLP measured at various sample temperatures. The dashed lines are guides to the eyes of the wavelength shifts of QD exciton lines and CMs.

We define the exciton-CM detuning as $\delta_X = E_X - E_{CM}$, representing the relative energy difference between exciton emission (E_X) and CM (E_{CM}). DOLP as a function of δ_X serves as an indicator of QD-cavity coupling, summarized in Fig 4.8(b) for device 1 and Fig 4.9(b) for device 2. Notably, the DOLP values are positive (> 0.5) for all QDs, attributed to both phonon scattering and pure dephasing [75], [77], [157]. The co-polarization of all QDs with CM1 suggests their simultaneous coupling with the same CM1 for both device 1 and device 2.

4.4 Spatially Avoided Crossing of QD Excitons with CM1

To spatially resolve the exciton emissions and CM1 along the vertical axis of the CCD, the sample is positioned such that the PL image's axis, corresponding to the x-axis of the *L*7 cavity, aligns parallel to the spectrometer slit. By appropriately selecting the lens focal length to focus the beam on the spectrometer slit, the far-field image of the higher-order CMs, extending along the x-axis of the cavity, can be spatially mapped. However, due to the limited spatial resolution (ε) of the objective with numerical aperture (N.A.), influenced by the long emission wavelength (λ) and low signal-to-noise ratio (SNR) resulting from relatively weak exciton emission intensities, the positions of the four QDs cannot be effectively identified using this method.

In Fig 4.8(a), the spectrally resolved far-field image of the spatial distribution of X2, X3, and CM1 of device 1 is illustrated at varying temperatures. Here, the vertical axis corresponds to the enlarged spatial distribution along the x-axis of the cavity. A saturated logarithmic color scale is employed to enhance the readability of excitons. As anticipated from the FDTD calculated electric field intensity pattern, CM0 exhibits a single spatial lobe, while CM1 displays two spatially extended lobes (refer to Fig 4.2). With increasing temperatures, X2 is tuned across CM1, while X3 is tuned away from CM1. The vertical positions of QD excitons are determined by Gaussian fitting of their line profiles, and their relative values to the center of CM1 as a function of detuning

δ_X are summarized in Fig 4.8(c) for *y*- and *x*-polarized components. Interestingly, the *y*-polarized components of QD excitons tend to coincide with the lower (upper) lobe of CM1 when they are brought into resonance with CM1 from the positive (negative) detuning side. Overall, this spatial behavior exhibits a shape of spatially avoided crossing within a detuning range of approximately

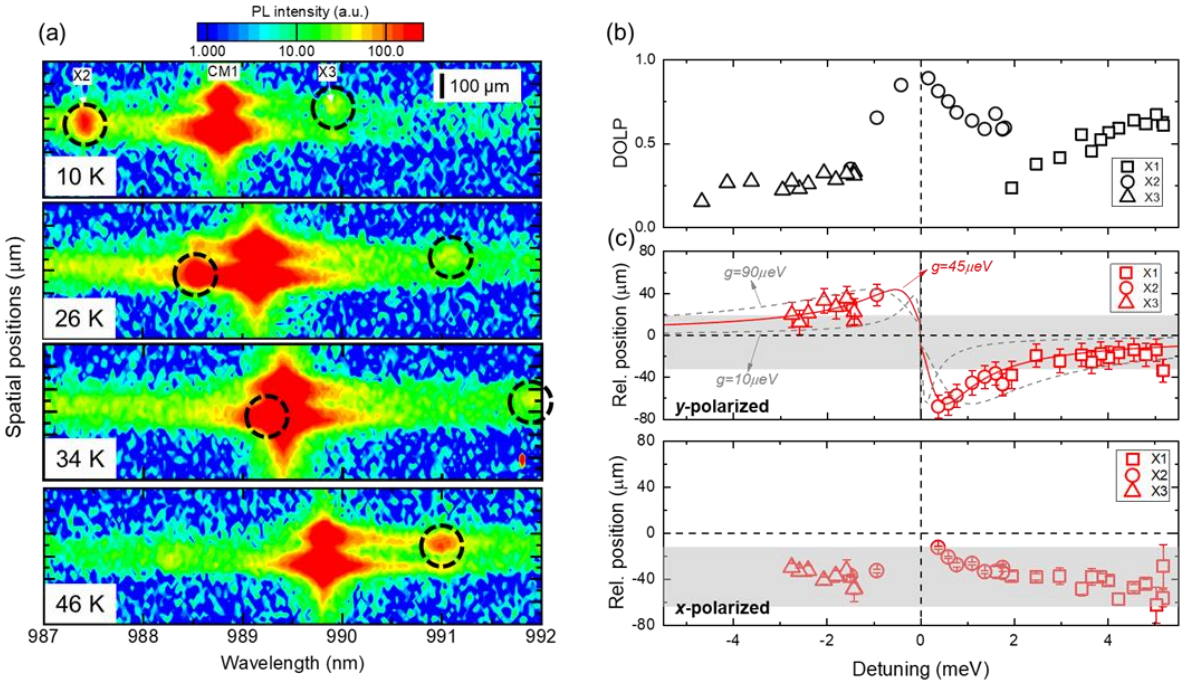

FIG 4.8 | Imaging of the position-wavelength map of QD excitons and CM1 for device 1 at varying temperatures (a) The black circles indicate X2 and X3 emission spots. The y axis corresponds to the vertical axis of the CCD. Vertical scale bar: 100 μm. Saturated logarithm color scales is used to facilitate the readibility of excitons. **(b)** DOLP of X1, X2, and X3 as a function of detuning. **(c)** The relative spatial position of *y*-polarized (upper figure) and *x*-polarized (lower figure) X1, X2, and X3 with respective to the center of CM1 as a function of detuning. The shaded area marks approximately the span of exciton relative positions at large detuning. The red curve is the fitting using W_{y1}/W_{y2} with $\kappa = 100$ μeV, $\gamma_y = 0.7$ μeV, χ_{21} = 0.9, χ_{22} = 0.2, and $g_2 = 45$ μeV. The two grey cruves correspond to fitting parameters $g_2 =$ 15 and 90 μeV.

± 3 meV, where the DOLP of QD exhibits large positive values. However, QD excitons in *x*-polarized directions do not demonstrate such spatial features, as depicted in the lower panel of Fig 4.8(c). It is noteworthy that in QW systems, the spatial features of the excitonic state arising from its superposition with the photonic state cannot be distinguished due to the extended nature of QW excitons. In contrast, in our presented QD system, the localized QD excitons, not superimposed with photonic states at large detuning, exhibit spatial coalescence with lobes of the extended photonic states at small detuning. This observation reveals how the subwavelength-confined excitonic states can be spatially modified from their original state due to interaction with a spatially extended cavity photonic state. Moreover, in the polaritonic picture, such deviated excitonic states can be interpreted as polaritons with enhanced excitonic components (lower polaritonic state at negative detuning or upper polaritonic state at positive detuning). However, spectral Rabi splitting is not resolved in our measurement, likely due to the much more pronounced CM1 emission intensity compared to QD excitons.

To further explore the influence of QD positions, a similar measurement is conducted on device 2, where QD excitons can be identified and associated with different QDs. As shown in Fig 4.9, once again, CM1 exhibits upper and lower spatial lobes along the x-axis of the cavity, while CM0 displays only a single lobe. As temperatures increase, QD2-X2 traverses CM1, while QD1-X1 moves out of resonance with CM1. QD2-X1, QD3-X1, and QD3-X2 approach CM1, whereas QD2-X3, QD1-X2, and QD1-X3 move away from CM1. The vertical positions of *y*-polarized components of the two central QDs (QD2 and QD3) exhibit a spatially avoided crossing with the center of CM1 within a detuning range of approximately ± 3 meV, corresponding to large positive DOLP values, although QD3 is only at the positive detuning side in the measured temperature range. Intriguingly, excitons from the side QD (QD1) do not manifest such phenomena. Once

again, the avoided crossing is not observed in the *x*-polarized component of all QD excitons, as depicted in the lower panel of Fig 4.9(c).

A recent study [165] on the DOLP proposes a theory of Fano-like [342], [343] quantum interferences between QD decay channels when coupled to the CM0 of an *L*3 cavity: direct QD decay into x- and y-polarized free space modes (FMs) and QD decay into y-polarized FMs through cavity decay channels, as we also mentioned in Fig 2.9 in chapter 2. In our device, inspired by Ref [165], with four QDs and two lobes of CM1, for QD_j (j = 1, 2, 3, and 4), the total QD emission rate into the *y*-polarized free space mode mediated by lobe k (k=1, 2) is expressed as:

$$W_{yjk} = \frac{\kappa + \gamma_y}{2} - Re\left[\left(\frac{\kappa - \gamma_y}{2} - i\delta\right)^2 - \left(2|g_{jk}| - i\chi_{jk}\sqrt{\gamma_y \kappa}e^{-i\phi_{jk}}\right) \times \left(2|g_{jk}| - i\chi_{jk}\sqrt{\gamma_y \kappa}e^{i\phi_{jk}}\right)\right]^{1/2} \quad (4.1)$$

where κ and γ_y represent the cavity decay rate and direct QD decay rate into *y*-polarized FMs, respectively. g_{jk} denotes the coupling strength of QD_j with lobe k. χ_{jk} represents the spatial overlap of the direct emission patterns of QD_j and field patterns of lobe k. δ is the QD-CM detuning, and ϕ_{jk} is the relative phase difference between decay channels, which depends on the QD positions with respect to the lobe. In this framework, the observation of detuning-dependent spatial features of QD2, for instance, can be attributed to the dominance of W_{y21} over W_{y22} at positive δ, and vice versa for negative δ. Thus, in the small detuning region, we can phenomenologically use W_{y21}/W_{y22} to mimic the spatial feature of QD2 excitons, represented by the blue curve in Fig 4.9(b), with κ = 100 μeV, γ_y = 0.7 μeV, χ_{21} = 0.9, and χ_{22} = 0.2. Assuming $g_{21} = g_{22} = g_2$ for simplicity, the blue curve with $g_2 = 45$ μeV accurately mimics the behavior

of QD2. Similar analysis can be conducted on device 1, represented by the red curve in Fig 4.8(b), with a coupling strength of 45 μeV. Such coupling strength aligns well with similar multi-site-controlled QD systems [174]. It is interesting to note that QD2 and QD3, which are symmetric

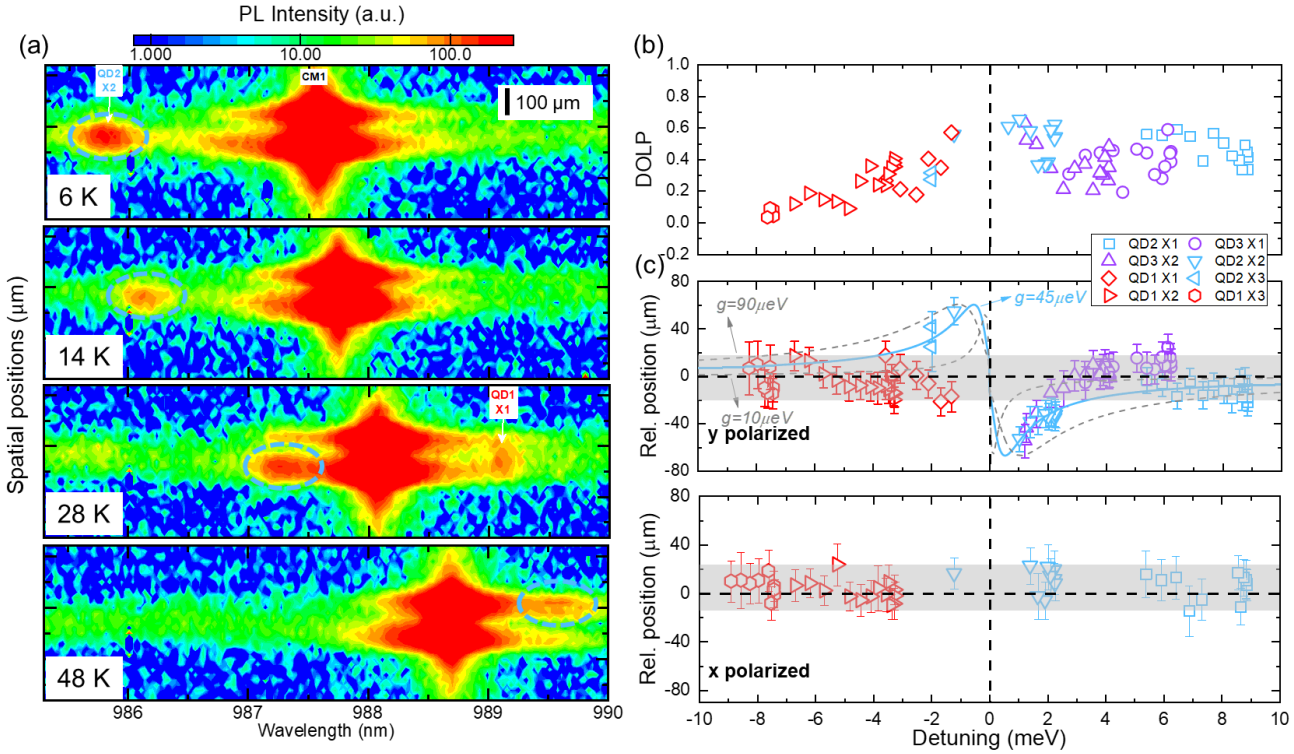

FIG 4.9 | Imaging of the position-wavelength map of QD excitons and CM1 for device 2 at varying temperatures. **(a)** The blue circles indicate QD2 X2 emission spots. The y axis corresponds to the vertical axis of the CCD. Vertical scale bar: 100 μm. Saturated logarithm color scales is used to facilitate the readibility of excitons. **(b)** DOLP of excitons corresponding to QD1-3 as a function of detuning. **(c)** The relative spatial position of *y*-polarized (upper) and *x*-polarized (lower) excitons corresponding to QD1-3 with respective to the center of CM1 as a function of detuning. The shaded area marks approximately the span of exciton relative positions at large detuning. The blue curve is the fitting of QD2 data using W_{y21}/W_{y22} with $\kappa = 100$ μeV, $\gamma_y = 0.7$ μeV, χ_{21} = 0.9, χ_{22} = 0.05, and $g_2 = 45$ μeV. The two grey cruves correspond to fitting parameters $g_2 = 15$ and 90 μeV.

with respect to the center of the cavity, exhibit the same spatial shape, as depicted in Fig 4.9(c). This suggests the existence of symmetry breaking of the two spatial lobes of CM1, possibly due to fabrication disorder of the PhC membrane or perturbation induced by the pyramid. This phenomenon leads to additional strongly confined localized modes of the CM1 spatial pattern, which constitutes an additional contribution to the above framework and needs further investigation [107], [245].

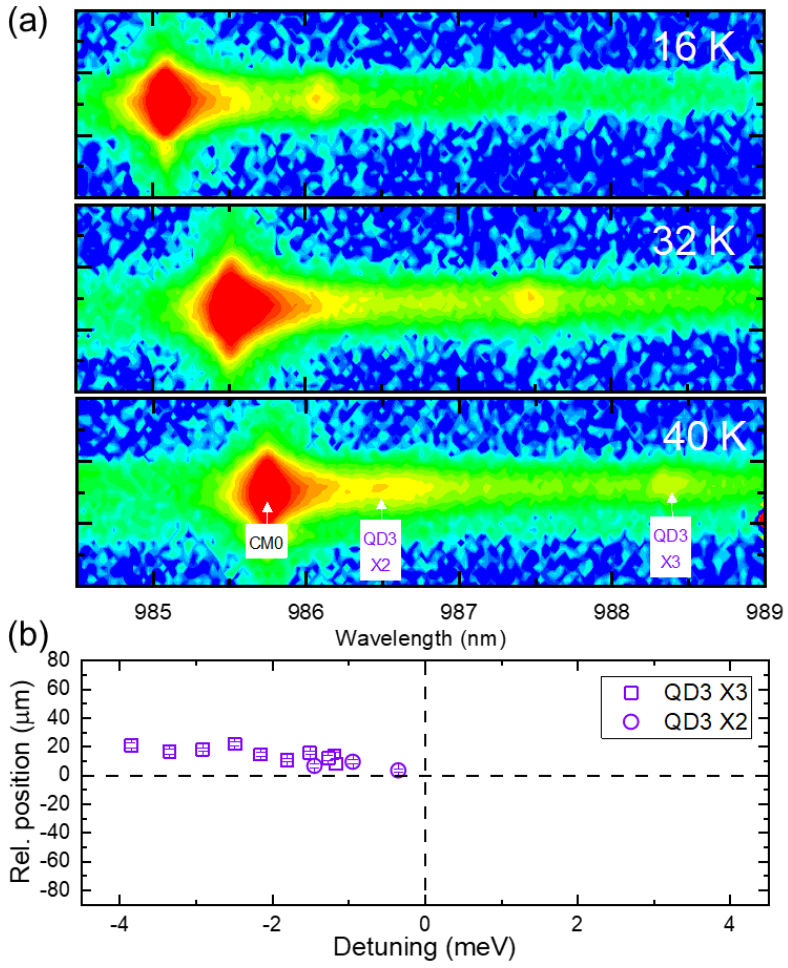

FIG 4.10 | Spatial- and spectrally-measurements of device 3 for reference. **(a)** CCD image of the position-wavelength map of QD excitons and CM0 for device 3 at T = 16 K, 32 K, and 40 K. **(b)** The relative spatial position of QD excitons QD3-X3 and QD3-X2 with respect to the center of CM0 as a function of detuning. Polarization is not resolved.

To further validate that the observed spatial avoided crossing phenomenon is specific to CM1, we extend our measurement to device 3 (with PhC hole radii r_3 = 36 nm), where we investigate the interaction of QD3 with CM0 as shown in Fig 4.10. Unlike CM1, CM0 is not spatially extended and exhibits a single lobe. Excitons from the central QD (QD3-X2 and QD3-X3) are tuned away from CM0 with increasing temperature. Within a negative detuning range of 4 meV, no avoided crossing is observed. This observation implies that the spatial avoided crossing phenomenon is specifically correlated with the extended feature of CM1.

4.5 Proposed Spatially Distributed Single-Photon Source

Based on our experimental observations, we propose the concept of a functional spatially distributed single photon source using site-controlled InGaAs QDs embedded in an *L*7 PhC cavity, evanescently coupled with two WGs along the x-axis, as illustrated in Fig 4.11. In this configuration, the two side WGs are terminated close to the two lobes of the CM1 to facilitate single photon extraction. As depicted in Fig 4.11(a), the detuning of excitons with CM1 can be controlled for QD2 to allow single photon propagation either to the left (negative detuning) or right (positive detuning) using evanescent field coupling. This operation can also be expressed in logical bases, as shown in the upper left inset of Fig 4.11(a). With positive detuning, the output state will be $|0_L 1_R\rangle$; with negative detuning, the output state is $|1_L 0_R\rangle$. Here, positive detuning is defined as logic 0 and negative detuning as logic 1, with left-propagating photon as 0 and right-propagating photon as 1. To construct a truth table for the outputs, we retrieve the PL intensity of exciton emission when it is tuned close to CM1 from prior spatially and spectrally resolved PL measurements. Specifically, the positive and negative detuning values used are +1.5027 meV and -0.5857 meV, respectively. The resulting truth table is shown in the lower right inset of Fig 4.11(a). We evaluate the output logic using the expression:

$$F = (1/2)Tr\left(\frac{M_{exp}{M_{ideal}}^{T}}{M_{ideal}{M_{ideal}}^{T}}\right), \tag{4.2}$$

It calculates the fidelity between the measured truth table M_{exp} and the ideal truth table M_{ideal}. We obtain an estimated fidelity of 70.76 ± 1.87 % for the output states [344]. Such logic operation is suitable for building single photon sources capable of switching operations, which control photon propagation along different directions. Particularly, using optical pumping from remote QDs [345]–[347], it can pave the way for possible low-photon-number optical switching [348], crucial components in linear optical quantum computers (LOQC) for quantum information routing. Furthermore, using the symmetry breaking of the CM1 lobes, as shown in Fig 4.11(b), within a $L7$ PhC cavity hosting two central QDs (QD2 and QD3) embedded, at a detuning where the CM1 energy is tuned in between the excitonic levels of QD2 and QD3, individual photons emitted from QD2 and QD3 (each possessing distinct wavelengths) can independently propagate towards the left (L) and right (R) directions. This phenomenon facilitates the realization of a tunable single-photon source for path encoding. By adjusting the CM1 to align with the midpoint between QD2 and QD3 [as depicted in the lower right inset of Fig 4.11(b)], single photons can be emitted through the left or right waveguides, encoded as |L> or |R>. Owing to the different emission energies of QD2 and QD3 (designated as ω2 and ω3, respectively), the resulting state can be represented as $|1_{\omega 2,\,L}\rangle$ or $|1_{\omega 3,\,R}\rangle$. Such a tunable single-photon source, capable of emitting photons of two distinct

colors, serves as a photon switch with varied path encodings, thereby presenting utility for spatial multiplexing in quantum communications [349].

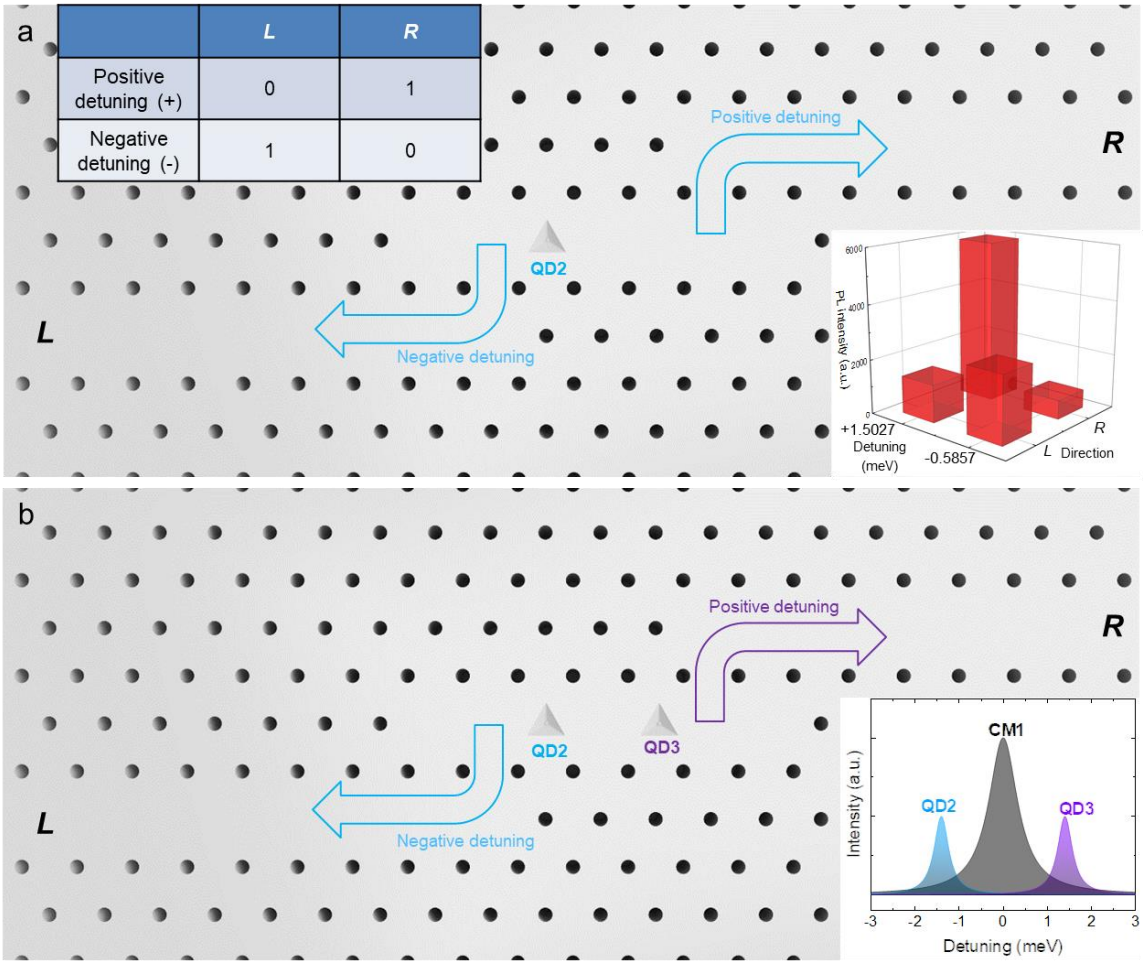

FIG 4.11 | Schematic of a proposed spatially distributed single-photon source. (a), L7 PhC cavity with embedded QD2 evanescently coupled with two PhC waveguides denoted by L and R. Upper left: logical operation of the single-photon source based on cavity detuning. Lower right: Measured output states in the logical bases retrieved from the PL measurements. **(b)**, L7 PhC cavity with embedded QD2 and QD3 evanescently coupled with two PhC waveguides denoted by L and R. Lower right: CM1 energy is tuned between QD2 and QD3, enabling a negatively-detuned QD2 exciton and a positively-detuned QD3 exciton within ± 3 meV.

4.6 Discussions

In summary, this chapter presents a direct experimental observation of the superposition of subwavelength-confined QD excitonic states, achieved through a complex system comprising four site-controlled QDs coupled with a spatially extended photonic state derived from a higher-order photonic mode of an *L*7 PhC cavity. This demonstration is facilitated by the wavelength-position mapping of QD-cavity interactions across varying detuning. Notably, our investigation reveals that excitonic states originating from QDs near the cavity center exhibit a coalescence with lobes of the CM1 mode, forming a spatial avoided crossing that varies with QD-cavity detuning. Furthermore, we observe the symmetry breaking of the two lobes of CM1, suggesting avenues for further exploration through techniques such as near-field scanning optical microscopy (NSOM) or high-energy resolution electron energy-loss spectroscopy, complemented by theoretical frameworks encompassing quantum interference phenomena. These observed phenomena hold significance in elucidating the spatial characteristics of QD excitonic states within tailored photonic environments during their interactions. They offer potential applications in spatially controlling single-photon transport to distant locations via detuning adjustments, with subsequent extraction facilitated by waveguides for practical logic operations. It is necessary to use site-controlled QD systems, as the observed phenomena are dependent on QD positioning. Additionally, based on the observed static phenomena, dynamic control of detuning could be realized through methods such as Stark-based ultrafast pump-probe techniques [350] or even at the few-photon level [351], laying groundwork for the development of fast all-optical switching or controlled quantum gates toward LOQC [352].

Chapter 5

Photophysics of O-band and Transition Metal Color Centers in Monolithic Silicon for Quantum Communications

5.1 Overview and Introduction

Building a practical quantum network is essential for scaling computational power, advancing quantum computers, and supporting the development of secure quantum communications [353]–[356]. To transmit flying qubits (e.g. photons) over long distances, the existing fiber communication infrastructure predominantly operates in the telecommunication wavelengths centered around 1310 nm (O-band) and 1550 (C-band), suggesting the need for telecommunicating quantum emitters. The incorporation of an intermediate node, such as a quantum repeater, can further increase the communications and network range [300], [357]–[364]. For this purpose, high dimensional energy-time entangled qubits emerge as a crucial platform, enabling efficient quantum information transport with high information capacity between high-fidelity quantum memory nodes [365]–[368]. Furthermore, for achieving low error-rate communications, the operation of the high-dimensional quantum channels in proximity to the fiber zero-dispersion wavelength around 1310 nm is preferred. This wavelength minimizes timing errors over long distances, enhancing state fidelity. Therefore, there is a critical need to develop a high-fidelity quantum node with near-unity radiative efficiency, eliminating possible non-radiative pathways. Importantly, such a quantum node should be integrable with integrated photonic devices, facilitating interfacing with O-band quantum channels. The extended excited state lifetime of defect center, achieved by eliminating non-radiative pathways, can be further enhanced through photonic cavity structures towards high-coherence fast photonic qubit interactions.

As we have seen in chapter 2-4 that the site-controlled pyramidal InGaAs QDs are promising solid-state single photon emitters, with great scalability, for on-chip quantum information processing through integrated quantum photonics using photonic crystals. In this chapter, we explore the potential of using emerging solid-state quantum emitters (or color centers) in Silicon hosts for quantum nodes, driven by several compelling reasons [26], [369], [370]. Besides GaAs systems, Silicon, being a dominant, scalable, and well-designed platform, stands out for nanoelectronic and nanophotonic circuits, proving effective control and interfacing capabilities for qubits. The ability to create reproducible color centers and donor defects with exceptional characteristics further enhances Silicon's appeal as a quantum computing platform. Furthermore, the recent development of isotopically purified ^{28}Si substrates, reaching up to 99.9998% purity, presents a host material devoid of magnetic field fluctuations, thereby supporting excellent qubit coherence [186]–[190]. Notably, spin qubits with extended lifetimes, reaching up to 3 hours for shallow phosphorus donors [191], and 2.14 s for deep selenium donors [29], [192] have been achieved, which are missing in InGaAs QD systems.

Defects/color centers in silicon, such as G, W, and T centers offer bright PL emissions near the O-band, long lifetimes, and narrow emission linewidths [22], [23], [25]–[28], [193], [194], [371]–[373], making them suitable for quantum applications. G and W centers, compatible with Silicon photonic devices, have been explored as bright single-photon sources with singlet-singlet transitions. However, they lack a spin-photon interface for quantum information storage and memory [22], [23], [207]. In contrast, T centers emerge as a compelling candidate due to their efficient coherent spin-photon interface in the telecommunication wavelengths [21], [24], [30], [90], [374], [375]. T centers exhibit a doublet-line with first (TX_0) and second excited state (TX_1) transition with 1.76 meV spacing, likely due to the internal stress [209]. The T center comprises

two carbon atoms occupying a single silicon site, with a hydrogen atom bonded to one of the carbon atoms in C_{1h} symmetry [376]. The formation of T centers is proposed to involve capturing an interstitial carbon-hydrogen complex at a substitutional carbon site. Upon photoexcitation, the T center site forms a bound exciton and an unpaired electron, where two electrons form a spin-0 singlet state, while the unpaired hole has a spin-3/2 state [209]. The optical transition of first (TX_0) and second (TX_1) excited state of T centers are measured at approximately 1325.9 nm (935.1 meV) and 1323.4 nm (936.86 meV) respectively [30], close to the O-band zero-dispersion wavelength. The inhomogeneous linewidth of zero-phonon line (ZPL) of TX_0 transition for an ensemble of T centers in natural silicon and ^{28}Si is measured as 26.9 μeV and 0.14 μeV, respectively. The measured lifetime of TX_0 transition is 0.94 μs, leading to a possible ZPL dipole moment of 0.73 Debye and a Debye-Waller factor of 0.23 at T = 1.4 K [30]. Spin resonance measurements have demonstrated a nuclear spin coherence time over a second from Hahn echo. These remarkable properties make T centers an attractive platform for building metropolitan-scale quantum networks.

In this chapter, we explore a unique optical transition of a 0.56 meV-split doublet at 1312.15 nm (943 meV), exhibiting a potential spin-photon interface even closer to zero-dispersion wavelength, with comparison of the T center transitions. This optical transition is attributed to a transition-metal defect comprising Cu and Ag atoms called $^{*}Cu^{m}_{n}$, featuring an isoelectronic bound exciton similar to T centers [377]–[379]. The $^{*}Cu^{m}_{n}$ defect was initially identified by McGuigan et al. in a lightly Cu-doped silicon substrate, alongside another defect around 1221 nm (1014 meV), termed Cu and consisting four Cu atoms [378], [380], [381]. The possible ground triplet state of $^{*}Cu^{m}_{n}$, similar to Nitrogen-vacancy-centers (NV-centers) in diamonds, is considered a promising candidate for stable and high-fluence qubits [26], [371]. This chapter involves an in-depth exploration of the photophysics and cryogenic μPL spectroscopy of the $^{*}Cu^{m}_{n}$ doublet transitions.

A comparative analysis is conducted with the T center transitions, including excitation power dependencies, temperature dependencies, lifetime measurements with thermal partition function and rate equation analyses. Electron spin resonances and magneto-PL on the $^{*}Cu^{m}_{n}$ transitions are examined. This chapter also outlines the process steps undertaken to improve the generation of T center and the $^{*}Cu^{m}_{n}$ paving the way for the development of optical spin-photon interfaces towards quantum memories and repeaters. For this purpose, we examine and identify the relevant transformations between the various color centers involving G, W, T centers, and $^{*}Cu^{m}_{n}$. We report an extended TX_0 lifetime up to 1.56 µs, owing to process optimization resulting in reduced lattice distortion. The bound exciton dynamics are examined using a rate equation model, shedding light on the carrier feeding process from higher excited states. Overall, these color centers in silicon exhibit unique potential for interfacing with energy-time entangled photonic qubits, positioning them as promising candidates for advancing high-rate quantum communications and high-fidelity telecommunicating quantum memories which can be difficult to be achieved using InGaAs QDs.

5.2 Sample Preparation and Process Variations

In our study, we implement a combination of various ion implantation and RTA processes to finely control and optimize the generation of silicon color centers. Here, the T centers are generated by the following process adapted from earlier studies [31], [382]. A float-zone (FZ) grown, dilute boron-doped silicon substrate, whose resistivity is 1000 to 2000 Ω · cm with carbon and hydrogen impurity concentrations less than 2×10^{16} cm^{-3}, is used. First, carbon ions are implanted into the silicon substrate at 7 degrees with 38 keV energy and a dose of 7×10^{12} cm^{-2}. This implantation recipe produces an ion profile whose peak concentration is at 118.8 nm from the surface with 42.8 nm straggle based on SRIM-2013 simulations, with profile shown in Fig 5.1(a)-I [383].

To repair the lattice damage caused by the carbon implantation, an RTA process is employed. The annealing is performed at 1000 °C for 20 seconds in an argon environment with a flow rate of

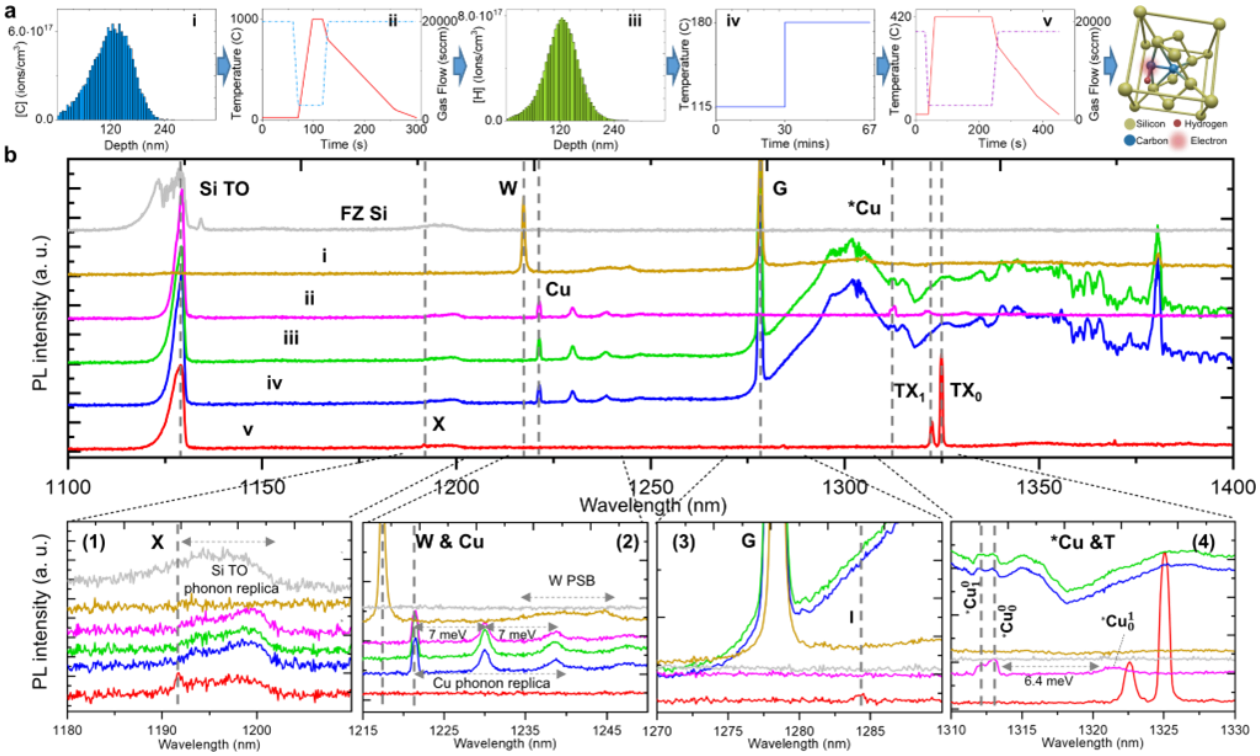

FIG 5.1 | Family of color centers in silicon and the T center generation recipe. FIG. 1. Family of color centers in silicon and the T center generation recipe (a) Process steps: (i) Simulated depth profile of carbon implantation with 38 keV ion energy. (ii) Temperature (solid line) and gas flow (dashed line) profiles for rapid thermal annealing recipe at 1000°C for 20 seconds. (iii) Simulated depth profile of hydrogen implantation with 9 keV ion energy. (iv) Hot plate temperature variation for H_2O treatment. (v) Temperature (solid line) and gas flow (dashed line) profiles for rapid thermal annealing at 420°C for 3 minutes. **(b)** Variation of the μPL spectrum at each process step, where each identified line is marked with dashed lines and the spectra are stacked with equal spacing vertically for easier identification. The X, W, G, and T emission lines are magnified at the bottom. The observed 0.56 meV-split *Cu doublet around 1312.15 nm is denoted as the low ($*Cu^0_0$) and high ($*Cu^0_1$) energy line. Fig 5.1 is published in [218].

3,000 sccm. The maximum temperature is achieved following a 28-second ramp-up, and a passive cooling is done under a high argon flow of 20,000 sccm. The temperature profile for this process is shown in Fig 5.1(a)-ii. This recipe is commonly used to introduce substitutional carbon defects in silicon to generate G centers, which are investigated as single-photon emitters [27], [207], [373]. Subsequently, to promote the formation of C-H groups necessary for the creation of T centers, hydrogen ions are implanted into the silicon substrate. This implantation is conducted at an angle of 7 degrees, with an implantation energy of 9 keV and a dose of 7×10^{12} cm^{-2}. The resulting hydrogen concentration profile is shown in Fig 5.1(a)-iii, with a peak concentration at 120.8 nm from the surface and a straggle of 38 nm, matching the carbon concentration [383]. Following this step, the samples then undergo a cleaning process using acetone and isopropyl alcohol, and they are then N_2 blow-dried.

In the subsequent processing steps, the samples undergo treatment in deionized water to facilitate hydrogen diffusion and bonding with carbon atoms. The treatment is performed in a controlled cleanroom under a fume hood, using a hot plate with a two-step process: (1) The samples are treated in deionized water with a hot plate temperature set at 115 °C for 30 minutes, (2) Subsequently, the hot plate temperature is increased to 180 °C and maintained for 37 minutes (Fig 5.1(a)-iv). This two-step treatment under the fume hood is optimized to apply a controllable amount of thermal energy, with the water surface temperature reaching up to 95.5 °C. Following the water treatment, the treated samples are placed into the RTA chamber as the final step to promote the binding of CH groups with substitutional carbon sites, facilitating the formation of T centers. Inside the nitrogen environment, the samples undergo annealing at 420 °C for 3 minutes within a SiC susceptor, whose thermal properties may affect the actual sample temperature during the annealing process. The duration of annealing is varied to examine the outcomes. Additionally, the study

includes testing samples that undergo annealing without the prior H_2O treatment, which is important to protect the samples from oxygen contamination that contributes to the broadening of T center PL emissions.

In Fig 5.1(b), the μPL spectrum taken between λ = 1100 and 1400 nm at 5 K after each process step provides insights into the T center formation mechanism and its precursors, with a comparison to untreated Si substrate. As a benchmark of lattice damage in silicon, it can be observed that the silicon transverse-optical (TO) transition line around 1130 nm (band-to-band transition) is completely destroyed under carbon implantation. Its recovery is observed in step ii with RTA process [217]. Hydrogen implantation shows a 10% decrease in Si TO line intensity compared to step ii due to its low atomic mass and thus less lattice damage. Interestingly, the subsequent deionized water treatment also serves as an annealing process, enhancing the Si TO line damaged by hydrogen implantation. After the second RTA process, a 30% decrease in Si TO line intensity is observed, which might be attributed to the replacement of the Si sites with the C-(C-H) complex, contributing to the T centers formation [209]. Similar trends in the Si phonon replica around 1195 nm are observed. After step v, a weak X center emission line at 1191.7 nm becomes evident, superimposed on the silicon phonon replica. The origins of the X center are uncertain, with initial propositions suggesting an interstitial nature with possible tetrahedral or tetragonal symmetry. Recent ab-initio studies on candidates like I3-X or I4-A defects remain inconclusive [384].

Following the carbon implantation in step i, before the annealing process to repair lattice damage, the formation of W and G centers is clearly observed. The ZPL transitions for W and G centers are observed at 1217.48 nm and 1278.5 nm, respectively, with Gaussian FWHM linewidths approximately of 0.65 nm and 0.8 nm. The G center, a carbon-related defect, is observed without any annealing. It is believed to be composed of two substitutional carbon sites connected by

interstitial silicon [27], [373]. The G center line disappears after annealing at 1000 °C for 20 seconds, indicating the displacement of implantation-induced silicon interstitials into the lattice during thermal annealing. The lifetime of the produced G center is measured up to 6.67 ns at 7.5 K, which is slightly longer than the 5.9 ns reported previously for the ensembles, indicating the dominance of nonradiative processes [25], [27]. The W center line exhibits a phonon sideband up to 1250 nm, while the G line phonon sideband extends up to 1400 nm, including a local vibrational mode at 1381 nm [385]. Annealing at 1000 °C for 20 seconds, as shown in Fig 5.1(a)-ii, however, leads to the disappearance of the G and W lines. This disappearance indicates the displacement of implantation-induced silicon interstitials into the lattice during thermal annealing. The W center is considered to be a cluster of interstitial silicon atoms in the lattice with a ZPL around 1218 nm [193], [204], [384], [386].

In step ii, the W emission line is replaced by three phonon replicas at 1221.45 nm, 1230.07 nm, and 1238.64 nm with FWHM linewidth of 0.58 nm, 1.2 nm, and 1.65 nm, respectively, as shown in Fig 5.1(b). These phonon replica emissions, approximately 7 meV apart from each other, indicate the energy of the involved phonons. The peak energies and separation are aligned with prior literature where it is identified as the Cu line, a complex involving four Cu atoms [378], [380], [387], [388]. We observe a similar structure for the $^{*}Cu^{m}_{n}$ doublet emission around 1312.15 nm (Fig 5.1(b)-4 and Fig 5.2(a)), consisting of 0.56 meV split low ($^{*}Cu^{0}_{0}$) and high ($^{*}Cu^{0}_{1}$) energy lines at 1312.98 and 1312.20 nm respectively. The superscript, m, denotes the number of phonons involved in the transition, indicating the phonon replicas, while the subscript, n, indicates the order of the transition in the excitonic energy ladder. Additionally, 6.4-meV phonon replicas are observed at 1321.64 nm ($^{*}Cu^{1}_{0}$) and 1331.06 nm ($^{*}Cu^{2}_{0}$). These emission peaks are formed after carbon implantation and RTA process at 1000 °C, after step ii. The fortuitous formation of Cu and $^{*}Cu^{m}_{n}$

peaks is attributed to possible Cu and Ag contamination during implantation and annealing steps,

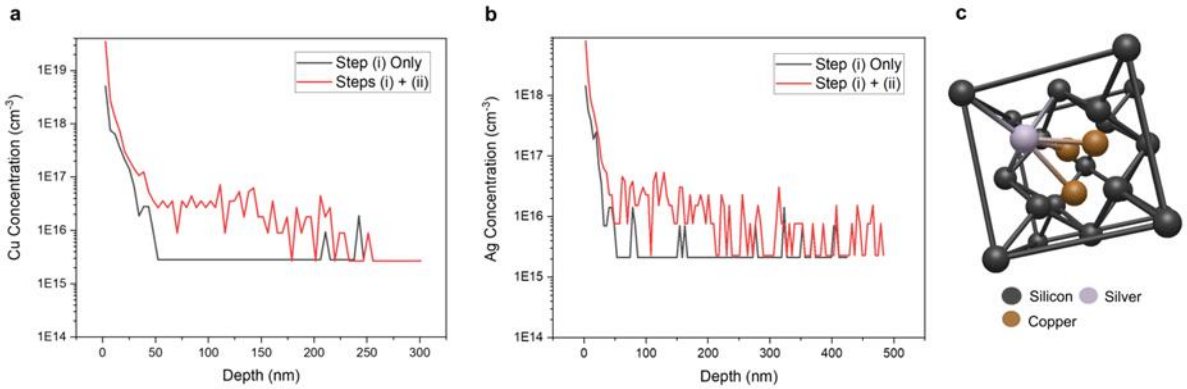

FIG 5.2 | SIMS profile of a silicon sample with PL emission corresponding to *Cu. (a) Copper concentration in the silicon sample at varying depths. The black line shows the sample with only the carbon implantation, which damages the native silicon lattice, introducing vacancies. The red line shows the sample with carbon implantation and annealing at 1000 C, healing the lattice, diffusing the impurities, and creating the defect centers. **(b)** Silver concentration in the silicon sample at varying depths. The black line shows the sample with only the carbon implantation, which damages the native silicon lattice, introducing vacancies. The red line shows the sample with carbon implantation and annealing at 1000 ˚C, healing the lattice, diffusing the impurities, and creating the defect centers. **(c)** The crystalline structure of the *Cu defect center in silicon. It is characterized by a substitutional silver and three interstitial copper atoms in a silicon lattice. The atoms in the diagram can be described as follows: black atoms are silicon, grey atom is silver, and brown atoms are copper. Fig 5.2 is published in [218].

supported by secondary ion mass spectrometry (SIMS) depth profile. Fig 5.2(a) and (b) shows the SIMS data for the Cu and Ag concentrations in our silicon samples that showed *Cu and Cu peaks. The samples were prepared according to Fig 5.1(a) steps i and/or ii. It appears that the annealing process increases the concentration of the Cu and Ag below the surface, likely due to diffusion. The concentration of silver and copper is above 1×10^{15} cm^{-3} below the surface and appears to

fluctuate around 1×10^{16} cm^{-3} below the surface after annealing. We believe that the relatively high concentration of Cu and Ag impurities was from the silicon wafer manufacturing process. Fig 5.2(c) shows the crystalline structure for the *Cu defect center. The Gaussian FWHM linewidth of the $^{*}Cu^{0}{}_{1}$ and $^{*}Cu^{0}{}_{0}$ emission is approximately 0.66 nm and 0.523 nm, respectively. These emissions disappear with deionized water treatment.

Furthermore, when we apply the RTA process in step v without any water treatment, we can observe $^{*}Cu^{0}{}_{1}$ and $^{*}Cu^{0}{}_{0}$ emissions alongside the T center TX_0 and TX_1 emissions. The phonon replica at 1321.64 nm manifests as a shoulder peak to TX_1, denoted as $^{*}Cu^{1}{}_{0}$. The PL spectrum resulting from such RTA-only treatment is shown as the blue line in Fig 5.2(a). Our initial studies using SIMS confirm that the earlier studies that emissions at 1221.45 nm, 1230.07 nm, and 1238.64 nm and the doublet emission denoted as $^{*}Cu^{0}{}_{1}$ and $^{*}Cu^{0}{}_{0}$ originate from residual Cu and/or Ag constituents during implantation. The 1221.45 nm emission and the 7 meV-apart phonon replicas are identified as Cu-line, which is a precipitation of four Cu atoms [377], [378], [387], [388]. On the other hand, the 1312.15 nm doublet emission and its phonon replica with 6.4 meV phonon

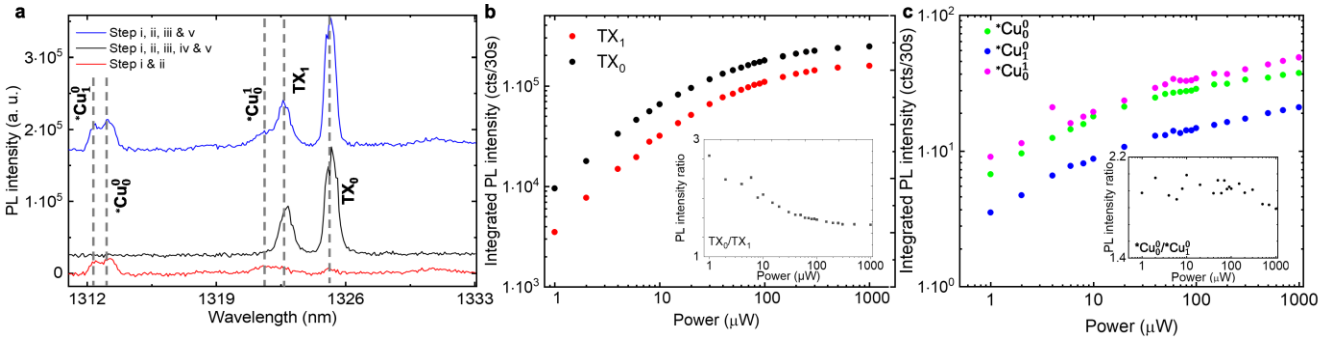

FIG 5.3 | Cryogenic μPL characterization of TX_0, TX_1 and $^{*}Cu^{m}{}_{n}$ transitions in silicon. (a) PL spectrum showing the formation of TX_0, TX_1, $^{*}Cu^{0}{}_{0}$,$^{*}Cu^{0}{}_{1}$, and $^{*}Cu^{1}{}_{0}$ peaks at different process steps (b) Excitation power dependence of the integrated PL intensity TX_0 and TX_1 emissions. Inset: ratio of TX_0/TX_1 intensities with increasing excitation power. (c) Excitation power dependence of the integrated PL intensity of $^{*}Cu^{0}{}_{0}$, $^{*}Cu^{0}{}_{1}$, and $^{*}Cu^{1}{}_{0}$ emissions. Fig 5.3 is published in [218].

energy at 1321.64 nm, are associated to a defect where a single Ag atom displaces one of the Cu atoms in the Cu line, which is denoted as the *Cu center [377]–[381], [389]. We were able to replicate the formation of Cu and *Cu^{m}_{n} emissions through deliberate Cu and Ag implantation into a Si wafer and RTA at 900 °C for 20 seconds. Notably, as shown in Fig 5.3(a), T centers and *Cu centers can coexist when the water treatment is omitted, suggesting that *Cu center is susceptible to hydrogenation under the available thermal budget, either via implantation or deionized water treatment used for hydrogen diffusion.

The G center emission is recovered after hydrogen implantation. It results from the implanted-proton-induced interstitials and persists after the deionized H_2O treatment [390]. However, it exhibits a high-intensity phonon sideband from 1280 nm to 1400 nm, with the previously reported E-line evident at 1381 nm [385], [391], as observed in step i. Furthermore, after step v, a small emission peak is observed around 1285 nm, corresponding to the I-center, a variation of the T center perturbed by the presence of oxygen atoms [216]. The oxygen concentration [O] is less than $2\times10^{16}cm^{-3}$ in the substrate.

As a result of the two-step H_2O treatment and RTA at 420 °C for 3 minutes, a clean TX_0 ZPL at 1325.1 nm with a 0.63 nm linewidth and a TX_1 line at 1322.65 nm with 0.79 nm linewidth are obtained. Fig 5.3(a) shows the TX_0 and TX_1 lines in the samples that are carbon and hydrogen implanted (after step iii), H_2O and RTA treated (after step v), and also the case where the samples are RTA treated only after step iii (without H_2O treatment). This indicates that, although deionized H_2O treatment facilitates high-purity sample development, it is not required to induce T-center formation [382]. The integrated PL intensity of TX_0 and TX_1 emissions as a function of excitation power is given in Fig 5.3(b). The integrated intensity is saturated around 300 μW. Presented in Fig 5.4(b) inset, at 1 μW excitation power, the ratio of ZPL intensity between TX_0

and TX_1 is around 2.725, which gradually decreases and reaches a minimum plateau point around 300 μW where TX_0 states saturate, while the optically injected carriers keep populating the TX_1 states up to 500 μW. The same analysis is done for $^{*}Cu^{0}{}_{1}$ and $^{*}Cu^{0}{}_{0}$ emission and the shoulder ($^{*}Cu^{1}{}_{0}$) emission we have discussed before. Similar to TX_0 and TX_1, the $^{*}Cu^{0}{}_{1}$ and $^{*}Cu^{0}{}_{0}$ intensities exhibit a saturation behavior at a higher excitation power. Note that the broad shoulder ($^{*}Cu^{1}{}_{0}$) emission follows the same trend as $^{*}Cu^{0}{}_{1}$ and $^{*}Cu^{0}{}_{0}$, suggesting such shoulder can be attributed to a phonon replica. Unlike the T center, the intensity ratio $^{*}Cu^{0}{}_{0}/^{*}Cu^{0}{}_{1}$ begins around 2, maintaining constant up to 100 μW, and slowly decreases at higher power. Note that Cu center phonon replicas appear at the higher energy side of $^{*}Cu^{0}{}_{1}$ and $^{*}Cu^{0}{}_{0}$ emissions (between 1221 nm and 1240 nm) (Fig 5.1(b)-2) while the T center spectrum (Fig 5.1(b)-4) is clean. As a result, a delayed decrease of the intensity ratio ($^{*}Cu^{0}{}_{0}/^{*}Cu^{0}{}_{1}$) can be due to the efficient carrier captured by the Cu centers.

5.3 Statistical Variations of T center and *Cu PL emissions

In the following, we perform a statistical study of PL emission of *Cu and T center emissions, which are shown in Fig 5.4 and Fig 5.5, respectively, measured with a 532 nm laser excitation at 300 μW at T = 5 K. Figure S1 shows the statistical variations in the TX0 and TX1 emissions over the surface of a FZ Si substrate with Carbon and Hydrogen implantation. Due to the local environmental variations for each T-center, such as neighboring impurities of Boron or Oxygen and local strain, we observe a variation in the peak energy, intensity, and linewidth. Fig 5.4(a) indicates a variation in the peak intensities for TX_0 and TX_1 with a standard deviation by a third of the mean intensity over the sample. On the other hand, we do not observe a significant change in the peak frequency (only 12 μeV for TX_0 and 14 μeV for TX_1), which is given in Fig 5.4(b). It can suggest that the local strain and the internal electric fields over the sample are mostly uniform.

Further studies under magnetic field would help to investigate the local-strain-related effects further. Fig 5.4(c) shows the variation in the inhomogeneous linewidths at T = 5 K. The standard deviations for TX_0 and TX_1 linewidths are measured as 30.5 µeV and 18.6 µeV, respectively. These values are comparable to the deviations in the peak energy shown in Fig 5.4(b), which may be explained by the inhomogeneous nature of the ensemble centers, while there is not a significant variation of impurity effects over the sample.

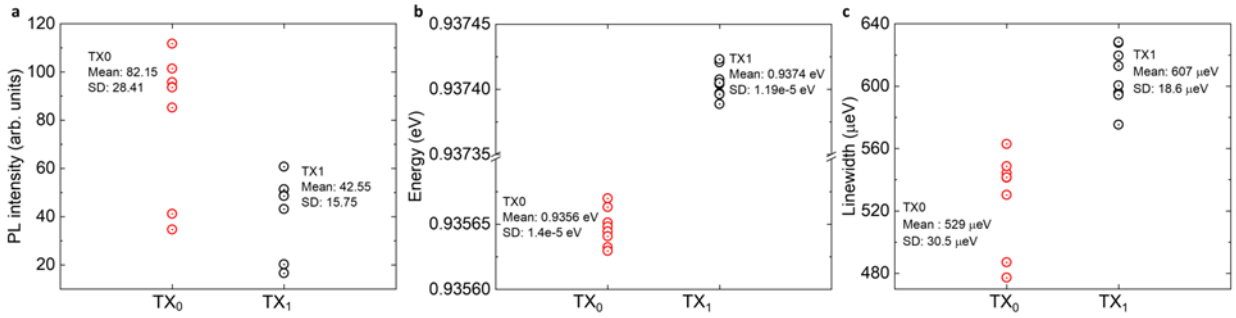

FIG 5.4 | Statistical variations of T center PL emission over a FZ Silicon substrate (a) The change in the normalized peak intensity over the sample excited by a 532 nm laser at 300 µW at T = 5 K, which shows a standard deviation of a third of the mean intensity over the sample. Each data point is measured at a random position on the sample much farther from each other than the excitation spot size. **(b)** The variation of the peak energy for TX_0 and TX_1. The y-axis is divided into two regimes to present TX_0 and TX_1 data together, separated by ~1.8 meV. The reported deviations are 12 µeV for TX_0 and 14 µeV for TX_1. **(c)** The standard deviations of the inhomogeneous linewidth for TX_0 and TX_1 over the sample is more than an order of magnitude less than the mean linewidths. Fig 5.4 is published in [218].

Fig 5.5 illustrates the variations in the PL emission of a FZ silicon sample containing $^{*}Cu^{0}_{1}$ and $^{*}Cu^{0}_{0}$ defects excited by a 532 nm laser (300 µW) at different locations on its surface. Due to the local variations in the formation and measurement of each defect center, such as neighboring impurities unrelated to the defect, local strain, and small temperature differences, we observe

variations in the PL peak energy, intensity, and linewidth. Fig 5.5(a) shows the variation in the emission intensity for $^{*}Cu^{0}_{1}$ and $^{*}Cu^{0}_{0}$. The standard deviation of intensity for $^{*}Cu^{0}_{0}$ is approximately a third of the mean intensity, while for $^{*}Cu^{1}_{0}$, the standard deviation is around one-seventh of the mean intensity. Similarly to the T-center, we do not observe a significant change in the peak energy at different locations on the sample (68 μeV for $^{*}Cu^{0}_{0}$ and 74 μeV for $^{*}Cu^{0}_{1}$). This suggests that the local strain and internal electric fields in the sample are mostly uniform, but further studies under magnetic field would reveal more information on the local-strain-related effects. The variation for the inhomogeneous linewidth is shown in Fig 5.5(c). The standard deviations for the linewidths of the *Cu centers are less than one-eighth of the mean linewidth. We

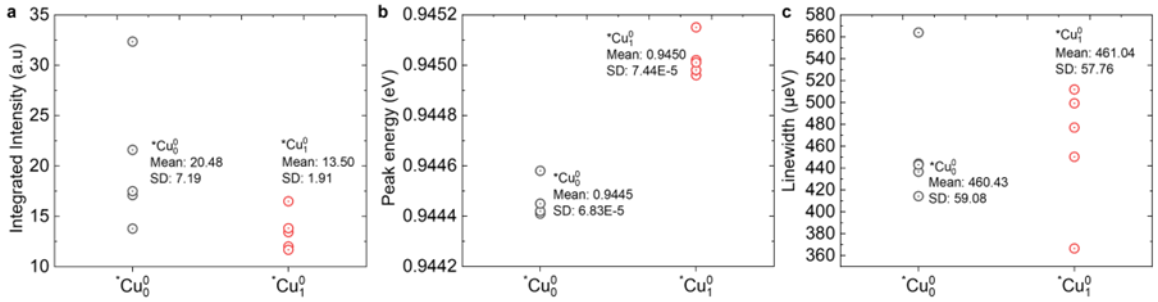

FIG 5.5 | Statistical variations of $^{*}Cu^{0}_{1}$ and $^{*}Cu^{0}_{0}$ PL emission over a FZ Silicon substrate (a) The change in the integrated PL intensity over the sample excited by a 532 nm laser at 300 μW at T = 5 K, which shows a standard deviation of a third of the mean intensity over the sample. Each data point is measured at a random position on the sample much farther from each other than the excitation spot size. (b) The variation of the peak energy for $^{*}Cu^{0}_{1}$ and $^{*}Cu^{0}_{0}$. The y-axis is divided into two regimes to present $^{*}Cu^{0}_{1}$ and $^{*}Cu^{0}_{0}$ data together, which are apart from each other by ~0.5 meV. The reported deviations are 68 μeV for $^{*}Cu^{0}_{0}$ and 74 μeV for $^{*}Cu^{0}_{1}$. (c) The standard deviations of the inhomogeneous linewidth for $^{*}Cu^{0}_{1}$ and $^{*}Cu^{0}_{0}$ over the sample is more than an order of magnitude less than the mean linewidths. Fig 5.5 is published in [218].

speculate this larger variation in linewidth compared to the T-center could be due to the fact that Cu and Ag are heavier compared to carbon and hydrogen atoms.

5.4 Temperature-Dependent Microphotoluminescence Spectroscopy of T-center and *Cu center Emissions

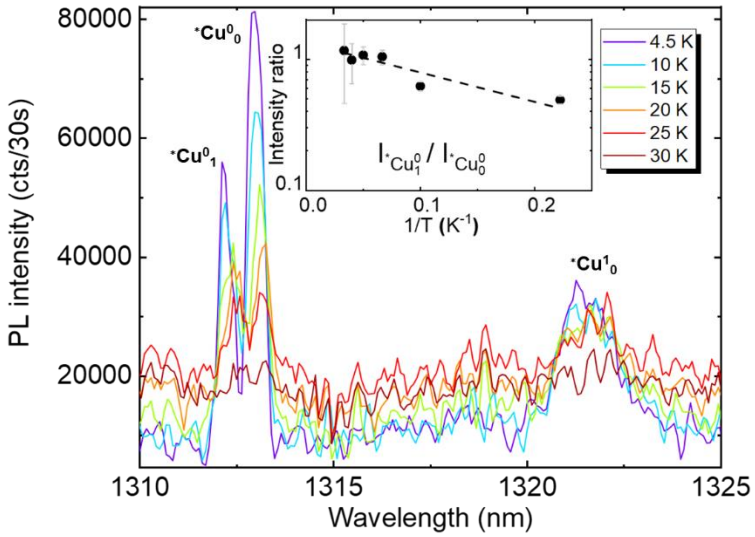

FIG 5.6 | Temperature-dependent PL spectra of *Cu emission. Inset: Intensity ratio of $^{*}Cu^{0}_{1}/^{*}Cu^{0}_{0}$ as a function of reciprocal temperature. Fig 5.6 is published in [218].

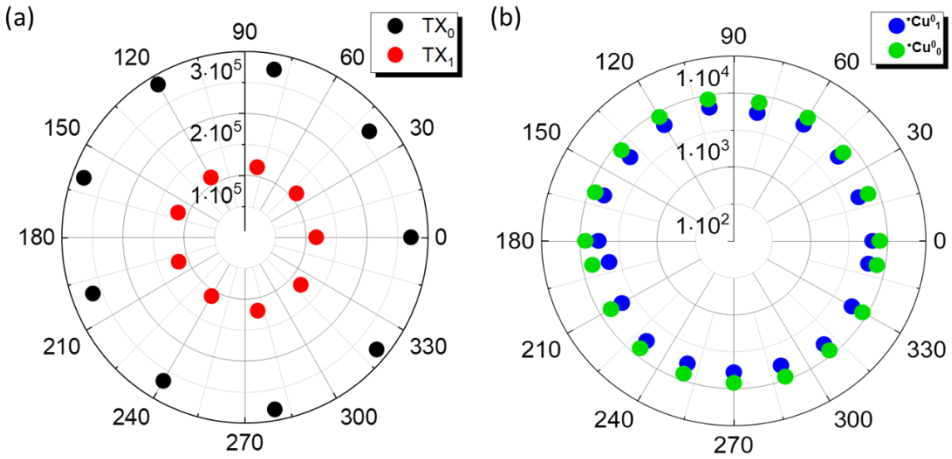

FIG 5.7 | Polarization-dependent PL intensity of the T center and *Cu center emission. Fig 5.7 is published in [218].

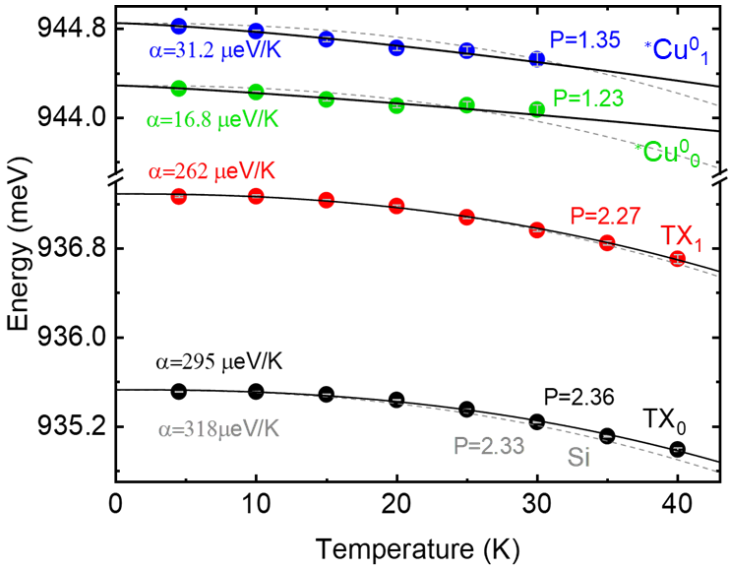

FIG 5.8 | Temperature-dependent PL peak energy of the T center and *Cu center emission. ZPL transition energy of TX_0 (black), TX_1 (red), $^{*}Cu^0_1$ (blue) and $^{*}Cu^0_0$ (green) as a function of temperature. The red solid and dashed curves denote the fit by the four-parameter Passler model. The grey dash curve is for bulk silicon. Fig 5.8 is published in [218].

In Fig 5.6, the temperature-dependent μPL spectra of the *Cu lines are measured, ranging from T = 4.5 K to 30 K, on a FZ silicon sample with carbon implantation and subsequent RTA process detailed in step i and ii of Fig 5.1(a). Both *Cu and T center show an isotropic polarization of the PL emission as expected from an ensemble of emitters. As shown in Fig 5.7(a) and (b), there is no preference of polarization between the doublets TX_0-TX_1 and $^{*}Cu^0_1$-$^{*}Cu^0_0$, which may cause a population transfer between them.

Fig 5.8 presents the transition energies of *Cu and T-center ZPL emission as a function of temperature extracted from Gaussian fits of their spectra measured at each temperature. At cryogenic temperatures, the thermal-induced redshift of the semiconductor bandgap can be well expressed by the four-parameter Passler model,

$$E(T) = E(0) - \alpha\Theta(2T/\Theta)^p. \quad (5.1)$$

α denotes the slope dE/dT in the limiting case of $T \to \infty$ and p is a dimensionless parameter related to the phonon dispersion coefficient $\sqrt{\frac{\langle\varepsilon_{ph}^2\rangle - \langle\varepsilon_{ph}\rangle^2}{\langle\varepsilon_{ph}\rangle}}$ and Θ approximately equals to the average phonon temperature [392]. For simple fitting purposes, Eq. (5.1) can be rewritten as a polynomial expression,

$$E(T) = E(0) - AT^p. \quad (5.2)$$

The temperature-dependent transition energy of $^*Cu^0_1$ and $^*Cu^0_0$, TX_0, and TX_1 ZPL emission are fitted using Eq. (5.2) and represented by the solid black curves. The dimensionless fitting parameter p are determined to be 1.25, 1.23, 2.27, and 2.36 for $^*Cu^0_1$, $^*Cu^0_0$, TX_1, and TX_0 transitions respectively. For comparative analysis, considering the defect centers are in a silicon matrix, we assume the average phonon temperature to be $\Theta \approx 406$ K [392] for silicon and are the same for these defect centers. Extracting the values of the coefficient α, we find them to be 31.2, 16.8, 262, and 295 μeV/K for $^*Cu^0_1$, $^*Cu^0_0$, TX_1, and TX_0 respectively. The silicon band gap variation with temperature is also plotted as grey dash lines for comparison, employing parameters to be $p = 2.33$, $\alpha = 318$ μeV/K, and $\Theta \approx 406$ K from literature [392]. In the cases of TX_0 and TX_1, their parameters closely align with silicon values, indicating a minor modification of the silicon matrix by the T center in the sample where steps i to v are performed. This implies that the annealing and H_2O treatment, which promotes the migration of carbon and hydrogen interstitials and leads to the T center formation, efficiently restores the lattice. In stark contrast, the red-shifting behavior of the transition energy of $^*Cu^0_1$ and $^*Cu^0_0$ emission exhibits a significant deviation from the silicon bandgap, resulting in a much smaller fitting parameter of p and α compared with the silicon and T center. This suggests that a significant distortion of the

silicon matrix occurs during step i, where the injected carbon ions and displaced silicon atoms occupy the interstitial sites, creating vacancies along the trajectory of the injected ions.

Step ii in Fig 5.1(a) promotes impurity migration, resulting in the formation of a 0.57 meV-split doublet luminescence centers. Notably, a much lower value of p and α indicate a more significant phonon dispersion, and a smaller slope at $T \rightarrow \infty$ suggests smaller zero-point renormalizations [393] by the dramatic modification of the electron-phonon interaction during its formation processes. This also aligns with the observation of the vanishing W center ZPL and the appearance of phonon replicas. The significant phonon dispersion also leads to a higher dependence of doublet splitting of the $^{*}Cu^{0}_{0}$ and $^{*}Cu^{0}_{1}$ lines compared to the T center doublet (TX_0 and TX_1). In Fig 5.9, it is observed that the peak energy difference between the $^{*}Cu^{0}_{1}$ and $^{*}Cu^{0}_{0}$ emissions is reduced by at least 0.1 meV untill about 30 K, before thermalization. On the other hand, the peak energy difference between TX_0 and TX_1 emissions remains somewhat constant across temperatures, likely owing to the smaller modification of the silicon matrix.

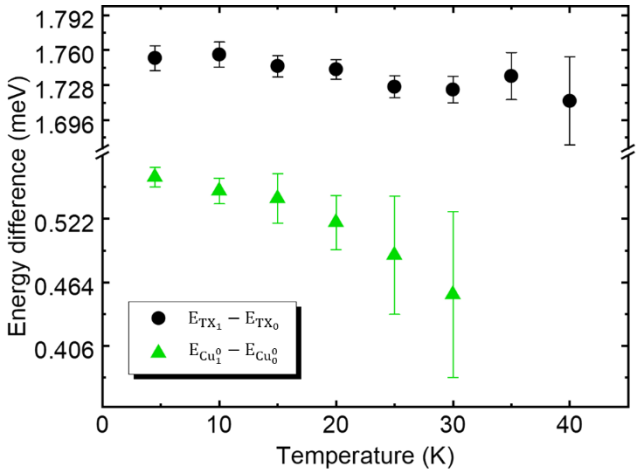

FIG 5.9 | Temperature-dependent peak energy difference of the T center and *Cu center emission. Energy difference of the ZPL transition between TX_0 and TX_1 (black), and $^{*}Cu^{0}_{1}$ and $^{*}Cu^{0}_{0}$ (green) as a function of temperature. Fig 5.9 is published in [218].

Fig 5.10(a) shows the integrated PL intensities of the $^{*}Cu^{0}_{1}$ and $^{*}Cu^{0}_{0}$, and T centers ZPL with increasing temperatures. TX_0 and TX_1 start to thermalize around T = 20 K, while the $^{*}Cu^{0}_{0}$ emission quenches at a much lower temperature. The PL intensity of the $^{*}Cu^{0}_{1}$ emission exhibits a plateau up to T = 15 K. The measured 1.75 ± 0.0113 meV spectroscopic splitting between the TX_0 and TX_1 emissions at T = 4.5 K matches the reported value [208]. The known dissociation energy of the bound exciton of 22.5 meV [208] can be well-reproduced by fitting the TX_0 intensity as a function of reciprocal temperature (black dots in Fig 5.10(b)) by a thermal partition function given by

$$I(T) = \frac{I(0)}{1+Aexp\left(-\frac{E_1}{kT}\right)+BT^{3/2}\exp\left(-\frac{E_2}{kT}\right)}. \quad (5.3)$$

Setting E_1 = 1.75 meV as the excess energy of the excited state TX_1 to TX_0 and E_2 = 22.5 meV as the activation energy to the silicon band edge, the fitting results are shown as black curves in the upper panel of Fig 5.10(b). For the $^{*}Cu^{0}_{1}$ and $^{*}Cu^{0}_{0}$, it is worth noting that their integrated PL intensity ratio $I_{*Cu^{0}_{1}}/I_{*Cu^{0}_{0}}$ (inset of Fig 5.6) leads to a Boltzmann factor with a thermal activation energy of E_a = 0.44 ± 0.12 meV, which agrees with the measured spectroscopic splitting of 0.56 ± 0.0089 meV within our experimental error. It suggests that, like TX_1 and TX_0, the Cu^{0}_{1} emission can be associated with a transition from the higher excited state to the lower $^{*}Cu^{0}_{0}$ state of the same defect center. As shown in the lower panel of Fig 5.10(b), Eq. (5.3) can be used to fit the $^{*}Cu^{0}_{0}$ PL intensity by setting E_1 to be the measured spectroscopic doublet splitting of 0.56 meV, with the resulting E_2 = 3.35 meV when the fit converges. This suggests a much smaller binding energy than the T center bound excitons and aligns with the much earlier intensity quenching of $^{*}Cu^{0}_{0}$ emission even below T = 10 K. The total binding energy E_B of the electron and hole associated with the exciton of the $^{*}Cu^{0}_{0}$ emission localized to this defect color center can be deduced to be 225.2 meV by subtracting the transition energy of $^{*}Cu^{0}_{0}$ by the silicon bandgap at low temperature. Like the T

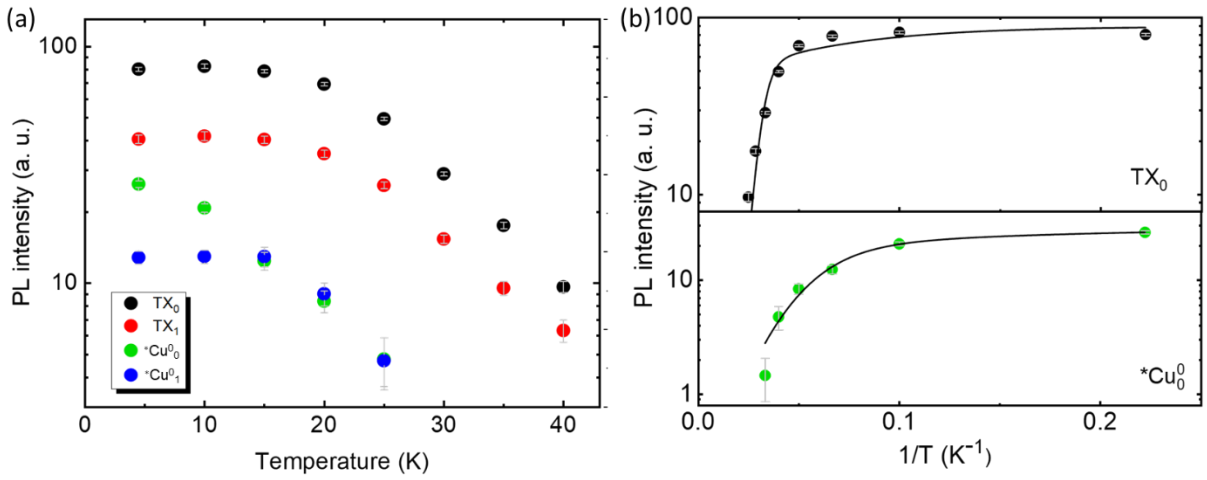

FIG 5.10 | Temperature-dependent PL intensity of the T center and *Cu center emission. (a) PL intensity of TX_0 (black), TX_1 (red), $^{*}Cu^0_0$ (green), and $^{*}Cu^0_1$ (blue) as a function of temperature. **(b)** PL intensity of TX_0 (black) and $^{*}Cu^0_0$ (green) as a function of reciprocal temperature. The black curves are fits according to Eq. (5.3). Fig 5.10 is published in [218].

center, $E_B \gg E_2$ probably suggests that such a 0.57 meV-split doublet related luminescence center consists of one strongly localized and another loosely Coulombic bound particles, which is potentially another candidate for a spin-photon interface in the telecommunication band. Note that the plateau in the PL intensity of $^{*}Cu^0_1$ emission below T = 15 K is likely due to the thermal-induced carrier populating from the lower energy $^{*}Cu^0_0$ state to $^{*}Cu^0_1$ state.

Finally, Fig 5.11 illustrates the temperature dependent FWHM linewidth of the studied emissions. Both the lower energy states, TX_0 and $^{*}Cu^0_0$ of the T-center and 0.56 meV-split doublet, exhibit a constant linewidth of about 542 µeV and 318 µeV, respectively, within our experimental error. However, for the higher energy states, the TX_1 linewidth remains constant at about 598 µeV until around T = 20 K and then increases to 927 µeV at T = 40 K. The linewidth of $^{*}Cu^0_1$ increases from 263 µeV to 444 µeV from T = 4.5 K to 15 K and then gradually decreases to 343 µeV at T =

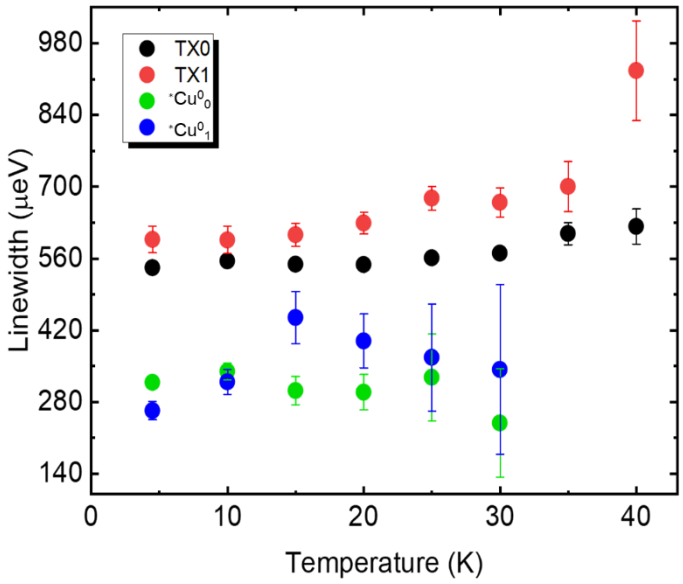

FIG 5.11 | Temperature-dependent linewidth of the T center and *Cu center emission. Linewidth of TX_0 (black), TX_1 (red), $^{*}Cu^{0}_{0}$ (green), and $^{*}Cu^{0}_{1}$ (blue) emissions as a function of temperature. Fig 5.11 is published in [218].

30 K. The observed linewidth broadening with respect to the Fourier transform-limited linewidth of T center (≤ 1 neV) can result from: (1) fluctuating environmental charges leading to pure exciton dephasing, or spectral diffusion, depending on the rate of energy Stark shifting; (2) ensemble emitting centers where individual ZPLs are shifted due to different local strains; (3) isotopic effects from natural silicon, in which the ^{29}Si with non-zero nuclear spin cause resonance shift and magnetic field fluctuations; and (4) phonon-assisted broadening. However, for temperature variation of the linewidth, the phonon contribution is not significant for T = 30 K. Therefore, we attribute the broadening of TX_1 with T ≤ 30 K to increasing charge fluctuations as a result of the thermal-induced electrons with increasing temperatures, considering the low excitation regime (32 μW). The sudden increase at high temperature (T = 40 K) can be due to increased phonon population and scattering. The minor variation of the TX_0 linewidth compared to the TX_1 linewidth can be attributed to its more localized exciton wavefunction, which also applies to the constant

behavior of linewidth for the lower energy $^{*}Cu^{0}_{0}$ state compared to the higher energy $^{*}Cu^{0}_{1}$ state. The dramatic increases of $^{*}Cu^{0}_{1}$ linewidth up to T = 30 K, aligned with its thermalization above T = 30 K as shown in Fig 5.10(a), can be attributed to increased charge fluctuations from the thermally induced carriers, considering the small activation energy of 0.56 meV from $^{*}Cu^{0}_{0}$ state to $^{*}Cu^{0}_{1}$ state. The subsequent decrease in the $^{*}Cu^{0}_{1}$ linewidth can be due to the charge stabilization of the fully occupied $^{*}Cu^{0}_{1}$ states at higher temperatures.

5.5 Photoluminescence Dynamics of T-center and *Cu Center Emissions

The lifetime of the T center, a most likely candidate for next-generation spin-photon interface, has been reported previously [30] but lacks in-depth study of its radiative and non-radiative bound exciton dynamics. To address this, we conducted temperature dependent TRPL measurements on TX_0 and TX_1 emissions. We excite the sample with a pulse laser (600 nm, pulse width ≈ 5 ps) at an angle of approximately 45 degrees with the sample surface via a plano-convex singlet lens, resulting in a large excitation spot with the diameter of approximately 40 μm. We achieved sufficient counts for the TRPL histogram integration while avoiding saturating the T centers. PL is collected from the excitation spot via a 20× (NA = 0.4) microscope objective perpendicular to the sample surface. The collected light passes through a 0.5-meter monochromator to a near-infrared (NIR) photomultiplier tube (PMT) unit with approximately 400 ps timing resolution attached to the exit port. The TRPL is then performed using the TCSPC technique introduced in chapter 1. The high-density 1200 grooves/mm grating provides a spectral resolution of 0.04 nm so that only the ZPL of TX_0 or TX_1 fed into the PMT, while rejecting the photons from the phonon sideband.

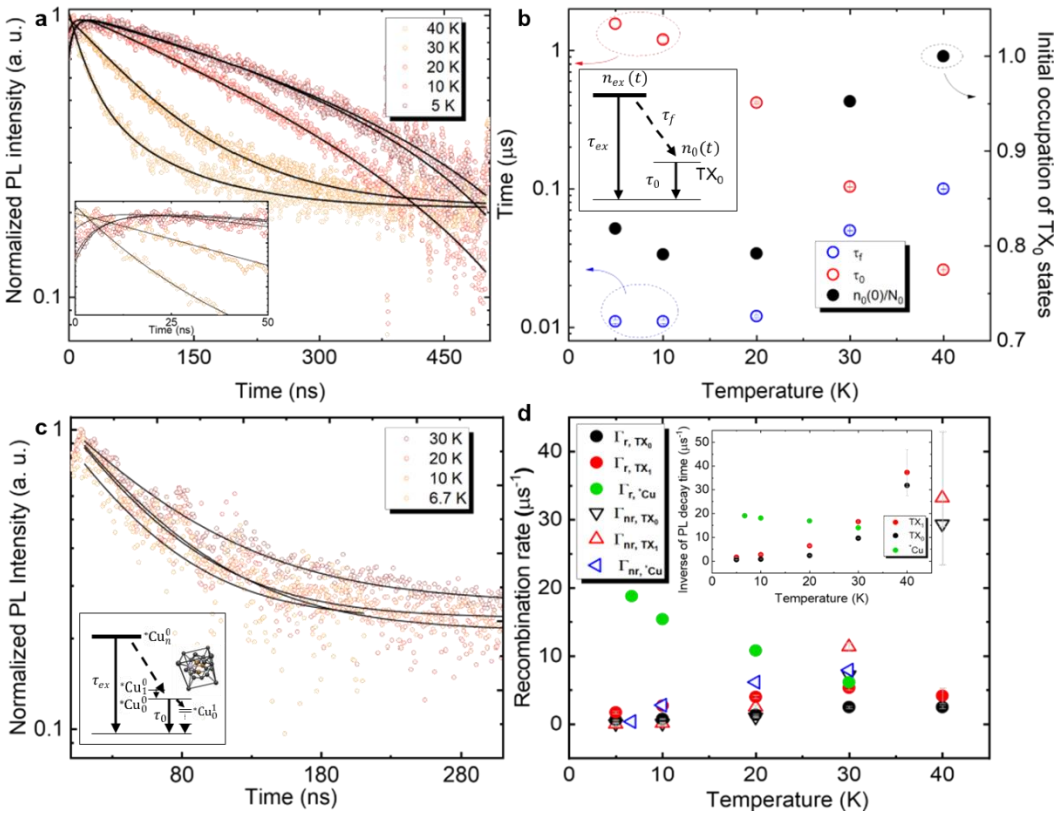

FIG 5.12 | T center and *Cu bound exciton radiative dynamics. (a) TRPL trace of TX_0 as a function of temperature-fitted rate equation. Inset: zoom-in of early TRPL rise time. **(b)** Radiative lifetime and carrier populations as a function of temperature, with the TX_0 state recombination mechanism depicted in the inset. The carrier populations of TX_0 and higher excited states are denoted as $n_0(t)$, and $n_{ex}(t)$ with corresponding lifetimes of τ_0 and τ_{ex}. τ_f denotes the relaxation time constant from the higher excited state to TX_0, and N_0 denotes the maximum available TX0 states. **(c)** TRPL trace of the combined doublet decay of *Cu exciton. **(d)** The inverse PL decay time of TX_0, TX_1, *Cu as a function of temperature. Inset: Bound exciton recombination rate as a function of temperature. $\Gamma_{nr,TX0}$, $\Gamma_{nr,TX1}$, $\Gamma_{r,TX0}$, $\Gamma_{r,TX1}$, $\Gamma_{r,*Cu}$, $\Gamma_{r,*Cu}$ denote the nonradiative and radiative recombination rate of TX0, TX1, and ∗Cu accordingly. Fig 5.12 is published in [218].

Fig 5.12(a) illustrates the resulting TRPL traces of TX_0 transition with sample temperatures ranging from T = 5 K to 40 K. The PL decay of TX_0 reveals a prolonged tail and remains unchanged

as the temperature increases until reaching T = 20 K, where it changes to a faster decay. Notably, the inset of Fig 5.12(a) reveals a slow rise in the TX_0 PL intensity at T = 5 and 10 K and gradually vanishes with increasing temperature. Such a slow rise component of the PL intensity and its variation with temperatures are neither observed in TX_1 states and G centers, and nor observed in prior W [193], G [27], [373] and T centers [30], [31], [382]. The TRPL for G center can be referred to Fig 5.13. We speculate that the carrier transition to TX_0 from the higher excited states (TX_2 to TX_{25}) [30] leads to this slow rise with the peak PL intensity. We phenomenologically explain this process using a simple two-level system coupled to the continuum of states, as shown in the inset of Fig 5.12(b).

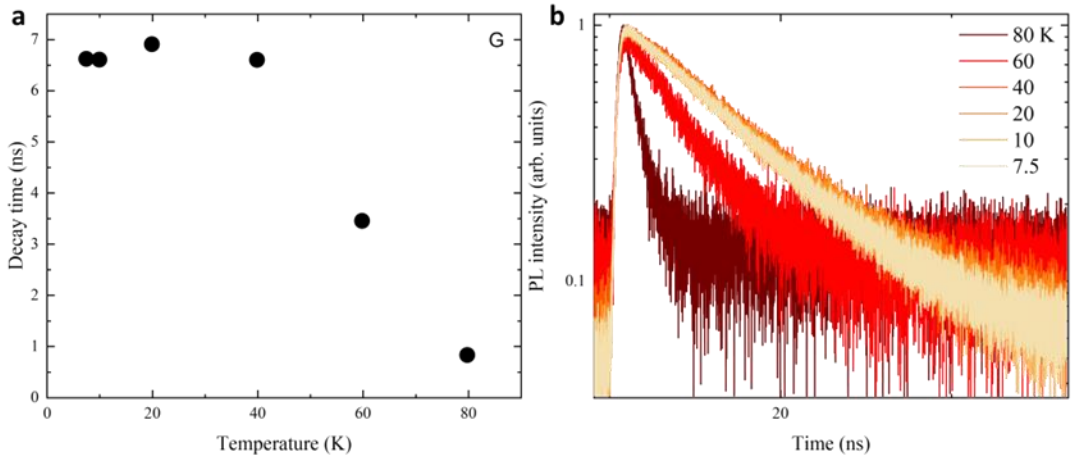

FIG 5.13 | G center exciton radiative dynamics. (a) Decay time as a function of temperature extracted from (b). (b) The raw data of the G-center TRPL traces. Fig 5.13 is published in [218].

The measured PL decay of TX_0 can be understood as the carrier relaxation from TX_0 to a ground state with a lifetime τ_0 (radiative and non-radiative) and a non-radiative carrier feeding from an effective higher excited state $n_{ex}(t)$ to TX_0 with a characteristic time constant τ_f. Note that since the carrier transition from the silicon band edge is fast (tens of fs) [394], [395] it cannot be resolved in

the measurement and thus absorbed into the initial carrier populations $n_0(0)$ and $n_{ex}(0)$. The rate equation governing the carrier populations $n_0(t)$ and $n_{ex}(t)$are expressed as follows:

$$\frac{dn_0}{dt} = \frac{n_0}{\tau_0} + \frac{n_{ex}}{\tau_f} N_0 \tag{5.4}$$

$$\frac{dn_{ex}}{dt} = -\frac{n_{ex}}{\tau_{ex}} - \frac{n_{ex}}{\tau_f} N_0 \tag{5.5}$$

Here, n_0 and n_{ex} represent the populations of the optically excited carriers in TX_0 and higher excited states, respectively. τ_0 is the decay time of the TX_0 state, and τ_{ex} is the effective lifetime of higher excitation states. τ_f denotes the characteristic time constant of the non-radiative carrier feeding to TX_0 states. N_0 denotes the total amount of available TX_0 states that can be occupied.

In Fig 5.12(a), the TRPL trace of TX_0 can be well modeled by the proposed mechanism, and the extracted fitting parameters are shown in Fig 5.12(b) as a function of temperature. At T = 5 K, we extract a prolonged decay time of τ_0 = 1.56 ± 0.13 μs, which is notably 65% longer than the previously reported 0.94 μs decay time [30] and is much closer to the expected lifetime between 2 to 10 μs [396]. As the temperature increases, τ_0 decreases to 26 ± 0.24 ns at T = 40 K, coinciding with the point where TX_0 emission nearly vanishes. Importantly, we observe the carrier transition lifetime of τ_f = 11 ± 0.3 ns at T = 5 and 10 K, contributing to the slow rising of TRPL traces and suddenly becoming slower with τ_f = 50 ± 0.3 ns at T = 30 K. The observed 11 ns carrier transition and the resulting slow PL rising only observed for TX_0 below T = 10 K can be attributed to a much more localized nature of TX_0 states. τ_f is three orders of magnitude faster than the decay of TX_0, indicating a strong coupling between the localized TX_0 and delocalized higher excited states.

Given that the pump power is fixed for TRPL measurement across all temperatures, the ratio of the initial occupation of TX_0 states to its total amount of available states $n_0(0)/N_0$, experiences

a sudden increase at T = 30 K. It indicates the onset of thermal dissociation of TX_0 bound exciton. Note that, due to the much slower temporary features of the PL, the timing resolution of the detector (approximately 400 ps) is negligible in the fit. We also perform the rate equation fitting by setting $n_{ex} = n_1$, where n_1 denotes the TX_1 carrier population, however, simultaneous fitting of $TX_1$and TX_0 PL decay could not be achieved. It agrees with the hypothesis that the non-radiative carrier transition is dominated by higher excited states. It is also consistent with our experimental setup using the above-silicon-bandgap excitation. The coupling between TX_1 and TX_0 states could be a much faster process that can only be investigated by resonantly pumping the TX_1 state. Fig 5.12(c) shows the temperature dependent TRPL of *Cu emissions. Due to the small 0.56 meV-splitting and experimental limitations, both $^{*}Cu^{0}_{0}$ and $^{*}Cu^{0}_{1}$ emissions are measured together with a spectral window spanning 1309 to 1316 nm. In the presence of increased lattice distortion (larger deviation of dashed model lines from the temperature-dependent fit of measured $^{*}Cu^{m}_{n}$ data from Si lattice in Fig 5.8), the decay of *Cu occurs at a faster rate, with an excited state lifetime τ_0 of 52.4 ± 4.8 ns at T = 6.7 K. We observe an increase in the fitted lifetime at higher temperatures, to 71.2 ± 2.1 ns at T = 30 K, due to the population transfer from $^{*}Cu^{0}_{0}$ to $^{*}Cu^{0}_{1}$ and higher excited states with slower decay rates. To delve deeper into the T center bound exciton recombination dynamics, we consider both radiative (Γ_r) and nonradiative (Γ_{nr}) recombination channels contributing to the μPL decay rate. The time-integrated μPL intensity (I) of TX_0 and TX_1 at temperature T is proportional to the quantum efficiency, given by $I(T) \propto \frac{\Gamma_r}{\Gamma_r+\Gamma_{nr}}$. Assuming that the radiative decay dominates the bound exciton recombination channel at T = 0 K, then I can be expressed as:

$$I(T) = I(0)\frac{\Gamma_r}{\Gamma_r+\Gamma_{nr}} = I(0)\frac{\Gamma_r}{\Gamma_{tot}}. \quad (5.6)$$

Here, $I(0)$ is extrapolated from Fig 5.10(a), and Γ_{tot} is the total decay rate extracted from the rate equation fit of TX_0 or the single exponential fit of TX_1. Then, the radiative recombination rate can be obtained from Eq. (5.6). The resulting μPL dynamical parameters of TX_0 and TX_1 as a function of temperature are plotted in Fig 5.12(d). The inverse of the μPL decay time of TX_1 (τ_1 = 0.60 ± 0.063 μs) is nearly twice of TX_0 at T = 5 K and shows a sudden increase after T = 30 K, consistent with TX_0 behavior. The extracted radiative and nonradiative bound exciton recombination rates of TX_0 and TX_1, along with the experimental error bars, are shown as black and red symbols. Compared with the non-radiative rate, the radiative rate of both TX_0 (black circle) and TX_1 (red circle) remains relatively constant at approximately 1.5 μs^{-1} and 3.6 μs^{-1} respectively, corresponding to a Fourier-transform limited linewidth of approximately 0.494 neV and 1.19 neV. The relatively temperature-independent radiative rates (below 30 K) suggest potentially the suppression of thermally induced fluctuation of the bound exciton wavefunction along any direction due to the three-dimensional quantum confinement [397]. A higher excited state (TX_1) is anticipated to be more delocalized, indicated by a larger TX_1 radiative rate. The slight increase in both TX_0 and TX_1 radiative rates with increasing temperature can be attributed to the thermal-induced delocalization of the bound exciton wavefunctions. Above T = 30 K, the dominance of fast non-radiative decay in both TX_0 and TX_1 recombination channels may stem from the thermal disassociation of bound excitons, or the Shockley-Read-Hall (SRH) process induced by unwanted impurities or vacancies in natural Si. This results in the quenching of the T center emission intensity above 30 K. On the other hand, the radiative decay of combined $^*Cu^m_n$ emissions show an anomalous behavior, decreasinng with increased temperature from 18.76 μs^{-1} at 6.7 K to 6.13 μs^{-1} at 30 K, while the non-radiative recombination rate increase to 7.88 μs^{-1}, becoming the

dominant decay channel. This counterintuitive phenomenon is attributed to the difference in decay rates and multiple phonon-assisted decay pathways (phonon replicas). It is speculated that the decay of decay is faster $^{*}Cu^{0}_{0}$ than $^{*}Cu^{0}_{1}$, with the latter becoming dominant due to the population transfer at higher temperatures, as indicated by the plateau in the $^{*}Cu^{0}_{1}$ observed in Fig 5.10(a). After 30 K, the radiative decay of both $^{*}Cu^{0}_{0}$ and $^{*}Cu^{0}_{1}$ is thermalized by non-radiative and phonon-assisted decay through $^{*}Cu^{n}_{1}$ states, which fall outside the spectral window of TRPL.

5.6 Magnetic-Field Induced Broadening in the Ensemble $^{*}Cu^{m}_{n}$ Color Centers

The T center bound exciton pairs with its ground state electron, which has a spin with an isotropic g-factor of g_E = 2.0005, forming a singlet state with an unpaired hole spin with an anisotropic g-factor in TX_0 state [382]. Under a magnetic field, the unpaired hole spin leads to Zeeman splitting and diamagnetic shifts. The anisotropic hole spin leads to different g-factors and diamagnetic shift coefficients based on the orientation of the defect in the lattice [30]. The total shift (ΔE) in the peak energy for spin-dependent lines can be expressed as

$$\Delta E = (\pm g_e \pm g_h)\mu_B B_z + \chi |B_z|^2. \quad (5.7)$$

Here, g_e and g_h represent the g-factors for electron and holes, μ_B is the Bohr magneton, χ is the diamagnetic shift due to higher-order Zeeman effect, and B_z is the applied magnetic field [398]. The splitting is crucial for establishing a spin-photon interface, a fundamental component in quantum memory applications. For this purpose, we examined the 0.56 meV-split $^{*}Cu$ doublet luminescence centers under a magnetic field to examine their potential.

For ensemble defects, each hole spins in a singlet state have a different g-factor due to their different orientations in the lattice, leading to an additional inhomogeneous broadening of the PL spectrum when subjected to a magnetic field along with the lifetime broadening, thermal broadening, and the spectral diffusion between individual defect emissions. The resulting

amplitude (A) of the spin-polarized photoluminescence adheres a Voigt-like profile that accounts for these effects, as expressed as the below [382], [398]:

$$\mathrm{A}(B_z, \Delta_f) = \int_{-\infty}^{\infty} \left(\frac{1}{\sigma_G \sqrt{2\pi}} e^{-\Delta_f / 2\sigma_G^2} \right) \times \frac{\sigma_L / 2\pi}{(\sigma_L/2)^2 + (\Delta_f - \varepsilon_{eff}|B_z|)^2} d\Delta_F. \tag{5.8}$$

Here, Δ_f is the detuning, σ_G and σ_L are the Gaussian-broadened and homogeneous linewidths, respectively. ε_{eff} is the effective average Zeeman factor dependent on the hole g-factor variations. This leads to an approximate Voigt linewidth (Γ) [382]:

$$\Gamma = \sqrt{(\Gamma_{B=0})^2 + (\varepsilon_{eff}|B_z|)^2} \tag{5.9}$$

To investigate the potential for a spin-photon interface, we conduct magneto-PL measurements of the magnetic-field-induced broadening of the 0.56 meV-split doublet emission under an out-of-plane DC magnetic field, ranging from 0 mT to 500 mT at T = 4.5 K. Instrumental limitations, and the broadening induced by the natural-Si substrate does not allow us to distinguish the spin-degeneracy-lifted transitions within the ensemble fully, but Fig 5.14(a) shows the magnetic field-induced broadening of the ensemble $^{*}\mathrm{Cu}^{m}_{n}$ color center transitions. At 4.5 K and 0 mT, the intrinsic Voigt linewidth is measured as 229 μeV for $^{*}\mathrm{Cu}^{0}_{0}$ line and 235.9 μeV for $^{*}\mathrm{Cu}^{0}_{1}$ line. While there is not a significant broadening observed for the $^{*}\mathrm{Cu}^{0}_{1}$ line, a notable linewidth broadening is observed for the $^{*}\mathrm{Cu}^{0}_{0}$ state, by 25% to 290 μeV. This linewidth broadening is much larger than the instrument resolution. Using Eq. (5.9), we extract the effective Zeeman factor ε_{eff} to be 364 μeV/T for the $^{*}\mathrm{Cu}^{0}_{0}$ state transition. Assuming similarity to T centers, we anticipate the involvement of an unpaired hole-spin interacting with the ground-state electron within the first-excited transition

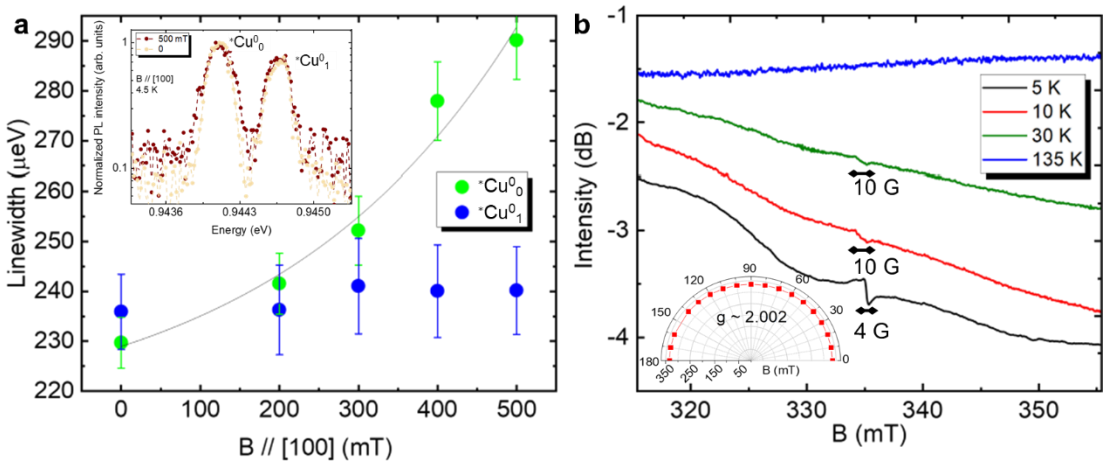

FIG 5.14 | Magnetic-field induced broadening in the ensemble of 0.56 meV-split doublet luminescence centers. (a) The Voigt-profile linewidth of $^{*}Cu^{0}_{0}$ and $^{*}Cu^{0}_{1}$ lines under DC magnetic field with intensity up to 500 mT. Compared to the zero-field linewidth of 230 μeV, we observe an increase in inhomogeneous linewidth of the $^{*}Cu^{0}_{0}$ line by 25% at 500 mT, while there is not a significant broadening in the $^{*}Cu^{0}_{1}$ line. Inset: PL spectrum of $^{*}Cu^{0}_{0}$ and $^{*}Cu^{0}_{1}$ lines as a function of DC magnetic field from 0 to 500 mT. The linewidth of the $^{*}Cu^{0}_{0}$ line is fitted using a hyperbolic equation to determine the mean Zeeman factor as 364 $\mu eV/T$. **(b)** Temperature-dependent electron spin resonance measurements reveals a spin resonance at 335 mT, leading to an isotropic g-factor around 2.002, consistent with an isotropic triplet state [381]. Inset: Goniometric electron spin resonance spectrum to determine isotropy of the spin states. Fig 5.14 is published in [218].

of the $^{*}Cu^{0}_{0}$ line. Further electron spin resonance (ESR) analysis (Fig 5.14(b)) reveals that the ensembles $^{*}Cu^{0}_{0}$ and $^{*}Cu^{0}_{1}$ defects form a lambda-type spin-photon interface. The degenerate ground level exhibits a split with an isotropic *g*-factor of 2.002 and a Lorentzian broadening of 4 G, consistent with earlier observations of the isotropic triplet nature of the $^{*}Cu^{0}_{0}$ peak [381]. The ESR resonance signal around 335 mT exhibits a Gaussian-like broadening of 10 G above 10 K, disappearing completely above 30 K, aligning with the thermalization of the $^{*}Cu^{n}_{m}$ PL emissions.

This further supports that the magnetic-field induced broadening in Fig 5.14(a) is attrubted to the spin degeneracy of *Cu state.

5.7 Discussions

In this chapter, we have examined the sequential process steps leading to the formation of $^{*}Cu^{m}_{n}$ and T center. During the T center formation process, we observe the presence of well-known G and W centers following the low-dose carbon implantation. Subsequently, upon annealing at 1000 °C, the G and W centers disappear, giving way to a doublet peak at 1312.15 nm ascribed as the $^{*}Cu^{0}_{0}$ and $^{*}Cu^{0}_{1}$ peaks, which are isoelectronic bound exciton emissions similar to T centers and originating from a Cu-Ag transition-metal color center. These optical transitions are present in the spectra of carbon implanted and annealed samples alongside the perturbed Cu-line phonon replicas. The Cu-line replicas between 1221.45 nm to 1238.64 nm, exhibiting a 7 meV phonon energy, confirm the predictions of the high electron-phonon coupling in W-centers. Furthermore, we observe that the doublet $^{*}Cu^{m}_{n}$ optical transitions persist alongside TX_0 and TX_1 if the H_2O treatment is omitted and only RTA is applied to the sample. This doublet emission holds the potential for a novel spin-photon interface at the O-band, and its magneto-optic properties are worth further investigated. We examine and compare the TX_0 and TX_1 with $^{*}Cu^{0}_{0}$ and $^{*}Cu^{0}_{1}$ transitions, unrevealing their origins. The temperature-tuned μPL measurement show that the $^{*}Cu^{0}_{0}$ and $^{*}Cu^{0}_{1}$ peaks result from transitions between lower and higher excited states, respectively, of the same color centers whose formation induces a more significant perturbation to the silicon lattice, compared to the less perturbative T centers, aligning with the presence of the W-line phonon replicas. Moreover, we estimate a much smaller exciton binding energy associated with this novel defect, as low as 3.35 meV.

Building upon the described process, we examine the bound exciton dynamics of the generated $^{*}Cu^{m}_{n}$ and T color centers. With TRPL measurements, we determine the radiative lifetimes of the $^{*}Cu^{m}_{n}$ transition to be 52.4 ± 4.8 ns. While for the T center, it is measured to be 1.56 ± 0.13 μs, representing a 65% increase compared to earlier studies [30]. The gradual introduction of H atoms through H2O treatment in our approach aims to create a sample predominantly occupied by defects such as T centers, minimizing the presence of other defects. This reduction in potential non-radiative decoherence pathways, as evidenced by the extended lifetime, is crucial for achieving high-fidelity network nodes. Simultaneously, cQED interactions can enhance the coherent emission rates of photonic qubit. Our experimental results are verified through fitting the rate equation model between TX0 and higher excited states, revealing a slow carrier transition between TX1 and TX0, corresponding to the observed early-time slow-rising dynamics in our measured

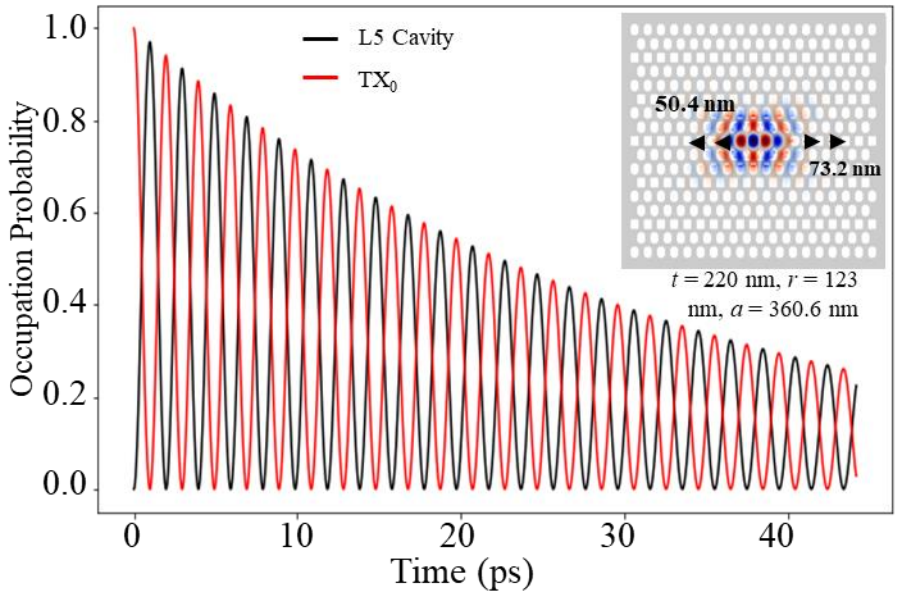

FIG 5.15 | Time evolution of occupation probability of TX0 exciton and photon in the strong coupling regime. Inset: L5 PhC cavity with membrane thickness (t), air hole radii (r), and lattice constant (a) to be 220, 123, and 360.6 nm, respectively. The first and third lateral hole are shifted by 50.4 nm and 73.2 nm, respectively. Fig 5.15 is published in [21].

TRPL histograms. Additionally, we extracted the radiative and non-radiative recombination rates of the 3D confined T-center bound excitons.

For the prospective coherent control of TX_0 state of T centers, an *L*5 PhC cavity is proposed with parameters: air hole radii (r) of 123 nm, lattice constant (a) of 360.6 nm, and thickness (t) of 220 nm, as illustrated in the inset of Fig 5.15. The first lateral holes on each side of the *L*5 cavity are shifted by 73.2 nm and the third lateral holes are shifted by 50.4 nm for Gaussian mode optimizations. This design results in an intrinsic cavity *Q*-factor of ~ 1.5×10^5 and a mode volume of ~ $1.4(\lambda/n)^3$. Using Lindblad master equations, the calculated Rabi frequency is determined to be 15.9 GHz. Considering the potential formation of 250 T centers within the *L*5 cavity, the time-evolution of the occupation probability of the exciton and photon is shown in Fig 5.15, with an ensemble Rabi frequency of 50 × 15.9 GHz. This indicates the feasibility of coherent control through strong coupling.

The observed and improved T center lifetimes contribute to the development of novel O-band quantum network nodes with high fidelity, involving cQED of the spin-photon interface for controlling and routing the photons [28], [370]. The $^{*}Cu^{m}_{n}$ doublet peak around 1312.15 nm provides a unique platform positioned at the zero-dispersion wavelengths within the O-band for qubit interactions. The determined radiative lifetimes of excited-state radiative, along with magneto-optic and ESR measurements support the application of these novel silicon color centers towards solid-state quantum memories in scalable and metropolitan quantum networks.

The optical properties of the relatively mature InGaAs QD system and recent rapidly developing silicon T centers are summarized in Table 5.1. InGaAs QD system still offers unmatched properties, including near unity quantum efficiency, large dipole moment, narrow homogeneous linewidth, high single photon purity, and high photon indistinguishability [9], [112],

[113] essential for quantum key distribution, quantum teleportation, multiphoton entanglement, and linear optical quantum computing. Especially, the site-controlled pyramidal InGaAs QD system provides an ideal platform for chip-scale cavity quantum electrodynamics for quantum information processing. However, InGaAs QD is still restricted by emission wavelength range of 850 - 1000 nm which needs to be frequency-converted to telecom band for long range quantum applications. It is also restricted by the relatively short spin coherence time due to coupling to the solid-state environment, therefore it may not be suitable for quantum information storage. On the other hand, silicon T centers host by isotopically pure ^{28}Si (magnetic noise free), although do not exhibit an optical performance compared to InGaAs QD, have recently caught people's eye due to their O-band optical transition, mature silicon integrated photonics and electronics platform, and long-lived electron/nuclear spin coherence suitable for efficient quantum memory, telecom spin-photon interface, microwave-to-optical telecom transduction, and fiber-based quantum networks that the InGaAs QDs currently cannot offer. Integrating T centers in photonic structures has been rapidly developing in recent years. However, its relatively small dipole moment may prevent the strong coupling regime from being observed. More importantly, site-controllability, which is achieved using pyramidal InGaAs QD, essential for enabling stronger light-matter interactions and scalable device application, is still lacking for silicon color centers and needs to be further

	Wavelength range	Optical lifetime	Homogeneous linewidth	Dipole moment	Quantum efficiency	$g^2(0)$	Indistinguishability	Electron spin lifetime T1	Electron spin coherence time T2	Nuclear spin coherence time T2	Site-control	Applications
InGaAs QDs	~ 850 nm – 1000 nm	~ 1 ns	~ 0.3 GHz [115]	~ 30 - 90 D [316]	Near unity [117]	~ 0.02 [116]	98% [116]	N/A	~ μs [428]	10 μs [429]	Yes (*inherently*)	High-rate quantum key distribution, quantum teleportation, multiphoton entanglement distribution, linear optical quantum computing, etc.
Silicon T centers	~ 1326 nm	~ 940 ns [30]	33 MHz (ensemble) [30] 1 GHz (single) [31]	1.52 D [30]	91% [31]	~ 0.2 [31]	60% [31]	~ hrs [30]	2.1 ms [30]	1.1 s [30]	Developing (Micropucks, FIB, etc.)	Quantum repeater, quantum memory, quantum transduction, metro-scale quantum networks, etc.

Table 5.1 | Comparison of quantum properties of InGaAs QDs and silicon T centers. The properties of InGaAs QD are based on ref [9], [113], [316], [399], [400]. And the properties of T centers are based on ref [30], [31].

developed. For quantum photonic applications, it is worth noting that the site controllability achieved by placing the emitter in a "position", such as using focused ion beam (FIB), may sometimes lead to inadvertent defect environment that would deteriorate the optical properties of the emitter. For silicon color centers, it is then important to develop its site controllability in an *inherently* way. Pyramidal QDs is an example of an *inherently* site-controlled quantum emitter.

Reference

[1] He, Y., He, Y. M., Wei, Y. J., Jiang, X., Chen, M. C., Xiong, F. L., Zhao, Y., Schneider, C., Kamp, M., Höfling, S., Lu, C. Y. & Pan, J. W. Indistinguishable Tunable Single Photons Emitted by Spin-Flip Raman Transitions in InGaAs Quantum Dots. *Phys Rev Lett* **111,** 237403 (2013).

[2] Somaschi, N., Giesz, V., De Santis, L., Loredo, J. C., Almeida, M. P., Hornecker, G., Portalupi, S. L., Grange, T., Antón, C., Demory, J., Gómez, C., Sagnes, I., Lanzillotti-Kimura, N. D., Lemaítre, A., Auffeves, A., White, A. G., Lanco, L. & Senellart, P. Near-Optimal Single-Photon Sources in the Solid State. *Nat Photonics* **10,** 340–345 (2016).

[3] Gazzano, O., Michaelis de Vasconcellos, S., Arnold, C., Nowak, A., Galopin, E., Sagnes, I., Lanco, L., Lemaître, A. & Senellart, P. Bright Solid-State Sources of Indistinguishable Single Photons. *Nat Commun* **4,** 1425 (2013).

[4] Santori, C., Fattal, D., Vučković, J., Solomon, G. S. & Yamamoto, Y. Indistinguishable Photons from a Single-Photon Device. *Nature* **419,** 594–597 (2002).

[5] Ollivier, H., Maillette de Buy Wenniger, I., Thomas, S., Wein, S. C., Harouri, A., Coppola, G., Hilaire, P., Millet, C., Lemaître, A., Sagnes, I., Krebs, O., Lanco, L., Loredo, J. C., Antón, C., Somaschi, N. & Senellart, P. Reproducibility of High-Performance Quantum Dot Single-Photon Sources. *ACS Photonics* **7,** 1050–1059 (2020).

[6] Huber, D., Reindl, M., Huo, Y., Huang, H., Wildmann, J. S., Schmidt, O. G., Rastelli, A. & Trotta, R. Highly Indistinguishable and Strongly Entangled Photons from Symmetric GaAs Quantum Dots. *Nat Commun* **8,** 15506 (2017).

[7] Mäntynen, H., Anttu, N., Sun, Z. & Lipsanen, H. Single-Photon Sources with Quantum Dots in III–V Nanowires. *Nanophotonics* **8,** 747–769 (2019).

[8] He, Y.-M., He, Y., Wei, Y.-J., Wu, D., Atatüre, M., Schneider, C., Höfling, S., Kamp, M., Lu, C.-Y. & Pan, J.-W. On-Demand Semiconductor Single-Photon Source with near-Unity Indistinguishability. *Nat Nanotechnol* **8,** 213–217 (2013).

[9] Senellart, P., Solomon, G. & White, A. High-Performance Semiconductor Quantum-Dot Single-Photon Sources. *Nat Nanotechnol* **12,** 1026–1039 (2017).

[10] Tchernij, S. D., Herzig, T., Forneris, J., Küpper, J., Pezzagna, S., Traina, P., Moreva, E., Degiovanni, I. P., Brida, G., Skukan, N., Genovese, M., Jakšić, M., Meijer, J. & Olivero, P. Single-Photon-Emitting Optical Centers in Diamond Fabricated upon Sn Implantation. *ACS Photonics* **4,** 2580–2586 (2017).

[11] Ditalia Tchernij, S., Lühmann, T., Herzig, T., Küpper, J., Damin, A., Santonocito, S., Signorile, M., Traina, P., Moreva, E., Celegato, F., Pezzagna, S., Degiovanni, I. P., Olivero, P., Jakšić, M., Meijer, J., Genovese, P. M. & Forneris, J. Single-Photon Emitters in Lead-Implanted Single-Crystal Diamond. *ACS Photonics* **5,** 4864–4871 (2018).

[12] Corte, E., Andrini, G., Nieto Hernández, E., Pugliese, V., Costa, Â., Magchiels, G., Moens, J., Tunhuma, S. M., Villarreal, R., Pereira, L. M. C., Vantomme, A., Correia, J. G., Bernardi, E., Traina, P., Degiovanni, I. Pietro, Moreva, E., Genovese, M., Ditalia Tchernij, S., Olivero, P., Wahl, U. & Forneris, J. Magnesium-Vacancy Optical Centers in Diamond. *ACS Photonics* **10,** 101–110 (2023).

[13] Leifgen, M., Schröder, T., Gädeke, F., Riemann, R., Métillon, V., Neu, E., Hepp, C., Arend, C., Becher, C., Lauritsen, K. & Benson, O. Evaluation of Nitrogen- and Silicon-Vacancy Defect Centres as Single Photon Sources in Quantum Key Distribution. *New J Phys* **16,** 023021 (2014).

[14] Knall, E. N., Knaut, C. M., Bekenstein, R., Assumpcao, D. R., Stroganov, P. L., Gong, W., Huan, Y. Q., Stas, P.-J., Machielse, B., Chalupnik, M., Levonian, D., Suleymanzade, A., Riedinger, R., Park, H., Lončar, M., Bhaskar, M. K. & Lukin, M. D. Efficient Source of Shaped Single Photons Based on an Integrated Diamond Nanophotonic System. *Phys Rev Lett* **129,** 053603 (2022).

[15] Fedyanin, D. Y. & Agio, M. Ultrabright Single-Photon Source on Diamond with Electrical Pumping at Room and High Temperatures. *New J Phys* **18,** 073012 (2016).

[16] Pezzagna, S., Rogalla, D., Wildanger, D., Meijer, J. & Zaitsev, A. Creation and Nature of Optical Centres in Diamond for Single-Photon Emission—Overview and Critical Remarks. *New J Phys* **13,** 035024 (2011).

[17] Simpson, D. A., Ampem-Lassen, E., Gibson, B. C., Trpkovski, S., Hossain, F. M., Huntington, S. T., Greentree, A. D., Hollenberg, L. C. L. & Prawer, S. A Highly Efficient Two Level Diamond Based Single Photon Source. *Appl Phys Lett* **94,** (2009).

[18] Schröder, T., Schell, A. W., Kewes, G., Aichele, T. & Benson, O. Fiber-Integrated Diamond-Based Single Photon Source. *Nano Lett* **11,** 198–202 (2011).

[19] Mizuochi, N., Makino, T., Kato, H., Takeuchi, D., Ogura, M., Okushi, H., Nothaft, M., Neumann, P., Gali, A., Jelezko, F., Wrachtrup, J. & Yamasaki, S. Electrically Driven Single-Photon Source at Room Temperature in Diamond. *Nat Photonics* **6,** 299–303 (2012).

[20] Babinec, T. M., Hausmann, B. J. M., Khan, M., Zhang, Y., Maze, J. R., Hemmer, P. R. & Lončar, M. A Diamond Nanowire Single-Photon Source. *Nat Nanotechnol* **5,** 195–199 (2010).

[21] Huang, J., Sarihan, M. C., Kang, J. H., Liang, B., Liu, W. & Wong, C. W. Cryogenic Optical Transitions of T Centers in Bulk Silicon and Silicon-on-Insulator for Cavi Ty Quantum Electrodynamics. *Frontiers in Optics + Laser Science 2021 (2021), paper JTu7A.2* JTu7A.2 (2021). doi:10.1364/FIO.2021.JTU7A.2

[22] Saggio, V., Errando-Herranz, C., Gyger, S., Panuski, C., Prabhu, M., De Santis, L., Christen, I., Ornelas-Huerta, D., Raniwala, H., Gerlach, C., Colangelo, M. & Englund, D. Cavity-Enhanced Single Artificial Atoms in Silicon. (2023). at <https://arxiv.org/abs/2302.10230v1>

[23] Lefaucher, B., Jager, J. B., Calvo, V., Durand, A., Baron, Y., Cache, F., Jacques, V., Robert-Philip, I., Cassabois, G., Herzig, T., Meijer, J., Pezzagna, S., Khoury, M., Abbarchi, M., Dréau, A. & Gérard, J. M. Cavity-Enhanced Zero-Phonon Emission from an Ensemble of G Centers in a Silicon-on-Insulator Microring. *Appl Phys Lett* **122,** 61109 (2023).

[24] DeAbreu, A., Bowness, C., Alizadeh, A., Chartrand, C., Brunelle, N. A., MacQuarrie, E. R., Lee-Hone, N. R., Ruether, M., Kazemi, M., Kurkjian, A. T. K., Roorda, S., Abrosimov, N. V., Pohl, H.-J., Thewalt, M. L. W., Higginbottom, D. B. & Simmons, S. Waveguide-Integrated Silicon T Centres. *Opt Express* **31,** 15045 (2023).

[25] Liu, W., Ivanov, V., Jhuria, K., Ji, Q., Persaud, A., Redjem, W., Simoni, J., Zhiyenbayev, Y., Kante, B., Lopez, J. G., Tan, L. Z. & Schenkel, T. Quantum Emitter Formation Dynamics and Probing of Radiation-Induced Atomic Disorder in Silicon. *Phys Rev Appl* **20,** 014058 (2023).

[26] Xiong, Y., Bourgois, C., Sheremetyeva, N., Chen, W., Dahliah, D., Song, H., Zheng, J., Griffin, S. M., Sipahigil, A. & Hautier, G. High-Throughput Identification of Spin-Photon Interfaces in Silicon. *Sci Adv* **9,** eadh8617 (2023).

[27] Beaufils, C., Redjem, W., Rousseau, E., Jacques, V., Kuznetsov, A. Yu., Raynaud, C., Voisin, C., Benali, A., Herzig, T., Pezzagna, S., Meijer, J., Abbarchi, M. & Cassabois, G. Optical Properties of an Ensemble of G-Centers in Silicon. *Phys Rev B* **97,** 035303 (2018).

[28] Redjem, W., Zhiyenbayev, Y., Qarony, W., Ivanov, V., Papapanos, C., Liu, W., Jhuria, K., Al Balushi, Z. Y., Dhuey, S., Schwartzberg, A., Tan, L. Z., Schenkel, T. & Kanté, B. All-Silicon Quantum Light Source by Embedding an Atomic Emissive Center in a Nanophotonic Cavity. *Nat Commun* **14,** 3321 (2023).

[29] Deabreu, A., Bowness, C., Abraham, R. J. S., Medvedova, A., Morse, K. J., Riemann, H., Abrosimov, N. V., Becker, P., Pohl, H. J., Thewalt, M. L. W. & Simmons, S. Characterization of the Si: Se+ Spin-Photon Interface. *Phys Rev Appl* **11,** 044036 (2019).

[30] Bergeron, L., Chartrand, C., Kurkjian, A. T. K., Morse, K. J., Riemann, H., Abrosimov, N. V., Becker, P., Pohl, H. J., Thewalt, M. L. W. & Simmons, S. Silicon-Integrated Telecommunications Photon-Spin Interface. *PRX Quantum* **1,** 020301 (2020).

[31] Higginbottom, D. B., Kurkjian, A. T. K., Chartrand, C., Kazemi, M., Brunelle, N. A., MacQuarrie, E. R., Klein, J. R., Lee-Hone, N. R., Stacho, J., Ruether, M., Bowness, C., Bergeron, L., DeAbreu, A., Harrigan, S. R., Kanaganayagam, J., Marsden, D. W., Richards, T. S., Stott, L. A., Roorda, S., Morse, K. J., Thewalt, M. L. W. & Simmons, S. Optical Observation of Single Spins in Silicon. *Nature 2022 607:7918* **607,** 266–270 (2022).

[32] Castelletto, S., Johnson, B. C., Ivády, V., Stavrias, N., Umeda, T., Gali, A. & Ohshima, T. A Silicon Carbide Room-Temperature Single-Photon Source. *Nat Mater* **13,** (2014).

[33] Lohrmann, A., Johnson, B. C., McCallum, J. C. & Castelletto, S. A Review on Single Photon Sources in Silicon Carbide. *Reports on Progress in Physics* **80,** (2017).

[34] Castelletto, S. Silicon Carbide Single-Photon Sources: Challenges and Prospects. *Materials for Quantum Technology* **1,** (2021).

[35] Wang, J., Zhou, Y., Wang, Z., Rasmita, A., Yang, J., Li, X., von Bardeleben, H. J. & Gao, W. Bright Room Temperature Single Photon Source at Telecom Range in Cubic Silicon Carbide. *Nat Commun* **9,** (2018).

[36] Fuchs, F., Soltamov, V. A., Väth, S., Baranov, P. G., Mokhov, E. N., Astakhov, G. V. & Dyakonov, V. Silicon Carbide Light-Emitting Diode as a Prospective Room Temperature Source for Single Photons. *Sci Rep* **3,** (2013).

[37] Lienhard, B., Schröder, T., Mouradian, S., Dolde, F., Tran, T. T., Aharonovich, I. & Englund, D. Bright and Photostable Single-Photon Emitter in Silicon Carbide. *Optica* **3,** (2016).

[38] Fuchs, F., Stender, B., Trupke, M., Simin, D., Pflaum, J., Dyakonov, V. & Astakhov, G. V. Engineering Near-Infrared Single-Photon Emitters with Optically Active Spins in Ultrapure Silicon Carbide. *Nat Commun* **6,** (2015).

[39] Radulaski, M., Widmann, M., Niethammer, M., Zhang, J. L., Lee, S. Y., Rendler, T., Lagoudakis, K. G., Son, N. T., Janzén, E., Ohshima, T., Wrachtrup, J. & Vučković, J. Scalable Quantum Photonics with Single Color Centers in Silicon Carbide. *Nano Lett* **17,** (2017).

[40] Zhao, H., Pettes, M. T., Zheng, Y. & Htoon, H. Site-Controlled Telecom-Wavelength Single-Photon Emitters in Atomically-Thin MoTe2. *Nat Commun* **12,** (2021).

[41] Luo, Y., Liu, N., Li, X., Hone, J. C. & Strauf, S. Single Photon Emission in WSe2 up 160 K by Quantum Yield Control. *2d Mater* **6,** (2019).

[42] Parto, K., Azzam, S. I., Banerjee, K. & Moody, G. Defect and Strain Engineering of Monolayer WSe2 Enables Site-Controlled Single-Photon Emission up to 150 K. *Nat Commun* **12,** (2021).

[43] Koperski, M., Nogajewski, K., Arora, A., Cherkez, V., Mallet, P., Veuillen, J. Y., Marcus, J., Kossacki, P. & Potemski, M. Single Photon Emitters in Exfoliated WSe2 Structures. *Nat Nanotechnol* **10,** (2015).

[44] Lyu, C., Zhu, Y., Gu, P., Qiao, J., Watanabe, K., Taniguchi, T. & Ye, Y. Single-Photon Emission from Two-Dimensional Hexagonal Boron Nitride Annealed in a Carbon-Rich Environment. *Appl Phys Lett* **117,** (2020).

[45] Iff, O., Tedeschi, D., Martín-Sánchez, J., Moczała-Dusanowska, M., Tongay, S., Yumigeta, K., Taboada-Gutiérrez, J., Savaresi, M., Rastelli, A., Alonso-González, P., Höfling, S., Trotta, R. & Schneider, C. Strain-Tunable Single Photon Sources in WSe2 Monolayers. *Nano Lett* **19,** (2019).

[46] Gupta, S., Wu, W., Huang, S. & Yakobson, B. I. Single-Photon Emission from Two-Dimensional Materials, to a Brighter Future. *Journal of Physical Chemistry Letters* **14,** (2023).

[47] Salomone, M., Re Fiorentin, M., Cicero, G. & Risplendi, F. Point Defects in Two-Dimensional Indium Selenide as Tunable Single-Photon Sources. *Journal of Physical Chemistry Letters* **12,** (2021).

[48] Zhou, X., Zhang, Z. & Guo, W. Dislocations as Single Photon Sources in Two-Dimensional Semiconductors. *Nano Lett* **20,** (2020).

[49] Kawabe, R., Takaki, H., Ibi, T., Maeda, Y., Nakagawa, K. & Maki, H. Pure and Efficient Single-Photon Sources by Shortening and Functionalizing Air-Suspended Carbon Nanotubes. *ACS Appl Nano Mater* **3,** (2020).

[50] Gifford, B. J., Kilina, S., Htoon, H., Doorn, S. K. & Tretiak, S. Controlling Defect-State Photophysics in Covalently Functionalized Single-Walled Carbon Nanotubes. *Acc Chem Res* **53,** (2020).

[51] Jeantet, A., Chassagneux, Y., Raynaud, C., Roussignol, Ph., Lauret, J. S., Besga, B., Estève, J., Reichel, J. & Voisin, C. Widely Tunable Single-Photon Source from a Carbon Nanotube in the Purcell Regime. *Phys Rev Lett* **116,** 247402 (2016).

[52] Ma, X., Hartmann, N. F., Baldwin, J. K. S., Doorn, S. K. & Htoon, H. Room-Temperature Single-Photon Generation from Solitary Dopants of Carbon Nanotubes. *Nat Nanotechnol* **10,** (2015).

[53] He, X., Htoon, H., Doorn, S. K., Pernice, W. H. P., Pyatkov, F., Krupke, R., Jeantet, A., Chassagneux, Y. & Voisin, C. Carbon Nanotubes as Emerging Quantum-Light Sources. *Nat Mater* **17,** (2018).

[54] Gong, Q. & Hu, X. *Photonic crystals: Principles and applications*. *Photonic Crystals: Principles and Applications* (2013). doi:10.4032/9789814364836

[55] Lalanne, P., Sauvan, C. & Hugonin, J. P. Photon Confinement in Photonic Crystal Nanocavities. *Laser Photon Rev* **2,** (2008).

[56] Englund, D., Fushman, I. & Vučković, J. General Recipe for Designing Photonic Crystal Cavities. *Opt Express* **13,** (2005).

[57] Akahane, Y., Asano, T., Song, B. S. & Noda, S. High-Q Photonic Nanocavity in a Two-Dimensional Photonic Crystal. *Nature* **425,** (2003).

[58] Joannopoulos, J. D., Johnson, S. G., Winn, J. N. & Meade, R. D. *Photonic crystals: Molding the flow of light*. *Photonic Crystals: Molding the Flow of Light (Second Edition)* (2011).

[59] Lai, Y., Pirotta, S., Urbinati, G., Gerace, D., Minkov, M., Savona, V., Badolato, A. & Galli, M. Genetically Designed L3 Photonic Crystal Nanocavities with Measured Quality Factor Exceeding One Million. *Appl Phys Lett* **104,** 241101 (2014).

[60] Prtljaga, N., Bentham, C., O'Hara, J., Royall, B., Clarke, E., Wilson, L. R., Skolnick, M. S. & Fox, A. M. On-Chip Interference of Single Photons from an Embedded Quantum Dot and an External Laser. *Appl Phys Lett* **108,** 251101 (2016).

[61] Purcell, E. M. in (1995). doi:10.1007/978-1-4615-1963-8_40

[62] Reithmaier, J. P., Sęk, G., Löffler, A., Hofmann, C., Kuhn, S., Reitzenstein, S., Keldysh, L. V., Kulakovskii, V. D., Reinecke, T. L. & Forchel, A. Strong Coupling in a Single Quantum Dot–Semiconductor Microcavity System. *Nature* **432,** 197–200 (2004).

[63] Hennessy, K., Badolato, A., Winger, M., Gerace, D., Atature, M., Gulde, S., Falt, S., Hu, E. L. & Imamoglu, A. Quantum Nature of a Strongly-Coupled Single Quantum Dot-Cavity System. *Nature* **445,** 896–899 (2006).

[64] Sprengers, J. P., Gaggero, A., Sahin, D., Jahanmirinejad, S., Frucci, G., Mattioli, F., Leoni, R., Beetz, J., Lermer, M., Kamp, M., Hfling, S., Sanjines, R. & Fiore, A. Waveguide Superconducting Single-Photon Detectors for Integrated Quantum Photonic Circuits. *Appl Phys Lett* **99,** (2011).

[65] Sahin, D., Gaggero, A., Weber, J. W., Agafonov, I., Verheijen, M. A., Mattioli, F., Beetz, J., Kamp, M., Hofling, S., Van De Sanden, M. C. M., Leoni, R. & Fiore, A. Waveguide Nanowire Superconducting Single-Photon Detectors Fabricated on GaAs and the Study of Their Optical Properties. *IEEE Journal of Selected Topics in Quantum Electronics* **21,** (2015).

[66] Sahin, D., Gaggero, A., Zhou, Z., Jahanmirinejad, S., Mattioli, F., Leoni, R., Beetz, J., Lermer, M., Kamp, M., Höfling, S. & Fiore, A. Waveguide Photon-Number-Resolving Detectors for Quantum Photonic Integrated Circuits. *Appl Phys Lett* **103,** (2013).

[67] Najafi, F., Mower, J., Harris, N. C., Bellei, F., Dane, A., Lee, C., Hu, X., Kharel, P., Marsili, F., Assefa, S., Berggren, K. K. & Englund, D. On-Chip Detection of Non-Classical Light by Scalable Integration of Single-Photon Detectors. *Nat Commun* **6,** (2015).

[68] Gyger, S., Zichi, J., Schweickert, L., Elshaari, A. W., Steinhauer, S., Covre da Silva, S. F., Rastelli, A., Zwiller, V., Jöns, K. D. & Errando-Herranz, C. Reconfigurable Photonics with On-Chip Single-Photon Detectors. *Nat Commun* **12,** (2021).

[69] Cavalier, P., Vilĺgier, J. C., Feautrier, P., Constancias, C. & Morand, A. Light Interference Detection On-Chip by Integrated SNSPD Counters. *AIP Adv* **1,** (2011).

[70] Krummheuer, B., Axt, V. M. & Kuhn, T. Theory of Pure Dephasing and the Resulting Absorption Line Shape in Semiconductor Quantum Dots. *Phys Rev B Condens Matter Mater Phys* **65,** (2002).

[71] Davanço, M., Hellberg, C. S., Ates, S., Badolato, A. & Srinivasan, K. Multiple Time Scale Blinking in InAs Quantum Dot Single-Photon Sources. *Phys Rev B Condens Matter Mater Phys* **89,** (2014).

[72] Iles-Smith, J., McCutcheon, D. P. S., Nazir, A. & Mørk, J. Phonon Scattering Inhibits Simultaneous Near-Unity Efficiency and Indistinguishability in Semiconductor Single-Photon Sources. *Nat Photonics* **11,** (2017).

[73] Carmele, A. & Reitzenstein, S. Non-Markovian Features in Semiconductor Quantum Optics: Quantifying the Role of Phonons in Experiment and Theory. *Nanophotonics* **8,** (2019).

[74] Löbl, M. C., Spinnler, C., Javadi, A., Zhai, L., Nguyen, G. N., Ritzmann, J., Midolo, L., Lodahl, P., Wieck, A. D., Ludwig, A. & Warburton, R. J. Radiative Auger Process in the Single-Photon Limit. *Nat Nanotechnol* **15,** (2020).

[75] Jarlov, C., Wodey, Lyasota, A., Calic, M., Gallo, P., Dwir, B., Rudra, A. & Kapon, E. Effect of Pure Dephasing and Phonon Scattering on the Coupling of Semiconductor Quantum Dots to Optical Cavities. *Phys Rev Lett* **117,** 076801 (2016).

[76] Huang, J., Liu, W., Cheng, X., Miranda, A., Dwir, B., Rudra, A., Kapon, E. & Wong, C. W. Single Site-Controlled Inverted Pyramidal InGaAs QD–Nanocavity Operating at the Onset of the Strong Coupling Regime. *J Appl Phys* **134,** 223103 (2023).

[77] Huang, J., Liu, W., Sarihan, M. C., Cheng, X., Miranda, A., Dwir, B., Rudra, A., Kapon, E. & Wong, C. W. Exciton-Polariton Dynamics of the Single Site-Controlled Quantum Dot-Nanocavity in the Coexisting Strong-Weak Coupling Regime. *New J Phys* **25,** 033015 (2023).

[78] Schubert, E. F. & Gessmann, T. in *Encyclopedia of Condensed Matter Physics* (2005). doi:10.1016/B0-12-369401-9/00498-8

[79] Akopian, N., Lindner, N. H., Poem, E., Berlatzky, Y., Avron, J., Gershoni, D., Gerardot, B. D. & Petroff, P. M. Entangled Photon Pairs from Semiconductor Quantum Dots. *Phys Rev Lett* **96,** (2006).

[80] Yamamoto, Y., Santori, C. & Pelton, M. Regulated and Entangled Photons from a Single Quantum Dot. *Phys Rev Lett* **84,** (2000).

[81] Huber, D., Reindl, M., Aberl, J., Rastelli, A. & Trotta, R. Semiconductor Quantum Dots as an Ideal Source of Polarization-Entangled Photon Pairs on-Demand: A Review. *Journal of Optics (United Kingdom)* **20,** (2018).

[82] Jayakumar, H., Predojević, A., Kauten, T., Huber, T., Solomon, G. S. & Weihs, G. Time-Bin Entangled Photons from a Quantum Dot. *Nature Communications 2014 5:1* **5,** 1–5 (2014).

[83] Aumann, P., Prilmüller, M., Kappe, F., Ostermann, L., Dalacu, D., Poole, P. J., Ritsch, H., Lechner, W. & Weihs, G. Demonstration and Modelling of Time-Bin Entangled Photons from a Quantum Dot in a Nanowire. *AIP Adv* **12,** 55115 (2021).

[84] Prilmüller, M., Huber, T., Müller, M., Michler, P., Weihs, G. & Predojević, A. Hyper-Entanglement of Photons Emitted by a Quantum Dot. in *2017 Conference on Lasers and Electro-Optics, CLEO 2017 - Proceedings* **2017-January,** (2017).

[85] Javadi, A., Ding, D., Appel, M. H., Mahmoodian, S., Löbl, M. C., Söllner, I., Schott, R., Papon, C., Pregnolato, T., Stobbe, S., Midolo, L., Schröder, T., Wieck, A. D., Ludwig, A., Warburton, R. J. & Lodahl, P. Spin-Photon Interface and Spin-Controlled Photon Switching in a Nanobeam Waveguide. *Nat Nanotechnol* **13,** 398–403 (2017).

[86] Ding, D., Appel, M. H., Javadi, A., Zhou, X., Löbl, M. C., Söllner, I., Schott, R., Papon, C., Pregnolato, T., Midolo, L., Wieck, A. Di., Ludwig, A., Warburton, R. J., Schröder, T. & Lodahl, P. Coherent Optical Control of a Quantum-Dot Spin-Qubit in a Waveguide-Based Spin-Photon Interface. *Phys Rev Appl* **11,** 031002 (2019).

[87] Appel, M. H., Tiranov, A., Javadi, A., Löbl, M. C., Wang, Y., Scholz, S., Wieck, A. D., Ludwig, A., Warburton, R. J. & Lodahl, P. Coherent Spin-Photon Interface with Waveguide Induced Cycling Transitions. *Phys Rev Lett* **126,** 013602 (2021).

[88] Dusanowski, Ł., Nawrath, C., Portalupi, S. L., Jetter, M., Huber, T., Klembt, S., Michler, P. & Höfling, S. Optical Charge Injection and Coherent Control of a Quantum-Dot Spin-Qubit Emitting at Telecom Wavelengths. *Nature Communications 2022 13:1* **13,** 1–8 (2022).

[89] Chan, M. L., Tiranov, A., Appel, M. H., Wang, Y., Midolo, L., Scholz, S., Wieck, A. D., Ludwig, A., Sørensen, A. S. & Lodahl, P. On-Chip Spin-Photon Entanglement Based on Photon-Scattering of a Quantum Dot. *npj Quantum Information 2023 9:1* **9,** 1–7 (2023).

[90] Higginbottom, D. B., Asadi, F. K., Chartrand, C., Ji, J. W., Bergeron, L., Thewalt, M. L. W., Simon, C. & Simmons, S. Memory and Transduction Prospects for Silicon T Center Devices. *PRX Quantum* **4,** (2023).

[91] Cogan, D., Su, Z.-E., Kenneth, O. & Gershoni, D. Deterministic Generation of Indistinguishable Photons in a Cluster State. *Nat Photonics* **17,** 324–329 (2023).

[92] Larsen, M. V., Guo, X., Breum, C. R., Neergaard-Nielsen, J. S. & Andersen, U. L. Deterministic Generation of a Two-Dimensional Cluster State. *Science (1979)* **366,** 369–372 (2019).

[93] Schwartz, I., Cogan, D., Schmidgall, E. R., Don, Y., Gantz, L., Kenneth, O., Lindner, N. H. & Gershoni, D. Deterministic Generation of a Cluster State of Entangled Photons. *Science (1979)* **354,** 434–437 (2016).

[94] Vezvaee, A., Hilaire, P., Doty, M. F. & Economou, S. E. Deterministic Generation of Entangled Photonic Cluster States from Quantum Dot Molecules. *Phys Rev Appl* **18,** L061003 (2022).

[95] Economou, S. E., Lindner, N. & Rudolph, T. Optically Generated 2-Dimensional Photonic Cluster State from Coupled Quantum Dots. *Phys Rev Lett* **105,** 093601 (2010).

[96] Lindner, N. H. & Rudolph, T. Proposal for Pulsed On-Demand Sources of Photonic Cluster State Strings. *Phys Rev Lett* **103,** 113602 (2009).

[97] Gimeno-Segovia, M., Rudolph, T. & Economou, S. E. Deterministic Generation of Large-Scale Entangled Photonic Cluster State from Interacting Solid State Emitters. *Phys Rev Lett* **123,** 070501 (2019).

[98] Tiurev, K., Appel, M. H., Mirambell, P. L., Lauritzen, M. B., Tiranov, A., Lodahl, P. & Sørensen, A. S. High-Fidelity Multiphoton-Entangled Cluster State with Solid-State Quantum Emitters in Photonic Nanostructures. *Phys Rev A (Coll Park)* **105,** L030601 (2022).

[99] Dutta, H. S., Goyal, A. K., Srivastava, V. & Pal, S. Coupling Light in Photonic Crystal Waveguides: A Review. *Photonics Nanostruct* **20,** (2016).

[100] Hughes, S., Ramunno, L., Young, J. F. & Sipe, J. E. Extrinsic Optical Scattering Loss in Photonic Crystal Waveguides: Role of Fabrication Disorder and Photon Group Velocity. *Phys Rev Lett* **94,** (2005).

[101] Gerace, D. & Andreani, L. C. Effects of Disorder on Propagation Losses and Cavity Q-Factors in Photonic Crystal Slabs. *Photonics Nanostruct* **3,** (2005).

[102] Faggiani, R., Baron, A., Zang, X., Lalouat, L., Schulz, S. A., O'Regan, B., Vynck, K., Cluzel, B., De Fornel, F., Krauss, T. F. & Lalanne, P. Lower Bound for the Spatial Extent of Localized Modes in Photonic-Crystal Waveguides with Small Random Imperfections. *Sci Rep* **6,** (2016).

[103] Crane, T., Trojak, O. J., Vasco, J. P., Hughes, S. & Sapienza, L. Anderson Localization of Visible Light on a Nanophotonic Chip. *ACS Photonics* **4,** (2017).

[104] Segev, M., Silberberg, Y. & Christodoulides, D. N. Anderson Localization of Light. *Nat Photonics* **7,** (2013).

[105] John, S. Strong Localization of Photons in Certain Disordered Dielectric Superlattices. *Phys Rev Lett* **58,** (1987).

[106] Anderson, P. W. Absence of Diffusion in Certain Random Lattices. *Physical Review* **109,** (1958).

[107] Sapienza, L., Thyrrestrup, H., Stobbe, S., Garcia, P. D., Smolka, S. & Lodahl, P. Cavity Quantum Electrodynamics with Anderson-Localized Modes. *Science (1979)* **327,** 1352–1355 (2010).

[108] Intonti, F., Vignolini, S., Riboli, F., Zani, M., Wiersma, D. S., Balet, L., Li, L. H., Francardi, M., Gerardino, A., Fiore, A. & Gurioli, M. Tuning of Photonic Crystal Cavities by Controlled Removal of Locally Infiltrated Water. *Appl Phys Lett* **95,** 173112 (2009).

[109] Mosor, S., Hendrickson, J., Richards, B. C., Sweet, J., Khitrova, G., Gibbs, H. M., Yoshie, T., Scherer, A., Shchekin, O. B. & Deppe, D. G. Scanning a Photonic Crystal Slab Nanocavity by Condensation of Xenon. *Appl Phys Lett* **87,** 1–3 (2005).

[110] Vignolini, S., Riboli, F., Wiersma, D. S., Balet, L., Li, L. H., Francardi, M., Gerardino, A., Fiore, A., Gurioli, M. & Intonti, F. Nanofluidic Control of Coupled Photonic Crystal Resonators. *Appl Phys Lett* **96,** 141114 (2010).

[111] Speijcken, N. W. L., Dündar, M. A., Casas Bedoya, A., Monat, C., Grillet, C., Domachuk, P., Nötzel, R., Eggleton, B. J. & Van Der Heijden, R. W. In Situ Optofluidic Control of Reconfigurable Photonic Crystal Cavities. *Appl Phys Lett* **100,** 261107 (2012).

[112] Lu, C.-Y. & Pan, J.-W. Quantum-Dot Single-Photon Sources for the Quantum Internet. *Nat Nanotechnol* **16,** 1294–1296 (2021).

[113] Tomm, N., Javadi, A., Antoniadis, N. O., Najer, D., Löbl, M. C., Korsch, A. R., Schott, R., Valentin, S. R., Wieck, A. D., Ludwig, A. & Warburton, R. J. A Bright and Fast Source of Coherent Single Photons. *Nat Nanotechnol* **16,** 399–403 (2020).

[114] Stranski, I. N. & Krastanow, L. Zur Theorie Der Orientierten Ausscheidung von Ionenkristallen Aufeinander. *Monatsh Chem* **71,** 351–364 (1937).

[115] Henini, M. Self-Assembled Quantum Dots. *III-Vs Review* **10,** 25–30 (1997).

[116] Petroff, P. M. Semiconductor Self-Assembled Quantum Dots: Present Status and Future Trends. *Advanced Materials* **23,** (2011).

[117] Skolnick, M. S. & Mowbray, D. J. Recent Developments in the Physics and Applications of Self-Assembled Quantum Dots. in *Physica E Low Dimens Syst Nanostruct* **21,** (2004).

[118] Skolnick, M. S. & Mowbray, D. J. Self-Assembled Semiconductor Quantum Dots: Fundamental Physics and Device Applications. *Annu Rev Mater Res* **34,** (2004).

[119] Tartakovskii, A. *Quantum dots: Optics, electron transport and future applications*. *Quantum Dots: Optics, Electron Transport and Future Applications* **9781107012585,** (2012).

[120] Franchi, S., Trevisi, G., Seravalli, L. & Frigeri, P. Quantum Dot Nanostructures and Molecular Beam Epitaxy. *Progress in Crystal Growth and Characterization of Materials* **47,** (2003).

[121] Winger, M., Volz, T., Tarel, G., Portolan, S., Badolato, A., Hennessy, K. J., Hu, E. L., Beveratos, A., Finley, J., Savona, V. & Imamoğlu, A. Explanation of Photon Correlations in the Far-off-Resonance Optical Emission from a Quantum-Dot-Cavity System. *Phys Rev Lett* **103,** (2009).

[122] Gong, M., Zhang, W., Guo, G. C. & He, L. Exciton Polarization, Fine-Structure Splitting, and the Asymmetry of Quantum Dots under Uniaxial Stress. *Phys Rev Lett* **106,** (2011).

[123] Seguin, R., Schliwa, A., Rodt, S., Potschke, K., Pohl, U. W. & Bimberg, D. Size-Dependent Fine-Structure Splitting in Self-Organized InAs/GaAs Quantum Dots. *Phys Rev Lett* **95,** (2005).

[124] Gammon, D., Snow, E. S., Shanabrook, B. V., Katzer, D. S. & Park, D. Fine Structure Splitting in the Optical Spectra of Single Gaas Quantum Dots. *Phys Rev Lett* **76,** (1996).

[125] Bayer, M., Ortner, G., Stern, O., Kuther, A., Gorbunov, A. A., Forchel, A., Hawrylak, P., Fafard, S., Hinzer, K., Reinecke, T. L., Walck, S. N., Reithmaier, J. P., Klopf, F. & Schäfer, F. Fine Structure of Neutral and Charged Excitons in Self-Assembled In(Ga)As/(Al) GaAs Quantum Dots. *Phys Rev B Condens Matter Mater Phys* **65,** (2002).

[126] Kadantsev, E. & Hawrylak, P. Theory of Exciton Fine Structure in Semiconductor Quantum Dots: Quantum Dot Anisotropy and Lateral Electric Field. *Phys Rev B Condens Matter Mater Phys* **81,** (2010).

[127] Kapon, E., Hwang, D. M. & Bhat, R. Stimulated Emission in Semiconductor Quantum Wire Heterostructures. *Phys Rev Lett* **63,** 430 (1989).

[128] Biasiol, G., Reinhardt, F., Gustafsson, A. & Kapon, E. Self-Limiting OMCVD Growth of GaAs on V-Grooved Substrates with Application to InGaAs/GaAs Quantum Wires. *J Electron Mater* **26,** 1194–1198 (1997).

[129] Kapon, E., Reinhardt, F., Biasiol, G. & Gustafsson, A. Surface and Interface Properties of Quantum Nanostructures Grown on Nonplanar Substrates. *Appl Surf Sci* **123–124,** 674–681 (1998).

[130] Hartmann, A., Loubies, L., Reinhardt, F. & Kapon, E. Self-Limiting Growth of Quantum Dot Heterostructures on Nonplanar {111}B Substrates. *Appl Phys Lett* **71,** (1997).

[131] Biasiol, G., Kapon, E., Ducommun, Y. & Gustafsson, A. Self-Ordering of Quantum-Wire Superlattices on V-Grooved Substrates. *Phys Rev B* **57,** R9416 (1998).

[132] Biasiol, G. & Kapon, E. Mechanisms of Self-Ordering of Quantum Nanostructures Grown on Nonplanar Surfaces. *Phys Rev Lett* **81,** 2962 (1998).

[133] Biasiol, G., Lelarge, F., Leifer, K. & Kapon, E. Mechanisms of Self-Ordering of Nanostructures in Nonplanar OMCVD Growth. *J Cryst Growth* **195,** 596–602 (1998).

[134] Biasiol, G. & Kapon, E. Mechanism of Self-Limiting Epitaxial Growth on Nonplanar Substrates. *J Cryst Growth* **201–202,** 62–66 (1999).

[135] Biasiol, G., Gustafsson, A., Leifer, K. & Kapon, E. Mechanisms of Self-Ordering in Nonplanar Epitaxy of Semiconductor Nanostructures. *Phys Rev B* **65,** 205306 (2002).

[136] Hartmann, A., Ducommun, Y., Loubies, L., Leifer, K. & Kapon, E. Structure and Photoluminescence of Single AlGaAs/GaAs Quantum Dots Grown in Inverted Tetrahedral Pyramids. *Appl Phys Lett* **73,** 2322–2324 (1998).

[137] Hartmann, A., Ducommun, Y., Leifer, K. & Kapon, E. Structure and Optical Properties of Semiconductor Quantum Nanostructures Self-Formed in Inverted Tetrahedral Pyramids. *Journal of Physics: Condensed Matter* **11,** 5901 (1999).

[138] Leifer, K., Hartmann, A., Ducommun, Y. & Kapon, E. Carrier Transport and Luminescence in Inverted-Pyramid Quantum Structures. *Appl Phys Lett* **77,** 3923–3925 (2000).

[139] Baier, M. H., Pelucchi, E., Kapon, E., Varoutsis, S., Gallart, M., Robert-Philip, I. & Abram, I. Single Photon Emission from Site-Controlled Pyramidal Quantum Dots. *Appl Phys Lett* **84,** 648–650 (2004).

[140] Malko, A., Baier, M. H., Pelucchi, E., Chek-Al-Kar, D., Oberli, D. Y. & Kapon, E. Correlated Photon Emission from Semiconductor Quantum Dots Grown in Inverted Pyramids. *Physica E Low Dimens Syst Nanostruct* **26,** 194–198 (2005).

[141] Malko, A., Oberli, D. Y., Baier, M. H., Pelucchi, E., Michelini, F., Karlsson, K. F., Dupertuis, M. A. & Kapon, E. Single-Photon Emission from Pyramidal Quantum Dots: The Impact of Hole Thermalization on Photon Emission Statistics. *Phys Rev B Condens Matter Mater Phys* **72,** 195332 (2005).

[142] Malko, A., Baier, M. H., Karlsson, K. F., Pelucchi, E., Oberli, D. Y. & Kapon, E. Optimization of the Efficiency of Single-Photon Sources Based on Quantum Dots under Optical Excitation. *Appl Phys Lett* **88,** 81905 (2006).

[143] Baier, M. H., Malko, A., Pelucchi, E., Oberli, D. Y. & Kapon, E. Quantum-Dot Exciton Dynamics Probed by Photon-Correlation Spectroscopy. *Phys Rev B* **73,** 205321 (2006).

[144] Baier, M. H., Watanabe, S., Pelucchi, E. & Kapon, E. High Uniformity of Site-Controlled Pyramidal Quantum Dots Grown on Prepatterned Substrates. *Appl Phys Lett* **84,** 1943–1945 (2004).

[145] Watanabe, S., Pelucchi, E., Dwir, B., Baier, M., Leifer, K. & Kapon, E. Growth and Optical Characterization of Dense Arrays of Site-Controlled Quantum Dots Grown in Inverted Pyramids. *Physica E Low Dimens Syst Nanostruct* **21,** 193–198 (2004).

[146] Leifer, K., Pelucchi, E., Watanabe, S., Michelini, F., Dwir, B. & Kapon, E. Narrow (≈4 MeV) Inhomogeneous Broadening and Its Correlation with Confinement Potential of Pyramidal Quantum Dot Arrays. *Appl Phys Lett* **91,** (2007).

[147] Karlsson, K. F., Troncale, V., Oberli, D. Y., Malko, A., Pelucchi, E., Rudra, A. & Kapon, E. Optical Polarization Anisotropy and Hole States in Pyramidal Quantum Dots. *Appl Phys Lett* **89,** 251113 (2006).

[148] Troncale, V., Karlsson, K. F., Oberli, D. Y., Byszewski, M., Malko, A., Pelucchi, E., Rudra, A. & Kapon, E. Excited Excitonic States Observed in Semiconductor Quantum Dots Using Polarization Resolved Optical Spectroscopy. *J Appl Phys* **101,** 81703 (2007).

[149] Karlsson, K. F., Dupertuis, M. A., Oberli, D. Y., Pelucchi, E., Rudra, A., Holtz, P. O. & Kapon, E. Fine Structure of Exciton Complexes in High-Symmetry Quantum Dots: Effects of Symmetry Breaking and Symmetry Elevation. *Phys Rev B Condens Matter Mater Phys* **81,** 161307 (2010).

[150] Dupertuis, M. A., Karlsson, K. F., Oberli, D. Y., Pelucchi, E., Rudra, A., Holtz, P. O. & Kapon, E. Symmetries and the Polarized Optical Spectra of Exciton Complexes in Quantum Dots. *Phys Rev Lett* **107,** 127403 (2011).

[151] Karlsson, K. F., Oberli, D. Y., Dupertuis, M. A., Troncale, V., Byszewski, M., Pelucchi, E., Rudra, A., Holtz, P. O. & Kapon, E. Spectral Signatures of High-Symmetry Quantum Dots and Effects of Symmetry Breaking. *New J Phys* **17,** 103017 (2015).

[152] Gallo, P., Felici, M., Dwir, B., Atlasov, K., Karlsson, K. F., Rudra, A., Mohan, A., Biasiol, G., Sorba, L. & Kapon, E. Integration of Site-Controlled Pyramidal Quantum Dots and Photonic Crystal Membrane Cavities. *2008 Conference on Quantum Electronics and Laser Science Conference on Lasers and Electro-Optics, CLEO/QELS* **92,** 263101 (2008).

[153] Felici, M., Gallo, P., Mohan, A., Dwir, B., Rudra, A. & Kapon, E. Site-Controlled InGaAs Quantum Dots with Tunable Emission Energy. *Small* **5,** 938–943 (2009).

[154] Rigal, B., Jarlov, C., Rudra, A., Gallo, P., Lyasota, A., Dwir, B. & Kapon, E. Site-Controlled InGaAs/GaAs Pyramidal Quantum Dots Grown by MOVPE on Patterned Substrates Using Triethylgallium. *J Cryst Growth* **414,** 187–191 (2015).

[155] Kulkova, I. V., Lyasota, A., Jarlov, C., Rigal, B., Rudra, A., Dwir, B. & Kapon, E. Emission Wavelength Control of Ordered Arrays of InGaAs/GaAs Quantum Dots. *J Cryst Growth* **464,** 69–74 (2017).

[156] Surrente, A., Felici, M., Gallo, P., Rudra, A., Dwir, B. & Kapon, E. Dense Arrays of Site-Controlled Quantum Dots with Tailored Emission Wavelength: Growth Mechanisms and Optical Properties. *Appl Phys Lett* **111,** 221102 (2017).

[157] Calic, M., Gallo, P., Felici, M., Atlasov, K. A., Dwir, B., Rudra, A., Biasiol, G., Sorba, L., Tarel, G., Savona, V. & Kapon, E. Phonon-Mediated Coupling of InGaAs/GaAs Quantum-Dot Excitons to Photonic Crystal Cavities. *Phys Rev Lett* **106,** 227402 (2011).

[158] Jarlov, C., Lyasota, A., Ferrier, L., Gallo, P., Dwir, B., Rudra, A. & Kapon, E. Exciton Dynamics in a Site-Controlled Quantum Dot Coupled to a Photonic Crystal Cavity. *Appl Phys Lett* **107,** 191101 (2015).

[159] Lyasota, A., Borghardt, S., Jarlov, C., Dwir, B., Gallo, P., Rudra, A. & Kapon, E. Integration of Multiple Site-Controlled Pyramidal Quantum Dot Systems with Photonic-Crystal Membrane Cavities. *J Cryst Growth* **414,** 192–195 (2015).

[160] Rigal, B., Drahi, D., Jarlov, C., Dwir, B., Rudra, A., Kulkova, I., Lyasota, A. & Kapon, E. Probing Disorder and Mode Localization in Photonic Crystal Cavities Using Site-Controlled Quantum Dots. *J Appl Phys* **123,** 43109 (2018).

[161] Rigal, B., Dwir, B., Rudra, A., Kulkova, I., Lyasota, A. & Kapon, E. Single Photon Extraction and Propagation in Photonic Crystal Waveguides Incorporating Site-Controlled Quantum Dots. *Appl Phys Lett* **112,** 51105 (2018).

[162] Delgoffe, A., Miranda, A., Rigal, B., Lyasota, A., Rudra, A., Dwir, B. & Kapon, E. Tilted-Potential Photonic Crystal Cavities for Integrated Quantum Photonics. *Opt Express* **27,** 21822 (2019).

[163] Yu, Y., Delgoffe, A. M., Miranda, A., Lyasota, A., Dwir, B., Rudra, A. & Kapon, E. Remote Excitation between Quantum Emitters Mediated by an Optical Fano Resonance. *Optica* **8,** 1605 (2021).

[164] Rigal, B., Jarlov, C., Gallo, P., Dwir, B., Rudra, A., Calic, M. & Kapon, E. Site-Controlled Quantum Dots Coupled to a Photonic Crystal Molecule. *Appl Phys Lett* **107,** 141103 (2015).

[165] Lyasota, A., Jarlov, C., Nyman, M., Miranda, A., Calic, M., Dwir, B., Rudra, A., Shevchenko, A. & Kapon, E. Mode Interference Effect in Optical Emission of Quantum Dots in Photonic Crystal Cavities. *Phys Rev X* **12,** 021042 (2022).

[166] Mereni, L. O., Marquardt, O., Juska, G., Dimastrodonato, V., O'Reilly, E. P. & Pelucchi, E. Fine-Structure Splitting in Large-Pitch Pyramidal Quantum Dots. *Phys Rev B Condens Matter Mater Phys* **85,** (2012).

[167] Mohan, A., Gallo, P., Felici, M., Dwir, B., Rudra, A., Faist, J., Kapon, E., Gallo, P., Felici, M., Dwir, B., Rudra, A., Kapon, E. & Faist, J. Record-Low Inhomogeneous Broadening of Site-Controlled Quantum Dots for Nanophotonics. *Small* **6,** 1268–1272 (2010).

[168] Dimastrodonato, V., Pelucchi, E., Zestanakis, P. A. & Vvedensky, D. D. Transient and Self-Limited Nanostructures on Patterned Surfaces. *Phys Rev B Condens Matter Mater Phys* **87,** (2013).

[169] Ćalić, M. Cavity Quantum Electrodynamics with Site-Controlled Pyramidal Quantum Dots in Photonic Crystal Cavities. *PhD thesis, EPFL* **5957,** (2013).

[170] Juska, G., Murray, E., Dimastrodonato, V., Chung, T. H., Moroni, S. T., Gocalinska, A. & Pelucchi, E. Conditions for Entangled Photon Emission from (111)B Site-Controlled Pyramidal Quantum Dots. *J Appl Phys* **117,** 134302 (2015).

[171] Juska, G., Dimastrodonato, V., Mereni, L. O., Gocalinska, A. & Pelucchi, E. Towards Quantum-Dot Arrays of Entangled Photon Emitters. *Nat Photonics* **7,** 527–531 (2013).

[172] Rigal, B., Joanesarson, K., Lyasota, A., Jarlov, C., Dwir, B., Rudra, A., Kulkova, I. & Kapon, E. Propagation Losses in Photonic Crystal Waveguides: Effects of Band Tail Absorption and Waveguide Dispersion. *Opt Express* **25,** 28908 (2017).

[173] Lyasota, A., Jarlov, C., Gallo, P., Rudra, A., Dwir, B. & Kapon, E. Deterministic Coupling of a System of Multiple Quantum Dots to a Single Photonic Cavity Mode. *Appl Phys Lett* **111,** (2017).

[174] Calic, M., Jarlov, C., Gallo, P., Dwir, B., Rudra, A. & Kapon, E. Deterministic Radiative Coupling of Two Semiconductor Quantum Dots to the Optical Mode of a Photonic Crystal Nanocavity. *Sci Rep* **7,** (2017).

[175] Delgoffe, A. M. Functional Elements for Quantum-Dot-Based Integrated Quantum Photonics. (2020). doi:10.5075/EPFL-THESIS-7533

[176] Bardeen, J. & Brattain, W. H. The Transistor, a Semi-Conductor Triode [14]. *Physical Review* **74,** (1948).

[177] Kilby, J. S. Invention of the Integrated Circuit. *IEEE Trans Electron Devices* **23,** (1976).

[178] Deal, B. E. & Early, J. M. The Evolution of Silicon Semiconductor Technology: 1952–1977. *J Electrochem Soc* **126,** (1979).

[179] Huff, H. R. Moore's Law: Beyond Planar Silicon CMOS and into the Nano Era. *Electrochemical Society Interface* **14,** (2005).

[180] Simmons, S. Scalable Fault-Tolerant Quantum Technologies with Silicon Color Centers. *PRX Quantum* **5,** 010102 (2024).

[181] Liu, X., Akahane, K., Jahan, N. A., Kobayashi, N., Sasaki, M., Kumano, H. & Suemune, I. Single-Photon Emission in Telecommunication Band from an InAs Quantum Dot Grown on InP with Molecular-Beam Epitaxy. *Appl Phys Lett* **103,** (2013).

[182] Haffouz, S., Zeuner, K. D., Dalacu, D., Poole, P. J., Lapointe, J., Poitras, D., Mnaymneh, K., Wu, X., Couillard, M., Korkusinski, M., Schöll, E., Jöns, K. D., Zwiller, V. & Williams, R. L. Bright Single InAsP Quantum Dots at Telecom Wavelengths in Position-Controlled InP Nanowires: The Role of the Photonic Waveguide. *Nano Lett* **18,** (2018).

[183] Portalupi, S. L., Jetter, M. & Michler, P. InAs Quantum Dots Grown on Metamorphic Buffers as Non-Classical Light Sources at Telecom C-Band: A Review. *Semicond Sci Technol* **34,** (2019).

[184] Lettner, T., Gyger, S., Zeuner, K. D., Schweickert, L., Steinhauer, S., Reuterskiöld Hedlund, C., Stroj, S., Rastelli, A., Hammar, M., Trotta, R., Jöns, K. D. & Zwiller, V. Strain-Controlled Quantum Dot Fine Structure for Entangled Photon Generation at 1550 Nm. *Nano Lett* **21,** (2021).

[185] Birowosuto, M. D., Sumikura, H., Matsuo, S., Taniyama, H., Van Veldhoven, P. J., Nötzel, R. & Notomi, M. Fast Purcell-Enhanced Single Photon Source in 1,550-Nm Telecom Band from a Resonant Quantum Dot-Cavity Coupling. *Sci Rep* **2,** (2012).

[186] Ramanayaka, A. N., Tang, K., Hagmann, J. A., Kim, H. S., Simons, D. S., Richter, C. A. & Pomeroy, J. M. Use of Quantum Effects as Potential Qualifying Metrics for 'Quantum Grade Silicon'. *AIP Adv* **9,** (2019).

[187] Tang, K., Kim, H. S., Ramanayaka, A. N., Simons, D. S. & Pomeroy, J. M. Targeted Enrichment of 28Si Thin Films for Quantum Computing. *J Phys Commun* **4,** 035006 (2020).

[188] Dwyer, K. J., Pomeroy, J. M., Simons, D. S., Steffens, K. L. & Lau, J. W. Enriching 28Si beyond 99.9998 % for Semiconductor Quantum Computing. *J Phys D Appl Phys* **47,** 345105 (2014).

[189] Dwyer, K. J., Kim, H. S., Simons, D. S. & Pomeroy, J. M. Temperature-Dependent Si 29 Incorporation during Deposition of Highly Enriched Si 28 Films. *Phys Rev Mater* **1,** 064603 (2017).

[190] Tang, K., Kim, H. S., Ramanayaka, A. N. R., Simons, D. S. & Pomeroy, J. M. A Compact, Ultra-High Vacuum Ion Source for Isotopically Enriching and Depositing 28Si Thin Films. *Review of Scientific Instruments* **90,** (2019).

[191] Saeedi, K., Simmons, S., Salvail, J. Z., Dluhy, P., Riemann, H., Abrosimov, N. V., Becker, P., Pohl, H.-J., Morton, J. J. L. & Thewalt, M. L. W. Room-Temperature Quantum Bit Storage Exceeding 39 Minutes Using Ionized Donors in Silicon-28. *Science (1979)* **342,** 830–833 (2013).

[192] Morse, K. J., Abraham, R. J. S., DeAbreu, A., Bowness, C., Richards, T. S., Riemann, H., Abrosimov, N. V., Becker, P., Pohl, H. J., Thewalt, M. L. W. & Simmons, S. A Photonic Platform for Donor Spin Qubits in Silicon. *Sci Adv* **3,** (2017).

[193] Baron, Y., Durand, A., Udvarhelyi, P., Herzig, T., Khoury, M., Pezzagna, S., Meijer, J., Robert-Philip, I., Abbarchi, M., Hartmann, J. M., Mazzocchi, V., Gérard, J. M., Gali, A., Jacques, V., Cassabois, G. & Dreaú, A. Detection of Single W-Centers in Silicon. *ACS Photonics* **9,** 2337–2345 (2022).

[194] Hollenbach, M., Klingner, N., Jagtap, N. S., Bischoff, L., Fowley, C., Kentsch, U., Hlawacek, G., Erbe, A., Abrosimov, N. V., Helm, M., Berencén, Y. & Astakhov, G. V. Wafer-Scale Nanofabrication of Telecom Single-Photon Emitters in Silicon. *Nat Commun* **13,** (2022).

[195] Malmbekk, H., Vines, L., Monakhov, E. V. & Svensson, B. G. Hydrogen-Related Defects in Boron Doped p-Type Silicon. *Physica Status Solidi (C) Current Topics in Solid State Physics* **8,** (2011).

[196] Mukashev, B. N., Abdullin, K. A., Gorelkinskii, Y. V. & Tokmoldin, S. Z. Self-Interstitial Related Reactions in Silicon Irradiated by Light Ions. *Mater Sci Eng B Solid State Mater Adv Technol* **58,** (1999).

[197] Leary, P., Jones, R. & Öberg, S. Interaction of Hydrogen with Substitutional and Interstitial Carbon Defects in Silicon. *Phys Rev B Condens Matter Mater Phys* **57,** (1998).

[198] Newman, R. C. Defects in Silicon. *Reports on Progress in Physics* **45,** (1982).

[199] Srour, J. R., Marshall, C. J. & Marshall, P. W. Review of Displacement Damage Effects in Silicon Devices. *IEEE Trans Nucl Sci* **50 III,** (2003).

[200] Davies, G. The Optical Properties of Luminescence Centres in Silicon. *Phys Rep* **176,** (1989).

[201] Zhiyenbayev, Y., Redjem, W., Ivanov, V., Qarony, W., Papapanos, C., Simoni, J., Liu, W., Jhuria, K., Tan, L. Z., Schenkel, T. & Kanté, B. Scalable Manufacturing of Quantum Light Emitters in Silicon under Rapid Thermal Annealing. *Opt Express* **31,** (2023).

[202] Wagner, J., Thonke, K. & Sauer, R. Excitation Spectroscopy on the 0.79-EV (C) Line Defect in Irradiated Silicon. *Phys Rev B* **29,** (1984).

[203] Kürner, W., Sauer, R., Dörnen, A. & Thonke, K. Structure of the 0.767-EV Oxygen-Carbon Luminescence Defect in 450°C Thermally Annealed Czochralski-Grown Silicon. *Phys Rev B* **39,** (1989).

[204] Davies, G., Lightowlers, E. C. & Ciechanowskat, Z. E. The 1018 Mev (w or I1) Vibronic Band in Silicon. *Journal of Physics C: Solid State Physics* **20,** (1987).

[205] O'Donnell, K. P., Lee, K. M. & Watkins, G. D. Origin of the 0.97 EV Luminescence in Irradiated Silicon. *Physica B+C* **116,** (1983).

[206] Canham, L. T., Barraclough, K. G. & Robbins, D. J. 1.3-Mm Light-Emitting Diode from Silicon Electron Irradiated at Its Damage Threshold. *Appl Phys Lett* **51,** (1987).

[207] Chartrand, C., Bergeron, L., Morse, K. J., Riemann, H., Abrosimov, N. V., Becker, P., Pohl, H.-J., Simmons, S. & Thewalt, M. L. W. Highly ^{28}Si Reveals Remarkable Optical

Linewidths and Fine Structure for Well-Known Damage Centers. *Phys Rev B* **98,** 195201 (2018).

[208] Irion, E., Bürger, N., Thonke, K. & Sauer, R. The Defect Luminescence Spectrum at 0.9351 EV in Carbon-Doped Heat-Treated or Irradiated Silicon. *Journal of Physics C: Solid State Physics* **18,** (1985).

[209] Safonov, A. N., Lightowlers, E. C., Davies, G., Leary, P., Jones, R. & Öberg, S. Interstitial-Carbon Hydrogen Interaction in Silicon. *Phys Rev Lett* **77,** (1996).

[210] Safonov, A. N. & Lightowlers, E. G. Photoluminescence Characterisation of Hydrogen-Related Centres in Silicon. *Materials Science and Engineering: B* **58,** (1999).

[211] Lightowlers, E. C., Jeyanathan, L., Safonov, A. N., Higgs, V. & Davies, G. Luminescence from Rod-like Defects and Hydrogen Related Centres in Silicon. *Materials Science and Engineering B* **24,** (1994).

[212] Lightowlers, E. C. & Safonov, A. N. Photoluminescence Vibrational Spectroscopy of Defects Containing the Light Impurities Carbon and Oxygen in Silicon. *Materials Science Forum* **258–263,** (1997).

[213] Safonov, A. N. & Lightowlers, E. C. Hydrogen Related Optical Centers in Radiation Damaged Silicon. *Materials Science Forum* **143–4,** (1994).

[214] Schmidt, D. C., Svensson, B. G., Seibt, M., Jagadish, C. & Davies, G. Photoluminescence, Deep Level Transient Spectroscopy and Transmission Electron Microscopy Measurements on MeV Self-Ion Implanted and Annealed n-Type Silicon. *J Appl Phys* **88,** (2000).

[215] Lightowlers, E. C., Newman, R. C. & Tucker, J. H. Hydrogen-Related Luminescence Centres in Thermally Treated Czochralski Silicon. *Semicond Sci Technol* **9,** (1994).

[216] Gower, J., Davies, G., Lightowlers, E. C. & Safonov, A. N. The I Centre : A Hydrogen Related Defect in Silicon. *Materials Science Forum* **258–263,** (1997).

[217] Henry, A., Monemar, B., Lindström, J. L., Bestwick, T. D. & Oehrlein, G. S. Photoluminescence Characterization of Plasma Exposed Silicon Surfaces. *J Appl Phys* **70,** (1991).

[218] Sarihan, M. C., Huang, J., Kang, J. H., Fan, C., Liu, W., Azizur-Rahman, K. M., Liang, B. & Wong, C. W. Photophysics of O-Band and Transition Metal Color Centers in Monolithic Silicon for Quantum Communications. (2023). at <http://arxiv.org/abs/2310.19510>

[219] Grynberg, G., Aspect, A., Fabre, C. & Cohen-Tannoudji, C. Introduction to Quantum Optics: From the Semi-Classical Approach to Quantized Light. (2010). doi:10.1017/CBO9780511778261

[220] Reithmaier, J. P. Strong Exciton–Photon Coupling in Semiconductor Quantum Dot Systems. *Semicond Sci Technol* **23,** 123001 (2008).

[221] Loudon, R. *The Quantum Theory of Light Third Edition*. - *Libri_OPTICS* (2000).

[222] TCSPC and Time Tagging Electronics | PicoQuant. at <https://www.picoquant.com/products/category/tcspc-and-time-tagging-modules>

[223] Quality Factor Calculations for a Resonant Cavity – Ansys Optics. at <https://optics.ansys.com/hc/en-us/articles/360041611774-Quality-factor-calculations-for-a-resonant-cavity>

[224] Tan, S. M. Computational Toolbox for Quantum and Atomic Optics. *Journal of Optics B: Quantum and Semiclassical Optics* **1,** 424–432 (1999).

[225] Ekert, A. K. Quantum Cryptography Based on Bellâs Theorem. *Phys Rev Lett* **67,** 661–663 (1991).

[226] Dada, A. C., Leach, J., Buller, G. S., Padgett, M. J. & Andersson, E. Experimental High-Dimensional Two-Photon Entanglement and Violations of Generalized Bell Inequalities. *Nat Phys* **7,** 677–680 (2011).

[227] Gao, W. B., Fallahi, P., Togan, E., Miguel-Sanchez, J. & Imamoglu, A. Observation of Entanglement between a Quantum Dot Spin and a Single Photon. *Nature* **491,** 426–430 (2012).

[228] Weber, J. H., Kambs, B., Kettler, J., Kern, S., Maisch, J., Vural, H., Jetter, M., Portalupi, S. L., Becher, C. & Michler, P. Two-Photon Interference in the Telecom C-Band after Frequency Conversion of Photons from Remote Quantum Emitters. *Nat Nanotechnol* **14,** 23–26 (2019).

[229] Kim, J.-H., Aghaeimeibodi, S., Carolan, J., Englund, D. & Waks, E. Hybrid Integration Methods for On-Chip Quantum Photonics. *Optica* **7,** 291 (2020).

[230] Briegel, H.-J. J., Dür, W., Cirac, J. I. & Zoller, P. Quantum Repeaters: The Role of Imperfect Local Operations in Quantum Communication. *Phys Rev Lett* **81,** 5932–5935 (1998).

[231] Reinhard, A., Volz, T., Winger, M., Badolato, A., Hennessy, K. J., Hu, E. L. & Imamoglu, A. Strongly Correlated Photons on a Chip. *Nat Photonics* **6,** 93–96 (2011).

[232] Kim, H., Bose, R., Shen, T. C., Solomon, G. S. & Waks, E. A Quantum Logic Gate between a Solid-State Quantum Bit and a Photon. *Nat Photonics* **7,** 373–377 (2013).

[233] Sun, S., Kim, H., Luo, Z., Solomon, G. S. & Waks, E. A Single-Photon Switch and Transistor Enabled by a Solid-State Quantum Memory. *Science (1979)* **361,** 57–60 (2018).

[234] Wang, H., He, Y.-M., Chung, T.-H., Hu, H., Yu, Y., Chen, S., Ding, X., Chen, M.-C., Qin, J., Yang, X., Liu, R.-Z., Duan, Z.-C., Li, J.-P., Gerhardt, S., Winkler, K., Jurkat, J., Wang, L.-J., Gregersen, N., Huo, Y.-H., Dai, Q., Yu, S., Höfling, S., Lu, C.-Y. & Pan, J.-W. Towards Optimal Single-Photon Sources from Polarized Microcavities. *Nat Photonics* **13,** 770–775 (2019).

[235] Nowak, A. K., Portalupi, S. L., Giesz, V., Gazzano, O., Dal Savio, C., Braun, P.-F., Karrai, K., Arnold, C., Lanco, L., Sagnes, I., Lemaître, A. & Senellart, P. Deterministic and Electrically Tunable Bright Single-Photon Source. *Nat Commun* **5,** 3240 (2014).

[236] Yoshle, T., Scherer, A., Hendrickson, J., Khitrova, G., Gibbs, H. M., Rupper, G., Ell, C., Shchekin, O. B. & Deppe, D. G. Vacuum Rabi Splitting with a Single Quantum Dot in a Photonic Crystal Nanocavity. *Nature* **432,** 200–203 (2004).

[237] Hennessy, K., Badolato, A., Winger, M., Gerace, D., Atatüre, M., Gulde, S., Fält, S., Hu, E. L. & Imamoğlu, A. Quantum Nature of a Strongly Coupled Single Quantum Dot-Cavity System. *Nature* **445,** 896–899 (2007).

[238] Bose, R., Cai, T., Choudhury, K. R., Solomon, G. S. & Waks, E. All-Optical Coherent Control of Vacuum Rabi Oscillations. *Nat Photonics* **8,** 858–864 (2014).

[239] Liu, Y.-C., Luan, X., Li, H.-K., Gong, Q., Wong, C. W. & Xiao, Y.-F. Coherent Polariton Dynamics in Coupled Highly Dissipative Cavities. *Phys Rev Lett* **112,** 213602 (2014).

[240] Volz, T., Reinhard, A., Winger, M., Badolato, A., Hennessy, K. J., Hu, E. L. & Imamoğlu, A. Ultrafast All-Optical Switching by Single Photons. *Nat Photonics* **6,** 605–609 (2012).

[241] Kasprzak, J., Reitzenstein, S., Muljarov, E. A., Kistner, C., Schneider, C., Strauss, M., Höfling, S., Forchel, A. & Langbein, W. Up on the Jaynes-Cummings Ladder of a Quantum-Dot/Microcavity System. *Nat Mater* **9,** 304–308 (2010).

[242] Englund, D., Majumdar, A., Faraon, A., Toishi, M., Stoltz, N., Petroff, P. & Vučković, J. Resonant Excitation of a Quantum Dot Strongly Coupled to a Photonic Crystal Nanocavity. *Phys Rev Lett* **104,** 073904 (2010).

[243] Najer, D., Söllner, I., Sekatski, P., Dolique, V., Löbl, M. C., Riedel, D., Schott, R., Starosielec, S., Valentin, S. R., Wieck, A. D., Sangouard, N., Ludwig, A. & Warburton, R. J. A Gated Quantum Dot Strongly Coupled to an Optical Microcavity. *Nature* **575,** 622–627 (2019).

[244] Lodahl, P., Mahmoodian, S. & Stobbe, S. Interfacing Single Photons and Single Quantum Dots with Photonic Nanostructures. *Rev Mod Phys* **87,** 347–400 (2013).

[245] Gao, J., Combrie, S., Liang, B., Schmitteckert, P., Lehoucq, G., Xavier, S., Xu, X., Busch, K., Huffaker, D. L., De Rossi, A. & Wong, C. W. Strongly Coupled Slow-Light Polaritons in One-Dimensional Disordered Localized States. *Sci Rep* **3,** 1994 (2013).

[246] Osada, A., Ota, Y., Katsumi, R., Kakuda, M., Iwamoto, S. & Arakawa, Y. Strongly Coupled Single-Quantum-Dot–Cavity System Integrated on a CMOS-Processed Silicon Photonic Chip. *Phys Rev Appl* **11,** 024071 (2019).

[247] Badolato, A., Hennessy, K., Atatüre, M., Dreiser, J., Hu, E., Petroff, P. M. & Imamoğlu, A. Deterministic Coupling of Single Quantum Dots to Single Nanocavity Modes. *Science (1979)* **308,** 1158–1161 (2005).

[248] Muller, A., Fang, W., Lawall, J. & Solomon, G. S. Creating Polarization-Entangled Photon Pairs from a Semiconductor Quantum Dot Using the Optical Stark Effect. *Phys Rev Lett* **103,** 217402 (2009).

[249] Xie, Z., Zhong, T., Shrestha, S., Xu, X., Liang, J., Gong, Y.-X., Bienfang, J. C., Restelli, A., Shapiro, J. H., Wong, F. N. C. & Wong, C. W. Harnessing High-Dimensional Hyperentanglement through a Biphoton Frequency Comb. *Nat Photonics* **9,** 536–542 (2015).

[250] Cheng, X., Chang, K.-C., Xie, Z., Lee, Y. S., Sarihan, M. C., Kumar, A., Li, Y., Kocaman, S., Zhong, T., Yu, M., Kwong, D.-L., Shapiro, J. H., Wong, F. N. C. & Wong, C. W. An Efficient On-Chip Single-Photon SWAP Gate for Entanglement Manipulation. in *Conference on Lasers and Electro-Optics* FM2R.5 (OSA, 2020). doi:10.1364/CLEO_QELS.2020.FM2R.5

[251] Liu, J., Su, R., Wei, Y., Yao, B., Silva, S. F. C. da, Yu, Y., Iles-Smith, J., Srinivasan, K., Rastelli, A., Li, J. & Wang, X. A Solid-State Source of Strongly Entangled Photon Pairs with High Brightness and Indistinguishability. *Nat Nanotechnol* **14,** 586–593 (2019).

[252] Arsenault, A. C., Clark, T. J., Von Freymann, G., Cademartiri, L., Sapienza, R., Bertolotti, J., Vekris, E., Wong, S., Kitaev, V., Manners, I., Wang, R. Z., John, S., Wiersma, D. & Ozin, G. A. From Colour Fingerprinting to the Control of Photoluminescence in Elastic Photonic Crystals. *Nat Mater* **5,** 179–184 (2006).

[253] Sun, S., Kim, H., Solomon, G. S. & Waks, E. A Quantum Phase Switch between a Single Solid-State Spin and a Photon. *Nat Nanotechnol* **11,** 539–544 (2016).

[254] Russo, A., Barnes, E. & Economou, S. E. Photonic Graph State Generation from Quantum Dots and Color Centers for Quantum Communications. *Phys Rev B* **98,** 085303 (2018).

[255] Schwartz, I., Schmidgall, E. R., Gantz, L., Cogan, D., Bordo, E., Don, Y., Zielinski, M. & Gershoni, D. Deterministic Writing and Control of the Dark Exciton Spin Using Single Short Optical Pulses. *Phys Rev X* **5,** 011009 (2015).

[256] Layden, D., Chen, M. & Cappellaro, P. Efficient Quantum Error Correction of Dephasing Induced by a Common Fluctuator. *Phys Rev Lett* **124,** 020504 (2020).

[257] Schöll, E., Hanschke, L., Schweickert, L., Zeuner, K. D., Reindl, M., Covre da Silva, S. F., Lettner, T., Trotta, R., Finley, J. J., Müller, K., Rastelli, A., Zwiller, V. & Jöns, K. D. Resonance Fluorescence of GaAs Quantum Dots with Near-Unity Photon Indistinguishability. *Nano Lett* **19,** 2404–2410 (2019).

[258] Nawrath, C., Olbrich, F., Paul, M., Portalupi, S. L., Jetter, M. & Michler, P. Coherence and Indistinguishability of Highly Pure Single Photons from Non-Resonantly and Resonantly Excited Telecom C-Band Quantum Dots. *Appl Phys Lett* **115,** 023103 (2019).

[259] Auffèves, A., Gerace, D., Gérard, J.-M., Santos, M. F., Andreani, L. C. & Poizat, J.-P. Controlling the Dynamics of a Coupled Atom-Cavity System by Pure Dephasing. *Phys Rev B* **81,** 245419 (2010).

[260] Bayer, M. & Forchel, A. Temperature Dependence of the Exciton Homogeneous Linewidth in $In_{0.60}Ga_{0.40}As$/GaAs Self-Assembled Quantum Dots. *Phys Rev B Condens Matter Mater Phys* **65,** 1–4 (2002).

[261] Roy, C. & Hughes, S. Influence of Electron-Acoustic Phonon Scattering on Intensity Power Broadening in a Coherently Driven Quantum-Dot Cavity System. *Phys Rev X* **1,** 1–19 (2011).

[262] Roy, C. & Hughes, S. Phonon-Dressed Mollow Triplet in the Regime of Cavity Quantum Electrodynamics: Excitation-Induced Dephasing and Nonperturbative Cavity Feeding Effects. *Phys Rev Lett* **106,** 247403 (2011).

[263] Majumdar, A., Kim, E. D., Gong, Y., Bajcsy, M. & Vučković, J. Phonon Mediated Off-Resonant Quantum Dot-Cavity Coupling under Resonant Excitation of the Quantum Dot. *Phys Rev B Condens Matter Mater Phys* **84,** 085309 (2011).

[264] Morreau, A. & Muljarov, E. A. Phonon-Induced Dephasing in Quantum-Dot-Cavity QED. *Phys Rev B* **100,** 115309 (2019).

[265] Ates, S., Ulrich, S. M., Ulhaq, A., Reitzenstein, S., Löffler, A., Höfling, S., Forchel, A. & Michler, P. Non-Resonant Dot–Cavity Coupling and Its Potential for Resonant Single-Quantum-Dot Spectroscopy. *Nat Photonics* **3,** 724–728 (2009).

[266] Naesby, A., Suhr, T., Kristensen, P. T. & Mørk, J. Influence of Pure Dephasing on Emission Spectra from Single Photon Sources. *Phys Rev A* **78,** 045802 (2008).

[267] Auffèves, A., Gérard, J. M. & Poizat, J. P. Pure Emitter Dephasing: A Resource for Advanced Solid-State Single-Photon Sources. *Phys Rev A* **79,** 053838 (2009).

[268] Cui, G. & Raymer, M. G. Emission Spectra and Quantum Efficiency of Single-Photon Sources in the Cavity-QED Strong-Coupling Regime. *Phys Rev A* **73,** (2006).

[269] Valente, D., Suffczyński, J., Jakubczyk, T., Dousse, A., Lemaître, A., Sagnes, I., Lanco, L., Voisin, P., Auffèves, A. & Senellart, P. Frequency Cavity Pulling Induced by a Single Semiconductor Quantum Dot. *Phys Rev B* **89,** 041302 (2014).

[270] Giesz, V. *Cavity-enhanced Photon-Photon Interactions With Bright Quantum Dot Sources*.

[271] Tawara, T., Kamada, H., Tanabe, T., Sogawa, T., Okamoto, H., Yao, P., Pathak, P. K. & Hughes, S. Cavity-QED Assisted Attraction between a Cavity Mode and an Exciton Mode in a Planar Photonic-Crystal Cavity. *Opt Express* **18,** 2719 (2010).

[272] Echeverri-Arteaga, S., Vinck-Posada, H. & Gómez, E. A. The Strange Attraction Phenomenon in CQED: The Intermediate Quantum Coupling Regime. *Optik (Stuttg)* **183,** 389–394 (2019).

[273] Echeverri-Arteaga, S., Vinck-Posada, H. & Gómez, E. A. Explanation of the Quantum Phenomenon of Off-Resonant Cavity-Mode Emission. *Phys Rev A (Coll Park)* **97,** 043815 (2018).

[274] Toda, Y., Moriwaki, O., Nishioka, M. & Arakawa, Y. Efficient Carrier Relaxation Mechanism in In Gaas/Gaas Self-Assembled Quantum Dots Based on the Existence of Continuum States. *Phys Rev Lett* **82,** 4114–4117 (1999).

[275] Vasanelli, A., Ferreira, R. & Bastard, G. Continuous Absorption Background and Decoherence in Quantum Dots. *Phys Rev Lett* **89,** 216804 (2002).

[276] Jarlov, C. Cavity Quantum Electrodynamics with Systems of Site-Controlled Quantum Dots and Photonic Crystal Cavities. *PhD thesis, EPFL* **7039,** (2016).

[277] John, S., Soukoulis, C., Cohen, M. H. & Economou, E. N. Theory of Electron Band Tails and the Urbach Optical-Absorption Edge. *Phys Rev Lett* **57,** 1777–1780 (1986).

[278] Urbach, F. The Long-Wavelength Edge of Photographic Sensitivity and of the Electronic Absorption of Solids. *Physical Review* **92,** 1324–1324 (1953).

[279] Jarlov, C., Gallo, P., Calic, M., Dwir, B., Rudra, A. & Kapon, E. Bound and Anti-Bound Biexciton in Site-Controlled Pyramidal GaInAs/GaAs Quantum Dots. *Appl Phys Lett* **101,** 191101 (2012).

[280] Cade, N. I., Gotoh, H., Kamada, H., Nakano, H. & Okamoto, H. Fine Structure and Magneto-Optics of Exciton, Trion, and Charged Biexciton States in Single InAs Quantum Dots Emitting at 1.3 μm. *Phys Rev B* **73,** 115322 (2006).

[281] Muljarov, E. A. & Zimmermann, R. Dephasing in Quantum Dots: Quadratic Coupling to Acoustic Phonons. *Phys Rev Lett* **93,** 237401 (2004).

[282] Ware, M. E., Stinaff, E. A., Gammon, D., Doty, M. F., Bracker, A. S., Gershoni, D., Korenev, V. L., Bădescu, Ş. C., Lyanda-Geller, Y. & Reinecke, T. L. Polarized Fine Structure in the

Photoluminescence Excitation Spectrum of a Negatively Charged Quantum Dot. *Phys Rev Lett* **95,** 177403 (2005).

[283] Johnsson, M., Góngora, D. R., Martinez-Pastor, J. P., Volz, T., Seravalli, L., Trevisi, G., Frigeri, P. & Muñoz-Matutano, G. Ultrafast Carrier Redistribution in Single InAs Quantum Dots Mediated by Wetting-Layer Dynamics. *Phys Rev Appl* **11,** 54043 (2019).

[284] Huber, D., Lehner, B. U., Csontosová, D., Reindl, M., Schuler, S., Covre Da Silva, S. F., Klenovský, P. & Rastelli, A. Single-Particle-Picture Breakdown in Laterally Weakly Confining GaAs Quantum Dots. *Phys Rev B* **100,** 235425 (2019).

[285] Poem, E., Kodriano, Y., Tradonsky, C., Lindner, N. H., Gerardot, B. D., Petroff, P. M. & Gershoni, D. Accessing the Dark Exciton with Light. *Nat Phys* **6,** 993–997 (2010).

[286] Ortner, G., Bayer, M., Larionov, A., Timofeev, V. B., Forchel, A., Lyanda-Geller, Y. B., Reinecke, T. L., Hawrylak, P., Fafard, S. & Wasilewski, Z. Fine Structure of Excitons in [Formula Presented] Coupled Quantum Dots: A Sensitive Test of Electronic Coupling. *Phys Rev Lett* **90,** 4 (2003).

[287] Smoleński, T., Kazimierczuk, T., Goryca, M., Jakubczyk, T., Kłopotowski, L., Cywiński, L., Wojnar, P., Golnik, A. & Kossacki, P. In-Plane Radiative Recombination Channel of a Dark Exciton in Self-Assembled Quantum Dots. *Phys Rev B Condens Matter Mater Phys* **86,** 241305 (2012).

[288] Laussy, F. P., del Valle, E. & Tejedor, C. Luminescence Spectra of Quantum Dots in Microcavities. I. Bosons. *Phys Rev B* **79,** 235325 (2009).

[289] Srinivasan, K. & Painter, O. Linear and Nonlinear Optical Spectroscopy of a Strongly Coupled Microdisk–Quantum Dot System. *Nature* **450,** 862–865 (2007).

[290] Kim, H., Sridharan, D., Shen, T. C., Solomon, G. S. & Waks, E. Strong Coupling between Two Quantum Dots and a Photonic Crystal Cavity Using Magnetic Field Tuning. *Opt Express* **19,** 2589 (2011).

[291] QuCoa Quantum Correlation Analysis Software.

[292] Brouri, R., Beveratos, A., Poizat, J.-P. & Grangier, P. Photon Antibunching in the Fluorescence of Individual Color Centers in Diamond. *Opt Lett* **25,** 1294 (2000).

[293] Kiraz, A., Falth, S., Becher, C., Gayral, B., Schoenfeld, W. V., Petroff, P. M., Zhang, L., Hu, E. & Imamoglu, A. Photon Correlation Spectroscopy of a Single Quantum Dot. *Phys Rev B* **65,** 161303 (2001).

[294] Tamariz, S., Callsen, G., Stachurski, J., Shojiki, K., Butté, R. & Grandjean, N. Towards Bright and Pure Single Photon Emitters at 300 K Based on GaN Quantum Dots on Silicon. *ACS Photonics* **7,** 1515–1522 (2020).

[295] Echeverri-Arteaga, S., Vinck-Posada, H., Villas-Bôas, J. M. & Gómez, E. A. Pure Dephasing vs. Phonon Mediated off-Resonant Coupling in a Quantum-Dot-Cavity System. *Opt Commun* **460,** 125115 (2020).

[296] Faraon, A., Fushman, I., Englund, D., Stoltz, N., Petroff, P. & Vučković, J. Coherent Generation of Non-Classical Light on a Chip via Photon-Induced Tunnelling and Blockade. *Nat Phys* **4,** 859–863 (2008).

[297] Faraon, A., Majumdar, A. & Vučković, J. Generation of Nonclassical States of Light via Photon Blockade in Optical Nanocavities. *Phys Rev A (Coll Park)* **81,** 033838 (2010).

[298] Majumdar, A., Bajcsy, M. & Vuckovic, J. Probing the Ladder of Dressed States and Nonclassical Light Generation in Quantum Dot-Cavity QED. *Phys Rev A* **85,** 041801 (2011).

[299] Wells, L. M., Kalliakos, S., Villa, B., Ellis, D. J. P., Stevenson, R. M., Bennett, A. J., Farrer, I., Ritchie, D. A. & Shields, A. J. Photon Phase Shift at the Few-Photon Level and Optical Switching by a Quantum Dot in a Microcavity. *Phys Rev Appl* **11,** 061001 (2019).

[300] Coste, N., Fioretto, D., Belabas, N., Wein, S. C., Hilaire, P., Frantzeskakis, R., Gundin, M., Goes, B., Somaschi, N., Morassi, M., Lemaître, A., Sagnes, 1 I., Harouri, A., Economou, S. E., Auffeves, A., Krebs, O., Lanco, L. & Senellart, P. High-Rate Entanglement between a Semiconductor Spin and Indistinguishable Photons. *Nat Photonics* **17,** 582–587 (2022).

[301] Mabuchi, H. & Doherty, A. C. Cavity Quantum Electrodynamics: Coherence in Context. *Science (1979)* **298,** 1372–1377 (2002).

[302] Dory, C., Fischer, K. A., Müller, K., Lagoudakis, K. G., Sarmiento, T., Rundquist, A., Zhang, J. L., Kelaita, Y. & Vuèkovic, J. Complete Coherent Control of a Quantum Dot Strongly Coupled to a Nanocavity. *Scientific Reports 2016 6:1* **6,** 1–8 (2016).

[303] Pscherer, A., Meierhofer, M., Wang, D., Kelkar, H., Martín-Cano, D., Utikal, T., Götzinger, S. & Sandoghdar, V. Single-Molecule Vacuum Rabi Splitting: Four-Wave Mixing and Optical Switching at the Single-Photon Level. *Phys Rev Lett* **127,** 133603 (2021).

[304] Fan, L. B., Shu, C. C., Dong, D., He, J., Henriksen, N. E. & Nori, F. Quantum Coherent Control of a Single Molecular-Polariton Rotation. *Phys Rev Lett* **130,** 043604 (2023).

[305] Rezus, Y. L. A., Walt, S. G., Lettow, R., Renn, A., Zumofen, G., Götzinger, S. & Sandoghdar, V. Single-Photon Spectroscopy of a Single Molecule. *Phys Rev Lett* **108,** 093601 (2012).

[306] Wang, D., Kelkar, H., Martin-Cano, D., Rattenbacher, D., Shkarin, A., Utikal, T., Götzinger, S. & Sandoghdar, V. Turning a Molecule into a Coherent Two-Level Quantum System. *Nature Physics 2019 15:5* **15,** 483–489 (2019).

[307] Luo, Y., Chen, G., Zhang, Y., Zhang, L., Yu, Y., Kong, F., Tian, X., Zhang, Y., Shan, C., Luo, Y., Yang, J., Sandoghdar, V., Dong, Z. & Hou, J. G. Electrically Driven Single-Photon Superradiance from Molecular Chains in a Plasmonic Nanocavity. *Phys Rev Lett* **122,** 233901 (2019).

[308] Hilaire, P., Vidro, L., Eisenberg, H. S. & Economou, S. E. Near-Deterministic Hybrid Generation of Arbitrary Photonic Graph States Using a Single Quantum Emitter and Linear Optics. *Quantum* **7,** 992 (2023).

[309] Laucht, A., Hauke, N., Villas-Bôas, J. M., Hofbauer, F., Böhm, G., Kaniber, M. & Finley, J. J. Dephasing of Exciton Polaritons in Photoexcited InGaAs Quantum Dots in GaAs Nanocavities. *Phys Rev Lett* **103,** 087405 (2009).

[310] Gonzalez-Tudela, A., del Valle, E., Cancellieri, E., Tejedor, C., Sanvitto, D. & Laussy, F. P. Effect of Pure Dephasing on the Jaynes-Cummings Nonlinearities. *Opt Express* **18,** 7002 (2010).

[311] Vagov, A., Glässl, M., Croitoru, M. D., Axt, V. M. & Kuhn, T. Competition between Pure Dephasing and Photon Losses in the Dynamics of a Dot-Cavity System. *Phys Rev B* **90,** 075309 (2014).

[312] Hohenester, U., Laucht, A., Kaniber, M., Hauke, N., Neumann, A., Mohtashami, A., Seliger, M., Bichler, M. & Finley, J. J. Phonon-Assisted Transitions from Quantum Dot Excitons to Cavity Photons. *Phys Rev B* **80,** 201311 (2009).

[313] Moody, G., Sorger, V. J., Blumenthal, D. J., Juodawlkis, P. W., Loh, W., Sorace-Agaskar, C., Jones, A. E., Balram, K. C., Matthews, J. C. F., Laing, A., Davanco, M., Chang, L., Bowers, J. E., Quack, N., Galland, C., Aharonovich, I., Wolff, M. A., Schuck, C., Sinclair, N., Lončar, M., Komljenovic, T., Weld, D., Mookherjea, S., Buckley, S., Radulaski, M., Reitzenstein, S., Pingault, B., Machielse, B., Mukhopadhyay, D., Akimov, A., Zheltikov, A., Agarwal, G. S., Srinivasan, K., Lu, J., Tang, H. X., Jiang, W., McKenna, T. P., Safavi-Naeini, A. H., Steinhauer, S., Elshaari, A. W., Zwiller, V., Davids, P. S., Martinez, N., Gehl, M., Chiaverini, J., Mehta, K. K., Romero, J., Lingaraju, N. B., Weiner, A. M., Peace, D., Cernansky, R., Lobino, M., Diamanti, E., Vidarte, L. T. & Camacho, R. M. 2022 Roadmap on Integrated Quantum Photonics. *Journal of Physics: Photonics* **4,** 012501 (2022).

[314] Kiravittaya, S., Rastelli, A. & Schmidt, O. G. Advanced Quantum Dot Configurations. *Reports on Progress in Physics* **72,** 046502 (2009).

[315] Hartmann, A., Ducommun, Y., Leifer, K. & Kapon, E. Structure and Optical Properties of Semiconductor Quantum Nanostructures Self-Formed in Inverted Tetrahedral Pyramids. *Journal of Physics: Condensed Matter* **11,** 5901 (1999).

[316] Khitrova, G., Gibbs, H. M., Kira, M., Koch, S. W. & Scherer, A. Vacuum Rabi Splitting in Semiconductors. *Nat Phys* **2,** 81–90 (2006).

[317] Schaibley, J. R., Burgers, A. P., McCracken, G. A., Steel, D. G., Bracker, A. S., Gammon, D. & Sham, L. J. Direct Detection of Time-Resolved Rabi Oscillations in a Single Quantum Dot via Resonance Fluorescence. *Phys Rev B* **87,** 115311 (2013).

[318] Press, D., Götzinger, S., Reitzenstein, S., Hofmann, C., Löffler, A., Kamp, M., Forchel, A. & Yamamoto, Y. Photon Antibunching from a Single Quantum-Dot-Microcavity System in the Strong Coupling Regime. *Phys Rev Lett* **98,** 117402 (2007).

[319] Yamaguchi, M., Lyasota, A., Yuge, T. & Ota, Y. Time-Resolved Physical Spectrum in Cavity Quantum Electrodynamics. *Phys Rev Res* **4,** 023052 (2022).

[320] Laussy, F. P., Del Valle, E. & Tejedor, C. Strong Coupling of Quantum Dots in Microcavities. *Phys Rev Lett* **101,** 083601 (2008).

[321] Gies, C., Gericke, F., Gartner, P., Holzinger, S., Hopfmann, C., Heindel, T., Wolters, J., Schneider, C., Florian, M., Jahnke, F., Höfling, S., Kamp, M. & Reitzenstein, S. Strong Light-Matter Coupling in the Presence of Lasing. *Phys Rev A (Coll Park)* **96,** 023806 (2017).

[322] Schatzl, M., Hackl, F., Glaser, M., Brehm, M., Rauter, P., Simbula, A., Galli, M., Fromherz, T. & Schäffler, F. Local Density-of-States Mapping in Photonic Crystal Resonators by Deterministically Positioned Germanium Quantum Dots. (2016). at <http://arxiv.org/abs/1607.06701>

[323] Gopinath, A., Miyazono, E., Faraon, A. & Rothemund, P. W. K. Engineering and Mapping Nanocavity Emission via Precision Placement of DNA Origami. *Nature* **535,** 401–5 (2016).

[324] Sapienza, R., Coenen, T., Renger, J., Kuttge, M., van Hulst, N. F. & Polman, A. Deep-Subwavelength Imaging of the Modal Dispersion of Light. *Nat Mater* **11,** 781–787 (2012).

[325] La China, F., Intonti, F., Caselli, N., Lotti, F., Vinattieri, A., Vico Triviño, N., Carlin, J. F., Butté, R., Grandjean, N. & Gurioli, M. Vectorial Near-Field Imaging of a GaN Based Photonic Crystal Cavity. *Appl Phys Lett* **107,** (2015).

[326] Caselli, N., Intonti, F., La China, F., Riboli, F., Gerardino, A., Bao, W., Bargioni, A. W., Li, L., Linfield, E. H., Pagliano, F., Fiore, A. & Gurioli, M. Ultra-Subwavelength Phase-Sensitive Fano-Imaging of Localized Photonic Modes. *Light Sci Appl* **4,** e326–e326 (2015).

[327] Le Thomas, N., Alexander, D. T. L., Cantoni, M., Sigle, W., Houdré, R. & Hébert, C. Imaging of High-Q Cavity Optical Modes by Electron Energy-Loss Microscopy. *Phys Rev B Condens Matter Mater Phys* **87,** 155314 (2013).

[328] Kasprzak, J., Richard, M., Kundermann, S., Baas, A., Jeambrun, P., Keeling, J. M. J., Marchetti, F. M., Szymańska, M. H., André, R., Staehli, J. L., Savona, V., Littlewood, P. B., Deveaud, B. & Dang, L. S. Bose-Einstein Condensation of Exciton Polaritons. *Nature* **443,** 409–14 (2006).

[329] Deng, H., Haug, H. & Yamamoto, Y. Exciton-Polariton Bose-Einstein Condensation. *Rev Mod Phys* **82,** 1489–1537 (2010).

[330] Kavokin, A., Liew, T. C. H., Schneider, C., Lagoudakis, P. G., Klembt, S. & Hoefling, S. Polariton Condensates for Classical and Quantum Computing. *Nature Reviews Physics 2022 4:7* **4,** 435–451 (2022).

[331] Byrnes, T., Kim, N. Y. & Yamamoto, Y. Exciton-Polariton Condensates. *Nature Physics 2014 10:11* **10,** 803–813 (2014).

[332] Schneider, C., Winkler, K., Fraser, M. D., Kamp, M., Yamamoto, Y., Ostrovskaya, E. A. & Höfling, S. Exciton-Polariton Trapping and Potential Landscape Engineering. *Reports on Progress in Physics* **80,** 016503 (2017).

[333] Denning, E. V., Wubs, M., Stenger, N., Mørk, J. & Kristensen, P. T. Cavity-Induced Exciton Localization and Polariton Blockade in Two-Dimensional Semiconductors Coupled to an Electromagnetic Resonator. *Phys Rev Res* **4,** L012020 (2022).

[334] Bastarrachea-Magnani, M. A., Camacho-Guardian, A. & Bruun, G. M. Attractive and Repulsive Exciton-Polariton Interactions Mediated by an Electron Gas. *Phys Rev Lett* **126,** 127405 (2021).

[335] Ferrier, L., Wertz, E., Johne, R., Solnyshkov, D. D., Senellart, P., Sagnes, I., Lemaître, A., Malpuech, G. & Bloch, J. Interactions in Confined Polariton Condensates. *Phys Rev Lett* **106,** 126401 (2011).

[336] Aladinskaia, E., Cherbunin, R., Sedov, E., Liubomirov, A., Kavokin, K., Khramtsov, E., Petrov, M., Savvidis, P. G. & Kavokin, A. Spatial Quantization of Exciton-Polariton Condensates in Optically Induced Traps. *Phys Rev B* **107,** 045302 (2023).

[337] Ouellet-Plamondon, C., Sallen, G., Morier-Genoud, F., Oberli, D. Y., Portella-Oberli, M. T. & Deveaud, B. Spatial Multistability Induced by Cross Interactions of Confined Polariton Modes. *Phys Rev B* **93,** 085313 (2016).

[338] Askitopoulos, A., Liew, T. C. H., Ohadi, H., Hatzopoulos, Z., Savvidis, P. G. & Lagoudakis, P. G. Robust Platform for Engineering Pure-Quantum-State Transitions in Polariton Condensates. *Phys Rev B Condens Matter Mater Phys* **92,** 035305 (2014).

[339] Cerna, R., Sarchi, D., Paraïso, T. K., Nardin, G., Léger, Y., Richard, M., Pietka, B., El Daif, O., Morier-Genoud, F., Savona, V., Portella-Oberli, M. T. & Deveaud-Plédran, B. Coherent Optical Control of the Wave Function of Zero-Dimensional Exciton Polaritons. *Phys Rev B Condens Matter Mater Phys* **80,** 121309 (2009).

[340] Kaitouni, R. I., El Daïf, O., Baas, A., Richard, M., Paraiso, T., Lugan, P., Guillet, T., Morier-Genoud, F., Ganière, J. D., Staehli, J. L., Savona, V. & Deveaud, B. Engineering the Spatial Confinement of Exciton Polaritons in Semiconductors. *Phys Rev B* **74,** 155311 (2006).

[341] Kim, N. Y., Kusudo, K., Wu, C., Masumoto, N., Löffler, A., Höfling, S., Kumada, N., Worschech, L., Forchel, A. & Yamamoto, Y. Dynamical D-Wave Condensation of Exciton–Polaritons in a Two-Dimensional Square-Lattice Potential. *Nature Physics 2011 7:9* **7,** 681–686 (2011).

[342] Yang, X., Husko, C., Wong, C. W., Yu, M. & Kwong, D. L. Observation of Femtojoule Optical Bistability Involving Fano Resonances in High- Q Vm Silicon Photonic Crystal Nanocavities. *Appl Phys Lett* **91,** (2007).

[343] Yamaguchi, M., Lyasota, A. & Yuge, T. Theory of Fano Effect in Cavity Quantum Electrodynamics. *Phys Rev Res* **3,** (2021).

[344] Cheng, X., Chang, K. C., Xie, Z., Sarihan, M. C., Lee, Y. S., Li, Y., Xu, X. A., Vinod, A. K., Kocaman, S., Yu, M., Lo, P. G. Q., Kwong, D. L., Shapiro, J. H., Wong, F. N. C. & Wong,

C. W. A Chip-Scale Polarization-Spatial-Momentum Quantum SWAP Gate in Silicon Nanophotonics. *Nature Photonics 2023 17:8* **17,** 656–665 (2023).

[345] Zhai, L., Nguyen, G. N., Spinnler, C., Ritzmann, J., Löbl, M. C., Wieck, A. D., Ludwig, A., Javadi, A. & Warburton, R. J. Quantum Interference of Identical Photons from Remote GaAs Quantum Dots. *Nat Nanotechnol* **17,** (2022).

[346] Giesz, V., Portalupi, S. L., Grange, T., Antón, C., De Santis, L., Demory, J., Somaschi, N., Sagnes, I., Lemaître, A., Lanco, L., Auffèves, A. & Senellart, P. Cavity-Enhanced Two-Photon Interference Using Remote Quantum Dot Sources. *Phys Rev B Condens Matter Mater Phys* **92,** (2015).

[347] Patel, R. B., Bennett, A. J., Farrer, I., Nicoll, C. A., Ritchie, D. A. & Shields, A. J. Two-Photon Interference of the Emission from Electrically Tunable Remote Quantum Dots. *Nat Photonics* **4,** (2010).

[348] Bose, R., Sridharan, D., Kim, H., Solomon, G. S. & Waks, E. Low-Photon-Number Optical Switching with a Single Quantum Dot Coupled to a Photonic Crystal Cavity. *Phys Rev Lett* **108,** 227402 (2012).

[349] Xavier, G. B. & Lima, G. Quantum Information Processing with Space-Division Multiplexing Optical Fibres. *Communications Physics 2020 3:1* **3,** 1–11 (2020).

[350] Hayat, A., Lange, C., Rozema, L. A., Darabi, A., Van Driel, H. M., Steinberg, A. M., Nelsen, B., Snoke, D. W., Pfeiffer, L. N. & West, K. W. Dynamic Stark Effect in Strongly Coupled Microcavity Exciton Polaritons. *Phys Rev Lett* **109,** 033605 (2012).

[351] Stolz, T., Hegels, H., Winter, M., Röhr, B., Hsiao, Y. F., Husel, L., Rempe, G. & Dürr, S. Quantum-Logic Gate between Two Optical Photons with an Average Efficiency above 40%. *Phys Rev X* **12,** 021035 (2022).

[352] Kok, P., Munro, W. J., Nemoto, K., Ralph, T. C., Dowling, J. P. & Milburn, G. J. Linear Optical Quantum Computing with Photonic Qubits. *Rev Mod Phys* **79,** 135–174 (2007).

[353] Wei, S.-H., Jing, B., Zhang, X.-Y., Liao, J.-Y., Yuan, C.-Z., Fan, B.-Y., Lyu, C., Zhou, D.-L., Wang, Y., Deng, G.-W., Song, H.-Z., Oblak, D., Guo, G.-C., Zhou, Q., Wei, S.-H., Jing, B., Zhang, X.-Y., Liao, J.-Y., Yuan, C.-Z., Fan, B.-Y., Lyu, C., Zhou, D.-L., Wang, Y., Deng, G.-W., Song, H.-Z., Guo, G.-C., Zhou, Q. & Oblak, D. Towards Real-World Quantum Networks: A Review. *Laser Photon Rev* **16,** 2100219 (2022).

[354] Ritter, S., Nölleke, C., Hahn, C., Reiserer, A., Neuzner, A., Uphoff, M., Mücke, M., Figueroa, E., Bochmann, J. & Rempe, G. An Elementary Quantum Network of Single Atoms in Optical Cavities. *Nature 2012 484:7393* **484,** 195–200 (2012).

[355] Reiserer, A. & Rempe, G. Cavity-Based Quantum Networks with Single Atoms and Optical Photons. *Rev Mod Phys* **87,** (2015).

[356] Wolfowicz, G., Heremans, F. J., Anderson, C. P., Kanai, S., Seo, H., Gali, A., Galli, G. & Awschalom, D. D. Quantum Guidelines for Solid-State Spin Defects. *Nat Rev Mater* **6,** (2021).

[357] Hermans, S. L. N., Pompili, M., Beukers, H. K. C., Baier, S., Borregaard, J. & Hanson, R. Qubit Teleportation between Non-Neighbouring Nodes in a Quantum Network. *Nature* **605,** (2022).

[358] Munro, W. J., Piparo, N. Lo, Dias, J., Hanks, M. & Nemoto, K. Designing Tomorrow's Quantum Internet. *AVS Quantum Science* **4,** (2022).

[359] Reiserer, A. Colloquium: Cavity-Enhanced Quantum Network Nodes. *Rev Mod Phys* **94,** (2022).

[360] Bhaskar, M. K., Riedinger, R., Machielse, B., Levonian, D. S., Nguyen, C. T., Knall, E. N., Park, H., Englund, D., Lončar, M., Sukachev, D. D. & Lukin, M. D. Experimental Demonstration of Memory-Enhanced Quantum Communication. *Nature 2020 580:7801* **580,** 60–64 (2020).

[361] Qin, W., Miranowicz, A. & Nori, F. Proposal of Ensemble Qubits with Two-Atom Decay. (2023). at <https://arxiv.org/abs/2302.06781v1>

[362] Levonian, D. S., Riedinger, R., Machielse, B., Knall, E. N., Bhaskar, M. K., Knaut, C. M., Bekenstein, R., Park, H., Lončar, M. & Lukin, M. D. Optical Entanglement of Distinguishable Quantum Emitters. *Phys Rev Lett* **128,** (2022).

[363] Stas, P. J., Huan, Y. Q., Machielse, B., Knall, E. N., Suleymanzade, A., Pingault, B., Sutula, M., Ding, S. W., Knaut, C. M., Assumpcao, D. R., Wei, Y. C., Bhaskar, M. K., Riedinger, R., Sukachev, D. D., Park, H., Lončar, M., Levonian, D. S. & Lukin, M. D. Robust Multi-Qubit Quantum Network Node with Integrated Error Detection. *Science (1979)* **378,** (2022).

[364] Lei, Y., Lei, Y., Lei, Y., Asadi, F. K., Zhong, T., Kuzmich, A., Simon, C., Hosseini, M., Hosseini, M. & Hosseini, M. Quantum Optical Memory for Entanglement Distribution. *Optica, Vol. 10, Issue 11, pp. 1511-1528* **10,** 1511–1528 (2023).

[365] Cozzolino, D., Da Lio, B., Bacco, D. & Oxenløwe, L. K. High-Dimensional Quantum Communication: Benefits, Progress, and Future Challenges. *Adv Quantum Technol* **2,** (2019).

[366] Erhard, M., Krenn, M. & Zeilinger, A. Advances in High-Dimensional Quantum Entanglement. *Nature Reviews Physics* **2,** (2020).

[367] Yang, S., Sarihan, M. C., Chang, K. C., Wong, C. W. & Dolecek, L. Efficient Information Reconciliation for Energy-Time Entanglement Quantum Key Distribution. in *Conf Rec Asilomar Conf Signals Syst Comput* **2019-November,** (2019).

[368] Chang, K. C., Cheng, X., Sarihan, M. C., Vinod, A. K., Lee, Y. S., Zhong, T., Gong, Y. X., Xie, Z., Shapiro, J. H., Wong, F. N. C. & Wong, C. W. 648 Hilbert-Space Dimensionality in a Biphoton Frequency Comb: Entanglement of Formation and Schmidt Mode Decomposition. *npj Quantum Information 2021 7:1* **7,** 1–11 (2021).

[369] Berkman, I. R., Lyasota, A., de Boo, G. G., Bartholomew, J. G., Lim, S. Q., Johnson, B. C., McCallum, J. C., Xu, B.-B., Xie, S., Abrosimov, N. V., Pohl, H.-J., Ahlefeldt, R. L., Sellars, M. J., Yin, C. & Rogge, S. Millisecond Electron Spin Coherence Time for Erbium Ions in Silicon. (2023). at <https://arxiv.org/abs/2307.10021v2>

[370] Gritsch, A., Gritsch, A., Ulanowski, A., Ulanowski, A., Reiserer, A. & Reiserer, A. Purcell Enhancement of Single-Photon Emitters in Silicon. *Optica, Vol. 10, Issue 6, pp. 783-789* **10,** 783–789 (2023).

[371] Lee, C. W., Singh, M., Tamboli, A. C. & Stevanović, V. Transition Metal Impurities in Silicon: Computational Search for a Semiconductor Qubit. *NPJ Comput Mater* **8,** (2022).

[372] Durand, A., Baron, Y., Redjem, W., Herzig, T., Benali, A., Pezzagna, S., Meijer, J., Kuznetsov, A. Y., Gérard, J. M., Robert-Philip, I., Abbarchi, M., Jacques, V., Cassabois, G. & Dréau, A. Broad Diversity of Near-Infrared Single-Photon Emitters in Silicon. *Phys Rev Lett* **126,** (2021).

[373] Redjem, W., Durand, A., Herzig, T., Benali, A., Pezzagna, S., Meijer, J., Kuznetsov, A. Yu., Nguyen, H. S., Cueff, S., Gérard, J.-M., Robert-Philip, I., Gil, B., Caliste, D., Pochet, P., Abbarchi, M., Jacques, V., Dréau, A. & Cassabois, G. Single Artificial Atoms in Silicon Emitting at Telecom Wavelengths. *Nat Electron* **3,** 738–743 (2020).

[374] Sarihan, M. C., Huang, J., Liu, W., Kang, J. H., Liang, B. & Wong, C. W. Cryogenic O-Band Photoluminescence Spectroscopy of T-Centers in Monolithic Si for Mesoscopic Cavity Quantum Electrodynamics. in *2022 Conference on Lasers and Electro-Optics, CLEO 2022 - Proceedings* (2022). doi:10.1364/cleo_at.2022.jtu3b.36

[375] Fan, C., Sarihan, M. C., Huang, J., Azizur-Rahman, K. M., Kang, J. H., Liang, B., Liu, W. & Wong, C. W. Cryogenic Optical Spectroscopy of Color-Centers in Si for Quantum Information Processing. in *2023 Conference on Lasers and Electro-Optics, CLEO 2023* (2023). doi:10.1364/cleo_at.2023.jth2a.8

[376] Song, L. W., Zhan, X. D., Benson, B. W. & Watkins, G. D. Bistable Interstitial-Carbon Substitutional-Carbon Pair in Silicon. *Phys Rev B* **42,** (1990).

[377] Steger, M., Yang, A., Stavrias, N., Thewalt, M. L. W., Riemann, H., Abrosimov, N. V., Churbanov, M. F., Gusev, A. V., Bulanov, A. D., Kovalev, I. D., Kaliteevskii, A. K., Godisov, O. N., Becker, P. & Pohl, H. J. Reduction of the Linewidths of Deep Luminescence Centers in Si28 Reveals Fingerprints of the Isotope Constituents. *Phys Rev Lett* **100,** (2008).

[378] Steger, M., Yang, A., Sekiguchi, T., Saeedi, K., Thewalt, M. L. W., Henry, M. O., Johnston, K., Riemann, H., Abrosimov, N. V., Churbanov, M. F., Gusev, A. V., Kaliteevskii, A. K., Godisov, O. N., Becker, P. & Pohl, H. J. Photoluminescence of Deep Defects Involving Transition Metals in Si: New Insights from Highly Enriched 28Si. *J Appl Phys* **110,** (2011).

[379] Vinh, N. Q., Phillips, J., Davies, G. & Gregorkiewicz, T. Time-Resolved Free-Electron Laser Spectroscopy of a Copper Isoelectronic Center in Silicon. *Phys Rev B Condens Matter Mater Phys* **71,** (2005).

[380] McGuigan, K. G., Henry, M. O., Lightowlers, E. C., Steele, A. G. & Thewalt, M. L. W. A New Photoluminescence Band in Silicon Lightly Doped with Copper. *Solid State Commun* **68,** (1988).

[381] McGuigan, K. G., Henry, M. O., Carmo, M. C., Davies, G. & Lightowlers, E. C. A Uniaxial Stress Study of a Copper-Related Photoluminescence Band in Silicon. *Materials Science and Engineering B* **4,** (1989).

[382] MacQuarrie, E. R., Chartrand, C., Higginbottom, D. B., Morse, K. J., Karasyuk, V. A., Roorda, S. & Simmons, S. Generating T Centres in Photonic Silicon-on-Insulator Material by Ion Implantation. *New J Phys* **23,** 103008 (2021).

[383] Ziegler, J. F., Ziegler, M. D. & Biersack, J. P. SRIM - The Stopping and Range of Ions in Matter (2010). *Nucl Instrum Methods Phys Res B* **268,** (2010).

[384] Santos, I., Aboy, M., López, P., Marqués, L. A. & Pelaz, L. Insights on the Atomistic Origin of X and W Photoluminescence Lines in C-Si from Ab Initio Simulations. *J Phys D Appl Phys* **49,** (2016).

[385] Ivanov, V., Simoni, J., Lee, Y., Liu, W., Jhuria, K., Redjem, W., Zhiyenbayev, Y., Papapanos, C., Qarony, W., Kanté, B., Persaud, A., Schenkel, T. & Tan, L. Z. Effect of Localization on Photoluminescence and Zero-Field Splitting of Silicon Color Centers. *Phys Rev B* **106,** (2022).

[386] Cherkova, S. G., Skuratov, V. A. & Volodin, V. A. Luminescence Properties of FZ Silicon Irradiated with Swift Heavy Ions. *Semiconductors* **53,** (2019).

[387] Estreicher, S. K. & Carvalho, A. The CuPL Defect and the Cus1Cui3 Complex. *Physica B Condens Matter* **407,** 2967–2969 (2012).

[388] Fujimura, T. & Shirai, K. Revisiting the Stable Structure of the Cu4 Complex in Silicon. *Jpn J Appl Phys* **60,** (2021).

[389] Vincent, T. M. & Estreicher, S. K. Ag and Ag-Cu Interactions in Si. *J Appl Phys* **128,** (2020).

[390] Schenkel, T., Redjem, W., Persaud, A., Liu, W., Seidl, P. A., Amsellem, A. J., Kanté, B. & Ji, Q. Exploration of Defect Dynamics and Color Center Qubit Synthesis with Pulsed Ion Beams. *Quantum Beam Science* **6,** (2022).

[391] Thonke, K., Klemisch, H., Weber, J. & Sauer, R. New Model of the Irradiation-Induced 0.97-EV (G) Line in Silicon: A Cs - Si* Complex. *Phys Rev B* **24,** 5874–5886 (1981).

[392] Pässler, R. Parameter Sets Due to Fittings of the Temperature Dependencies of Fundamental Bandgaps in Semiconductors. *Phys Status Solidi B Basic Res* **216,** (1999).

[393] Cardona, M. & Thewalt, M. L. W. Isotope Effects on the Optical Spectra of Semiconductors. *Rev Mod Phys* **77,** (2005).

[394] Sjodin, T., Petek, H. & Dai, H. L. Ultrafast Carrier Dynamics in Silicon: A Two-Color Transient Reflection Grating Study on a (111) Surface. *Phys Rev Lett* **81,** (1998).

[395] Wörle, M., Holleitner, A. W., Kienberger, R. & Iglev, H. Ultrafast Hot-Carrier Relaxation in Silicon Monitored by Phase-Resolved Transient Absorption Spectroscopy. *Phys Rev B* **104,** L041201 (2021).

[396] Dhaliah, D., Xiong, Y., Sipahigil, A., Griffin, S. M. & Hautier, G. First-Principles Study of the T Center in Silicon. *Phys Rev Mater* **6,** (2022).

[397] Rosales, D., Bretagnon, T., Gil, B., Kahouli, A., Brault, J., Damilano, B., Massies, J., Durnev, M. V. & Kavokin, A. V. Excitons in Nitride Heterostructures: From Zero- to One-Dimensional Behavior. *Phys Rev B Condens Matter Mater Phys* **88,** (2013).

[398] McGuyer, B. H., McDonald, M., Iwata, G. Z., Tarallo, M. G., Skomorowski, W., Moszynski, R. & Zelevinsky, T. Precise Study of Asymptotic Physics with Subradiant Ultracold Molecules. *Nat Phys* **11,** 32–36 (2015).

[399] Stockill, R., Le Gall, C., Matthiesen, C., Huthmacher, L., Clarke, E., Hugues, M. & Atatüre, M. Quantum Dot Spin Coherence Governed by a Strained Nuclear Environment. *Nat Commun* **7,** 12745 (2016).

[400] Gangloff, D. A., Éthier-Majcher, G., Lang, C., Denning, E. V, Bodey, J. H., Jackson, D. M., Clarke, E., Hugues, M., Le Gall, C. & Atatüre, M. Quantum Interface of an Electron and a Nuclear Ensemble. *Science* **364,** 62–66 (2019).